UNDERSTANDING PROCESSING-MICROSTRUCTURE-PROPERTY RELATIONSHIPS AND THE ASSOCIATED DEFORMATION MECHANISMS IN ATI 718PLUS NI-BASED SUPERALLOY

By

Geeta Kumari

A DISSERTATION

Submitted to
Michigan State University
in partial fulfillment of the requirements
for the degree of

Materials Science and Engineering – Doctor of Philosophy

2024

ABSTRACT

A superalloy is a multi-metal alloy system that exhibits a good combination of high-temperature properties, such as resistance to thermal creep deformation, oxidation, and corrosion and has a service temperature often above 0.7 times the absolute melting temperature. Alloy ATI 718Plus is a relatively new Ni-based superalloy developed to improve upon the properties of Inconel 718. It shows improvement in service temperature up to 704 ºC (55 ºC more than IN718) and formability similar to IN 718 and better than that of Waspaloy because of its chemical composition, microstructure and major strengthening phase, gamma prime (γ'). The microstructure plays a vital role in controlling the mechanism of particle-dislocations interaction during deformation as the mechanism changes with particle size. The basic understanding of the active deformation mechanism with a unimodal distribution with average γ' particle size is well studied in the literature, but consideration of smaller and larger precipitates together, called bimodal microstructure, is still lacking. This study seeks to understand the development of a bimodal γ' precipitate size distribution in ATI 718Plus and its stability under various thermal and tensile stress conditions.

In this study, the initial selection of the solutionizing temperature was conducted for subsequent aging treatment. The as-processed sample underwent heat treatment at 1000°C for 1 hr, followed by water quenching (WQ). The aging process encompassed single-step and two-step methods with varied parameters, including time, temperature, and cooling rate. For the two-step treatment, the sample was heated to 900°C for 2 hr, then WQ to room temperature before being heated to 720°C for 10 hr and WQ again. The resultant microstructure displayed a uniform bimodal distribution of γ' precipitates, with sizes of 11 and 55 nm for smaller and larger precipitates, respectively. Samples

were prepared for characterization using scanning electron microscopy (SEM), transmission electron microscopy (TEM), and Atom Probe Tomography (APT).

The developed microstructures underwent tensile testing to failure to assess their yield strengths (YS), ultimate tensile strengths (UTS), and elongations-to-failure (ε_f). Some of the tensile samples, intentionally unloaded after achieving 2-4% engineering strain, were evaluated using TEM to investigate the γ' precipitate-dislocation interactions. In the case of unimodal samples, weak-pair shearing was observed to be the dominant mechanism for smaller γ' precipitates (~14 nm), while both strong-pair shearing and dislocation loops were observed for the microstructures containing larger γ' precipitates (~48 nm). The microstructure containing a bimodal distribution of γ' precipitates exhibited shearing as a dominant mechanism and also resulted in the highest strength values. The combined influence of temperature and elastic tensile stress on γ' precipitate stability was examined. Under simultaneous application of temperature and stress (creep), γ' precipitate growth accelerated in contrast to unstressed samples. The amount of growth varied with crystal orientations in the creep-deformed sample.

KEYWORDS: Nickel-based superalloy, ATI 718Plus, Gamma Prime (γ') precipitation, Bimodal γ' size microstructure, Particle-dislocation interaction, Tensile deformation, Thermal and stress application, Electron microscopy.

Dedicated to Baba Saheb (Dr. B. R. Ambedkar) for the inspiration and my parents for their unwavering support.

ACKNOWLEDGEMENTS

The culmination of this Ph.D. journey has been an arduous yet immensely rewarding endeavor, and it is with profound gratitude that I acknowledge the contributions and support of those who have made this journey possible.

First and foremost, I am profoundly grateful to my academic advisors, **Dr. Carl J. Boehlert, Dr. S. Sankaran,** and **Dr. M. Sundararaman** for their unwavering guidance and mentorship. A special thanks to Dr. Carl J. Boehlert for providing me the opportunity to come to MSU, which was a life-changing experience for me. His dedication to fostering my growth as a researcher and his inexhaustible patience in steering me through challenges have left an indelible mark on my academic and personal development. I would like to express my heartfelt thanks to the members of my doctoral committee at MSU, **Dr. Martin Crimp, Dr. Thomas Bieler**, and **Dr. Arun Ross**, and the doctoral committee at IITM, **Ganesh S. Sundara Raman, Kamaraj M, Subramanya V Sarma, Arockiarajan A,** and **Arunachalam N**, for their invaluable feedback and constructive criticism that have enriched the quality of this dissertation. My gratitude extends to **Dr. Philip Eisenlohr** of MSU for his willingness to engage in rigorous discussions during the metals meeting and practice presentation sessions.

I extend my deepest appreciation to **Dr. Shanelle N. Foster** for providing me the opportunity to be a part of her sponsored Office of Naval Research (ONR) project, which allowed me to broaden my horizons in the area of materials science. I would like to thank **Dr. Per Askeland, Dr. Alexandra Zevalkink, Ms Anne Eisenlohr** of MSU and **Dr. Jonathan Poplawsky, Dr. Kinga Unocic**, and Mr. **James P. Burns** at CNMS-ORNL for helping to conduct some of my experiments and mentoring me. I thank Mr. Kevin Bockenstedt of ATI Specialty Metals for providing the material for this work. I am thankful to the technical staff of the MME department, IITM, without

whom the experiments would never have been successful. I would like to specifically thank **Mr. Raki** for SEM imaging. I am grateful for the timely support and collaborative facility (TEM) provided by **IGCAR, India**, which allowed me to perform my experiments in a timely manner. I am profoundly thankful for the financial support provided by the National Science Foundation INTERN program and the US Department of Energy, Office of Basic Energy Science, which has enabled me to focus wholeheartedly on my research without the burden of financial constraints.

My heartfelt appreciation goes out to my fellow graduate students and colleagues at MSU (Dr. David Hernandez Escobar, Dr. Natalia Pajares, Mr. Tanzilur Rahman, Mr. Zackery Thune) and IITM (Dr. Sai Rajeshwari, Dr. Melwin Sajan, Dr. Maheshwari, Mr. Shubhashis Dixit, Mr. Avnish Kumar, Mr. Uma Sankar, Mr. Abhinav Karnati). Their camaraderie, collaborative spirit, and shared passion for research have created a nurturing academic community that I am privileged to be a part of. I would also like to extend my appreciation to undergraduate interns, Mr. Raul J. Vega Torres and Mr. Prottoy Samir, for their help in performing heat-treatments and hardness measurements.

To my friends, I owe an immeasurable debt of gratitude. Your unwavering encouragement, understanding, and love have provided the emotional sustenance necessary to navigate the challenges of this journey. It was not easy for them to console me during my tough times and motivate me to keep going. A special mention to my Internship mentor, **Dr. B.S. Murty**, for igniting the spark of research in me and guiding me to pursue doctoral studies as my career choice.

Finally, I reserve my deepest thanks for my parents, **Jiut Das** and **Dulari Devi,** my sister (**Reeta Kumari**), my brother (**Sunil Kumar**), and my partner (**Pranav Pillai**), whose unending support, sacrifices, and unwavering belief in my abilities have been the bedrock of my academic journey.

Your sacrifices have not been in vain, and this dissertation stands as a testament to your love and dedication.

In closing, I recognize that this journey has been a collective effort, and I am profoundly grateful to each and every individual who has played a part, no matter how small, in shaping my academic and personal growth. This dissertation is as much a reflection of your contributions as it is of my own perseverance and dedication.

TABLE OF CONTENTS

LIST OF SYMBOLS ix

LIST OF ABBREVIATIONS xi

CHAPTER 1. INTRODUCTION 1

CHAPTER 2. BACKGROUND AND LITERATURE 5

CHAPTER 3. MOTIVATION AND OBJECTIVES 43

CHAPTER 4. EXPERIMENTAL METHODS 46

CHAPTER 5. RESULTS 77

CHAPTER 6. DISCUSSION 135

CHAPTER 7. SUMMARY AND CONCLUSIONS 165

CHAPTER 8. FUTURE WORK SCOPE 168

BIBLIOGRAPHY 171

APPENDIX A: CODE FOR STRENGTHENING MODEL CALCULATIONS 182

APPENDIX B: SCHMID FACTOR CALCULATION 187

LIST OF SYMBOLS

a	Lattice parameter
a_{γ}	Lattice parameter of gamma matrix
$a_{\gamma'}$	Lattice parameter of gamma prime precipitate
b	Burger's vector
D	Average grain size
E	Young's modulus
F	Force acting on dislocation
f	Volume percent/fraction of gamma prime precipitate
l	Intercept line length
L	Inter-particle spacing from center-to-center
L_s	Inter-particle spacing from surface-to-surface
n	Temporal exponent
R	Gamma prime precipitate radius
Rc	Critical particle radius from shearing to looping
R_m	Critical particle radius from weak-pair to strong-pair shearing
t	Holding time
T	Dislocation line tension
w	Number fraction
k	Locking constant for grain boundary hardening
l_1	Segment length of leading dislocations
x_i	Atomic fraction of the substitutional element i
γ	Gamma matrix

γ_{APB}	Anti-phase boundary energy
δ	Delta phase
δ_m	Lattice misfit
ε_f	Elongation-to-failure
η	Eta phase
θ	Bowing angle
λ	Wavelength
λ_c	degree of cubicity
λ_c	Degree of cubicity
μ	Shear modulus
σ_{gb}	Grain boundary strengthening
σ_i	Friction stress to crystal lattice
σ_p	Precipitation strengthening
σ_{ss}	Solid solution strengthening
σ_y	Yield strength
$\Lambda 1$	Effective length of leading dislocation
γ'	Gamma prime
γ''	Gamma double prime

LIST OF ABBREVIATIONS

AC	Air cooling
APB	Anti-phase boundary
APBE	Anti-phase boundary energy
ASTM	American society for testing and materials
BCT	Body centered tetragonal
BF	Bright-field
CCT	Continuous-cooling-transformation
CI	Confidence index
CNMS	Center for nanophase materials
CRSS	Critical resolved shear stress
DF	Dark-field
EBSD	Electron back scattered diffraction
EDM	Electrical discharge machining
EDS	Energy dispersive X-ray spectroscopy
EELS	Electron energy loss spectroscopy
FC	Furnace cooling
FCC	Face centered cubic
FEG	Field-emission gun
FEPA	Federation of European Producers of Abrasives
FIB	Focus ion beam
HAADF	High-Angle Annular Dark-Field
HCP	Hexagonal closed pack

ICDD	International crystal diffraction data
IGCAR	Indira Gandhi Center for Atomic Research
IITM	Indian Institute of Technology Madras
IN718	Inconel 718
IPF	Inverse pole figure
OES	Optical emission spectroscopy
OM	Optical microscopy
ORNL	Oak Ridge National Laboratory
PFZ	Precipitate-free-zone
PSD	Precipitate size distribution
RT	Room temperature
SA	Standard aged
SADP	Selected area diffraction pattern
SD	Standard deviation
SEM	Scanning electron microscopy
SF	Stacking fault
ST	Solution-treated
STEM	Scanning Transmission Electron Microscopy
TCP	Topologically closed packed
TEM	Transmission electron microscopy
TTT	Time-temperature-transformation
UTS	Ultimate tensile strength
WBDF	Weak-beam dark-field

WQ	Water quenching
XRD	X-ray diffraction
YS	Yield strength

CHAPTER 1. INTRODUCTION

Superalloys represent an important class of materials known for their extraordinary high-temperature structural and environmental attributes, making them applicable in industries where performance under extreme conditions is paramount (R C Reed & C.M.F.Rae, 2014; Roger C. Reed, 2006). These alloys are distinguished by their excellent resistance to thermal creep deformation, oxidation, and corrosion, often exhibiting exceptional serviceability at temperatures that surpass 70% of their absolute melting point. Within this remarkable sphere of materials, the emergence of ATI 718Plus (hereafter referred to as 718Plus), a nickel-based alloy, stands as a promising innovation to elevate the already notable characteristics of Inconel 718 (Wei Di Cao & Kennedy, 2005). The primary objective of this alloy's development is the augmentation of service temperatures while retaining the formability of Inconel 718 and, notably, surpassing that of Waspaloy (Richard L. Kennedy, Cao, Bayha, & Jeniski, 2004). The superior performance of 718Plus is underpinned by its distinctive chemical composition, intricate microstructure, and the preeminent strengthening phase, gamma prime (γ').

The precipitation and growth of γ' precipitates in superalloys during cooling from high-temperatures are complex processes. The effect of cooling rates on the γ' precipitate evolution has also been studied, but varying results have been reported. With faster cooling, such as water quenching (WQ), uniform size γ' spherical precipitates tend to form with relatively high number density (Singh et al., 2011). With decreased continuous cooling rates, bimodal or multimodal (more than two different average sizes of the γ' precipitate) size distributions tend to develop (Alabbad, Li, & Tin, 2019; Singh et al., 2011). Multimodal γ' precipitate size distributions can be obtained with a controlled cooling rate through single-step isothermal aging. In contrast, bimodal γ' precipitate size distributions can be obtained using carefully-designed two-step aging. Several

studies have been aimed at predicting the multimodal γ' precipitate evolution, but only a few of them have been validated with experimental studies (Balikci & Erdeniz, 2010; Goodfellow et al., 2018; Radis et al., 2009; Singh et al., 2011; Wen, Simmons, Shen, Woodward, & Wang, 2003).

The size and distributions of the γ' precipitate play an indispensable role in dictating the deformation mechanisms and, hence, the mechanical properties. Ni-based superalloys used in gas turbine engine applications often have a bimodal or trimodal distribution of the γ' phase precipitates (Donachie & Donachie, 2002; Joseph, Persson, & Colliander, n.d.; Masoumi, Shahriari, Jahazi, Cormier, & Devaux, 2016; Roger C. Reed, 2006; Smith et al., 2015); hence, it is important to incorporate the multimodal size distribution into a predictive model. While an extensive body of knowledge surrounds the active mechanisms within an unimodal distribution of γ' precipitates, the exploration of multimodal distributions, encompassing both different sizes of the precipitates, remains relatively unexplored (Anbarasan et al., 2018; M. Anderson, Thielin, Bridier, Bocher, & Savoie, 2017; Bergstrom & Bayha, 2005; Joseph et al., n.d.; E. T. McDevitt & Bentley, 2009). Galindo-Nava et al. (Galindo-Nava, Connor, & Rae, 2015) developed a predictive model for the yield strength (YS) of unimodal and multimodal γ' Ni-based superalloys. However, they studied the different unimodal distributions and then combined the idea for multi-modal prediction. Reports on bimodal or multimodal contributions using experimental techniques are lacking (Goodfellow, 2018).

It is also well known that the service environment, especially the nature of stress and working temperature, has a large effect on the thermal stability and the kinetics of precipitation. The evolution of the gamma double prime (γ") phase in such environments is well understood for IN718 (Mahadevan et al., 2012; Sundararaman, Mukhopadhyay, & Banerjee, 1988b). However, for

718Plus, the γ' microstructure evolution and stability are not yet fully understood, nor how they will alter the mechanical properties.

This study is a comprehensive exploration aimed at unraveling the process of developing a bimodal γ' precipitate size distribution within 718Plus and, concurrently, scrutinizing its stability under a diverse array of thermal and tensile stress conditions. The initial stage of this inquiry involves the selection of the solutionizing temperature, a pivotal step in laying the foundation for subsequent aging treatments. The process was followed by aging treatments to develop both unimodal and bimodal distributions, where critical parameters such as time, temperature, and cooling rate are meticulously manipulated. Characterization techniques such as optical microscopy (OM), scanning electron microscopy (SEM), transmission electron microscopy (TEM), and atom probe tomography (APT) were used. The mechanical behavior of the alloy was a focus of the work, which included room temperature (RT) tensile testing to access the properties, such as YS, ultimate tensile strength (UTS), elongation-to-failure (ε_f) and creep testing.

This dissertation is structured into eight distinct chapters, each serving a specific purpose in the overall narrative of this research. Chapter 1 presents a brief introduction which serves as the gateway to this dissertation, providing an initial glimpse into the area of research that has been introduced in this work. Within chapter 2, an extensive exploration of the existing literature is presented. This chapter provides a robust foundation by furnishing background information on the 718Plus superalloy, the intricacies of γ' phase precipitation and growth, and the mechanisms underpinning strengthening and deformation. Furthermore, it identifies research gaps associated with previous research endeavors, directing the course of this study. Chapter 3 outlines the motivation and objective of this dissertation. It unveils the driving forces that propelled this study, revealing why it is significant to address the identified gaps. Within chapter 4, the methodology

used in this work is described. It contains detailed information on the materials, equipment, and procedures deployed, providing a comprehensive understanding of the experimental framework. All the results of the experimental work performed are presented in Chapter 5. This chapter comprises four distinct subsections, each dedicated to presenting the outcomes corresponding to the objectives outlined in Chapter 3. It also includes preliminary results for both as-processed and solution-treated (ST) alloys. Similarly, chapter 6 presents the discussion of the results presented in chapter 5 in four different subsections. Chapter 7 is a summary and conclusion of the work, offering a comprehensive summary of the key findings. The final chapter, Chapter 8, lists the potential avenues for further research based upon the findings of this dissertation.

CHAPTER 2. BACKGROUND AND LITERATURE

2.1 SUPERALLOY

A superalloy, also known as “high-performance alloy”, is a multi-metal alloy system that exhibits a good combination of high-temperature properties, such as resistance to creep deformation, oxidation, and corrosion, and hence has a relatively high service temperature, often above 0.7 times the absolute melting temperature. Superalloys, which are based on cobalt (Co), iron (Fe), or nickel (Ni), depending upon their application, were primarily Fe-based before the 1940s (Bowman, 2000; Donachie & Donachie, 2002; Furrer & Fecht, 1999; Ghosh, 2002; Kracke, 2010; Nathal, 2008; Roger C. Reed, 2006; Segersäll, 2013). The development of the vacuum melting technique led to composition control, especially with respect to impurities, and enabled systematic study of the effects of multiple elemental additions on the microstructure and properties. It also led to the development of directional solidification and paved the way to produce single-crystalline superalloys in late 1960s (Bowman, 2000).

Figure 2-1 represents a schematic of a gas turbine engine highlighting different sections, including the intake, compressor, combustion, and exhaust. It also shows the change in temperature and pressure from the intake to the exhaust regions, where the temperature and pressure are highest in the combustion section (Leishman, 2022). Figure 2-2 depicts a schematic of a gas turbine engine for which the different colors represent sections where different materials are commonly used. The combustion zone and turbine are where Ni-based superalloys are used because of their excellent high-temperature properties. The temperature in the combustion chamber, Figure 2-1, can reach as high as 1930° C (3506° F), necessitating the use of cooling air. Proper mixing of air and fuel helps in maintaining a sustainable temperature inside the combustion section. At the turbine outlet, the temperature is reduced to about 1070° C (1958° F) for jet engines (Testa, Brunoro, & Giaretta,

1979). Because of the demanding high-temperature property requirements such as resistance to creep, corrosion, and oxidation, Ni-based superalloys are used for components in that section (Eksergian, 1957; Lewandowski, 2015; Testa et al., 1979).

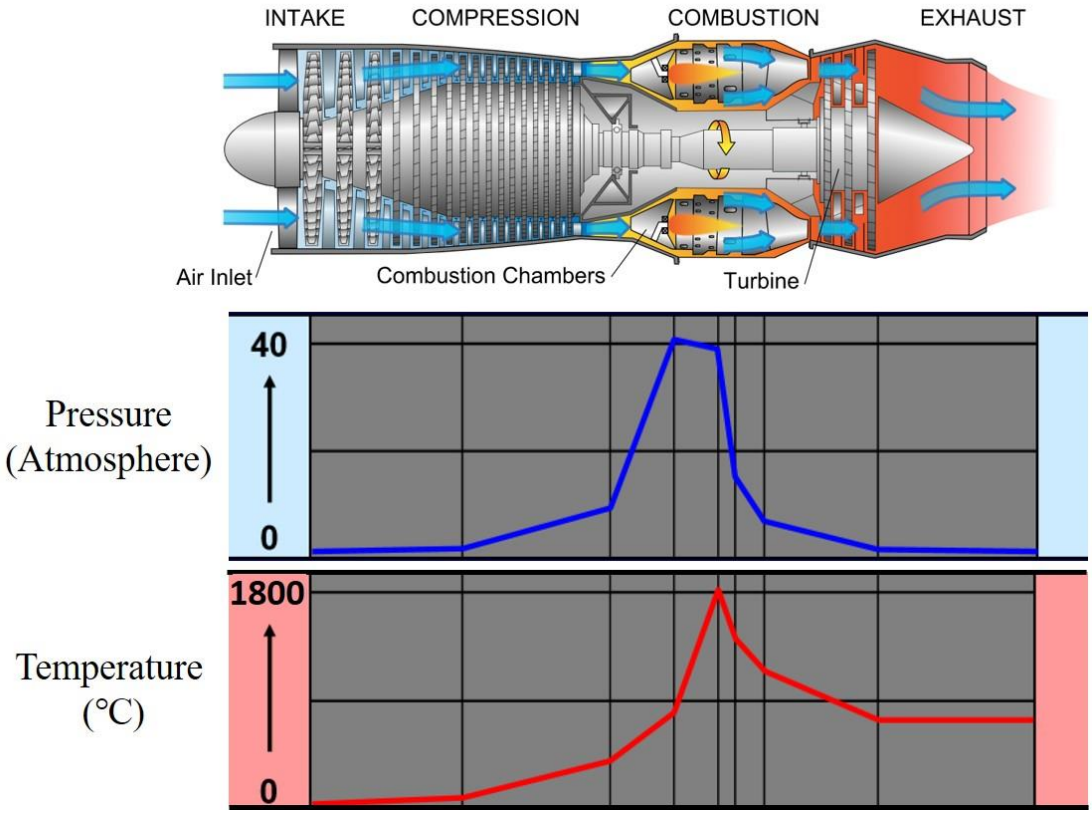

Figure 2-1: A schematic representation of a gas turbine engine and the associated pressure and temperature profiles during its use (Leishman, 2022).

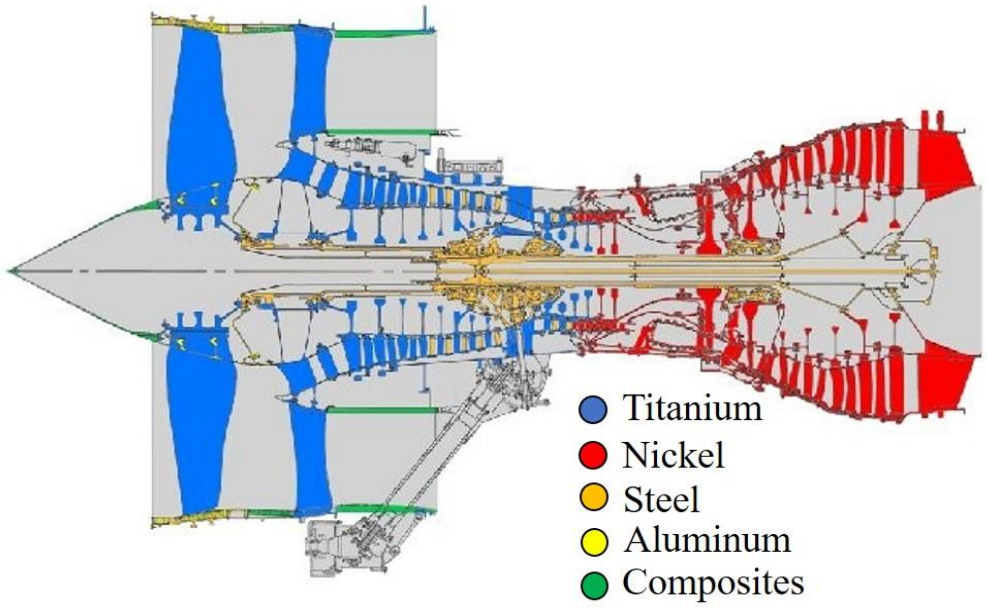

Figure 2-2: A schematic of a gas turbine engine highlighting the locations of commonly used alloys; credit: Rolls Royce.

Superalloys are strengthened by multiple precipitate phases having several alloying elements. The ordered nature of these precipitates and their associated strengthening capabilities at temperatures up to ~800 °C make superalloys suitable for high-temperature applications in a gas turbine engine (Roger C. Reed, 2006). Microstructures of Ni-based superalloys may contain the following phases depending on the alloying elements:

- Gamma (γ) matrix phase: This has a face-centered cubic (FCC) crystal structure majorly containing Ni with other elements (Figure 2-3a) such as Fe, Co, chromium (Cr), ruthenium (Ru), rhenium (Re), tungsten (W), and molybdenum (Mo), all of which are FCC austenite-phase stabilizers and assist in solid-solution strengthening.
- Gamma prime (γ') precipitate phase: This is often coherent with the γ matrix and exhibits the ordered FCC crystal structure ($L1_2$), Figure 2-3b. This phase generally consists of elements with atomic radii less than those of the base alloy element, such as aluminum

(Al), titanium (Ti), and tantalum (Ta). This phase is ordered, typically Ni_3Al, and provides strengthening.

- Gamma double prime (γ") precipitate phase: This ordered phase is rich in Nb and can form the body-centered tetragonal (BCT) crystal, Figure 2-3c. The typical composition for the metastable γ' phase is Ni_3Nb.
- Delta (δ) and Eta (η): The δ precipitates (orthorhombic, Figure 2-3d) are a stable phase mostly located at the matrix grain boundaries. Although the typical composition of the δ phase is Ni_3Nb, it may contain Al and Ti (R C Reed & C.M.F.Rae, 2014). η also typically forms on the grain boundaries with a chemistry of $Ni_3Al_{0.5}Nb_{0.5}$ and forms the hexagonal, $D0_{24}$ crystal structure, Figure 2-3e.
- Carbides and borides: Carbon (C), boron (B), and zirconium (Zr) tend to segregate to the γ matrix phase grain boundaries and form carbides and borides (Bowman, 2000; Ghosh, 2002; Roger C. Reed, 2006). Common types of carbides are $M_{23}C_6$ and M_6C. Borides tend to form when B combines with Cr and Mo.
- Topologically closed-packed (TCP) phases such as σ, μ, Laves, etc. can also be found in some superalloys, especially when they are exposed to high-temperature (near the service temperature). The general chemistry for TCP phases is A_xB_y, where A and B are transition metals. An excessive concentration of elements, such as Mo, Cr, Re, and W, promotes the sformation of these phases.

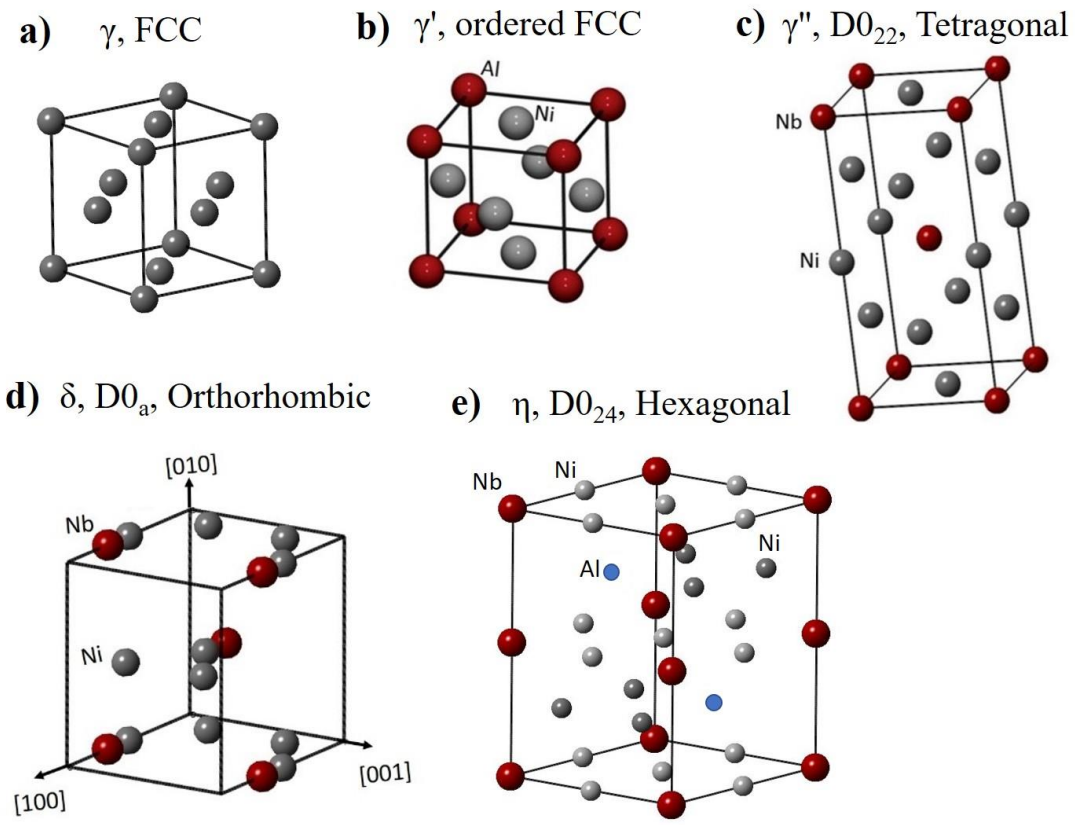

Figure 2-3: Crystal structures of different phases in superalloys, a) γ-phase, b) γ'- phase, c) γ''- phase, d) δ- phase, e) η- phase; Created using CrystalMaker (Hassan & Corney, 2017).

2.1.1 Inconel 718

Inconel 718 (IN718) is one of the most widely used Fe-Ni-based superalloys (Bowman, 2000; Donachie & Donachie, 2002). It has been extensively used in gas turbine engine components, such as the turbine shaft, the turbine disc, and high-pressure turbine blades. This alloy is strengthened mainly by the γ'' phase (Sundararaman et al., 1988b). The γ'' is a metastable phase in IN718, and upon prolonged aging, it transforms into the equilibrium δ phase, which has a needle/plate-shaped morphology (Sundararaman et al., 1988b). This transformation, as well as the faster coarsening kinetics of the metastable γ'' phase at higher temperatures, limits its useful service temperature to 650 °C (Thomas, El-Wahabi, Cabrera, & Prado, 2006). In addition to the γ'' phase, a small amount

of γ' phase also precipitates in the alloy. The volume percentage of the γ' precipitates tends to be about 16%, and the ratio of γ''-to- γ' tends to be 4:1 (Boesch & Canada, 1969; Dahotre et al., 1993; Han, Deb, & Chaturvedi, 1982; Sundararaman et al., 1988b; Sundararaman, Mukhopadhyay, & Banerjee, 1997).

2.1.2 Rene 41 and Waspaloy

γ' precipitate strengthened alloys such as Rene 41 and Waspaloy are popularly used in jet engine applications. Rene 41 has a relatively high service temperature (up to 980 °C) and is widely used in hot section parts of jet engines (Atabay, Sanchez-Mata, & Brochu, 2020). Waspaloy has a service temperature of around 700 °C as is typically used for rotating components that do not exceed 870 °C (Maurer, Jackman, & Domingue, 1980). Although the γ' precipitates render these alloys as a suitable candidate for high-temperature application, they are not easily welded. High amounts of γ'-forming alloy elements, such as Al and Ti, enhance hot cracking during processing. These alloys contain a relatively large amount of expensive alloying elements, such as Co, Ti and Ni, leading to relatively high fabrication costs.

2.1.3 ATI 718Plus

Extensive efforts have been focused on improving the mechanical properties of turbine engine materials since the beginning of the 1990s. The material requirements for high-temperature applications include high-temperature stability, good workability, and reasonable cost. As a result of various synthesis and optimization efforts, a new alloy has been recently (in 2005) developed by ATI Specialty Materials (North Carolina, United States) named ATI 718Plus (Wei Di Cao & Kennedy, 2005; Jeniski Jr. & Kennedy, 2006; Jeniski & Kennedy, n.d.; Richard L. Kennedy et al., 2004). 718Plus, which is a derivative of IN718, exhibits a better combination of properties than IN718, which makes it a good candidate for replacement of IN718 in some applications (Wei Di

Cao & Kennedy, 2005). IN718 has a limited service temperature due to the metastable γ" phase, which transforms to the δ phase at a higher temperature, whereas alloys like Waspaloy have higher service temperatures but suffer from high fabrication costs due to their poor workability and expensive elemental additions (Jeniski & Kennedy, n.d.; R. Kennedy & McDevitt, 2008; Thomas et al., 2006a). 718Plus has γ' as its major strengthening phase, which is stable up to around 700 °C (55 °C higher than IN718) (Wei-di Cao & Kennedy, 2004; R. Kennedy & McDevitt, 2008; R.L. Kennedy, 2005; Sofuoglu, Cakir, Gurgen, & Kushan, 2017). A comparison of the chemical compositions for the mentioned alloys is provided in Table 2-1.

Table 2-1: Nominal compositions of 718Plus, IN718, and Waspaloy (R. Kennedy & McDevitt, 2008).

Alloys	**Chemistry (Wt.%)**											
	C	**Ni**	**Cr**	**Mo**	**W**	**Co**	**Fe**	**Nb**	**Ti**	**Al**	**P**	**B**
718Plus	0.020	B	18	2.8	1	9	10	5.4	0.7	1.5	0.006	0.004
IN718	0.025	B	18	2.8	-	--	18	5.4	1	0.5	0.006	0.004
Waspaloy	0.035	B	19.4	4.3	-	13	≤ 2	---	3	1.3	0.006	0.006

Table 2-2: Some typical mechanical properties of 718Plus, IN718, Waspaloy at various temperatures (R. Kennedy & McDevitt, 2008).

Temperature	**20 °C**			**649 °C**			**704 °C**		
Alloys	**YS, MPa**	**UTS, MPa**	**ε_f, %**	**YS, MPa**	**UTS, MPa**	**ε_f, %**	**YS, MPa**	**UTS, MPa**	**ε_f, %**
718Plus	1205	1509	22	1023	1305	24	1005	1174	24
IN718	1202	1459	20	1008	1134	21	936	1049	20
Waspaloy	1087	1441	27	979	1342	23	885	1087	39

The advantages in 718Plus were achieved by decreasing the amount of Fe by 8 wt. % and increasing the amounts of Co and W by 9 wt. % and 1 wt. %, respectively, compared to IN718. Also, the increase in the Al/Ti ratio and total Al+Ti content (approximately 2.2 wt. %) favors the formation of γ' as the primary strengthening phase (Wei Di Cao & Kennedy, 2005; Wei-di Cao & Kennedy, 2004). The addition of heavy elements such as Nb and W favors sluggish bulk diffusion and slows the precipitation kinetics of the γ' phase in 718Plus compared with Waspaloy, thereby providing a larger working temperature window without significant microstructural changes (Wei-di Cao & Kennedy, 2004). Various research has reported the enhancement in mechanical properties of IN718Plus compared to IN718, such as high-temperature YS and $\square_f$, creep and stress rupture resistance, and low notch sensitivity (Wei-di Cao & Kennedy, 2004; R. Kennedy & McDevitt, 2008; Kushan, Uzgur, Uzunonat, & Diltemiz, 2012; Technologies, 2008). This is summarized in Table 2-2. McDevitt et al. observed that crack growth rates in 718Plus in the temperature range 649 to 704 °C were lower than those for IN718 and comparable to those for Waspaloy under non-dwell-fatigue conditions, while they were comparable to those for alloy 720 in dwell-fatigue tests (E. T. McDevitt, Oppenheimer, Kearsey, & Tsang, 2012). The combination of mechanical properties offered by 718Plus is expected to make it attractive to the aerospace industry for turbine engine applications. This was one reason why this alloy was investigated in this work.

2.2 HEAT TREATMENT OF 718PLUS AND SIMILAR ALLOYS

A polycrystalline Ni-based superalloy for turbine disc applications generally undergoes a two-stage thermomechanical treatment. The function of the initial stage, which typically involves hot-forging or hot-forging followed by solution-treatment, is to both obtain the desired grain size of the γ matrix and to dissolve the γ' precipitate that evolved during solidification and cooling after

hot forging. The temperatures used in the initial stage are either sub-solvus or super-solvus. If the treatment is performed below the solvus temperature of the δ phase, it is called a sub-solvus treatment and super-solvus if above (E. McDevitt, 2011).

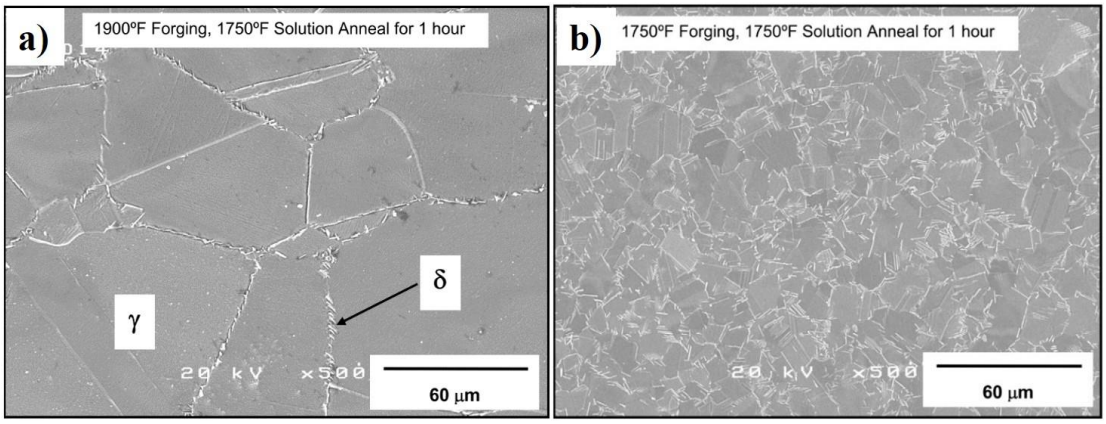

Figure 2-4: Secondary electron scanning electron microscope (SE-SEM) micrographs of a forged + solution annealed 718Plus alloy, a) super-solvus ST, b) sub-solvus ST (etched with modified Kalling's reagent) (E. McDevitt, 2011).

Figure 2-4 shows two differently forged + ST 718Plus microstructures. One is from a sample treated at a super-solvus temperature (1900 °F/1038 °C), showing the microstructure with a small amount of the δ phase (white contrast on grain boundaries) and a large γ grain size; see Figure 2-4a. The sub-solvus temperature (1750 °F/954 °C) resulted in a larger amount of δ phase and a smaller γ grain size; see Figure 2-4b. The solution treatment time must be long enough to dissolve the γ' phase and obtain a supersaturated γ matrix phase independent of whether the alloy was forged above or below the δ solvus temperature. During sub-solvus solution treatment, a portion of the γ' phase typically remains in the ST microstructure and is referred to as primary γ'. The second stage of heat-treatment is an aging treatment for the nucleation and growth of the γ' precipitate. The aging treatment can involve single or multiple steps depending on the strategy to change the size distribution of the γ' precipitates, which will be discussed in detail in the next section.

2.2.1 γ' Precipitation Studies

The precipitation and growth of γ' precipitates are complex processes during cooling from high temperatures, which depends mostly on the temperature, time, and cooling rate (Babu, Miller, Vitek, & David, 2001; T. Gabb et al., 2000; Jackson & Reed, 1999a). Microstructures that exhibit γ' precipitates on grain boundaries before aging, such precipitates can range up to a few microns in size and are referred to as primary γ' precipitates. During aging, secondary γ' precipitates nucleate in the supersaturated matrix and grow until their diffusion fields overlap. Upon further cooling, based on the supersaturation of the matrix, another batch of the γ' precipitates can nucleate, which are referred to as tertiary γ' precipitates. There can be a subsequent aging treatment step (two-step aging) for the coarsening of the existing γ' precipitates or the nucleation of the tertiary γ' precipitates, and this can result in different γ' precipitate size distributions. Figure 2-5 shows examples of different γ' precipitate containing microstructures for different Ni-base superalloys; Figure 2-5a: unimodal distribution, Figure 2-5b: bimodal distribution, and Figure 2-5c: trimodal distribution.

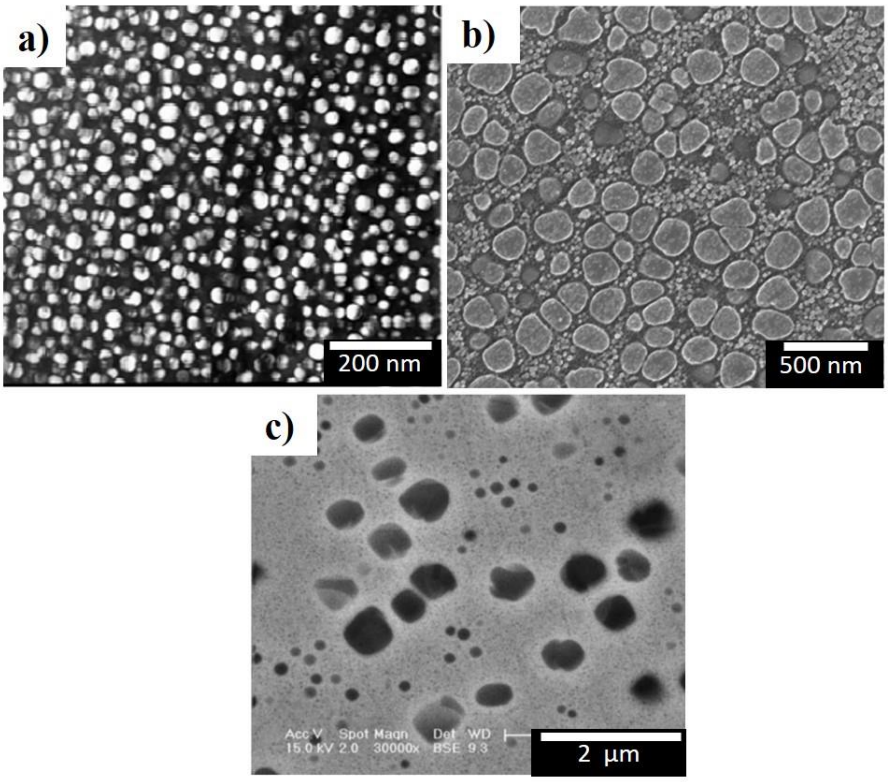

Figure 2-5: SEM micrographs showing different distributions of the γ' precipitates a) Unimodal distribution in 718Plus after ST + two-step aging (788 ˚C/8 h + 704 ˚C/8 h) (Löhnert & Pyczak, 2010), b) Bimodal distribution in RR1000 after ST (1125 ˚C/4 h)+ single step aging(800 ˚C/12 h) (Connor et al., 2014) b) Trimodal distribution in IN738LC after ST (1200 ˚C/4 h) + double step aging (1140 ˚C/4 h and 1120 ˚C/10 min) (Balikci & Erdeniz, 2010).

The size and morphology of the γ' precipitates can be tailored by controlling the cooling rate, aging temperature, and time (Balikci & Erdeniz, 2010). For example, Figure 2-6 shows the evolution of different γ' precipitate morphologies in Waspaloy after a solution treatment with varying cooling rates. A faster cooling rate, such as that experienced during WQ, could result in no γ' precipitation, whereas slower cooling, such as that experienced during 20 ℃/min to 1 ℃/min controlled cooling, could result in γ' precipitates with increasing average diameters with a range of 10-100 nm and shapes that are not spherical and ultimately irrregular.

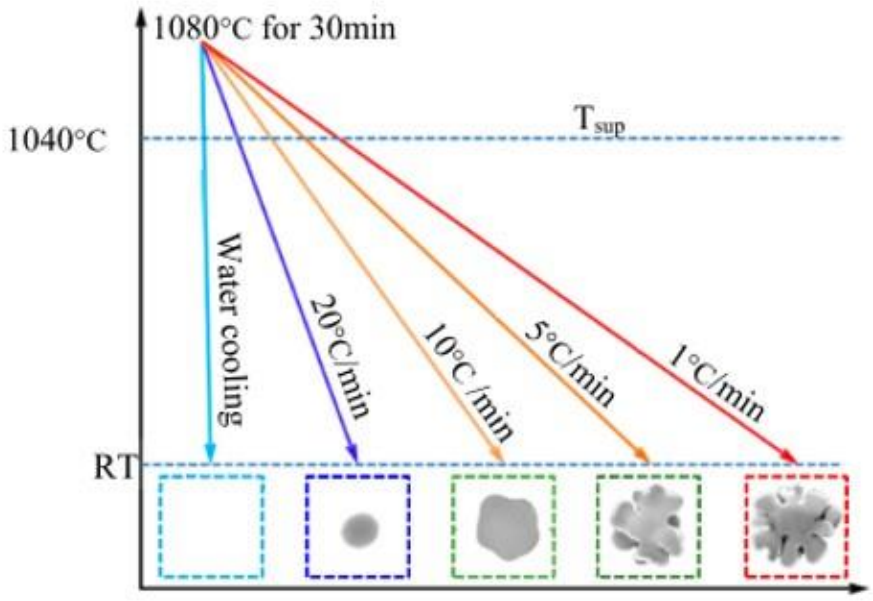

Figure 2-6: The evolution of various γ' precipitate morphology with different cooling rates after a solution treatment in Waspaloy (Wang et al., 2021).

Several studies have reported multimodal γ' precipitate size distributions for samples that were continuously cooled after the ST followed by single-step aging at a constant temperature (Babu et al., 2001; T. Gabb et al., 2000; Jackson & Reed, 1999a; Radis et al., 2009; Sarosi, Wang, Simmons, Wang, & Mills, 2007; Torster et al., 1997). ST followed by WQ to room temperature (RT) followed by one-step aging at a constant temperature resulted in uniform size γ' spherical precipitates with a relatively high number density (Singh et al., 2011; Torster et al., 1997). With decreased continuous cooling rates followed by a lower temperature aging, bimodal or multimodal γ' size distributions tend to develop (Alabbad et al., 2019; T. P. Gabb et al., 2008; Radis et al., 2009; Sarosi et al., 2007; Singh et al., 2011). Several studies have been aimed at predicting the γ' precipitate size and shape evolution (T. Gabb et al., 2000; T. P. Gabb et al., 2008; Wen et al., 2003), and some have been validated with experimental studies (Babu et al., 2001; Jackson & Reed, 1999a; Radis et al., 2009).

Masoumi et al. have studied the reprecipitation mechanisms and kinetics of γ′ precipitates during cooling in AD730 superalloy and reported the possibility of extending the model to other Ni-based superalloy systems (Masoumi et al., 2016). The study showed the change in morphology and distribution of the reprecipitated γ' phase during various thermal heating and cooling cycles. The γ' precipitate distribution changed to multi or unimodal distributions depending on the cooling rate. The unimodally distributed γ' can further transform into bimodal distribution after a long time aging or exposure as the precipitates coarsen. The microstructure becomes unstable due to increased lattice mismatch and divides into smaller spherical precipitates (Connor et al., 2014). Another possible explanation could be the dissolution of existing smaller (tertiary) γ' precipitates, which will provide a chemical driving force for the reprecipitation of the γ' precipitates. However, there is no direct microscopy evidence of such transformation. Unimodal distributions of such fine precipitates are difficult to obtain in practice and such microstructures are associated with reduced ductility (Connor et al., 2014). Radis et al. reported a multimodal γ' precipitate distribution after continuous cooling (0.017 K/s) for UDIMET 720 Li using experiments and computations (Radis et al., 2009). Babu et al. used a cooling rate of 1 K/s to obtain a multimodal γ' precipitate size distribution (Babu et al., 2001). Another investigation varied the cooling rate between 0.083-11 K/s and found that the slow cooling rate (0.66 K/s) was suitable for obtaining a multimodal γ' precipitate distribution (T. P. Gabb et al., 2008). These reports emphasize the importance of cooling rate on the evolution of γ' precipitates, but they have been mainly focused on continuous cooling from the ST temperature to the single-step aging temperature.

Multi-stage aging treatments are common for various Ni-based superalloys (An et al., 2019; Balikci & Erdeniz, 2010; Polkowska et al., 2019) as this helps to control the size and distribution of the γ and γ' phases in addition to the carbide-enriched phase(s) (Tejedor, Singh, & Pilidis, 2013),

but the microstructural evolution during the aging is not well understood. A two-step aging process, which includes initial aging at a higher temperature followed by subsequent aging at a lower temperature, can be categorized into two types based on the cooling rate between the two aging steps. In the **continuously cooled** two-step aging, the sample is slowly cooled within the furnace to reach the lower aging temperature, and then it is held at that temperature, as shown in Figure 2-7a. In the **interrupted cooled** type of two-step aging, the sample is cooled faster (i.e. WQ) to room temperature before heating again at the second aging temperature, as shown in Figure 2-7b.

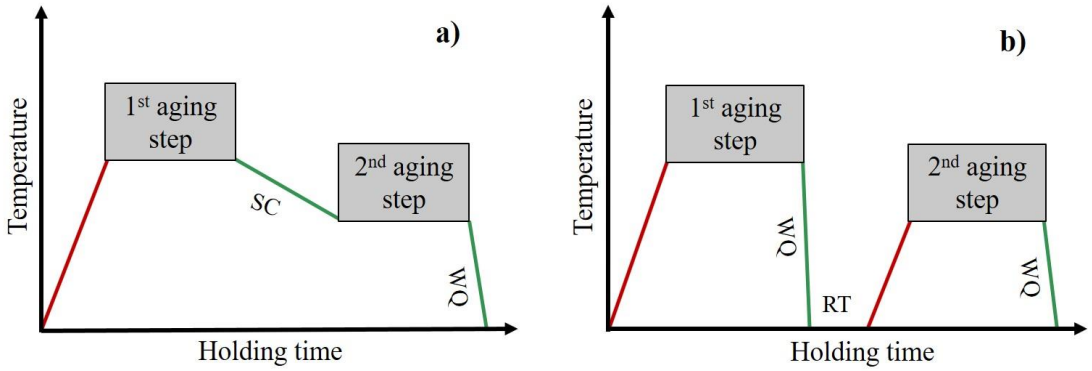

Figure 2-7: Schematics for two-step aging with a) continuously cooled, b) interrupted cooled portions between the two steps of aging. FC: furnace cooled, WQ: water quenched, RT: room temperature.

2.2.1.1 γ' Precipitate evolution in 718Plus

Different studies have been performed to understand the nucleation and growth of the secondary phase, γ', in 718Plus. Srinivasan et al. performed extensive studies to understand the phase evolution in 718Plus and have constructed both time-temperature-transformation (TTT) and continuous-cooling-transformation (CCT) diagrams (Srinivasan, Lawless, & Ott, 2012). The nose of the TTT curve was measured to be 843 °C, as shown in Figure 2-8. This study showed a unimodal distribution of the γ' precipitates after a two-step aging treatment on 718Plus. It also

highlighted the effect of cooling rate on the size and volume fraction of the γ' precipitates, where a decrease in the γ' precipitate size occurred with increasing cooling rate and the volume fraction of γ' precipitates reached a peak value at a cooling rate of 17˚C/min (Srinivasan et al., 2012).

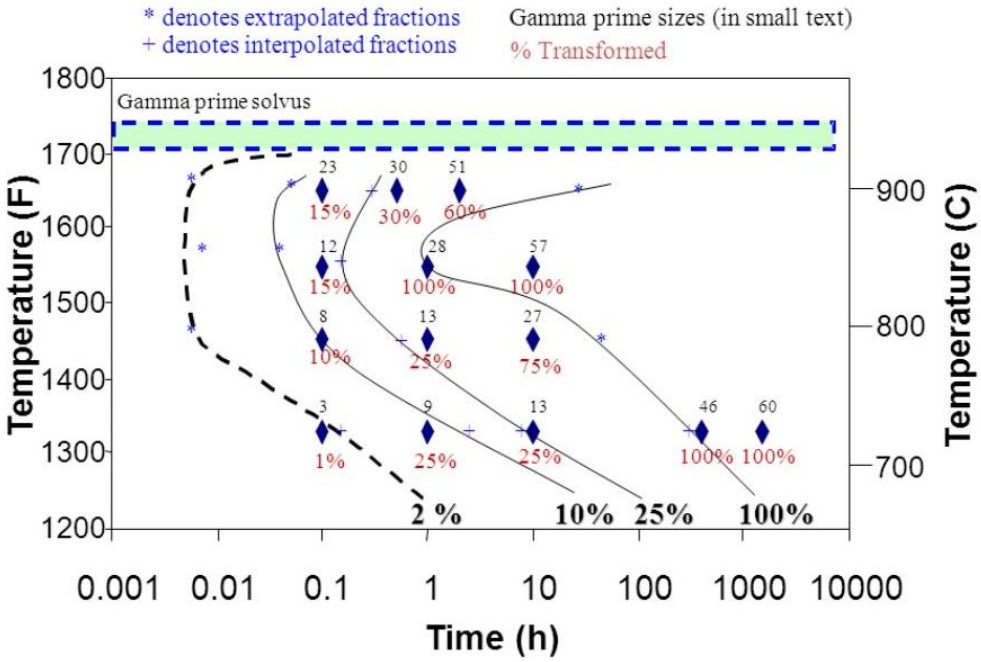

Figure 2-8: Time-Temperature-Transformation (TTT) curve for γ' precipitation in 718Plus (Srinivasan et al., 2012).

Xie et al. also experimentally determined the TTT diagram for IN718 and 718Plus and compared it with Thermo-Calc model results (Xie, Xu, et al., 2005). This comparative study showed that all the curves for the phase formation in 718Plus shift to higher temperatures and shorter times compared with those for IN718. Connor et al. showed that faster cooling (37˚C/min) results in larger lattice parameters for both the γ and γ' phases (Connor et al., 2014). This could be explained by the difference in composition of the two phases, which arises due to the time-dependent diffusion of the elements involved (Singh et al., 2011).

2.2.2 Grain boundary precipitation in 718Plus

Early studies on 718Plus initially identified the grain boundary precipitates as orthorhombic, Ni_3Nb, δ phase (shown in Figure 2-3d) (R.L. Kennedy, 2005; Radavich & Carneiro, 2005; Xie, Wang, et al., 2005). Some authors also reported the presence of a hexagonal closed pack (HCP) phase (Hassan & Corney, 2017; R. R. Unocic, Unocic, Hayes, Daehn, & Mills, 2010). However, most literature referred to the grain boundary precipitates as the δ phase. It was also proposed that the reported HCP phase was a new plate-like phase with a chemical structure of $Ni_3Al_{0.5}Nb_{0.5}$ (called η phase, shown in Figure 2-3e). It was believed that the η phase nucleates within the same microstructure as the δ phase, leading to the coexistence of both the δ phase and the η phase in 718Plus as reported by Lech et al. (Figure 2-9) (Hassan & Corney, 2017; Lech et al., 2019). The size of the δ phases on the η phases was found to be on the order of a few atomic layers, which makes it difficult to quantify or study them separately, Figure 2-9b.

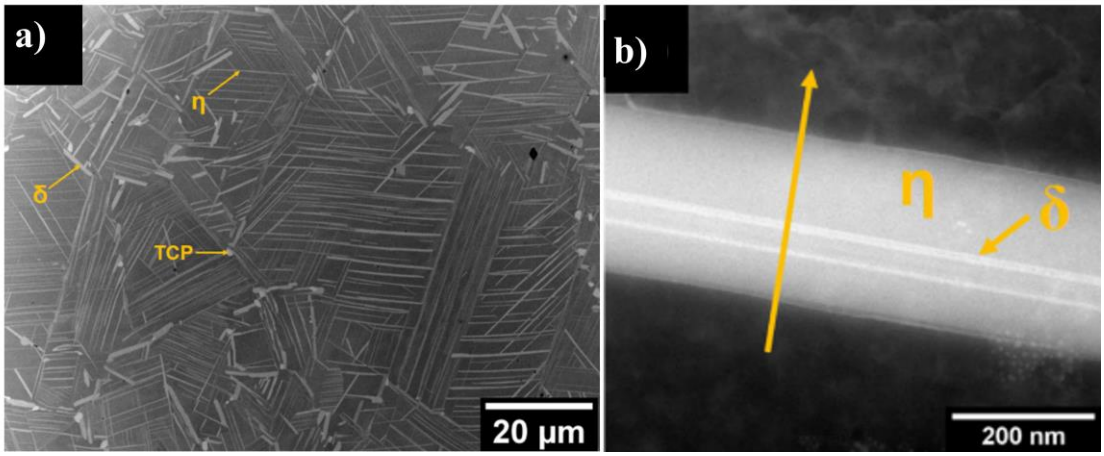

Figure 2-9: SEM micrographs of 718Plus showing the a) distribution of the grain boundary phases such as δ, η, and TCP, b) overlapping δ phase on the η phase (Lech et al., 2019).

These phases generally nucleate at grain boundaries but not on all grain boundaries. It has been reported that twin boundaries are resistant to the nucleation of the η phase due to their low

interfacial or grain boundary energy (Hassan & Corney, 2017). It is also believed that η/δ phases can transform from γ’ phase. As both phases share some common solute elements, such as Al and Nb, there could be competitive growth. Hence, various studies have reported a PFZ/γ’ denuded zone around the η/δ phase (Viskari, Cao, Norell, Sjöberg, & Stiller, 2011). The grain boundary phases exhibited in this dissertation have been referred to as the δ phase based on the early research on 718Plus (Covarrubias, 2010; Richard L. Kennedy et al., 2004).

2.3 EVOLUTION OF THE γ' PRECIPITATE UNDER THERMAL AND LOAD APPLICATION

The changing morphology and distributions of the γ' precipitates significantly affect the mechanical properties and the deformation behavior of the alloy. In the case of Ni-base superalloys, the changing morphology of the γ' precipitates has shown considerable influence on their high-temperature performance (Long et al., 2020; E. McDevitt, 2011). In the case of alloy 718Plus, the evolution of both the γ’ and δ precipitates influence the useful temperature range as well as the life of the alloy. This literature review has mainly highlighted the evolution of the γ’ precipitates.

2.3.1 Coarsening of the precipitates during thermal exposure

In the case of Ni-base superalloys, the changing morphology of the γ' precipitates influences the high-temperature creep properties. It is very difficult to inhibit the coarsening of these precipitates at high temperatures. The driving force for the process is the chemical potential, which is related to the curvature of the precipitates. The coarsening generally occurs with two different mechanisms (Wilson, 1976). One is the coalescence mechanism, where the precipitates migrate and coalesce together over the substrate surface. Another mechanism is the Ostwald ripening, where the larger precipitate grows at the expanse of the smaller precipitates. With the decrease in

the number of precipitates as they coarsen, the overall surface free energy of the alloy system reduced (Ham, Park, Kim, & Kim, 2014; Wilson, 1976; Yao, K.R.Elder, Guo, & Grant, 1993). The average precipitate size obeys the temporal law Equation (2.1) of coarsening as follows.

$$R^n \propto t \qquad (2.1)$$

Where, R is the precipitate radius, t is the aging time and n is the temporal exponent. The thermodynamic driving force for the coarsening is the reduction in γ/γ' interface energy. During thermal aging, the coarsening can be controlled by different mechanisms. Following the precipitation theory (Equation (2.1), the value of n or $(\text{time})^{1/n}$ influences the coarsening mechanism. The interface diffusion-controlled coarsening, where the mechanism is controlled by the solute absorption at the γ/γ' interface, is described as square rate law (n = 2) in Equation (2.1). Lifshitz, Slyozov, and Wagner successfully developed a theory which is known as the LSW theory for quantitative predictions of precipitate coarsening (Baldan, 2002; Lifshitz & Slyzov, 1961). This theory predicted the value of n as 3 for bulk or lattice diffusion-controlled coarsening (Equation (2.1)). They assumed that precipitates of the second phase are not only spheres but also fixed in the matrix, meaning that the centers of precipitates never change during the coarsening process. Since the predictions in LSW theory assume that precipitates are source points, it implies that LSW theory is valid for a system of essentially zero volume fraction of the second phase. But it is also worth noting that most of the commercial alloys have more than 10 volume percent of the second phase precipitates. Various modifications of LSW theory have also appeared in the literature for non-zero volume percentages (Baldan, 2002).

M. P. Jackson et al. (Jackson & Reed, 1999b) developed a model for alloy IN718 that simulates the two-dimensional evolution of the precipitates in a two-phase system undergoing diffusion-

controlled growth coarsening. Similar studies have focused on Al alloys by H. R. Shercliff et al. (Shercliff & Ashby, 1990a, 1990b) to develop a predictive model that describes the effect of both a two-step aging treatment and rolling deformation on the kinetics of aging. There is very limited work that has studied the multimodal γ' precipitate size distribution. Anderson et al. have recently developed a model incorporating the multimodal distribution for the kinetics prediction using RR1000 Ni-based superalloy (M. J. Anderson et al., 2020). This work identifies the limitation of the modelling results of Svoboda et al. (Svoboda, Fischer, Fratzl, & Kozeschnik, 2004). When applying Savoboda prediction on RR1000, tertiary precipitates are predicted to dissolve. However, the experimental results show an increase in their mean radius. The observed contradiction in the results can be attributed to the utilization of the mean-field theory in the presence of varying size distributions. Additionally, the research conducted by Balikci et al. also emphasised the importance of considering multimodal distributions (Balikci & Erdeniz, 2010). Their work highlights the shift in distribution patterns, transitioning from unimodal to bimodal and vice versa based on different aging durations and temperatures. While the mechanism for the unimodal precipitation kinetics matched well with the cube rate law theory, this correlation does not hold true for multimodal distributions. The reported variations in coarsening rates concerning the size differences of γ' precipitates call for more extensive investigations, particularly in the context of multimodal distributions within Ni-based superalloys. Lech et al. conducted a thermal exposure study on the 718Plus alloy. However, it's worth noting that the exposure temperature utilized in their study was considerably higher (850 °C) than the reported service temperature (704 °C) for this particular alloy (Lech et al., 2019). Consequently, the focus of their reports primarily centered on the evolution of the δ/η phase, with no discussion regarding morphological changes pertaining to γ' precipitates.

2.3.2 Microstructural changes during creep deformation

During service, the superalloy components experience high thermal and stress environments, which can cause changes in the microstructure and, eventually, the strength of the material. The materials only exposed to high-temperature environments (stress-free conditions) are likely to exhibit Ostwald ripening (discussed in section 2.3.1). Due to the combined application of stress and temperature, γ' precipitates tend to coarsen directionally, often referred to as rafting. The direction of the rafts depends on the overall stress (internal and externally applied stress). The internal stress arises from the δ_m given by Equation (2.10), and the sign of δ_m decides the direction of stress. The rafting of the γ' precipitates in the direction of the stress can provide enhanced creep resistance and high-temperature strength along that particular axis (Chiou, Jian, Yeh, Kuo, & Juang, 2016; Long et al., 2020). However, it can also lead to anisotropic properties, which need to be carefully considered in design and engineering applications (Kamaraj, 2003). A study by Latief et al. has reported a lower creep rupture life when stressed perpendicular to {110} planes on which micro-cracks formed (Latief, Kakehi, Murakami, & Kasai, 2012).

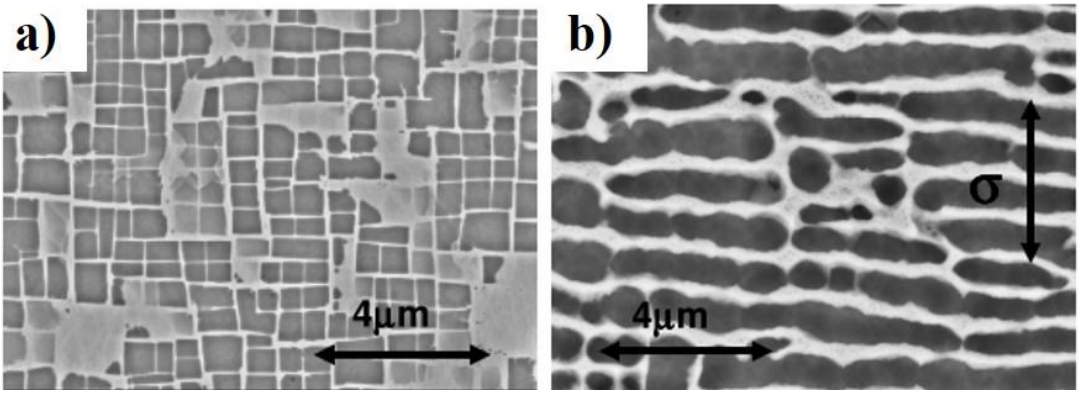

Figure 2-10: CMSX-4 a) initial microstructure b) after creep deformation at 1050°C using 80 MPa stress for 375 hr, exhibiting the rafting of γ' precipitate (Fedelich et al., 2012).

During prolonged high-temperature exposure, the presence of misfit stresses arising from the lattice mismatch can instigate the phenomenon of rafting (Fedelich et al., 2012; Yu et al., 2020).

In the absence of external mechanical stress, these misfit stresses tend to be relieved through the creation of a dislocation network (Epishin & Link, 2004; Long et al., 2020). Furthermore, the plastic activity resulting from the dislocation glide, coupled with the concurrent diffusion of alloying elements at elevated temperatures, gives rise to substantial microstructural modifications (Ali et al., 2020). Long et al. reported the preferential formation of cuboidal-shaped γ' precipitates on (100) planes due to the lowest Young's modulus in the γ matrix and γ' precipitates in the <100> direction (Long et al., 2020; Long, Mao, Liu, Zhang, & Han, 2018). Changes in the morphology or coarsening of γ' precipitates during creep can ultimately impact creep behavior. A theory relating to the precipitate coarsening suggested that the presence of strengthening γ' precipitates impede dislocation motion, and as these particles coarsen and decrease in number, the strain rate during tertiary creep is accelerated (Hayes, Unocic, & Nasrollahzadeh, 2015).

The creep behavior of the 718Plus alloy, as studied by Hayes et al., exhibited different deformation mechanisms depending on the test temperature (Hayes et al., 2015). At lower test temperatures (690 °C), shearing by partial dislocations was the dominant mechanism, resulting in the formation of stacking faults within the γ' precipitates. At the highest test temperature (734 °C), microtwinning was observed, created by the passage of paired Shockley partial dislocations. It is important to note that the proposed theories were developed by comparing high volume percent γ' precipitate containing microstructures (60-70%), while 718Plus has a low volume percent of γ' precipitates. Therefore, this alloy warrants further experimental investigation to validate the suggested theories independently.

2.4 STRENGTHENING MECHANISMS IN SUPERALLOYS

The mechanical strength of an alloy is significantly influenced by its microstructure, which is primarily controlled by the chemical composition and processing conditions (like forging and heat

treatment). In Ni-based superalloys, the size, distribution, composition, and morphology of γ' precipitates play a crucial role in determining the resulting strength. These alloys exhibit relatively high YS (σ_y) at both low and high temperatures due to various strengthening mechanisms, including precipitation strengthening (σ_p), solid solution strengthening (σ_{ss}), and grain boundary strengthening (σ_{gb}); see equation (2.2). However, the specific effects and contributions of these mechanisms in enhancing the strength can vary in different alloy systems, depending on their chemical compositions.

$$\sigma_y = \sigma_{gb} + \sigma_{ss} + \sigma_p \tag{2.2}$$

2.4.1 Grain Boundary Strengthening

The grain boundary strengthening can be explained using the Hall-Petch equation (see Equation (2.3) for polycrystalline metals containing equiaxed grain morphologies (Hall, 1951; Hansen, 2004).

$$\sigma_{gb} = \sigma_i + \frac{k}{\sqrt{D}} \tag{2.3}$$

where, D is the average grain diameter, σ_i is the friction stress to crystal lattice, and *k* is the locking constant for grain boundary hardening. The average grain size lies in the range of 10 to a few hundred microns for the validity of this equation. The values of σ_i and *k* have been found to be close to 21.8 MPa and 750 MPa $(\mu)^{-1/2}$, respectively, for Ni-based superalloys (Galindo-Nava, Connor, & Rae, 2015; Thomas, El-Wahabi, Cabrera, & Prado, 2006).

2.4.2 Solid Solution Strengthening

Ni-based superalloys contain different alloying elements, and the atoms of such elements may occupy the lattice sites of either the γ matrix or the γ' precipitates. Since most of the radii of these alloying elements are similar to the atomic radius of Ni, these elements form a substitutional solid

solution in the matrix, resulting in a relatively small local distortion of the matrix lattice parameter. During plastic deformation, the interaction of traveling dislocations along with a strain field developed due to the atomic size mismatch impedes dislocation motion and makes it stronger than the pure Ni matrix (Fleischer, 1963; Goodfellow, 2018; Roger C. Reed, 2006). Strengthening due to the σ_{ss} in multicomponent systems was proposed by Gypen and Deruyttere according to Equation (2.4):

$$\sigma_{ss} = \left(\sum_i \left(k_{s,i} C_i^p \right)^q \right)^{1/q} \tag{2.4}$$

where, q = 2 and p =1/2, $k_{s,i}$ is a strengthening constant for solute i, and C is the concentration of solute i. The σ_{ss} strengthening contribution changes as the solute concentration in the matrix changes (Goodfellow, 2018). Nb has the greatest impact (~200 MPa) on σ_{ss} before aging, but during the aging process, Nb diffuses from the γ matrix to the γ' and δ precipitates (Löhnert & Pyczak, 2010). Hence, the σ_p contribution increases and the σ_{ss} contribution decreases with increased aging time (Ahmadi et al., 2014).

2.4.3 Precipitation Strengthening

The precipitation strengthening (σ_p) includes contributions from shearing (τ_s) and non-shearing mechanisms (Orowan looping (σ_o)) as shown in equation (2.5). (Goodfellow, 2018; Raynor & Silcock, 1970). Shear strengthening (σ_s) includes coherency effects (τ_{coh}), modulus strengthening effects (τ_{mod}), interfacial energy effects (τ_{chem}), and anti-phase boundary (APB) effects (τ_{APB}); see equation (2.6), where τ_{APB} can have varying contribution from both weak-pair coupling (τ_{weak}) and strong-pair coupling (τ_{strong}) depending upon the size of the precipitate (discussed in detail in the section 2.5).

$$\sigma_p = \sigma_s + \sigma_o \tag{2.5}$$

$$\sigma_s = M\left(\tau_{coh}^q + \tau_{weak}^q + \tau_{strong}^q + \tau_{mod}^q + \tau_{chem}^q\right)^{1/q} \tag{2.6}$$

M is the Taylor orientation factor, which has a value of 3.06 for FCC polycrystalline materials [12, 35]. The exponent q, which ranges between 1 to 2, varies based on the influence of different effects. An experimentally-determined empirical value of 1.23 is typically assigned to q for alloys with low γ' volume fractions (Eckhard Nembach & Neite, 1985).

2.4.3.1 Modulus strengthening

Due to the distinct shear moduli (μ) of the matrix and precipitates, there exists a variation in dislocation energy between these two phases, ultimately influencing their motion characteristics. It can be calculated mathematically using the equation (2.7).

$$\tau_{mod} = \frac{2T}{bL}\left[\frac{\omega_1|\mu_p - \mu|b^2\left(\pi R/4b\right)^{\omega_2}}{2\pi T}\right]^{3/2} \tag{2.7}$$

where, b is the Burgers vector, L is the inter-precipitate spacing from center-to-center given by equation (2.8), μ is the shear modulus of the γ matrix, μ_p is the shear modulus of the precipitate, T is the dislocation line tension given by equation (2.9), R is the average radius of the precipitate, ω_1 and ω_2 are two constants with a value of 0.05 and 0.85, respectively.

$$L = \left(\frac{2\pi}{3f}\right)^{1/2} R \tag{2.8}$$

$$T = \frac{\mu b^2}{2} \tag{2.9}$$

2.4.3.2 Coherency strengthening

A precipitate phase can be called coherent with the matrix if the lattice parameters of the precipitate phase run continuously with the matrix phase at their interface, as shown in Figure 2-11a.

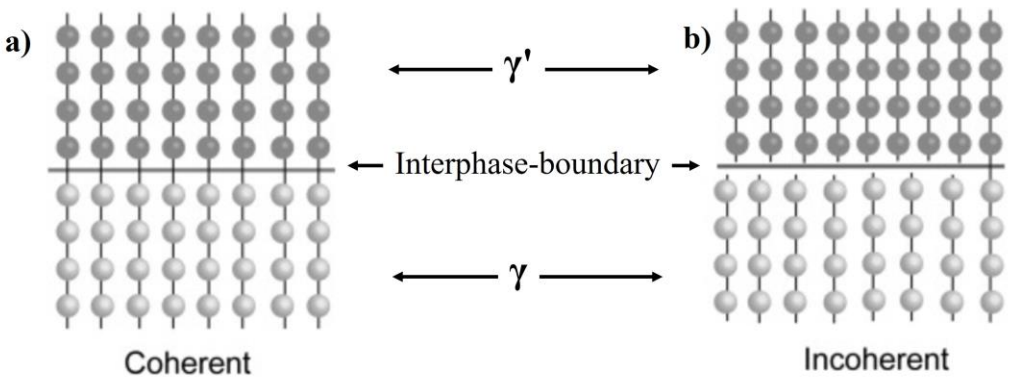

Figure 2-11: A schematic to show the atomic arrangement for coherency and incoherency between the γ and γ' phase.

If the difference in the continuity at the interface exceeds 5%, they are considered as incoherent phases, as shown in in Figure 2-11b. The coherency can be quantified as the δ_m between these two phases, which can be calculated according to the equation (2.10).

$$\delta_m = 2 \times \left[\frac{(a_{\gamma'} - a_{\gamma})}{(a_{\gamma'} + a_{\gamma})}\right] \qquad (2.10)$$

where, a_{γ} and $a_{\gamma'}$ are the lattice parameters of the γ and γ' phases (Roger C. Reed, 2006). The misfit is called positive if the lattice parameter of the precipitate is larger than the matrix and vice versa. The difference in the lattice parameter of the γ matrix and coherent γ' precipitate phase results in a strain field, which surrounds the precipitate and hinders the movement of dislocations from the matrix to the precipitate, thereby resulting in strengthening. Hence, misfit strongly influences the strengthening of the alloy. Some studies mentioned the lattice misfit value as independent of precipitate size and chemistry (Preuss et al., 2008), whereas the group of Singh (Singh et al., 2011) reports that the change in chemistry with different precipitate sizes (primary, secondary and tertiary γ') affects the misfit parameter.

2.4.3.3 Interfacial strengthening

As dislocations shear through the precipitates, the process generates new interfaces (highlighted by the red arrow in Figure 2-12), leading to an increase in the surface energy known as the interfacial energy. This phenomenon can be quantified using equation (2.11).

$$\tau_{chem} = \frac{2T}{bL}\left[\frac{b\gamma_{IFE}}{T}\right]^{3/2} \tag{2.11}$$

where, γ_{IFE} is the precipitate-matrix interface energy.

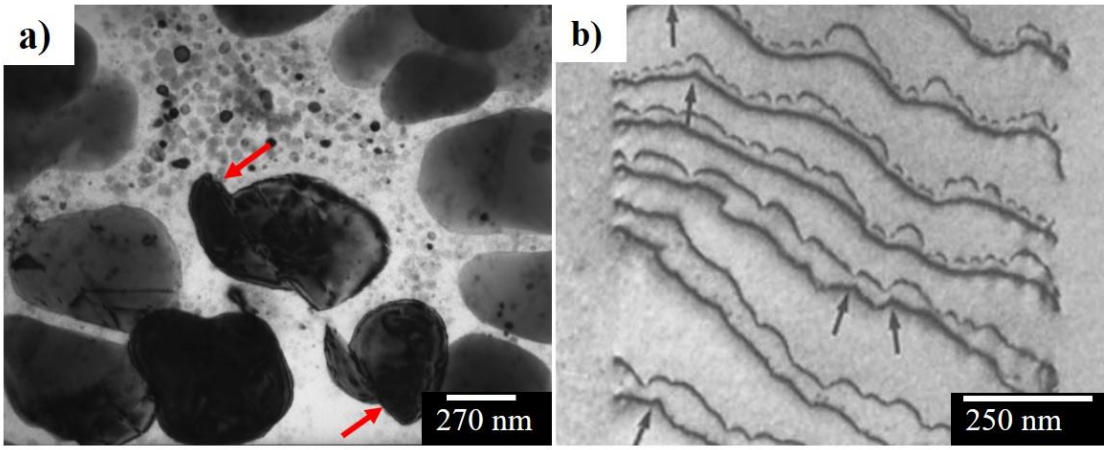

Figure 2-12: TEM bright field (BF) image shows a) the sheared precipitate and creation of a new interface (highlighted by red arrow) (Argon, 2007), b) paired edge dislocations in Nomic 105 (Eckhard Nembach & Neite, 1985).

2.4.3.4 Ordered Strengthening/Anti-Phase Boundary

The strength from precipitation comes mainly from the ordered γ' precipitate sitting coherently in the γ matrix. The interaction mechanism between γ' precipitates and dislocations changes with variations in the precipitate size (Eckhard Nembach & Neite, 1985). For smaller precipitates, dislocations tend to shear through the precipitates, as depicted in Figure 2-12a. This shearing process is accompanied by paired dislocations (Figure 2-12b), where the leading dislocation creates an APB upon shearing, and the trailing dislocation glides on the same plane to eliminate

it, thereby restoring the γ' structure (Ardell, 1985; Morris & Morris, 1990). A dislocation with Burger's vector of a/2<110> traveling in the γ matrix (disordered FCC) cannot enter the γ' phase (ordered FCC) without making an APB.

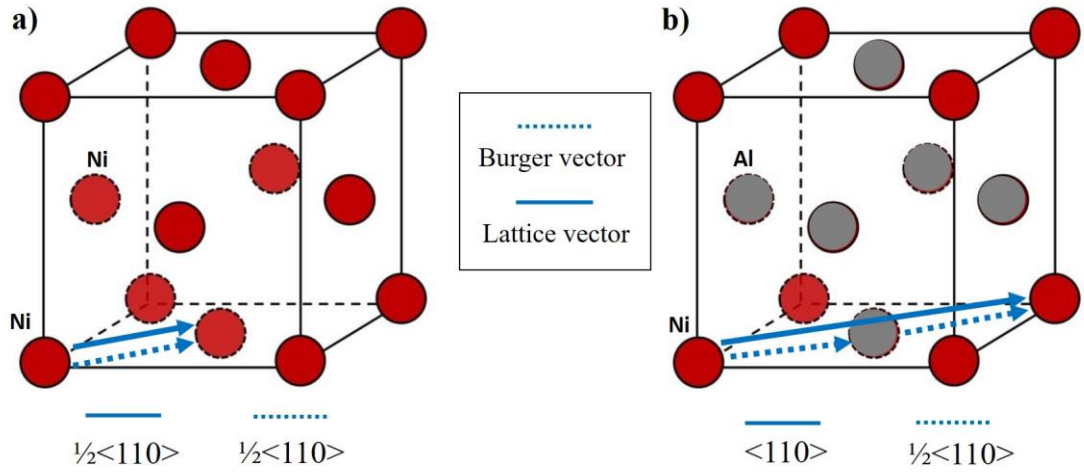

Figure 2-13: Unit cells showing the lattice vector and Burger's vector for the a) γ matrix phase, b) γ' precipitate phase; created using CrystalMaker.

In the case of the γ matrix (Figure 2-13a), the lattice vector (a/2<110>) is equal to the Burger's vector a/2<110>. Hence, a deformation that occurs by the passage of a single dislocation with a Burger's vector of a/2<110> type would not change the ordering. But, the lattice vector for the γ' precipitate is a<110> (Figure 2-13b). Therefore, when a dislocation of type a/2<110> enters the γ' precipitate, it moves the atom in a high energy or unfavorable position with an associated energy called anti-phase boundary energy (APBE). Therefore, the dislocations must travel in pairs to restore the stable structure of the γ' precipitate, Figure 2-13b. This pair of dislocations are also known as a super-dislocation.

2.4.3.5 Orowan Looping/Bowing

When precipitates exceed a critical radius indicated as R_m in Figure 2-14a), dislocations may bow around the precipitates as shown in Figure 2-14b. When the precipates are larger bowing or looping

requires a lower stress compared to shearing, as depicted in Figure 2-14a. This phenomenon is called Orowan bowing (Figure 2-14b) and is described by equation (2.12) (Gerold & Haberkorn, 1966; Raynor & Silcock, 1970).

$$\tau_{oro} = \frac{3\mu b}{2L} \tag{2.12}$$

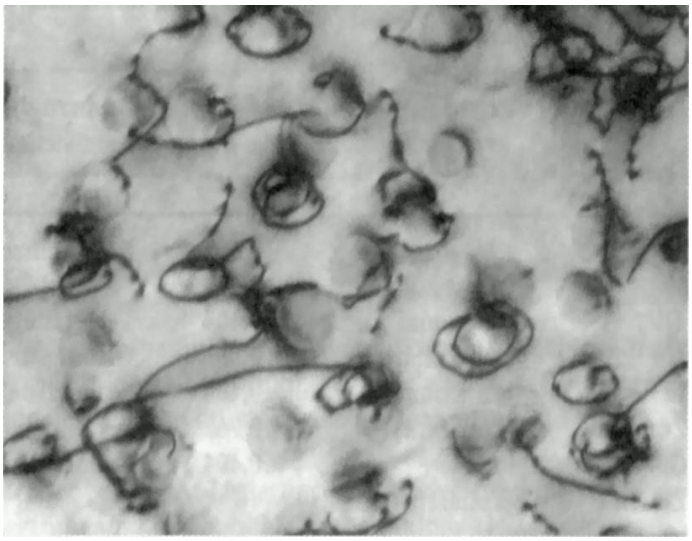

Figure 2-14: Dislocation loops around γ' precipitates for alloy Haynes 282 (Polkowska et al., 2019).

2.5 DEFORMATION MECHANISM AND YIELD STRENGTHENING IN Γ' PRECIPITATE ALLOYS

2.5.1 Deformation mechanism

The interactions between the γ' precipitates and dislocations depend on the size and volume fraction of the γ' precipitates [14, 26, 34]. For relatively small γ' precipitates, dislocations tend to shear through the precipitates, as depicted in Figure 2-15a. This shearing process is accompanied by paired dislocations, where the leading dislocation creates an APB upon shearing, and the trailing dislocation glides on the same plane to eliminate the APB and restore the γ' structure (Ardell, 1985; Eckhard Nembach & Neite, 1985). The nature of dislocation pairs can be

categorized as either weak-pair coupling or strong-pair coupling, contingent on the size of the precipitates. Weak-pair coupling is characterized by the gap between the paired dislocations, particularly noticeable in the context of smaller precipitates. Consequently, the trailing dislocation may not entirely traverse an individual precipitate, while the leading dislocation engages in precipitate cutting [16, 20]. Conversely, in the case of strong-pair coupling, the spacing between dislocation pairs approaches the diameter of the particle, owing to the heightened hindrance caused by increased APB energy with larger precipitates. As a result, the trailing dislocation is likely to enter the precipitate before the leading dislocation leaves the precipitate [16, 20]. Moreover, when interacting with relatively larger precipitates, dislocations tend to bow around them, giving rise to Orowan loops, as illustrated in Figure 2-14 and Figure 2-15b.

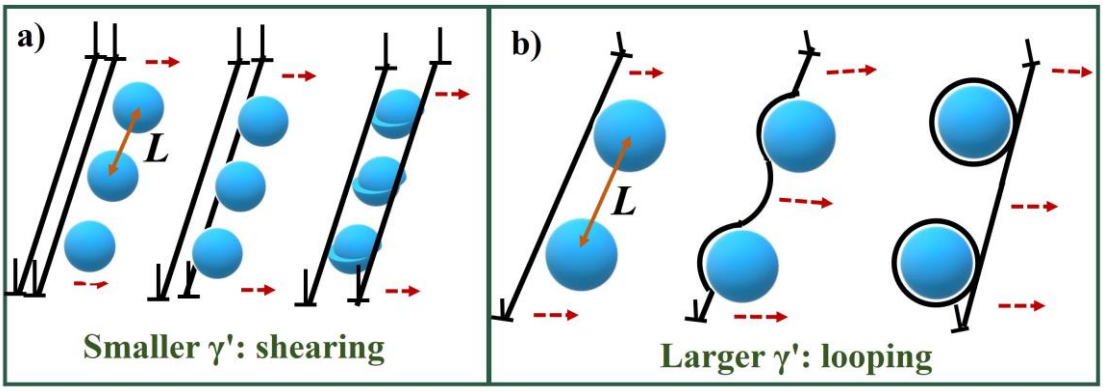

Figure 2-15: Schematic of potential precipitate-dislocation interactions a) shearing of smaller γ' precipitates, b) looping around larger γ' precipitates.

In addition to being related to the precipitate radius (R), the deformation mechanisms are related to the inter-particle spacing from center-to-center (L), which is related to precipitate volume fraction and determines the bowing angle (θ) (Collins & Stone, 2014). Essentially, as L increases, it becomes more favorable for dislocations to bow around precipitates. This bowing angle influences the resultant force that a precipitate of a given radius can withstand. The resultant force

can be calculated as the balance of dislocation line tensions (T) and opposing force (F) on the dislocation due to the APB, as depicted in Figure 2-16. Figure 2-16a illustrates how small precipitates exhibit minimal bowing and form high bowing angles ($120<\theta<180^{o}$) between the dislocation lines, and therefore they are more susceptible to shearing. The shearing of such precipitates (Figure 2-16a) is accompanied by weak-pair coupling. Figure 2-16b illustrates how larger precipitates form a bowing angle smaller than 120^{o}, and they are more difficult to shear than the smaller precipitates depicted in Figure 2-16a. Shearing of large precipitates (Figure 2-16b) is assisted by strong pair coupling. As the bowing angle approaches 0^{o}, the precipitate sizes increase to the level that they become basically non-shearable; see Figure 2-16c. Thus, for unimodal precipitate size distributions (PSDs), L informs whether weak-pair, strong-pair or Orowan looping will be the dominant mechanism.

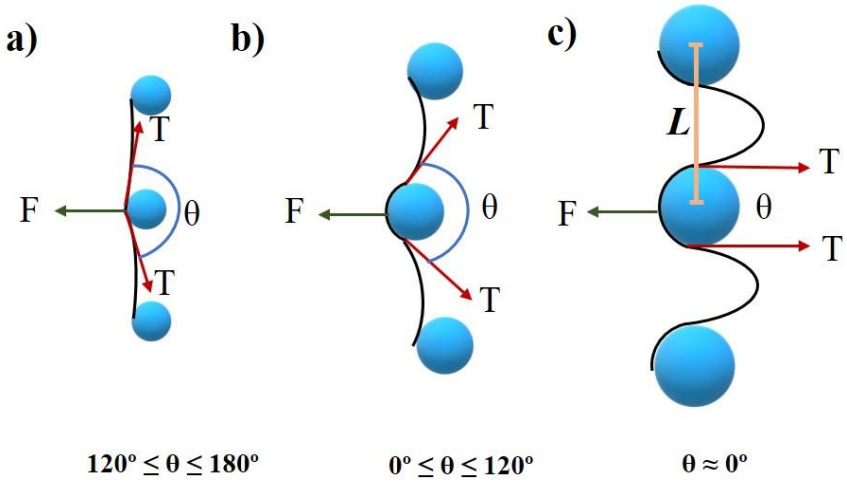

Figure 2-16: Schematic of forces (F and T) and bowing angles (θ) for different precipitate sizes. a) weak and shearable precipitate, b) strong and shearable precipitate, c) strong and non-shearable precipitate. Recreated from (Ahmadi et al., 2014).

Figure 2-17 depicts the relationship between the precipitate radius and the critical resolved shear stress (CRSS) for shearing or looping for a fixed precipitate volume fraction (Foreman & Makin,

1966; Sarosi et al., 2007; Viswanathan et al., 2004). For precipitate radii below R_m, the dominant mechanism is weak-pair coupling shearing, whereas for radii above R_m, strong-pair coupling shearing becomes dominant. As the precipitate size increases, the necessary stress for shearing also increases, and looping becomes dominant for precipitates with radii greater than R_c. The R_m and R_c vary with precipitate volume fraction (Eckhard Nembach & Neite, 1985; Raynor & Silcock, 1970).

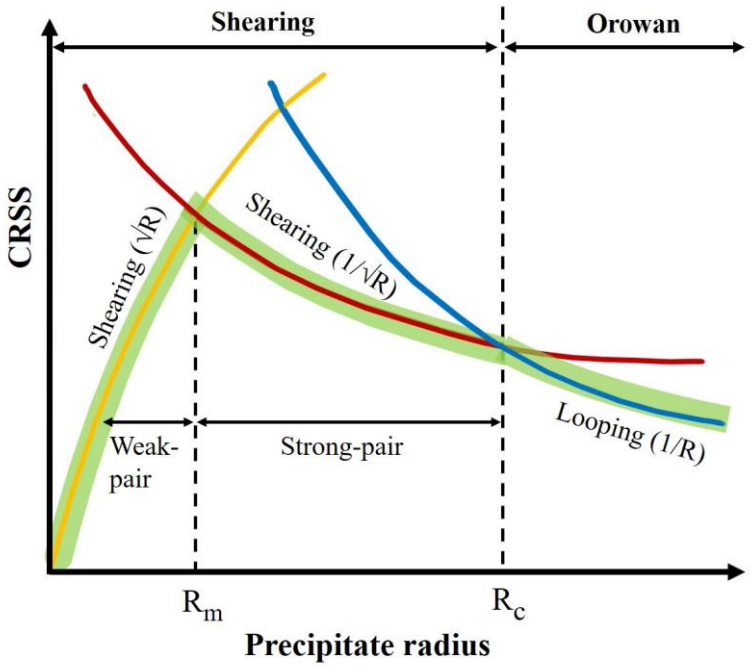

Figure 2-17: Schematic illustrating the relationship between the CRSS required for weak-pair coupling (τ_{weak}) shearing, strong-pair coupling (τ_{strong}) shearing, and looping as a function of γ' precipitate radius (R) for a fixed volume fraction (f) of the precipitate. The green shaded line shows the dominant mechanism for a given precipitate volume fraction [recreated from (Fang et al., 2022)].

2.5.2 Yield strength prediction

The strengthening mechanism in the alloy considerably changes with the microstructure (R C Reed & C.M.F.Rae, 2014; Strudel, 1996). Significant research has been undertaken to investigate the influence of γ' precipitates on predicting the YS of materials (Collins & Stone, 2014; Eckhard

Nembach & Neite, 1985; Goodfellow, 2018). Whitmore et al. (Ahmadi et al., 2014) have used integrated physical models that consider intrinsic, grain boundary, solid solution, and precipitate strengthening contributions and related them to the measured hardness and YS. This study reported that precipitation strengthening relating to the coherency strain and APB effects has a major influence on the final YS (Whitmore, Leitner, Povoden-Karadeniz, Radis, & Stockinger, 2012). Most of the predictive models have focused on point-sized γ' precipitates or unimodal size distributions (Goodfellow, 2018). However, there has been a recent interest in incorporating multimodal PSDs to predict YS, although such studies come with certain limitations (Collins & Stone, 2014; Jackson & Reed, 1999b; Kozar et al., 2009). The proposed model of Kozer et al. for multimodal distributions is only valid for fine-grain microstructures (i.e., <5 μm). Collins and Stone developed a strengthening model, but it is not designed to predict the YS of multimodal microstructures (Collins & Stone, 2014). Ahmadi *et al.* have focused on predicting the YS of 718Plus specifically, but similar to the work of Collins et al., their model is limited to unimodal γ' precipitate size distributions (Ahmadi et al., 2014). Galindo-Nava et al. have developed the only model which incorporates the contribution from different γ' precipitate sizes in multimodal microstructures (Galindo-Nava et al., 2015).

The strengthening contribution from the precipitates in a heat-treated polycrystalline superalloy has always been a point of discussion and an open area for research due to the complex contribution (refer to equation (2.2)). We will discuss the recent models that are being incorporated for the prediction of the YS, focusing on Orowan bowing and APB effect. Equation (2.12) for Orowan bowing was further modified by Brown and Ham as follows;

$$\tau_{orowan-modified} = \frac{\mu b}{2\pi\sqrt{1-\vartheta}} \frac{1}{L_s} \ln\left(\frac{\pi R}{2R_i}\right) \qquad (2.13)$$

L_s is the inter-particle spacing from surface-to-surface of the precipitates, defined by equation (2.14).

$$L_s = \left(\frac{8}{3\pi f}\right)^{1/2} 2R - 2R \tag{2.14}$$

Equations (2.15) and (2.16) depict a correlation between the precipitate size and the CRSS for the weak-pair and strong-pair shearing, respectively [12, 35].

$$\tau_{weak} = \frac{\gamma_{APB}}{2b}\left[\left(\frac{6Rf\gamma_{APB}}{2\pi T}\right)^{1/2} - f\right] \tag{2.15}$$

$$\tau_{strong} = \sqrt{\frac{3}{2}}\left(\frac{\mu b}{R}\right)\frac{f^{1/2}}{\pi^{3/2}}\left(\frac{\pi R\gamma_{APB}}{T} - 1\right)^{1/2} \tag{2.16}$$

where, γ_{APB} is the APB energy, f is the precipitate volume fraction, and T is defined by equation (2.8).

Galindo *et al.* discuss the dynamics of weak and strong pair-coupling configurations, with the critical size threshold, R_m, being a key determinant (Galindo-Nava et al., 2015). A modified equation (2.17), amalgamating both τ_{weak} and τ_{strong} that considers the change in effective inter-particle spacing is provided below;

$$\tau_{weak-strong\ modified} = \frac{\gamma_{APB} l_1}{2b(\Lambda_1 + 2R)} \tag{2.17}$$

where, l_1 is the segment length of leading dislocations given by equation (2.19a), R_m is the precipitate radius that provides the maximum strength, and it is defined by the equations (2.18), and Λ_1 is the effective length of the leading dislocation between the obstacle/precipitate calculated using equation (2.20).

$$R_m = \frac{\mu b^2}{2\gamma_{APB}} \tag{2.18}$$

$$l_1 = 2R, \qquad if\ R < R_m \tag{2.19a}$$

$$l_1 = 2(R^2 - (R - R_m)^2)^{1/2}, \qquad if\ R \geq R_m \tag{2.19b}$$

$$\Lambda_1 = max\left(\left(\frac{T}{\gamma_{APB}R}\right)^{1/2} L, L - l_1\right) \tag{2.20}$$

The extended form of equation (2.17) to encompass multimodal distributions (presented here as equation (2.21), which accommodates the presence of both larger (l) and smaller (s) size precipitates, was used by Galindo-Nava et. al., for the bimodal microstructure strengthening calculation (Galindo-Nava et al., 2015). The number fractions of the smaller (w_s) and larger (w_l) γ' precipitates were calculated by measuring the number of precipitates (N) of a particular size, for example, N_s for smaller γ' precipitates and N_l for larger γ' precipitates, using equation 16.

$$\tau_{multimodal} = \frac{\gamma_{APB}}{2b}\left(w_l \frac{l_1^l}{\left(\Lambda_1^l + 2R_l\right)} + w_s \frac{l_1^s}{(\Lambda_1^s + 2R_s)}\right) \tag{2.21}$$

$$w_l = \frac{N_l}{(N_s + N_l)} \tag{2.22a}$$

$$w_s = \frac{N_s}{(N_s + N_l)} \tag{2.22b}$$

For alloys like 718Plus consisting of low volume percent of γ' precipitate, hardly any study has been conducted pertaining to multimodal γ' PSDs. Ahmadi et al. have studied this alloy, but their research is confined to unimodal distributions only. Although research has been conducted on 718Plus, this alloy is still in its infancy, and the exploration of optimizing its properties through the development of multimodal γ' PSDs remains largely unexplored.

2.6 GAPS IN THE LITERATURE PERTAINING TO THIS DISSERTATION WORK

After conducting a thorough analysis of the literature discussed in this chapter, several critical gaps have been identified that need further exploration. Some of the gaps are focused on in this dissertation work from the list below:

2.6.1 Microstructural aspects

a) There is no clear processing technique/methodology to form a bimodal distribution of γ' precipitates. Some work has shown that two-step aging results in bimodal distributions, but the extent of the control of the precipitate size is not clear. A large amount of work in this dissertation is focused on developing a methodology (based on two-step aging treatments) to obtain bimodal distributions of the precipitates (one size being significantly larger than the other). This effort involved different cooling rates from the different aging temperatures, and such work had yet to be systematically performed. Therefore, this is a valuable contribution to the literature.

b) Optimizing the microstructure of ATI 718Plus for specific applications has proven to be elusive. Although this dissertation work did not focus on any specific applications, the methodology developed in this work can provide the basis for changing the γ' precipitate sizes to obtain the mechanical properties needed for specific applications.

c) The compositional changes in the matrix and the precipitates have not been characterized as a function of precipitate distribution, size, and volume fraction as this could lead to a change in overall strengthening of the alloy (e.g. supersaturation in the matrix leading to solid-solution strengthening). Using a suite of characterization tools, including Atom probe tomography (APT), SEM-EDS, STEM-EDS, ImageJ, etc., this dissertation has identified the compositional differences in the matrix and the precipitates as a function of precipitate

distribution, size, and volume percent. This is discussed with respect to diffusional aspects during the aging treatments.

d) While the coarsening rate of γ' precipitates has been extensively examined and established to follow a cubic rate law, there remains a lack of studies on the coarsening rate of multimodal precipitate size distributions. This dissertation work presents preliminary findings that offer a foundation for comprehending the kinetics and coarsening rate of bimodal γ' precipitate microstructures. Further investigations can build upon these results to enhance the understanding in this area.

2.6.2 Mechanical behavior

a) The strength ceiling of ATI 718Plus has yet to be discovered. Although this work did not identify the highest room temperature tensile strength for this alloy, the bimodal microstructure developed in this work proved to be stronger than the unimodal microstructures. It is noted that this microstructure still exhibited necking and ductile failure with over 30% elongation. Thus, further improvements in balancing the strength and elongation can be obtained using the processing-microstructure-property relationship understanding initiated in this dissertation work.

b) The optimal creep properties of ATI 718Plus have yet to be discovered, and knowledge of processing-microstructure-property relationships is still in its infancy. Although this work did not focus primarily on creep, some valuable contributions to understanding processing-microstructure-creep relationships are made. Understanding elevated temperature effects on the tensile, fatigue, and creep properties is a ripe area of research that has yet to be significantly explored for this promising alloy.

c) Research findings have indicated that the presence of δ/η phases along grain boundaries might serve as the initiation sites for cracks. Furthermore, the presence of dislocation substructures has been associated with increased resistance to grain boundary cracking, although the precise mechanism remains elusive. This dissertation work contributes by presenting fractographic analyses of creep-deformed samples, providing valuable insights from a microstructural perspective that may aid in unraveling the underlying mechanism.

2.6.3 Deformation mechanisms

a) While active deformation mechanisms for unimodal γ' PSDs have been established, the dominant mechanisms in microstructures containing multiple γ' PSDs remain unclear. This dissertation addresses this knowledge gap by focusing on the identification of deformation mechanisms during room temperature tension, considering precipitate distribution, size, and volume percent. Through meticulous post-deformation TEM characterization, this study identified Orowan bowing and precipitate shearing as active mechanisms, and their variations are linked to the precipitate size, distribution, and volume percent.

b) Existing strengthening models primarily pertain to unimodal γ' size distributions, leaving a notable gap in the literature regarding multimodal γ' size distributions. Recent efforts have aimed to develop models for multimodal distributions, but experimental correlation and validation have been lacking. This work was the first to experimentally and theoretically identify the dominant deformation mechanisms while also introducing a modified model to predict YS for bimodal microstructures. This will have a profound impact on future deformation behavior studies of this alloy and other low volume percent (up to 20%) γ' strengthened alloys.

CHAPTER 3. MOTIVATION AND OBJECTIVES

The objectives of this work were derived from the literature review and the noted gaps in the literature mentioned in the previous chapter in section 2.6.

Superalloys employed in gas turbine engine applications often exhibit a bimodal or tri-modal distribution of γ' phase precipitates (Donachie & Donachie, 2002; Joseph et al., n.d.; Masoumi et al., 2016; Roger C. Reed, 2006; Smith et al., 2015). However, there is limited available information regarding the stability and evolution of these γ' precipitates. This pertains to the alterations that occur within this distribution due to factors like aging temperature (exposure at the service temperature), duration, and stress (applied during service). Consequently, conducting experimental investigations into multimodal microstructures is of paramount importance for establishing meaningful correlations between structure and properties. Although research has been conducted on 718Plus, this alloy is still in its infancy, and the exploration of optimizing its properties through the development of multimodal γ' PSDs remains largely unexplored. To bridge this gap, an objective of understanding the development of bimodal γ' precipitate distribution was selected.

Developing predictive models for YS in superalloys is a challenging endeavor due to the complex nature of strengthening mechanisms. Predictive models for multimodal γ' PSD microstructures have been limited in their availability. The scarcity of experimental data containing multimodal microstructures further complicates the development of physical models. As a result, this study was undertaken to bridge the knowledge gap by establishing an experimental understanding of the relationship between microstructure and deformation mechanisms, both in unimodal and bimodal γ' precipitate microstructures.

While the microstructural transformations during deformation at RT and elevated temperatures in IN718 have been comprehensively studied (Sundararaman, Mukhopadhyay, & Banerjee, 1988a, 1992), the growth and stability of γ' precipitates in 718Plus have remained relatively unexplored. Therefore, this research seeks to shed light on the evolution of γ' precipitates under the influence of stress and thermal conditions, mimicking those encountered in service.

The primary objectives of this work can be categorized as follows:

- To develop a uniform bimodal distribution of γ' precipitates through different aging treatments. Particularly, emphasising on investigating the role of various aging parameters, such as temperature, holding time, and cooling rate, in the formation of this microstructure. The anticipated bimodal distribution of the γ' precipitates will comprise both larger and smaller γ' precipitates, as illustrated in Figure 3-1.

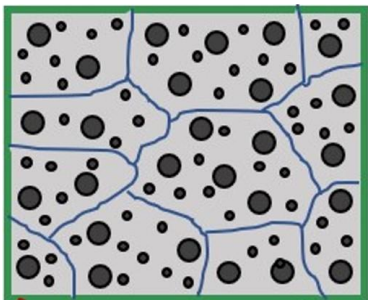

Figure 3-1: Schematic of targeted bimodal γ' precipitate size distribution.

- To ascertain the primary deformation and strengthening mechanism in a microstructure featuring bimodal distribution of γ' precipitates. Investigating deformation across various precipitate sizes and distributions (including unimodal and bimodal) will provide insights into the nature of interactions between dislocations and precipitates. Notably, 718Plus possesses a relatively low γ'-phase volume percent (20 %), suggesting that particle-particle interaction effects are likely to be less influential.

- To examine the stability and growth of the γ' phase when subjected to both thermal exposure and elastic tensile stress simultaneously. Comparing the microstructural changes between samples exposed solely to thermal conditions and those subjected to creep deformation will provide insights into the combined impact of stress and high-temperature exposure.

The general aim of this project is to experimentally provide strong insight into these aspects so that a realistic predictive capability model can be developed for the performance of the alloys. A flow chart for this study is provided in Figure 3-2.

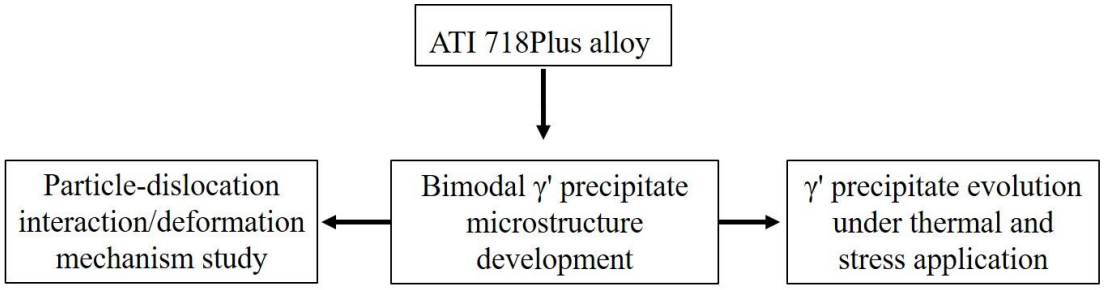

Figure 3-2: Overview of the objectives outlined for the dissertation.

CHAPTER 4. EXPERIMENTAL METHODS

4.1 MATERIALS

A 20-inch diameter billet of 718Plus was vacuum induction melted (VIM), then vacuum arc remelted (VAR) and further forged to a diameter of 10 inches, and supplied by ATI Metals, Pittsburgh, PA, Figure 4-1. The bulk composition of the alloy was measured using optical emission spectroscopy (OES), as provided in Figure 4-2. A detailed microstructural characterization was performed on the as-processed alloy using standard metallographic procedures. Samples with the dimensions of 1 cm^3 were cut from the as-processed alloy using a high-speed abrasive saw prior to heat-treatment for all the microstructural studies.

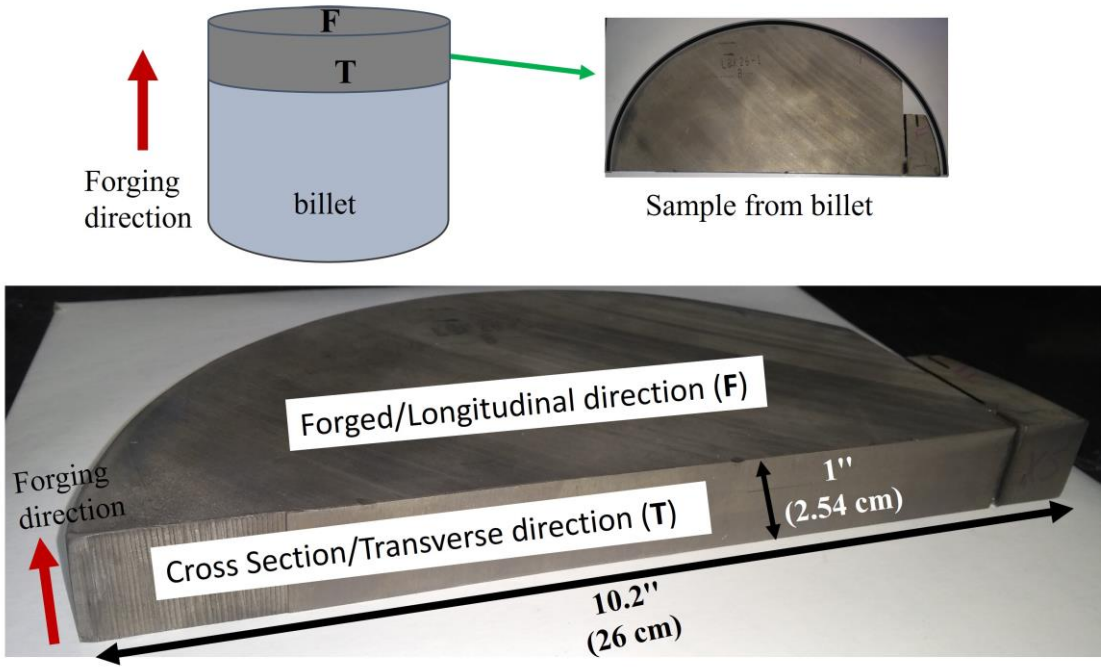

Figure 4-1: Schematic and digital images of the as-processed bulk 718Plus sample received from ATI Metals.

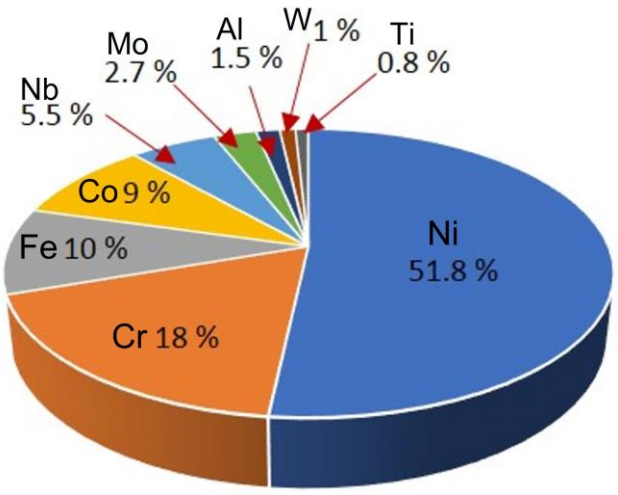

Figure 4-2: Chemical composition of the as-processed 718Plus (in weight percent, wt.%).

4.2 HEAT-TREATMENT

All of the heat treatments in this dissertation were performed in an open-air environment with a heating rate of 10 °C/min either Lindberg or Thermolyne 46200 box furnaces. The Lindberg furnace was used for the temperature range of 700-1100 °C, Figure 4-3a. The Thermolyne 46200 furnace was used for longer holding times, such as 24-500 hr at 700 °C; see Figure 4-3b. All of the furnaces were individually calibrated using an external k-type thermocouple and a thermocouple reader, for example; see Figure 4-3. Figure 4-4 is a schematic drawing representing the general heat-treatment steps for the alloy in this dissertation work. T and $f_{\gamma'}$ represent the temperature and volume percent of the γ' precipitates, respectively. The samples were first solution treated to achieve a single phase γ-matrix microstructure. After solutionizing, the samples were subjected to different aging treatments to produce different average γ' precipitate sizes and volume percentages in the matrix. For example, aging at temperature T_1 provided $f_{\gamma'1}$ volume fraction of the γ' precipitates with a certain average size.

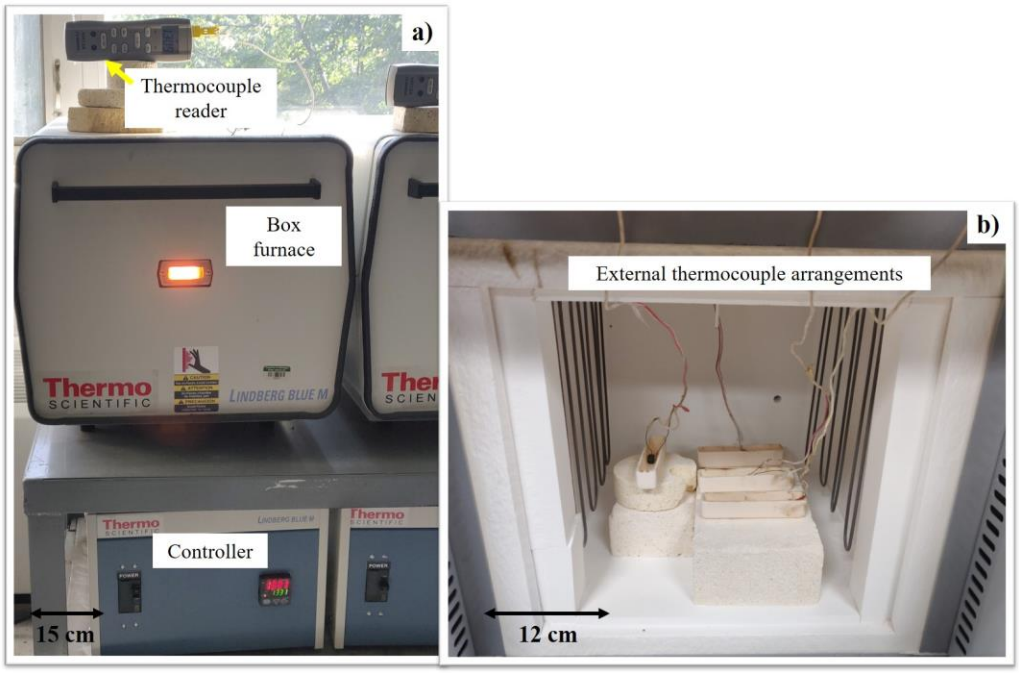

Figure 4-3: a) Digital images of the Lindberg furnace set up, including the external thermocouple and thermocouple reader, b) the Thermolyne 46200 furnace with the external thermocouples spot-welded to the samples.

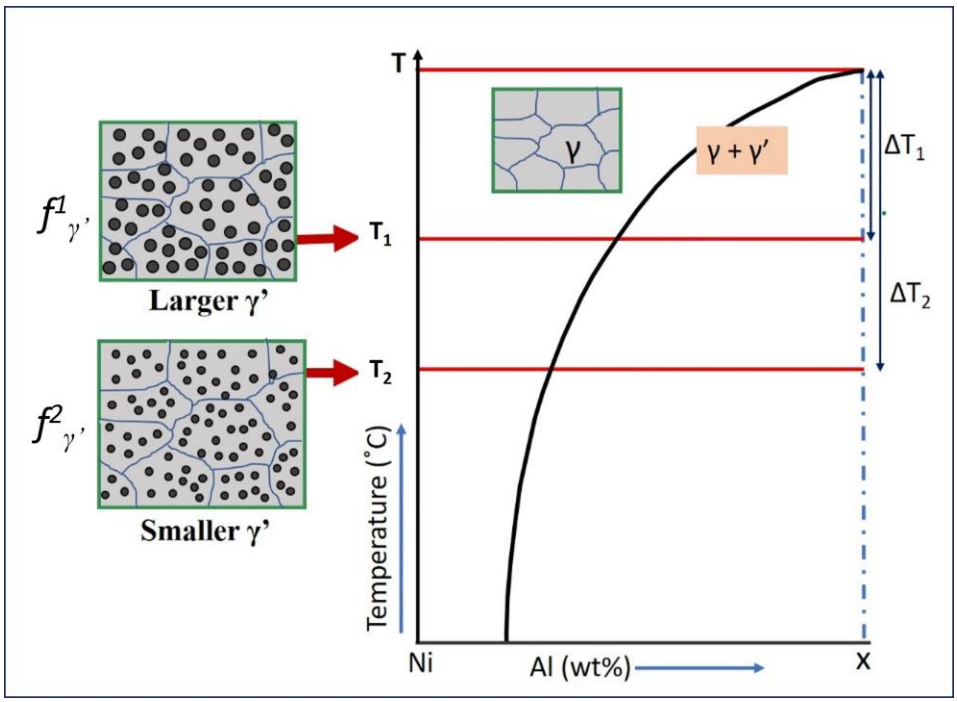

Figure 4-4: Schematic drawing of the N-Al binary phase diagram indicating the temperature ranges of the γ and γ' phases that were used to obtain the portrayed microstructures for 718Plus.

Based on the solvus temperature of the γ' phase (Srinivasan et al., 2012; Xie, Xu, et al., 2005), a range of temperatures was chosen for ST, and the holding time was kept constant at 1 hour for this work. The as-processed samples were ST at either 954 ℃, 1000 ℃, 1050 ℃, or 1100 ℃ for 1 hr, followed by WQ to RT; see Figure 4-5, to study the effect of ST on the microstructure. For the WQ to RT, a tap water was used.

4.2.1 Standard Aging Treatment

After solutionizing, all four samples were aged using the standard heat-treatment parameters available in the literature for 718Plus (W. D. Cao & Kennedy, 2001; R.L. Kennedy, 2005). Standard aging (SA) involves a two-step aging with a continuous cooling rate in between. It requires initial heating at 788 ℃ for 8 hr followed by furnace cooling (FC) with a cooling rate of 55 ℃/hr or faster to 704 ℃ and holding for 8 hr followed by air cooling (AC), refer to Figure 4-6. The samples taken out from the furnace for the AC was quickly transferred on a refractory brick. Based on the microstructures obtained from ST and ST-plus-aging samples, 1000 ℃ for 1 hr was used for the ST throughout the work.

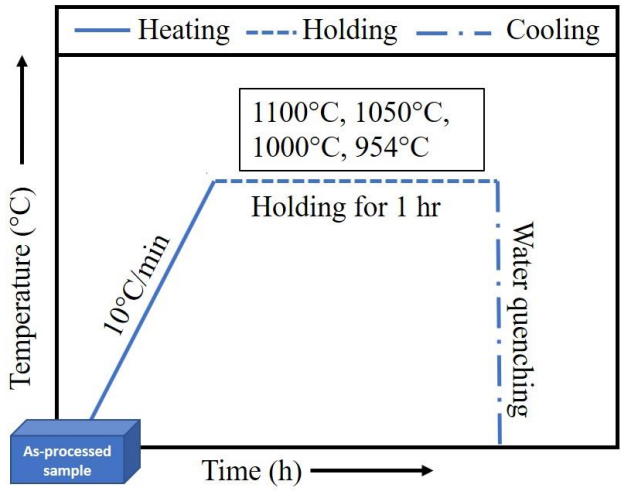

Figure 4-5: Schematic of the schedule used for the solutionizing treatments.

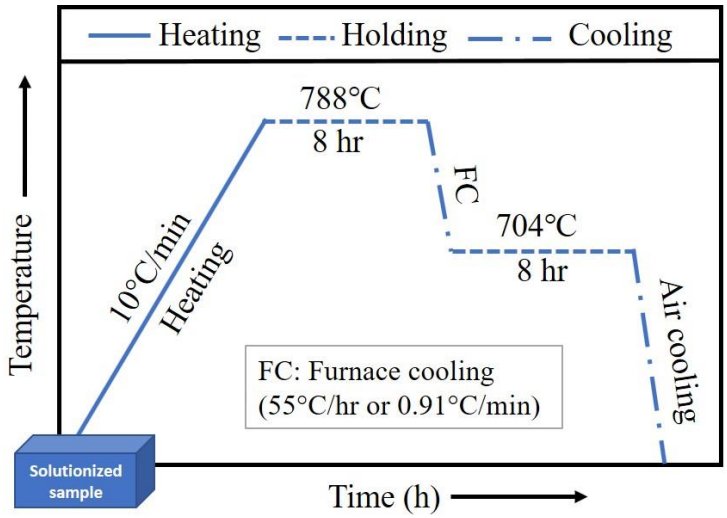

Figure 4-6: Schematic of the schedule used for standard aging of 718Plus.

4.2.2 Single-step aging for unimodal γ' size development

After ST at 1000 °C for 1 hr followed by WQ, samples were aged using various temperatures, holding times, and cooling methods to develop different γ' PSDs. Single-step aging treatments were conducted to achieve a uniform size distribution of γ' precipitates. The aging temperature and time range were chosen between 720-920 °C and 2-15 hr, respectively, based on the results obtained from Srinivasan et al. (Srinivasan et al., 2012).

Table 4-1: Single-step aging parameters used on the ST samples for obtaining unimodal size distributions of the γ' precipitates.

DESIGNATION	HEAT TREATMENT
A	720 °C - 10h - AC
B	720 °C - 10h - WQ
C	720 °C - 15h - WQ
D	750 °C - 10h - WQ
E	750 °C - 15h - WQ

Table 4-1 (cont'd)

F	900 ℃ - 2H - AC
G	900 ℃ - 2h - WQ
H	910 ℃ - 2h - WQ
I	920 ℃ - 2h - WQ

A lower aging temperature of 720-750 ℃ was chosen along with 10-15 hr of holding time to develop fine uniformly-distributed γ' precipitates; see sample A-E in Table 4-1. Later, a higher aging temperature was chosen to develop a larger γ' precipitate size. For this, temperatures of 900 ℃ or higher were chosen along with a holding time of 2 hr and varying cooling rates, refer to sample F-I in Table 4-1.

4.2.3 Two-step aging for bimodal γ' Size Development

Based on the single-step aging treatment results, two-step aging treatments were chosen to develop bimodal γ' precipitate size distributions. Both continuous cooling and interrupted cooling types were designed for this, Figure 4-7. Continuous cooling was performed between the two steps of the aging; see Figure 4-7a. As the cooling rates directly affect the resulting microstructure, an interrupted cooling to RT, using WQ, between the two-steps was also performed; see Figure 4-7b. Sample was initially aged at higher temperatures (900-930 ℃) to obtain the larger γ' precipitate size, followed by lower-temperature aging (720-750 ℃) to obtain smaller γ' precipitates; see sample J-M in Table 4-2 for each combination.

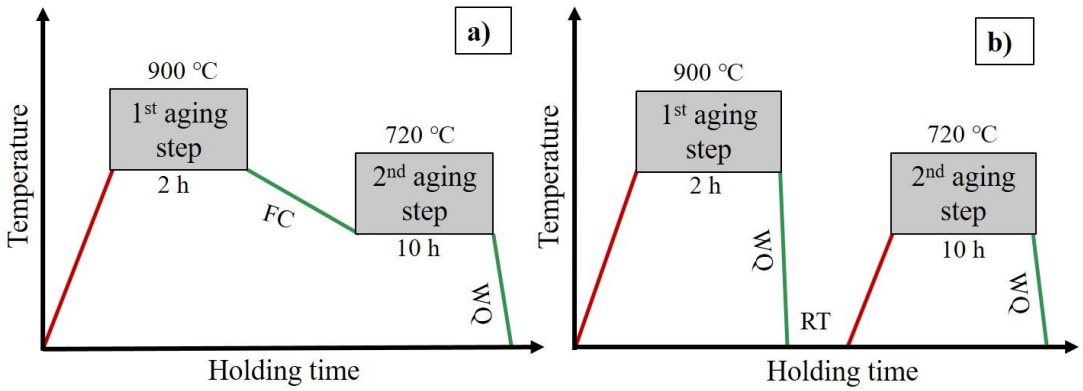

Figure 4-7: Schematic of a) two-step aging with continuous cooling at a rate of ~20 °C/min, b) two-step aging with interrupted cooling (i.e. WQ) between the two aging steps.

Table 4-2: Two-step aging parameters used on the ST samples for obtaining the bimodal γ' precipitate size distributions. The row highlighted in green represented the heat treatment used for the mechanical property testing of the bimodal samples throughout this dissertation work.

DESIGNATION	HEAT TREATMENT
J	900 °C - 2h - FC (~20 °C/min) to 720 °C - 10h - WQ
K	900 °C - 2h - FC (~20 °C/min) to 750 °C - 10h - WQ
L	930 °C - 2h - FC (~20 °C/min) to 720 °C - 10h - WQ
M	900 °C - 2h - WQ + 720 °C - 15h - WQ
N	900 °C - 3h - WQ + 720 °C - 10h - WQ
O	900 °C - 2h - WQ + 720 °C - 10h - WQ
P	900 °C - 2h - FT to 720 °C - 10h - WQ
Q	720 °C - 10h - WQ + 900 °C - 2h - WQ

Four more two-step aging treatments (sample N-Q) were conducted based on the microstructures obtained from the previous two-step aging treatments; see Table 4-2. In this study, the heat

treatment designated as O, highlighted by the green box in Table 4-2, was used throughout this work for obtaining the bimodal γ' size distribution.

4.3 METALLOGRAPHY

Specimens were hot-mounted using conductive and non-conductive mounting powder. They were then mechanically polished through 400, 600, 800, and 1200 US grit size (equivalent to Federation of European Producers of Abrasives (FEPA) 800, 1200, 2400, and 4000 grit, respectively) with SiC abrasive papers followed by diamond polishing with polycrystalline diamond paste of 9, 6, 3, l, and 0.25 µm precipitate sizes, respectively. The diamond paste polishing was performed using an ethanol-based lubricant. For EBSD characterization, the final polishing was conducted using colloidal silica, with 0.06 µm precipitate size and water. Final polishing on some of the samples for EBSD analysis was performed electrolytically using the following parameters: electrolyte: 20% H_2SO_4 in methanol at -35 ℃; voltage 24 V for 30 s. The cathode used for the electrical connection was made of platinum. A preferential chemical reaction can occur at different phases during etching (Porter, Easterling, & Sherif, 2009). Hence, multiple etchants were used for varying purposes. Freshly prepared Kalling's reagent (5 g $CuCl_2$ + 100 ml HCl + 100 ml ethanol) was used for swab etching for 60 s to study the grain boundaries. The electrolytic etching was performed to reveal the γ' and δ phases using the following parameters: electrolyte 170ml H_3PO_4 + 10 ml H_2SO_4 + 15 g CrO_3 at -20 ℃ temperature using 5 V voltage for 10 s. For all the electrolytic etching, the samples were removed from the non-conductive mount. Another etching was performed to calculate the volume percent of the γ' phase using a solution of 2.4% hydrofluoric acid, 61% lactic acid, and 36.6% nitric acid, which dissolved the γ' phase only.

4.4 MICROSTRUCTURAL CHARACTERIZATION

4.4.1 Optical Microscopy

An optical/light microscope was used to study the preliminary microstructure and the grain size of the as-processed 718Plus. A Nikon eclipse MA200 optical microscope was used to collect the micrographs. ImageJ software was used to help measure the grain size.

4.4.2 X-ray diffraction

X-ray diffraction (XRD) analysis was performed using a high-resolution Rigaku Ultima IV system with a copper (Cu) anode target (1.54 Å). The samples were lightly etched with 5% HCl in water to collect adequate intensity from the γ' phase. XRD patterns were collected with an accelerating voltage of 40 kV, beam intensity of 44 mA in a Bragg-Brentano configuration, and a 0.008° step size within the range of $20° < 2\theta < 100°$. The spectra collected were analyzed using Rigaku software. Figure 4-8 contains the reference phase peaks and the relative intensities considered for the analysis of the Ni (FCC) - γ phase and the Ni_3Al (ordered FCC) – γ' phase.

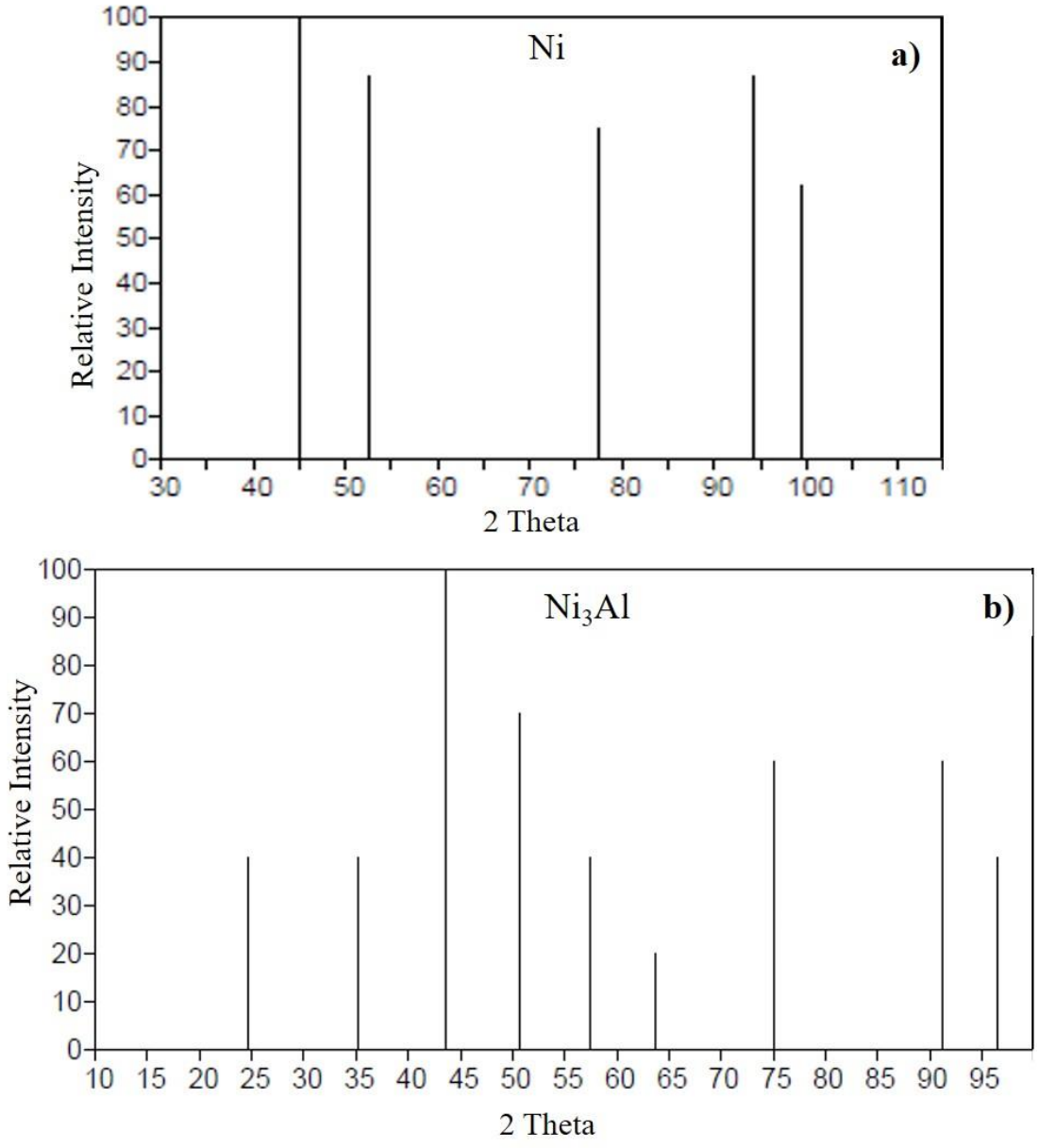

Figure 4-8: The peak locations and relative peak intensities for a) Ni (FCC) - γ phase, b) Ni_3Al (ordered FCC) – γ' phase (source: ICDD).

4.4.3 Scanning Electron Microscopy

SEM was used extensively in this work. A TESCAN MIRA-3 FEG (field-emission gun) SEM (see Figure 4-9a) was used for SE images, backscattered electron (BSE) images, energy dispersive

spectroscopy (EDS) analysis, and electron backscattered diffraction (EBSD) pattern collection. A Zeiss Auriga FIB-SEM (see Figure 4-9b) was used for SE and BSE image collection for some of the samples. An Apreo 2S HR-SEM (high-resolution SEM) was used for the SE images, BSE images, and EBSD pattern collection reported in section 5.3.1. The typical SEM imaging conditions included a 25 keV beam voltage, a 17-mm working distance, and a 20-nm spot size. To collect the images of the nanoscale γ' phase, a smaller working distance (13 mm) and a smaller spot size (10 nm) were used.

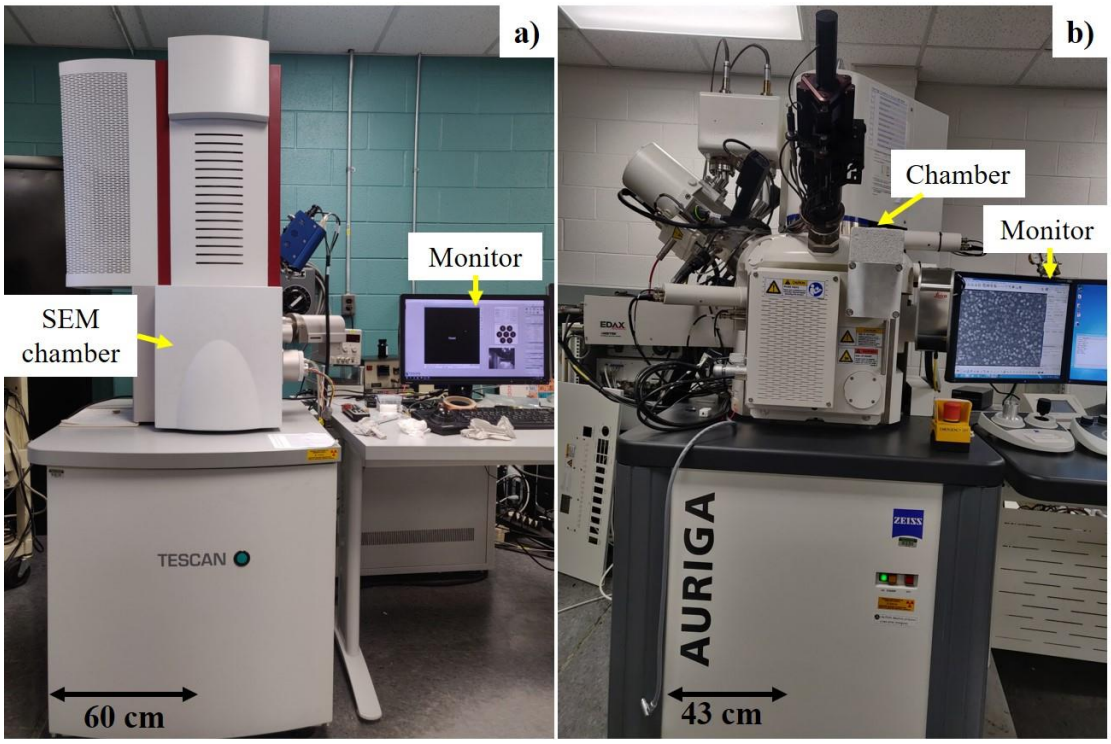

Figure 4-9: Digital Images of the SEMs used in this dissertation a) TESCAN MIRA-3 b) ZEISS AURIGA.

4.4.3.1 Electron Backscattered Diffraction

The EBSD technique was used to reveal the crystallographic/texture of the as-processed, solutionized samples, and creep-deformed samples. Unlike for the SEM imaging, the samples were tilted to 70° with respect to the horizontal plane towards the fluorescent phosphor screen when

performing the EBSD scans. EBSD orientation maps were acquired at a 20 keV beam voltage, working distances between 14 and 18 mm, and a step size of 2 µm. The EBSD datasets were analyzed using EDAX TSL OIM Analysis 6.1 and 7 for obtaining the pole figures (PF), inverse pole figure (IPF) maps, grain size distribution plots, and misorientation angle plots. The 'clean-up' procedures, which included neighbor confidence index (CI) correlation and grain dilation, were systematically applied to minimize the number of incorrectly indexed pixels. The neighbor CI correlation clean-up step replaced the orientation of the erroneous pixels (any pixel with CI < 0.05) with that of the neighboring pixel with the highest CI. Later, the grain dilation clean-up step was used to define the grains as any set of 5-10 neighboring pixels with a CI > 0.1 having a misorientation angle lower than 5 °.

4.4.3.2 Energy Dispersive Spectroscopy

The EDS technique was used in conjunction with SEM to estimate the elemental compositions of the different phases. The accelerating voltage plays a critical role in the spatial resolution during EDS analysis, as it determines the size of the interaction volume (i.e., the depth of X-ray excitation in the sample). According to the shown Zener equation (4.1), the X-ray production depth (Z_m) in a given material is a function of the accelerating voltage (E_0) in kV, the minimum emission voltage (E_C) in keV, the atomic mass (A), the atomic number (Z) and the density (ρ) in kg/m^3 (C. S. Smith, 1948).

$$Z_m = 0.033({E_0}^{1.7} - {E_C}^{1.7})\frac{A}{\rho\, Z} \qquad (4.1)$$

EDS point analysis and elemental maps were acquired using an EDAX TEAM detector installed in the TESCAN MIRA-3 FEG-SEM mentioned in section 5.1, with an accelerating voltage of 10 kV, which resulted in an interaction volume ~ 0.1 □m according to equation (4.1).

4.4.4 Transmission Electron Microscopy

Transmission electron microscopy (TEM) was used for high-resolution imaging of the γ' precipitate phase and the δ phase. The different TEMs were used at IIT Madras and Indira Gandhi Center for Atomic Research (IGCAR), Kalpakkam, India: the TECNAI T20 and TALOS 200X G2. The morphology and elemental distribution of the γ' precipitates in the various samples were analyzed using a FEI F200X Talos STEM located at the center for nanophase materials science (CNMS), Oak Ridge National Laboratory (ORNL).

4.4.4.1 TEM Sample Preparation

TEM characterization was performed on the as-processed, heat-treated (ST, aged) and aged-plus-deformed microstructures. All the heat-treated alloys were in a cubical shape of around 1 cm^3, whereas the aged-plus-deformed tensile-tested samples were in the shape of dogbone samples (refer to section 4.5.2 for dimensional details), as shown below in Figure 4-10. For the cubical samples, firstly, a piece of ~0.5 mm thickness was sliced using a low-speed diamond saw. In the case of the deformed samples, the gage section (thickness around ~0.6) was cut and used for further sample preparation.

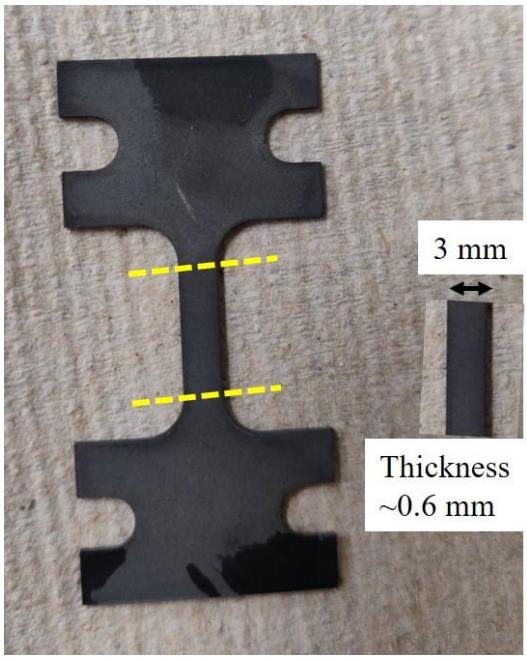

Figure 4-10: Digital image of a representative dog-bone shaped aged-plus-deformed sample used for tensile testing. TEM sample preparation was performed on the gage section of the sample indicated on the right-hand side.

The cut slices were mechanically thinned to 80-90 µm using progressively finer SiC paper through 1200 grit. Multiple 3-mm-diameter discs were then punched out of the thin foil using a SPI disc punch, followed by the cleaning of the discs using ethanol in an ultrasonicator to remove any organic impurities. Final thinning of the sample to electron transparency was performed using the jet electro-polishing technique. A Struers Tenupol 5 twin jet electro-polisher was used, and a solution of ethanol 90% + perchloric acid 10% was used as an electrolyte. The operative conditions included a voltage of 18 V while maintaining the temperature between -35 ℃ to -30 ℃ in the dual ramp flow mode. The average polishing time lasted around 3-5 minutes, depending upon the heat-treatment and deformation history of the samples. A two-step ethanol cleaning was used to remove the electrolyte from the polished samples, which were dried out on filter paper for at least 24 hours before putting them into the TEM. All the polished samples were first qualitatively viewed under an optical microscope for checking the dirt partciles on the sample.

4.4.4.2 TEM Imaging & analysis

The BF and dark field (DF) TEM images were collected based on the phases, such as DF imaging for γ' precipitate and dislocation. Selected area electron diffraction (SAED) patterns were also collected to identify the crystal structure for selected phases. The pattern indexing was carried out manually by measuring the distances in reciprocal space unit (nm^{-1}) and angle between spots and incorporating it into the equation (4.2),

$$R_{hkl}d_{hkl} = \lambda L \quad (4.2)$$

R_{hkl} is the distance between hkl and 000 plane on the diffraction pattern collected, which is related to the inter-planner spacing of the hkl plane (d_{hkl}). λL is the camera constant, where L is the distance between the sample and the screen. To index the patterns with unknown beam orientation, distance ratios and angles between the spots were consulted to the summarized table for low index reflections of Ni FCC crystal structure; see Figure 4-11. The value reported in Figure 4-11 could vary based on the lattice parameters of the element.

The morphology and elemental distribution of the γ' precipitates, γ matrix, and the precipitate-free zone (PFZ) for the aged sample (sample G) were analyzed by scanning transmission electron microscopy (STEM), using a FEI F200X Talos (200 kV). The instrument was equipped with an extreme field emission gun (X-FEG) electron source, high-angle annular dark-field (HAADF) detector and Super-X EDS (Energy dispersive X-ray spectroscopy) system with four silicon-drift detectors (SDD) (Bruker XFlash 120 mm^2) and operated with a solid angle of 0.9 steradian for chemical analysis. The TALOS 200X G2 TEM was mainly used for imaging the precipitate-dislocation interactions. Images of the dislocations were collected using weak-beam dark-field (WBDF) imaging in the two-beam condition for better resolution (Graef, 2003).

a) Table of distance ratios

	$1/d_{hkl}$ (nm^{-1})	111	200	220	113	222	133
$1/d_{hkl}$ (nm^{-1})		4.8	5.54	7.83	9.19	9.60	12.07
111	4.8	1	1.15	1.63	1.91	2.00	2.52
200	5.54	-	1	1.41	1.66	1.73	2.18
220	7.83	-	-	1	1.17	1.22	1.54
113	9.19	-	-	-	1	1.04	1.31
222	9.60	-	-	-	-	1	1.26
133	12.07	-	-	-	-	-	1

b) Table of angles

	111	200	220	113	222	133
111	-	54.7°	35.3°	29.5°	collinear	22.0°
200	-	-	45.0°	72.5°	54.7°	76.7°
220	-	-	-	64.7°	35.3°	50.0°
113	-	-	-	-	29.5°	26.0°
222	-	-	-	-	-	22.0°
133	-	-	-	-	-	-

Figure 4-11: Summary of low index reflection for FCC a) table of distance ratios of points in reciprocal lattice b) table of angles between reciprocal lattice vectors (source: DoITPoMS, University of Cambridge).

4.4.5 Atom Probe Tomography

APT, which provides a high resolution (0.3 nm of spatial resolution) three-dimensional image, was used for characterizing the sample containing the bimodal microstructure (sample O in Table 4-2) having finer and larger γ' precipitates of around 11 nm and 55 nm, respectively. The APT experiments were conducted in a LEAP 4000 XHR in laser mode with a 30 kV base temperature, 60 pJ laser energy, a 0.5 detection rate, and a pulse repetition rate set to acquire all ions between pulses. The technique was used to investigate the local compositions of the phases, such as the γ'

precipitate, γ matrix, and δ phase. The facility was accessed under the USER program at CNMS-ORNL.

4.4.5.1 Sample Preparation

The APT sample was prepared via a focus ion beam (FIB) equipped with SEM using Thermo fisher Nova 200 FIB-SEM using standard lift out, sharpening, and 2 kV cleaning techniques. Sample O, having a bimodal microstructure, was chosen for APT characterization. The samples were hot mounted and polished, similar to SEM sample preparation and slightly etched to reveal the grain boundary and grain boundary phase using Kalling's agent. Two different locations marked with green rectangles, one on the grain boundary for the δ phase (see Figure 4-13b) and another away from the grain boundaries for the γ' precipitates (see Figure 4-13a), were chosen on both the samples. After locating the areas of interest under FIB-SEM, APT needles were prepared via the in-situ lift-out procedure shown in Figure 4-12 and summarized below:

1) The identified area was protected with a platinum (Pt) layer to reduce the Ga implantation using an ion beam and ebeam (ebeam shown in step 1) with an accelerating voltage of 30 kV and a current of 0.3 nA. The green-marked region in step 2 of Figure 4-12 was the chosen area of interest (AOI).
2) A regular cross-section was milled from both sides of the Pt layer deposited, making an angle of 45º. An undercut was made to release the sample from bulk, and then a micromanipulator needle was brought closer and welded using Pt to the sample for lift-out; see steps 3 and 4.
3) The manipulator needle was brought down to a silicon (Si) microtip array coupon (steps 5 and 6). The sample was attached to the microtip via Pt welding (marked with a green rectangle in step 7),

4) A portion of the sample was cut free from the rest of the sample for one APT needle preparation; see steps 8 and 9. The welding and cutting steps were repeated to make multiple needles from the lift-out sample.
5) Repetitive annular milling was performed for the thinning of the needle and removal of the Pt layer from the sides of the sample; see steps 10 and 11.
6) The final APT needle was prepared after the removal of the Pt layer from the tip and any Ga-induced damage, leaving a needle with approximately a square cross-section of 200 x 200 nm and tip radii of 20-30 nm, as shown in step 12.

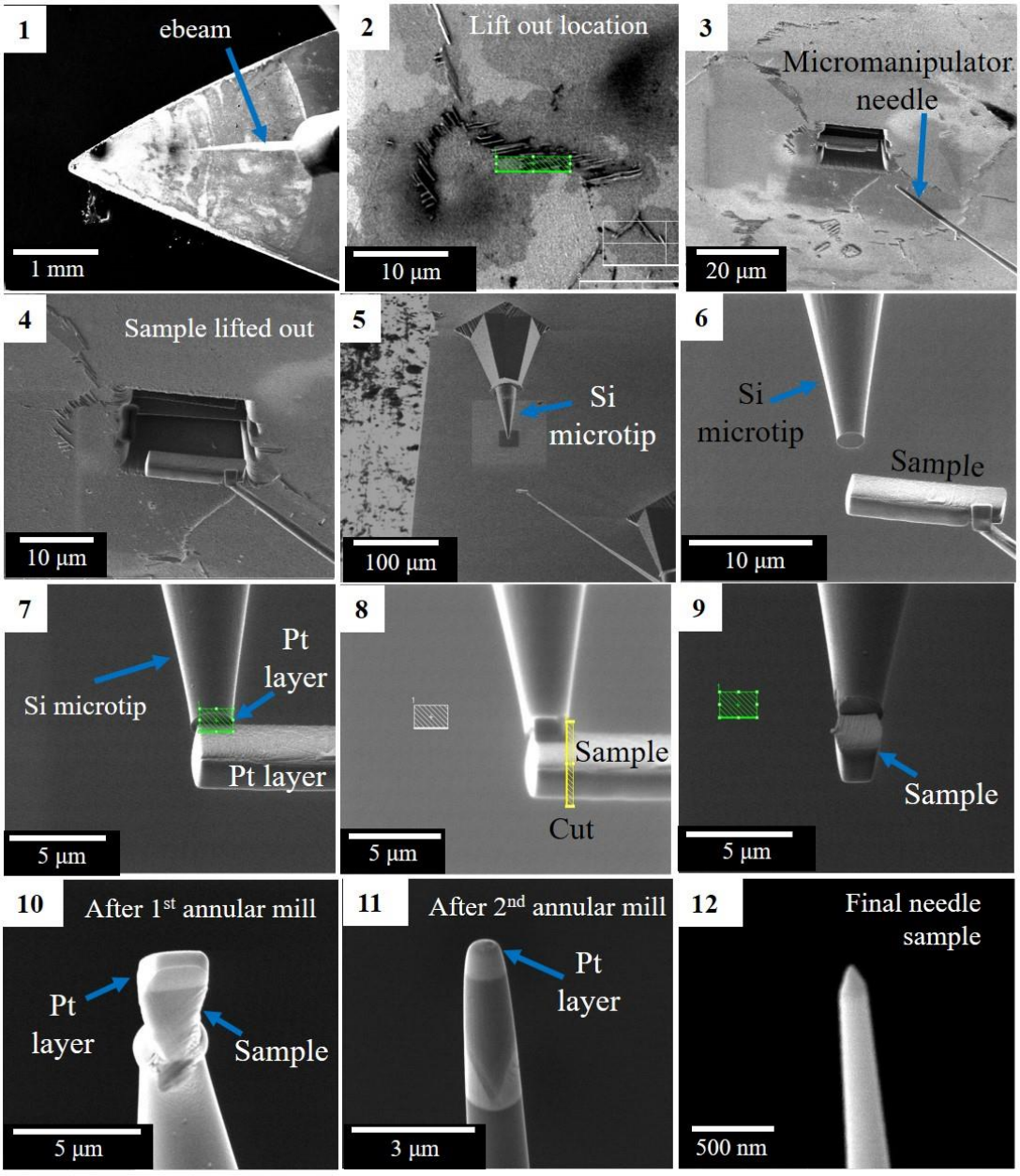

Figure 4-12: FIB-SEM images showing the stepwise APT needle sample preparation using in-situ lift-out.

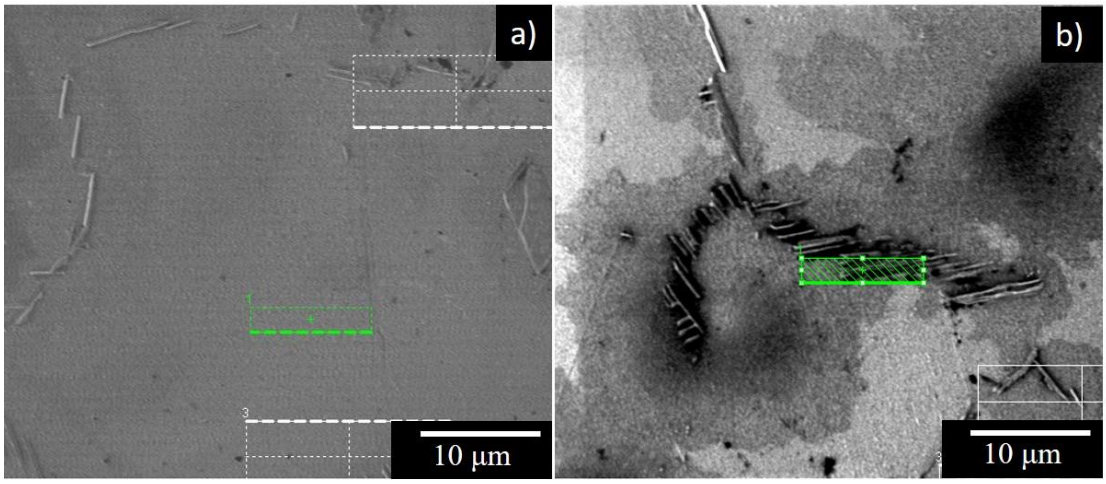

Figure 4-13: FIB view of APT needles locations marked with green rectangle a) away from grain boundary, b) on the grain boundary or grain boundary δ phase.

4.4.6 Micrograph analysis

The SEM and TEM micrographs were analyzed using ImageJ (NIH, USA) software. A total of three to four micrographs were used for analyzing the grain size or precipitate size to ensure statistical representations.

4.4.6.1 Grain size

The grain size calculation for as-processed and ST microstructures was carried out using the line intercept method as per American society for testing and materials (ASTM) standard E112-13 (E112, 2012). The number of grains intercepting the linear line (l) was counted to calculate the grain size (D). Five linear lines in different orientations were drawn on each micrograph to collect unbiased measurements.

4.4.6.2 γ' precipitate size and number fraction

The γ' precipitate size measurement was conducted using the diameter measurement method since all the observed precipitates were near spherical in morphology. The diameter was measured in both the vertical and horizontal directions (see Figure 4-14a) and then averaged to accommodate

the near spherical shape irregularity in some cases. A total of 120-150 precipitates were counted using three micrographs for each sample. The result from the above calculation was compared with that from the area method; see Figure 4-14b. A circle was drawn on the individual precipitates, and the diameter of the spherical precipitate was calculated using the area of the circle. Comparing the results from both methods, an insignificant difference (2-4 nm) was observed. Therefore, the diameter measurement method was used throughout the dissertation work. The number fraction (w) of the γ' precipitates was calculated by measuring the number of precipitates (N) of a particular size, for example, N_s for smaller γ' precipitates and N_l for larger γ' precipitates, using equation (4.3a).

$$w_s = \frac{N_s}{(N_s + N_l)} \tag{4.3a}$$

$$w_l = \frac{N_l}{(N_s + N_l)} \tag{4.3b}$$

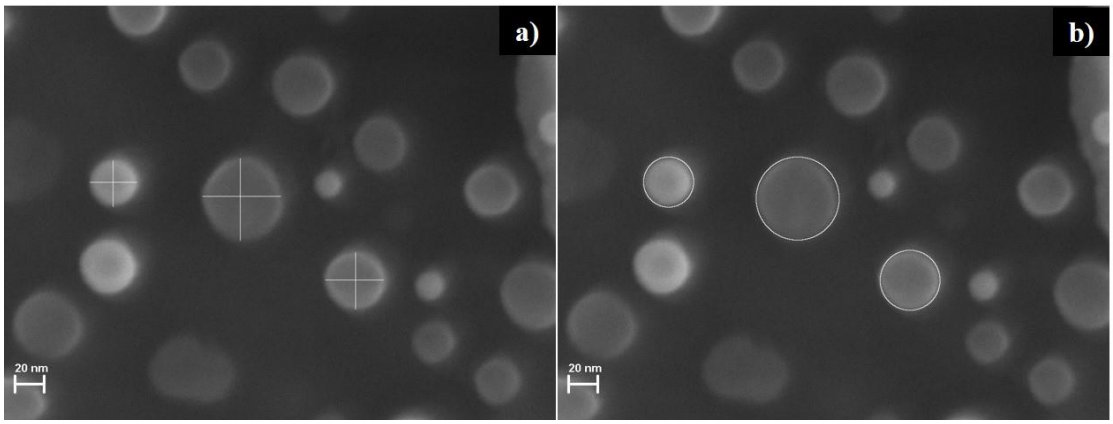

Figure 4-14: SEM Micrograph showing an example image for the γ' precipitate size measurements using ImageJ software, a) Diameter measurement method, b) Area measurement method.

- **Possible artefacts:**

a) Some precipitates with a diameter D could have their center out of the sample etched surface and could project an apparent diameter, D_{app} smaller than D as shown in Figure 4-15.

b) Due to multi-layer etching, precipitates from underneath (dark blue) could also be revealing alongwith the surface precipitates (light blue) as shown in Figure 4-15. This assumption can give rise to a higher area fraction measurement than the actual, for example Figure 4-16, both of the images are from the same sample but creating an illusion of higher precipitate volume fraction (Figure 4-16a) than Figure 4-16b micograph.

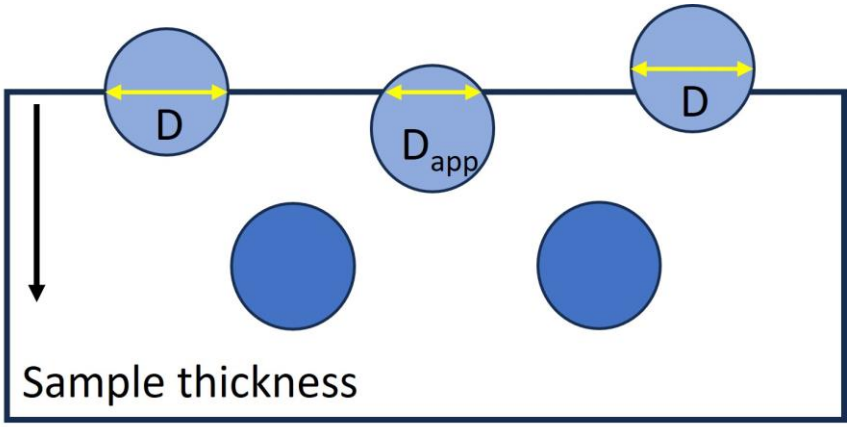

Figure 4-15: Schematic representation of spherical precipitates in an etched sample.

4.4.6.3 γ' precipitate volume percent

The volume percent analysis in this work was supported by the results of similar work conducted by Srinivasan et. al., on 718Plus alloy (Srinivasan et al., 2012). The similar single-step aging treatments included 720 °C for 10 hr followed by WQ (sample B) and 900 °C for 2 hr followed by WQ (sample G). Theyused TEM DF imaging and foil thickness measurements in the analysis of the volume percent analysis of the γ' precipitates, see Figure 4-17.

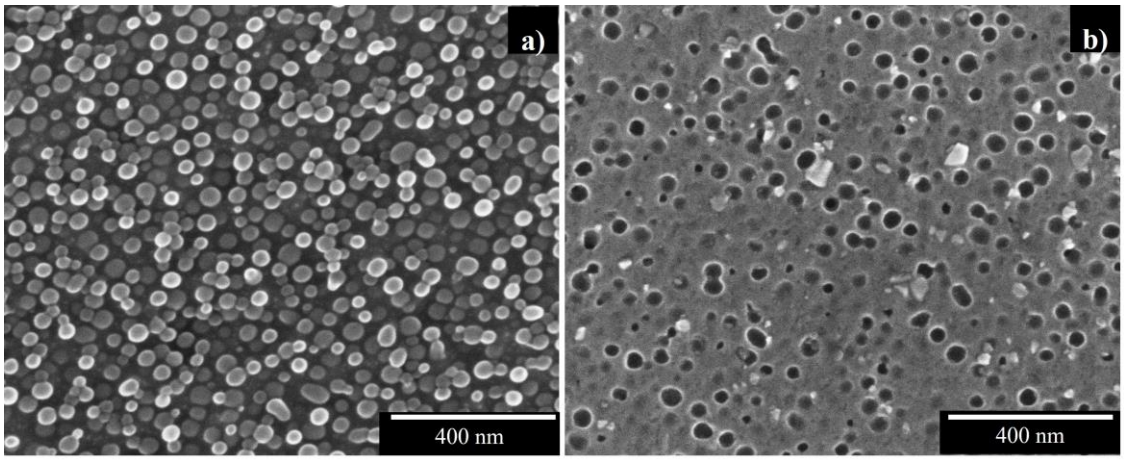

Figure 4-16: SE-SEM photomicrograph of sample G (900 °C-2h-WQ) to reveal the artifacts of volume percent analysis due to the etching techqniue a) γ matrix etching to reveal γ' precipitate at different depths from the surfaceilayer where brighter precipitates are located closer to the top surface, b) etching of the γ' precipitates shown as dark spheres.

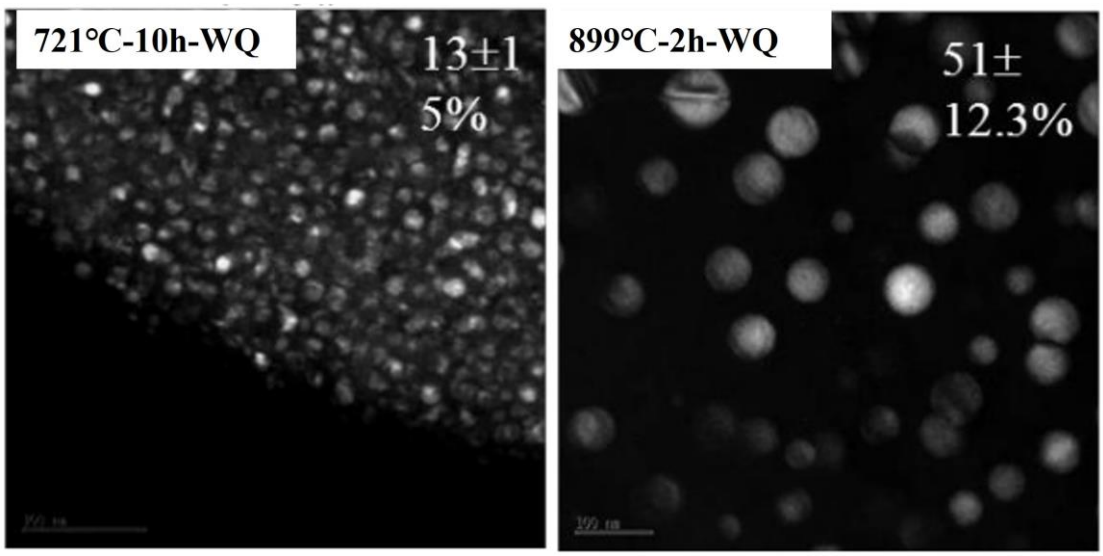

Figure 4-17: DF-TEM photomicrographs of the single-step aged samples showing a) fine γ' precipitates, b) large γ' precipitates (Srinivasan et al., 2012).

There were multiple steps used to obtain the γ' precipitate volume percent number on the sample aged at 900 °C. Firstly, a micrograph with γ' precipitates etched was used (dark spherical features shown in Figure 4-16b) to calculate the precipitate size (46 nm) and volume percent (12.8 %). The same sample but with the the γ matrix etched away leaving the γ' precipitates (bright spherical

features shown in Figure 4-16a) was used. In this case, only the brightest (white) contrast was considered to calculate the γ' precipitate size (48 nm) and γ' precipitate volume percent (13.3 %). Both the measurements resulted insimilar values, see Table 4-3. These values were within 5% of those reported by Srinivasan et. al, (Srinivasan et al., 2012). Since there was a good match for the larger γ' precipitates, these value for the smaller γ' precipitates (sample B) were directly adopted from the work by Srinivasan et. al, (Srinivasan et al., 2012). For the bimodal sample having both the smaller and the larger γ' precipitates, it was assumed that the γ' precipitate volume percent was are the sum of the individual γ' precipitate volume percents obtained from two individual one-step aging treatments; i.e 18 % (5% for smaller γ' precipitates and 13% for larger γ' precipitates).

Table 4-3: Comparison of the γ' precipitate size and volume percents for the sample aged at 900 °C-2h-WQ using different methods as well as that taken from (Srinivasan et al., 2012).

Method	γ' etched (dark contrast)	γ matrix etched (bright contrast)	Reported by Srinivasan et. al. (Srinivasan et al., 2012)
γ' precipitate size	46	48	51
γ' volume percent (%)	12.8	13.3	12.3

4.4.6.4 Degree of cubicity of γ' precipitate

The degree of cubicity (λ_c) of the γ' precipitate was determined by calculating the ratio of the edge length after eliminating round corners (represented as A in Figure 4-18b) to the largest edge length, including round corners (designated as B in Figure 4-18b) for each grain. A value of λ_c equates to 0 for a perfect square (A = 0) (Figure 4-18a) and 1 for a perfect square when A = B (Figure 4-18c).

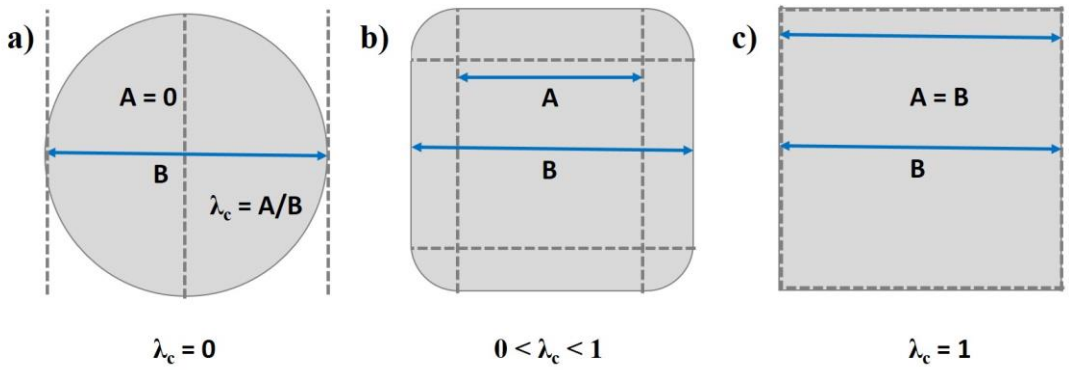

Figure 4-18: Schematic to show the calculation for λ_c for a) perfect sphere, b) cube with round corners, and c) perfect cube.

4.5 MECHANICAL TESTING

4.5.1 Hardness measurement

Vickers micro-hardness testing was conducted on the as-processed, ST, and aged microstructures to collect the average micro-hardness. The Leco M-400-G1 Vickers micro-hardness tester equipped with a four-sided diamond pyramidal indenter was used. Samples were mechanically polished to obtain a smooth surface up to 1200 US grit SiC paper. Measurements were performed on different regions of the samples (on grain boundaries and inside the grains) using a load of 1000 gram-force (gf) with a dwell time of 15 seconds. A total of 15 measurements were taken on each sample to obtain an average hardness value of each heat-treated conditions. The distance between two indents was ensured to be larger than 2.5 times the diagonal of the indentation to avoid plastic deformation effects, as referenced in ASTM E384 (ASTM E384-17, 2017).

4.5.2 Tensile Testing

The tensile properties of the as-processed alloy, ST at 1000 ℃, and aged alloys were studied in this work. The samples were initially cut from the as-processed alloy block and later heat-treated at different conditions. The cutting of the samples was performed using an electro-discharge

machine (EDM). All the specimens were ground and polished up to 600 US grit SiC abrasive paper to remove the surface defects and oxide layers caused by the high-temperature EDM cutting and heat-treatment. The flat dogbone-shaped geometry was used for tensile testing; see Figure 4-19 for complete dimensional details. Different geometries of specimens were used for the Zwick Roell Z100 universal tensile tester and Ernest Fullam miniature tensile tester; see Figure 4-19a and Figure 4-19b, respectively. The testing procedure involved a displacement rate of 0.025 mm/sec, resulting in an approximate strain rate of 0.001 s-1. The determination of various mechanical properties, including the 0.2% YS, UTS, ε_f, was carried out in accordance with ASTM standard E8-E8M-10 (ASTM E8, 2010).

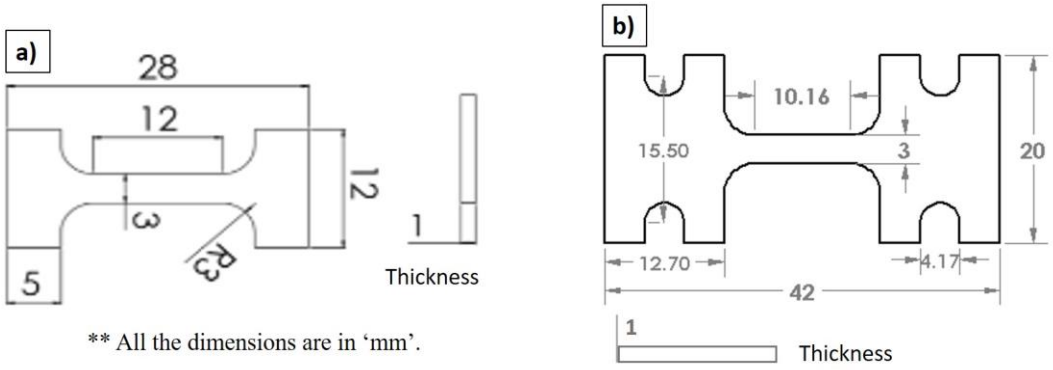

Figure 4-19: Dimensions of the flat-dogbone shaped samples used for tensile testing a) Zwick Roell universal tensile tester b) Ernest Fullam miniature tensile tester.

A Zwick Roell machine was used for tensile tests up to fracture to calculate the tensile properties such as YS, UTS, ε_f, etc., at RT for ST and aged alloys, Table 4-4. No extensometer or strain gage was employed, but the extension of the specimen was accounted for cross-head movement. The load versus elongation data was collected from the tests and used for further calculations.

Table 4-4: Sample details (heat-treatment and nomenclature) used for tensile testing.

Sample ID/ Nomenclature	**Heat-treatment**
ST	1000 ℃-1 hr-WQ
Sample 720	ST + 720 ℃-10 hr-WQ
Sample 900	ST + 900 ℃-2 hr-WQ
Sample Bimodal	ST + 900 ℃-2 hr-WQ plus 720 ℃-10 hr-WQ

The Ernest Fullam miniature was used for deforming another set of the above-mentioned aged alloys for interrupted tensile testing (2-4 % plastic deformation). The interrupted tensile tested specimens were used for precipitate-dislocation interaction studies.

4.5.3 Creep testing

The creep study of the aged sample (bimodal) was conducted using the Applied Tests System (ATS) machine (Figure 4-20) to study the simultaneous effect of thermal and stress application on the sample. The sample dimension used for the testing is shown in Figure 4-21. The deformation was carried out under uniaxial tensile loading with the help of a lever arm creep frame, as shown in Figure 4-20. The top and bottom of the sample were gripped (refer to Figure 4-21b). A thermocouple in the middle of the gage section was spot-welded to monitor the temperature using an external thermocouple reader. To record the deformation of the sample, a knife edge extensometer was used. Before running the high-temperature test, room-temperature loading was also done to monitor the elastic deflection, followed by unloading and heating to the desired temperature. The samples were soaked for 20 min after reaching the desired test temperature. Then, the sample was loaded to the applied creep load. The data (deflection, temperature, and load) was acquired periodically throughout the experiments.

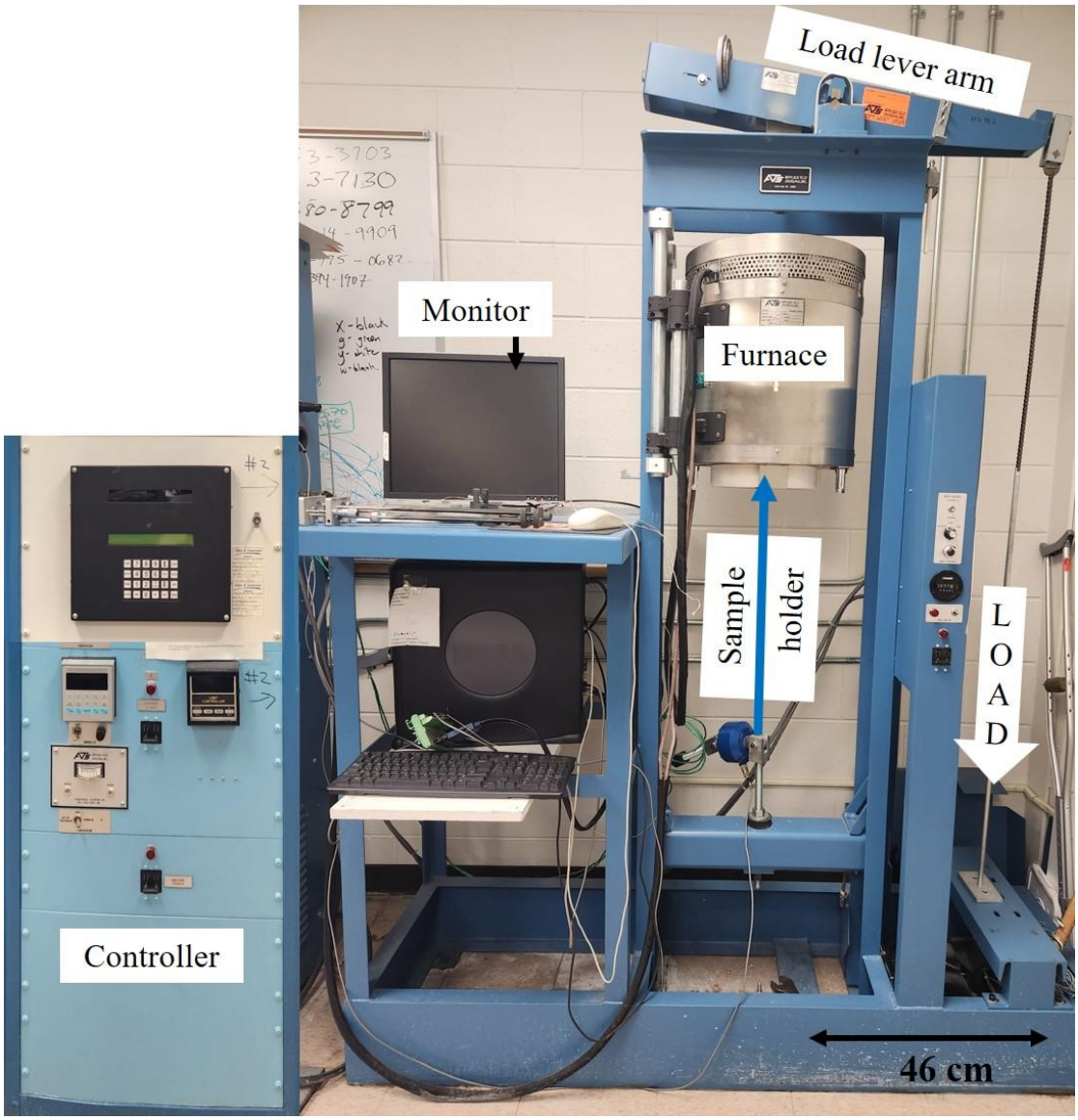

Figure 4-20: ATS creep tensile testing machine set up.

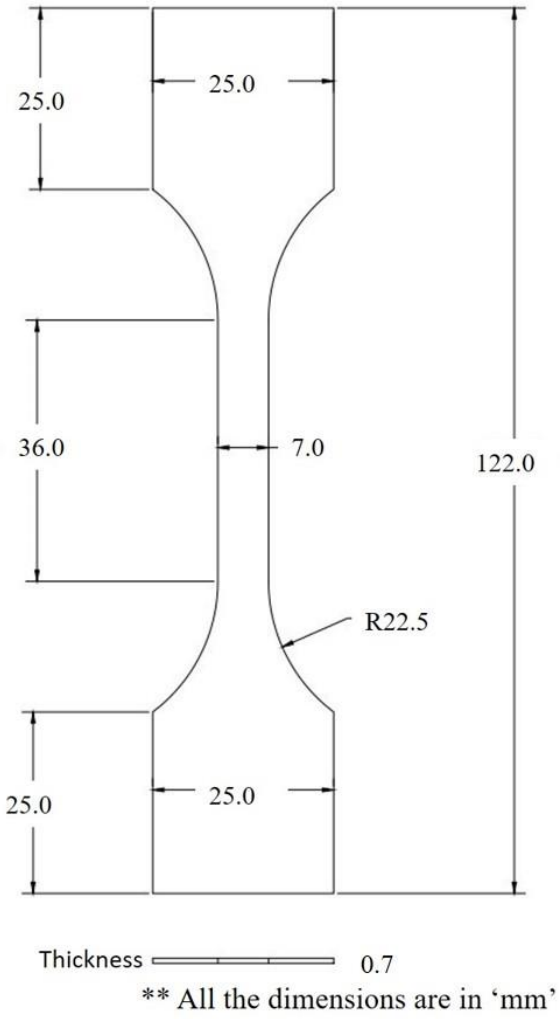

Figure 4-21: Schematic of the sample dimensions used for the creep testing.

Table 4-5: Creep testing parameters used for the bimodal sample.

Test ID	Temp (°C)	Stress (MPa)
20-49	680	550
20-52	704	650
20-53	704	650
20-55	680	550

Table 4-5 (cont'd)

20-56	680	550
20-57	704	550
20-58	704	550

4.5.3.1 Fractography of crept sample

Fractographic examination of the fractured surface generated from crept samples was carried out using SE and BSE imaging in the TESCAN MIRA 3 SEM. The fractured surfaces were cut and separated from the dog-bone samples, followed by ultrasonicate cleaning using ethanol before putting in SEM.

4.5.3.2 Critical resolved shear stress calculation

EBSD analysis of the creep-deformed sample (20-56) was conducted to study the change in γ' precipitates in individual grains. The sample directions with respect to the EBSD detector inside the SEM stage are indicated in Figure 4-22a, and the coordinates with respect to load direction are indicated in Figure 4-22b. An orientation matrix (α) was created using the Euler angles (ψ, θ, φ) for crystal orientation; see Figure 4-23. Further, the sample coordinate [1 0 0] for the stress direction was used to calculate the misorientation between the stress direction and the crystal orientation using equation (4.4). The CRSS was calculated using equation (4.5).

.

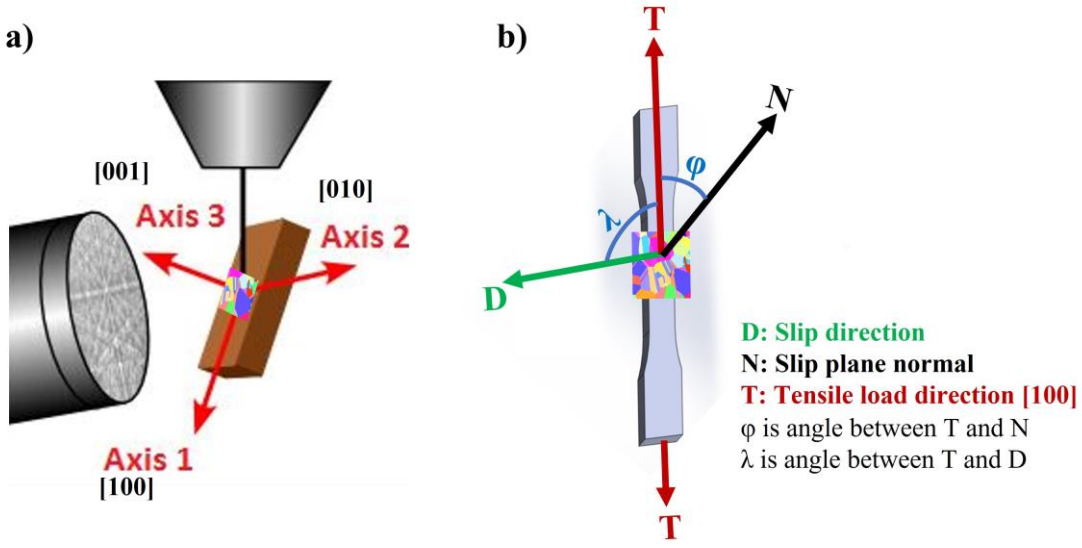

Figure 4-22: Schematic for sample co-ordinate a) with respect to EBSD detector b) with respect to tensile load direction.

$$[\alpha] = \begin{bmatrix} \cos\phi\cos\psi - \sin\phi\cos\theta\sin\psi & \cos\phi\sin\psi + \sin\phi\cos\theta\cos\psi & \sin\phi\sin\theta \\ -\sin\phi\cos\psi - \cos\phi\cos\theta\sin\psi & -\sin\phi\sin\psi + \cos\phi\cos\theta\cos\psi & \cos\phi\sin\theta \\ \sin\theta\sin\psi & -\sin\theta\cos\psi & \cos\theta \end{bmatrix}$$

Figure 4-23: Rotation/orientation matrix.

$$\sigma_{crystal} = [\alpha].[\sigma_{sample}] \quad (4.4)$$

$$CRSS = \sigma cos\varphi cos\lambda \quad (4.5)$$

where, σ is the applied load, φ is the angle between the stress direction and slip plane normal, and λ is the angle between stress direction and slip direction.

CHAPTER 5. RESULTS

In this chapter, the results from the study of the as-processed alloy, solution-treated alloy, aged alloys, and deformed alloys are presented. The chapter is divided into four major sections as follows:

a) The first section contains the preliminary results, which include microstructural characterization and mechanical properties of the as-processed alloy, ST alloy at different temperatures, and ST-plus-SA alloy.

b) The second section contains the detailed microstructural characterization of the material after aging treatments (single-step and two-step), which were conducted to develop both unimodal and bimodal γ' precipitate size distributions.

c) The third section reports the results from the aged samples, which were deformed under tensile load. The focus of this section is the precipitate-dislocation interactions.

d) The fourth and last section also contains information from aged samples which were deformed but at high temperatures (creep deformation). This section reports the effect of simultaneous application of load and temperature on the stability of the γ' precipitates.

Initially, the microstructural characterization involved using OM, SEM, and TEM to understand the phases present in the as-processed alloy. Based on the results obtained, the as-processed alloy was ST at different temperatures to dissolve the phases, especially the γ' precipitate phase. The solutionized samples were studied in detail, using SEM (SE images, EBSD) and Vickers hardness, in an attempt to discover a suitable solution treatment temperature prior to aging. After the solution treatments, aging treatments were conducted to develop different γ' precipitate size distributions. The aging treatments included single-step and two-step aging with varying parameters such as temperature, holding time, and cooling methods (i.e., WQ, FC, AC).

5.1 PRELIMINARY STUDIES: AS-PROCESSED ALLOY AND SOLUTIONIZED ALLOY

In this section, the results of the as-processed and ST microstructures are presented. The section is divided into two sub-sections, the first containing the preliminary investigation of the as-processed alloy and the second containing the detailed process of the selection of the solutionizing temperature.

5.1.1 Characterization of as-processed alloy

5.1.1.1 Microstructure

The as-processed alloy was characterized thoroughly using OM, SEM, and TEM. Metallographic samples cut from different orientations were imaged using OM to evaluate the grain size. Figure 5-1a is an OM micrograph taken from a section perpendicular to the forging direction (refer to Figure 4-1) showing an equiaxed grain structure. Figure 5-1b shows the elongated grain structure taken from a section parallel to the forging direction of the billet (refer to Figure 4-1). For the grain size measurement, only the micrographs exhibiting the equiaxed grains were used, and the average grain size was 87± 18 μm.

SE-SEM micrographs were acquired for the samples. The contrast evident among the grains was due to different etching rates for the different crystallographic orientations; see Figure 5-2a. The EBSD inverse pole figure map was collected to evaluate the texture of the alloy, Figure 5-2b. The associated pole figure indicated a maximum texture intensity of 4.5 times the random texture (approximately 100 grains), Figure 5-2c. The typical misorientation gradient within a given grain is provided in Figure 5-2d.

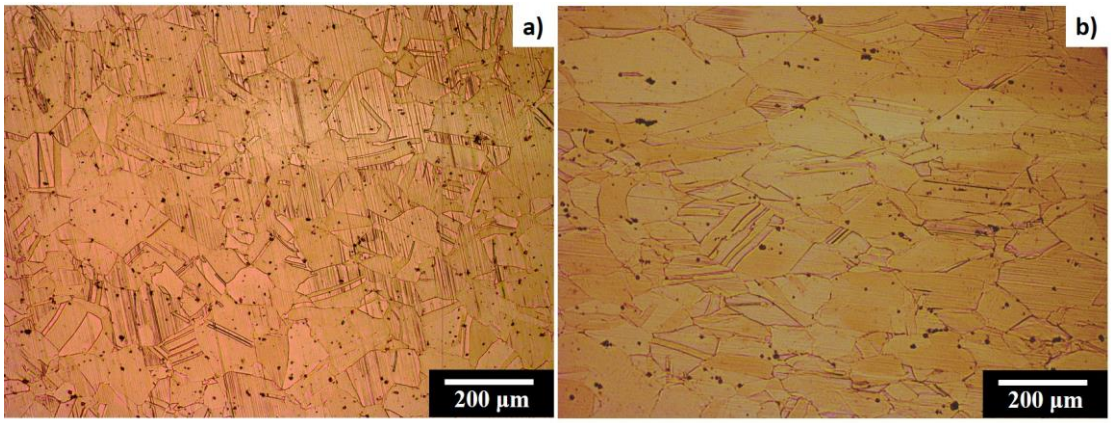

Figure 5-1: OM micrographs of the etched as-processed alloy microstructure, a) for a section perpendicular to the forging direction exhibiting equiaxed γ matrix grains, b) from a section perpendicular to the forging direction exhibiting elongated γ matrix grains.

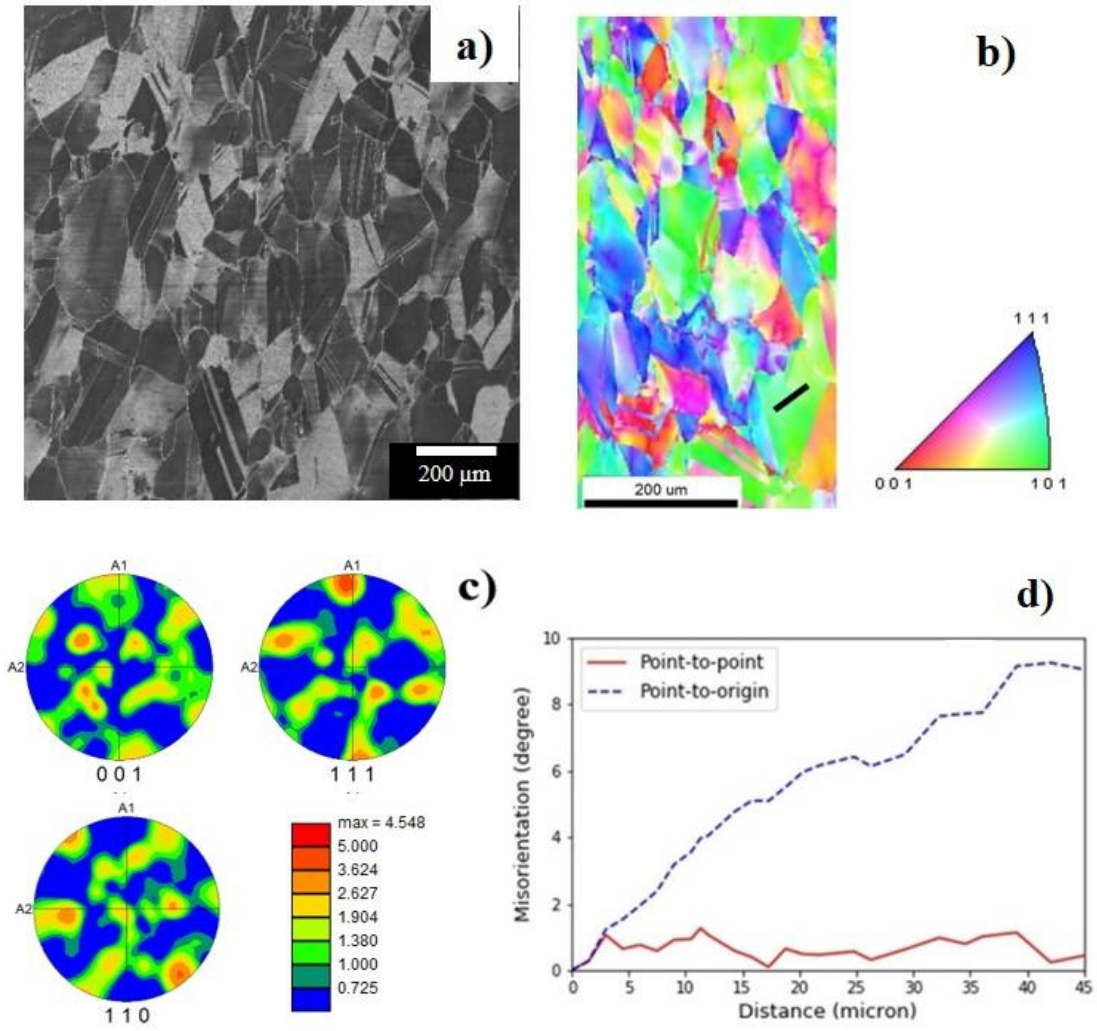

Figure 5-2: Data acquired for the as-processed alloy microstructure. (a) SE-SEM micrograph taken for a section perpendicular to the forging direction (b) EBSD inverse pole figure map, (c) Pole figures from the region shown in (b), (d) Misorientation within a typical grain from point-to-origin (blue) and point-to-point (red).

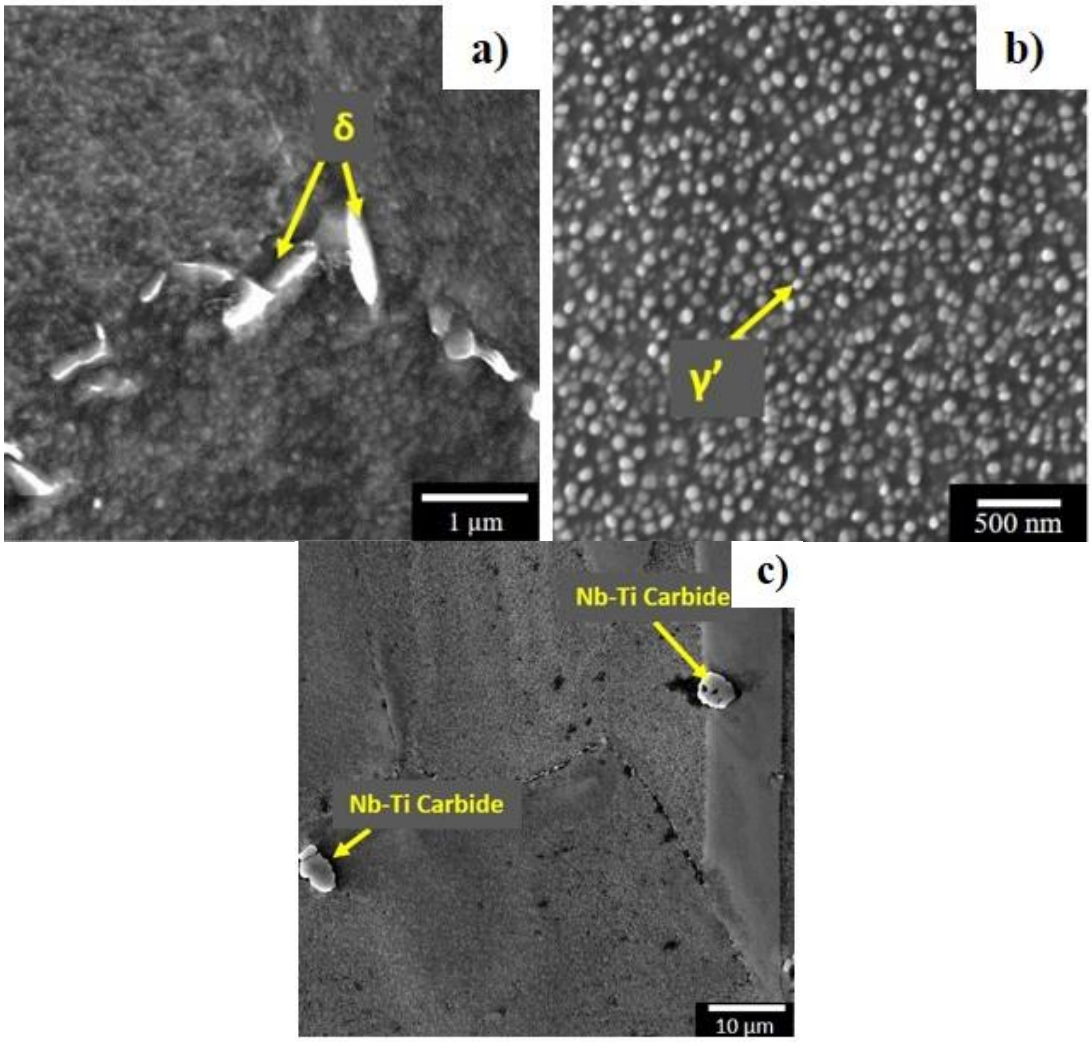

Figure 5-3: SE-SEM micrographs of the as-processed alloy microstructure revealing a) δ precipitates on grain boundaries highlighted by arrows, b) γ' spherical precipitates (lighter) with the γ matrix, c) Nb-Ti carbides near boundaries as highlighted by the yellow arrows.

Imaging of the etched sample at higher magnifications revealed that various phases were present. The samples were swab etched using Kalling's reagent to reveal the grain boundary and grain boundary phases, as mentioned in section 4.3. A disc/plate shaped grain boundary phase was observed (highlighted as δ with the yellow arrow); see Figure 5-3a. Using higher-magnification imaging of the electrolytically etched sample, spherical precipitates, highlighted as γ' phase in Figure 5-3b, were observed throughout the matrix. The average size of the γ' precipitates was 50

nm. Blocky precipitates were also observed near grain boundaries, highlighted as Nb-Ti carbide phases in Figure 5-3c. EDS analysis, performed in the SEM of the blocky precipitate highlighted with the red circle in Figure 5-4a, showed that it was a carbide precipitate rich in Nb and Ti, and no N peak was observed; see Figure 5-4b. Hence, it is believed not to be a carbo-nitride but a Nb-Ti carbide (Zhao, Lou, Ma, & Hu, 2008). XRD of the as-processed alloy microstructure was also conducted to confirm the presence of the γ' phase and other phases. For the XRD plot exhibited in Figure 5-5, the vertical axis (Intensity) was plotted in square root form to enhance the peak intensity of weak peaks. The peaks from the γ'-phase (ordered FCC) were observed and the disordered FCC γ-phase peaks were found to be overlapped with the γ'-phase peaks. Hence, the XRD result showed evidence of both γ and γ' in the as-processed microstructure.

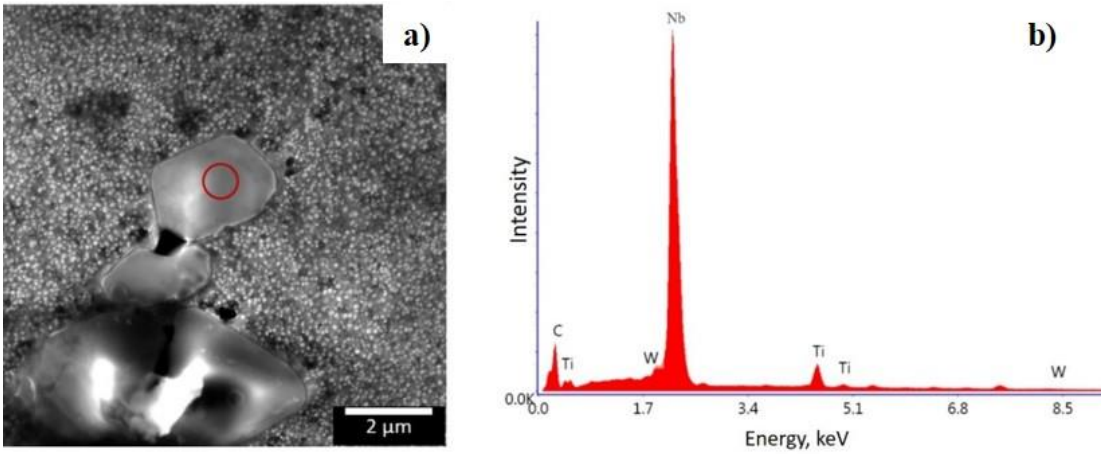

Figure 5-4: a) SE-SEM micrograph of a region containing a blocky precipitate in the as-processed material, b) EDS spectra of the precipitation region highlighted by the red circle in (a) suggesting that the precipitate is an Nb-Ti rich carbide.

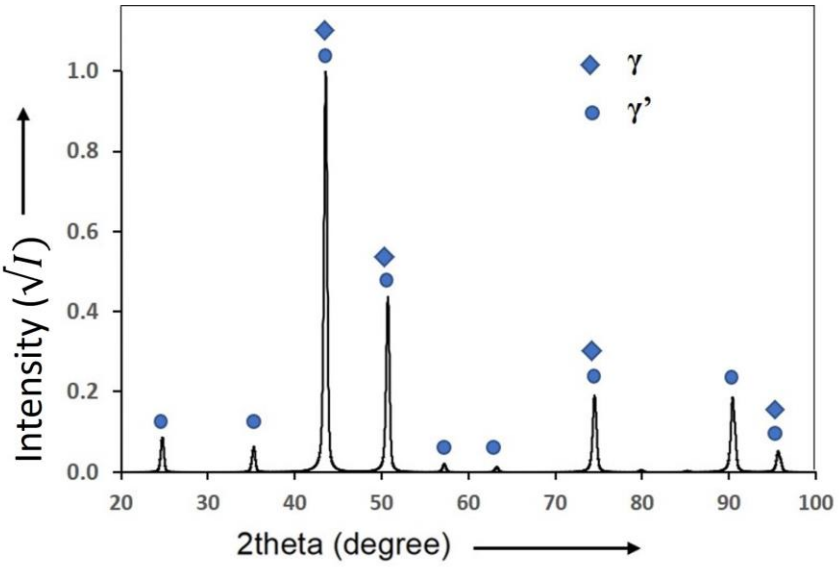

Figure 5-5: XRD plot of the intensity (square root) vs 2θ revealing overlapping of γ and γ' peaks for the as-processed alloy microstructure.

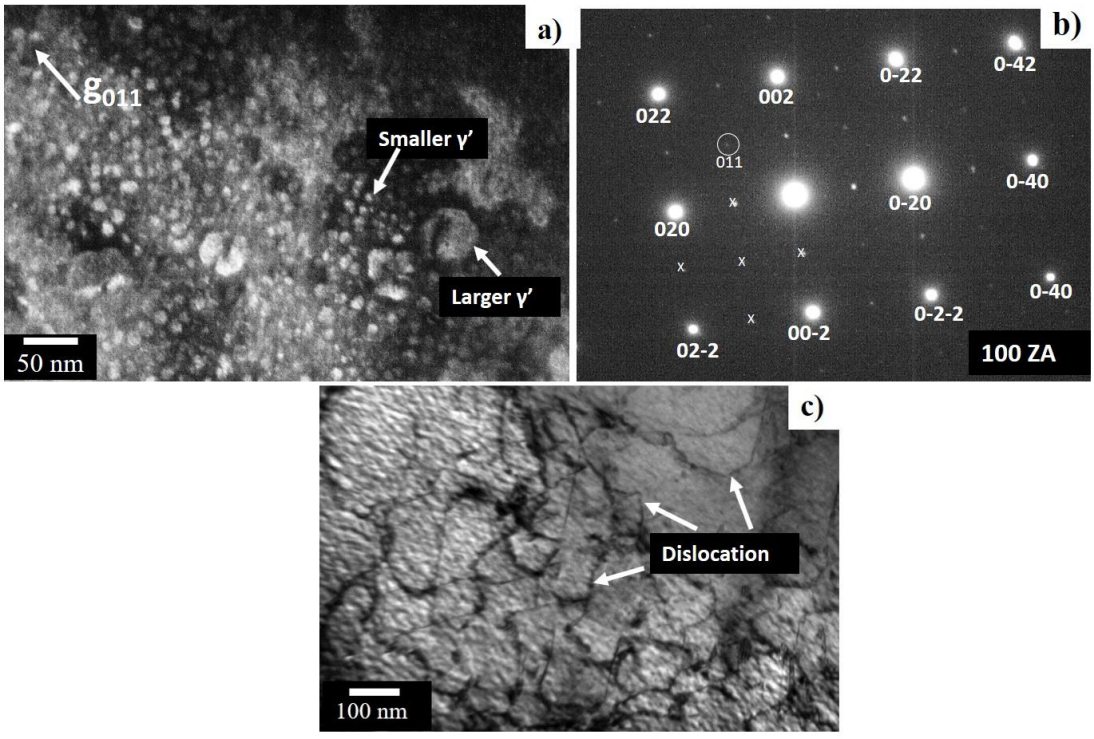

Figure 5-6: TEM images of the as-processed sample a) Darkfield micrograph revealing γ' precipitates, b) SAED pattern of the [100] zone axis where the (011) reflection was used to acquire the DF image in (a), c) Brightfield TEM micrograph showing dislocations.

TEM characterization was conducted to confirm that the spherical precipitates as the γ' phase. Figure 5-6a is a darkfield TEM image exhibiting fine γ' precipitates along with a few larger γ' precipitates, highlighted by arrows. The corresponding SAED pattern was also collected to identify the precipitate phase; see Figure 5-6b. The zone axis for the SAED pattern was identified as 100. The presence of the superlattice reflections (fine white dots in Figure 5-6b) along with the primitive reflections confirmed the presence of the γ' precipitates in the γ matrix. TEM brightfield images revealed the presence of dislocations in the sample; see Figure 5-6c.

5.1.1.2 Vicker's Microhardness

The average Vicker's microhardness of the as-processed alloy was 381 HV, presented in Figure 5-7.

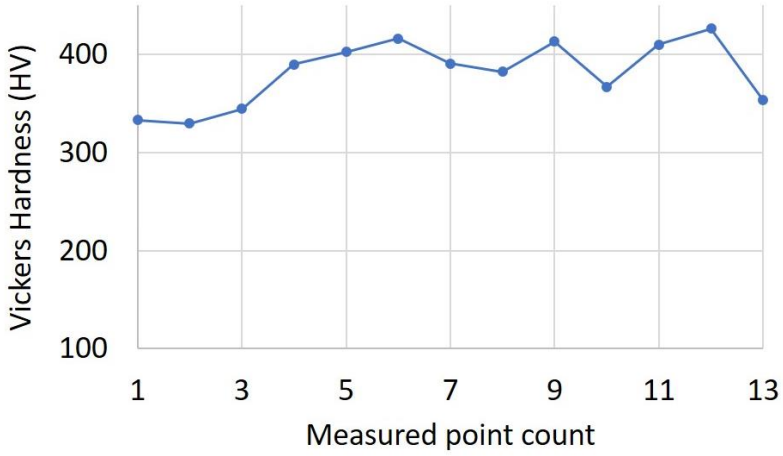

Figure 5-7: Vicker's microhardness for the as-processed alloy microstructure.

5.1.2 Selection of solution treatment temperature

5.1.2.1 Microstructure of solution-treated alloy

Solution treatments were conducted on the as-processed alloy to dissolve the existing γ' precipitates; refer to section 4.2 for experimental details. The EBSD inverse pole figure maps were collected from all four of the ST samples; see Figure 5-8. The inverse pole figure maps revealed

the decrease of the color gradient inside the γ matrix grains with the increase in solutionizing temperature. To investigate the decrease of the heterogenous plastic strain (evident due to the lessening color gradient) during the solutionizing, a point-to-point misorientation graph is provided for each ST sample (similar to the as-processed sample); see Figure 5-9. The average γ-phase grain sizes for the 954 °C, 1000 °C, 1050 °C and 1100 °C solutionized samples were 80 µm, 46 µm, 87 µm, and 157 µm, respectively.

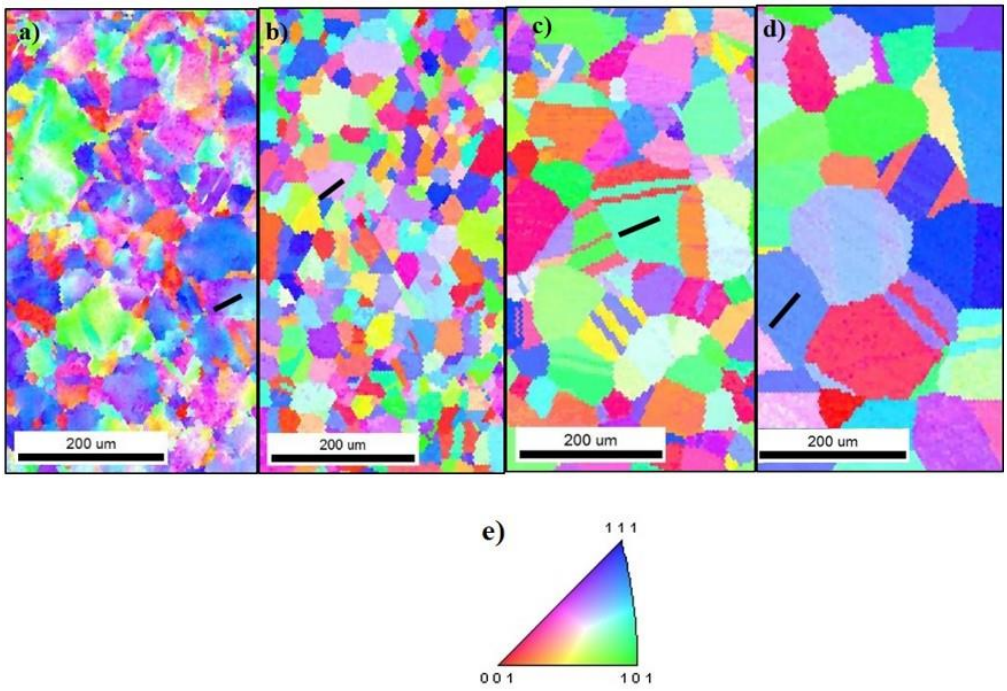

Figure 5-8: EBSD inverse pole figure maps comparing samples solutionized for 1 hr at (a) 954 °C, (b) 1000 °C, (c) 1050 °C, (d) 1100 °C, (e) FCC standard IPF triangle. The black solid line in each image was where the local misorientation (graphed in Figure 5-9) was measured.

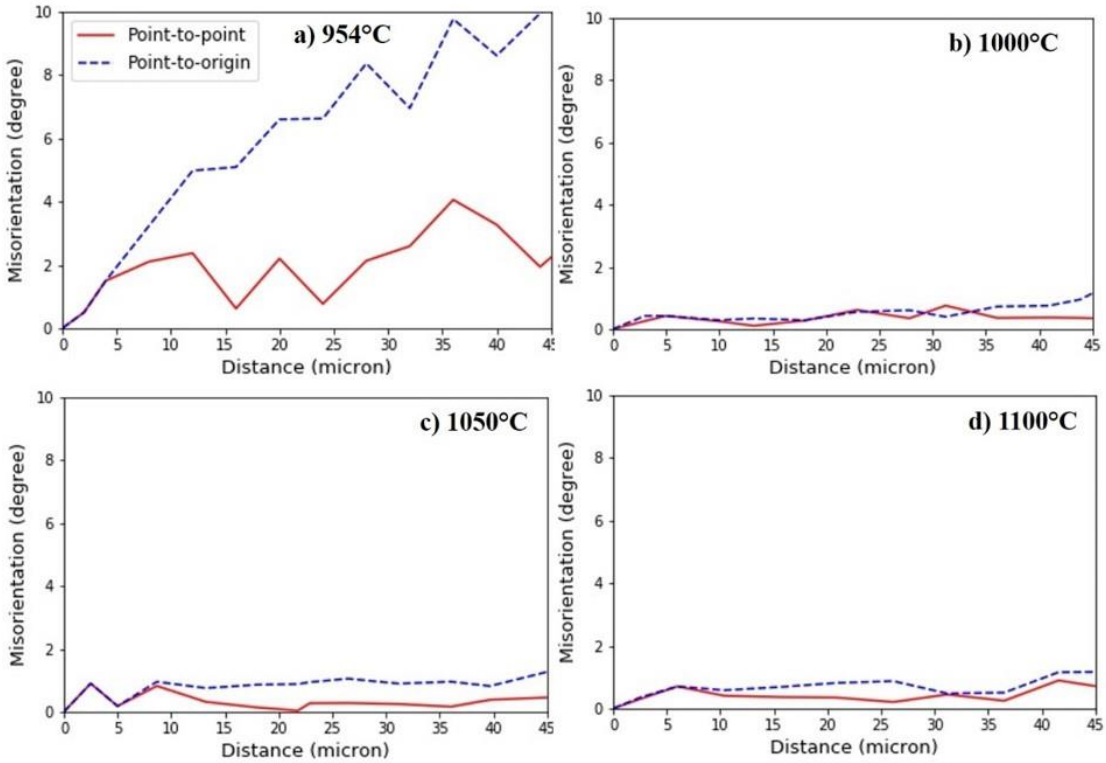

Figure 5-9: Misorientation (measured by EBSD) within a typical grain in solutionized samples a) 954 °C, b) 1000 °C, c) 1050 °C, d) 1100 °C; indiacted by blue lines for point-to-origin and red for point-to-point. The grains used for the measurement are indicated in Figure 5-8 using a black solid line.

SE-SEM images from all the solutionized alloys were used to compare the amount of the γ' and the δ phase present after the solution treatments. Figure 5-10 reveals the microstructure of a sample ST at 954 °C. The higher-magnification image (see Figure 5-10b) shows that some of the γ' phase is still present, and the δ phase was observed both near the grain boundaries and within the grains; see Figure 5-10a. The average length of the δ phase was 2.5 µm. It was noted that the average δ phase precipitate length was around 1µm in the as-processed alloy. A summary of the δ phase length is presented in Table 5-1 for the as-processed alloy and all the ST samples. A PFZ around the δ phase near the γ matrix grain boundaries was also observed, highlighted with red lines in Figure 5-10b.

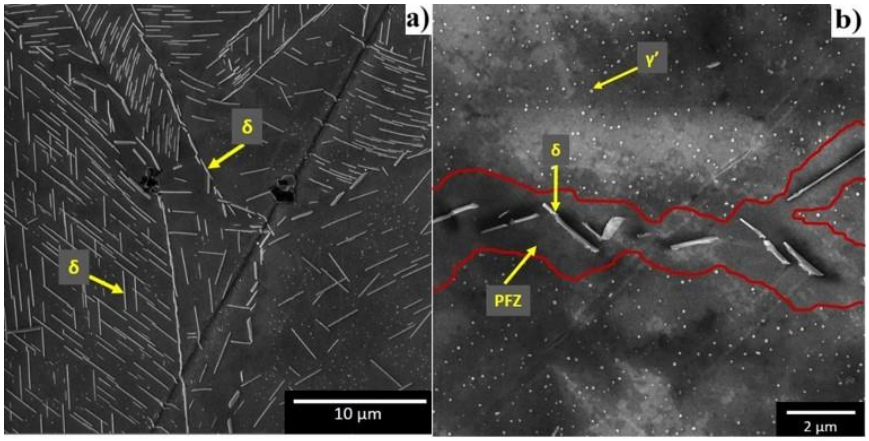

Figure 5-10: SE-SEM micrographs of the sample ST at 954 °C showing a) δ precipitates within the grains as well as near the grain boundaries b) γ' precipitate in the matrix of the γ phase and a PFZ near the δ phase.

Table 5-1: The average size (length) of the grain boundary δ phase from the ST samples and as-processed alloy.

Sample	**as-processed**	**945 °C ST**	**1000 °C ST**	**1050 °C ST**	**1100 °C ST**
γ grain size (µm)	87± 18	80± 38	46± 19	87± 22	157± 28
δ length (µm)	1	2.5	0.68	0.33	No δ

Figure 5-11a shows the 1000 °C ST microstructure where the δ-phase precipitates decorated the grain boundaries. The average size of the δ phase observed in the 1000 °C ST sample was approximately 0.68 µm, which was smaller than that in the as-processed alloy; see Table 5-1. Complete dissolution of the γ' phase occurred during the 1000 °C ST (Figure 5-11a), which was confirmed by TEM (Figure 5-12a). The corresponding SAED pattern in Figure 5-12b revealed fundamental reflections but did not exhibit any superlattice reflections. Figure 5-11b shows the 1050 °C ST microstructure, where no γ' precipitates were observed, and the δ-phase precipitate length (0.33 µm) was significantly smaller than that for the as-processed alloy (1 µm). The sample ST at 1100 °C; see Figure 5-11c, did not contain any γ' or δ-phase precipitates. The average amount of the carbide precipitates was also measured and compared to that of the as-processed alloy

(~0.2%). The change in the amount of the carbide precipitates after each of the solution treatments was insignificant and remained around 0.2%; see Figure 5-13.

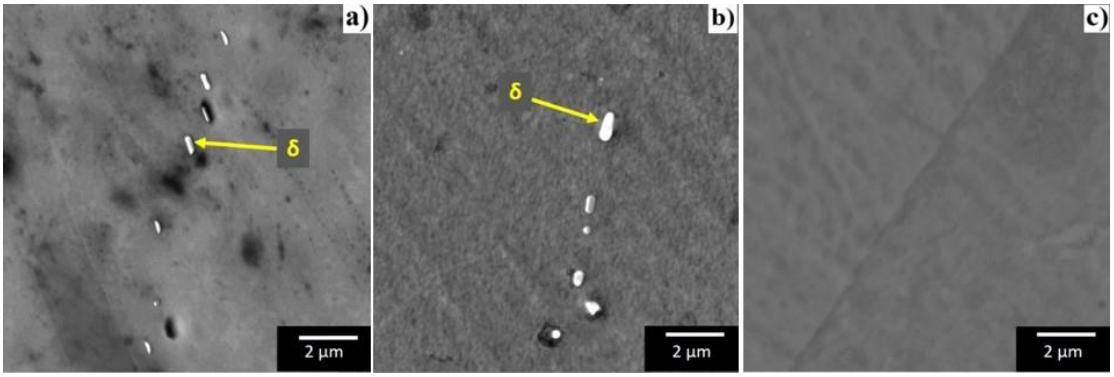

Figure 5-11: SE-SEM micrographs of samples ST at (a) 1000 °C (b) 1050 °C, (c) 1100 °C.

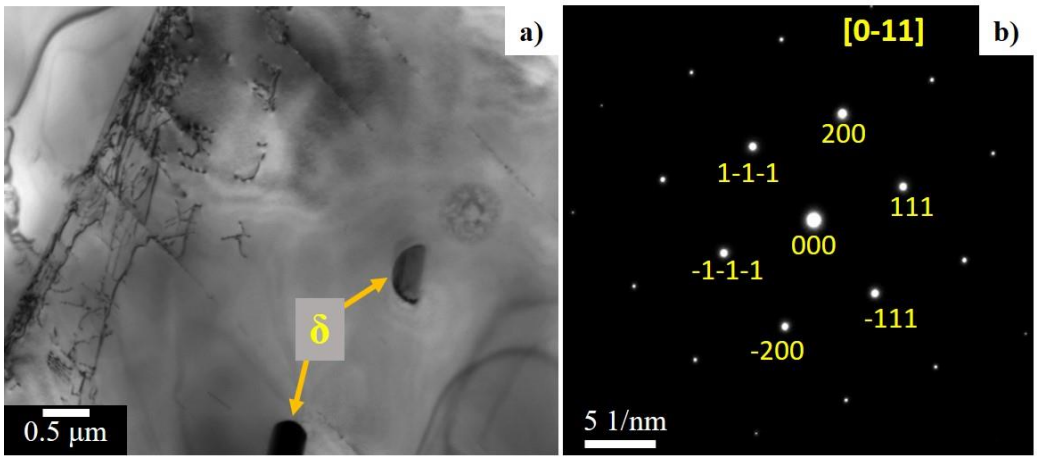

Figure 5-12: TEM images of a sample ST at 1000 °C a) Brightfield micrograph b) corresponding SAED Pattern in the [0-11] zone axis exhibiting only fundamental reflections.

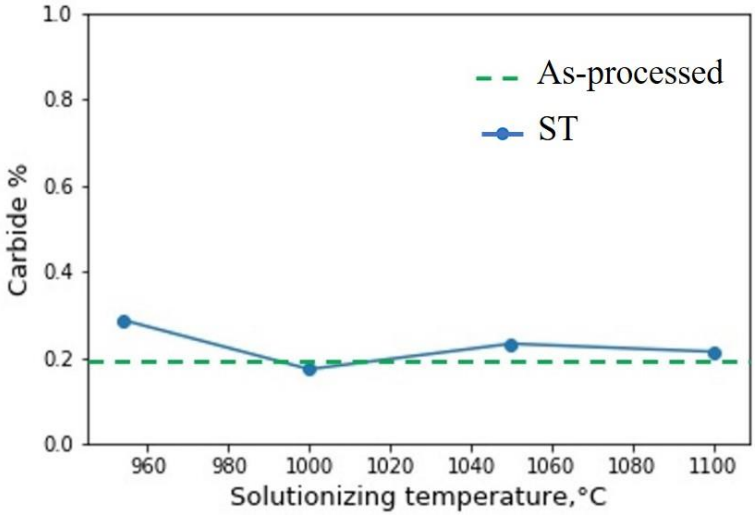

Figure 5-13: The area percent of the carbide phase found in the as-processed and ST alloys.

5.1.2.2 Microstructure of Solution-treated Plus Standard-Aged Alloys

After solutionizing, all the samples were aged using the parameters for this alloy provided in section 4.2 (E. McDevitt, 2011). High-magnification SEM SE images were taken for all of the ST-plus-SA samples to measure the γ' precipitate size; see Figure 5-14. The respective γ' precipitate size distribution from each sample is presented in Figure 5-15. The distribution curve was fitted into Gaussian distribution. Due to deep etching of the γ matrix phase, multi-layers of γ' precipitates were visible in the SE-SEM images, see Figure 5-14. This made it difficult to observe the matrix phase and measure the γ' precipitate volume percent alone. Hence, no volume perecent measurement was done for the ST-plus-SA samples.

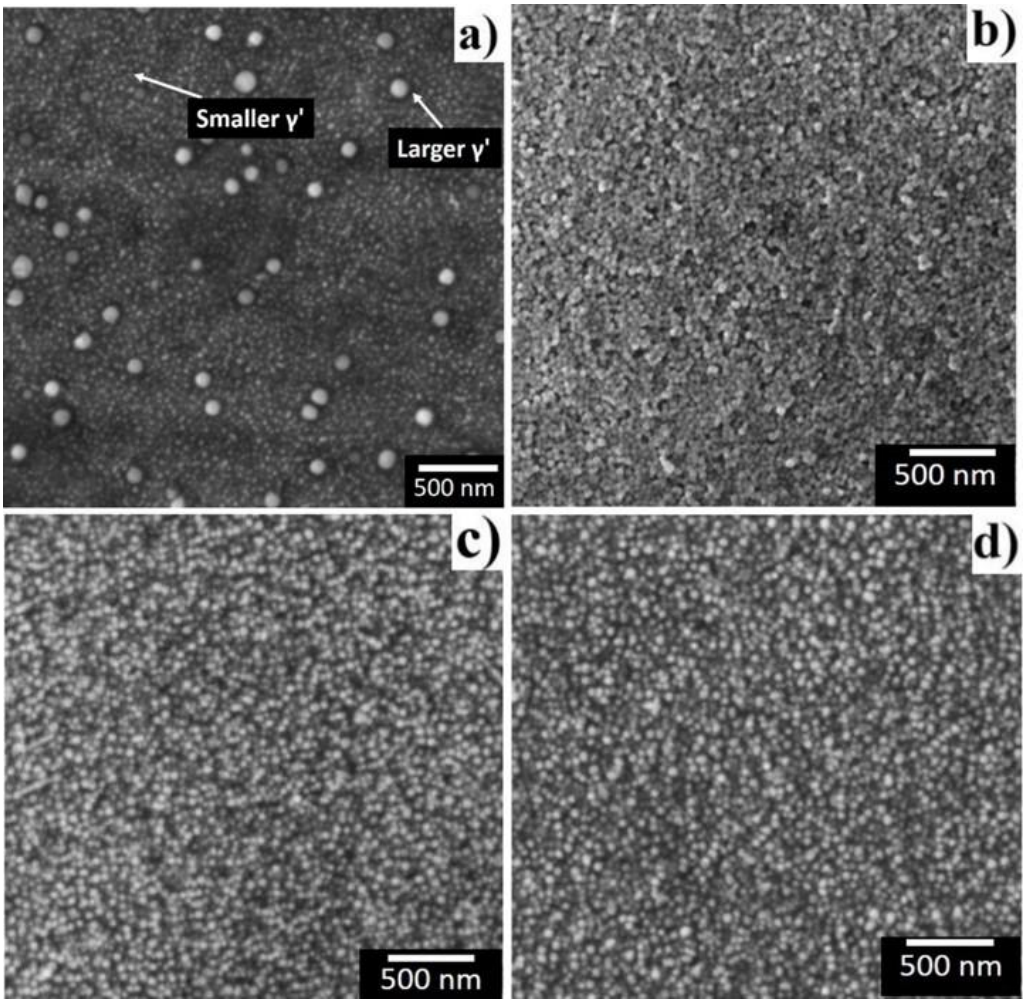

Figure 5-14: SE-SEM micrographs of ST-plus-SA samples that were solutionized at a) 954 ℃, b) 1000 ℃, c) 1050 ℃, (d) 1100 ℃. Note that there was a bimodal size distribution of the γ' precipitates in (a).

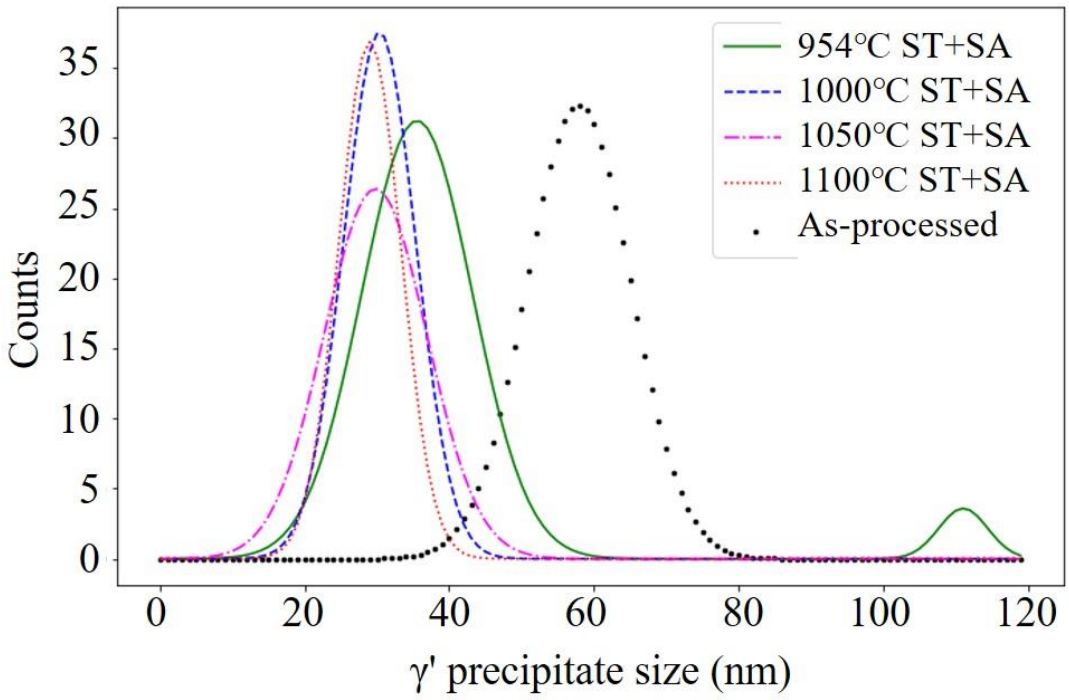

Figure 5-15: γ' precipitate size distribution of as-processed and ST-plus-SA samples.

5.1.2.3 Vickers microhardness

The average value of the Vickers microhardness for all the ST samples and ST-plus-SA samples was measured; see Table 5-2. Notably, the ST sample treated at 954 ℃ exhibited the highest average hardness, with a value of 229±37 HV. Conversely, the hardness of the ST-plus-SA sample displayed relatively consistent values, ranging from 405 to 422 HV, as detailed in Table 5-2.

Table 5-2: Average values for Vicker's hardness of all the ST samples and ST-plus-SA sample.

ST sample	**Hardness (HV)**	**ST-plus-SA sample**	**Hardness (HV)**
954 ℃	229±37	954 ℃ ST + SA	413±24
1000 ℃	171±7	1000 ℃ ST + SA	405±18
1050 ℃	158±5	1050 ℃ ST + SA	422±24
1100 ℃	156±5	1100 ℃ ST + SA	420±32

5.2 AGED ALLOY: DEVELOPMENT OF THE BIMODAL γ' SIZE DISTRIBUTION

In this section, the results of the ST-plus-aged alloys are presented. The section is divided into two major sub-sections. The first section contains the single-step aged samples used for the development of the unimodal γ' precipitate size distribution microstructure. The second section contains the two-step aged samples used for the development of the bimodal γ' precipitate size distribution microstructure. The major microstructural results reported in these sections are based on SEM micrographs. It also reports exploratory work for the bimodal sample microstructure and its in-depth characterization, which included SEM and TEM micrographs and chemical compositions measured using TEM and APT.

The ST samples were subjected to different aging treatments to produce different γ' precipitate sizes and distributions. Based on the results obtained from the single-step aging treatments, the aging temperatures for the two-step aging treatments were chosen.

5.2.1 Single-step aging

ST samples were initially subjected to single-step aging treatments within a temperature range of 720-750 °C, which is within the standard aging treatment temperature range for this alloy (704-788 °C), with the aim of developing a fine γ' precipitate size. The aging treatments for samples A-E were performed with varying holding times (between 10-15 hr) and cooling methods (AC, WQ); see Table 4-1. Similarly, to generate a larger γ' precipitate size, a higher temperature range of 900-920 °C was selected. The temperatures chosen for the single-step aging were based on the work of Srinivasan et al. (Srinivasan et al., 2012).

Samples A and B were aged at 720 °C for 10 hr, followed by AC and WQ (Table 5-3), respectively; see Figure 5-16. The average size of the γ' precipitates exhibited were 15 and 14 nm for the AC and WQ samples, respectively. Samples C-E were aged for increased holding time (15 hr) at

temperatures of 720℃ and 750 ℃, respectively. The average sizes and parameters for all the single-step aged samples are provided in Table 5-3. The area percent of the grain boundary δ phase (0.8 %) was virtually unchanged for all the samples aged in the range of 720-750 ℃ as the δ phase fraction was 0.8% for the ST sample, refer to Table 5-3. For example, in Figure 5-18, SEM micrographs from sample B and sample D aged at 720 ℃ and 750 ℃, respectively, exhibited almost the same amount of the δ phase.

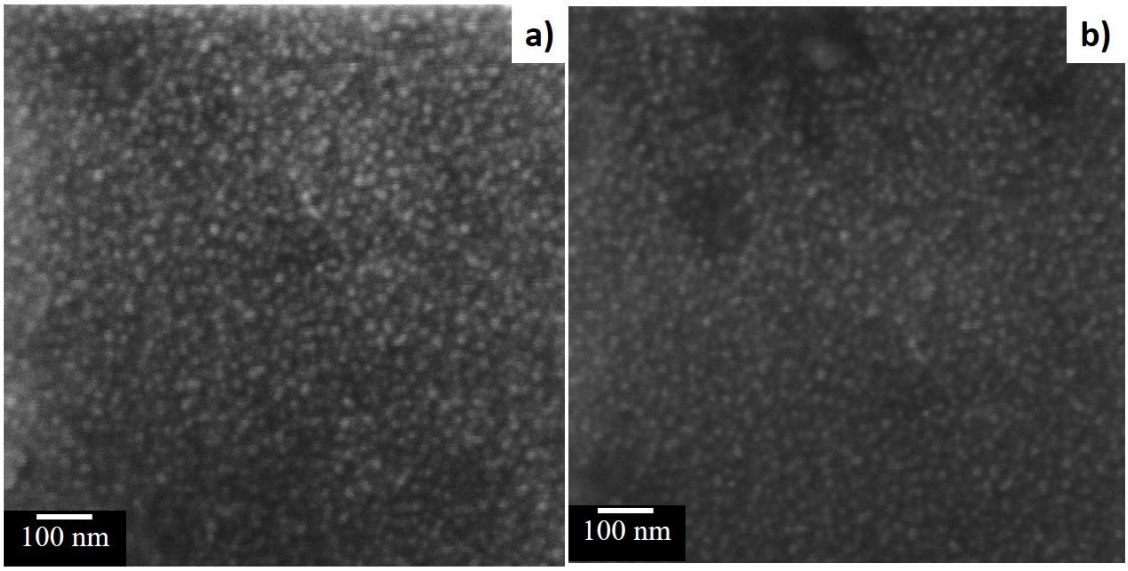

Figure 5-16: SE-SEM micrographs showing γ' precipitates from single-step aged samples; a) sample A (720 ℃-10 hr -AC), b) sample B (720 ℃-10 hr -WQ).

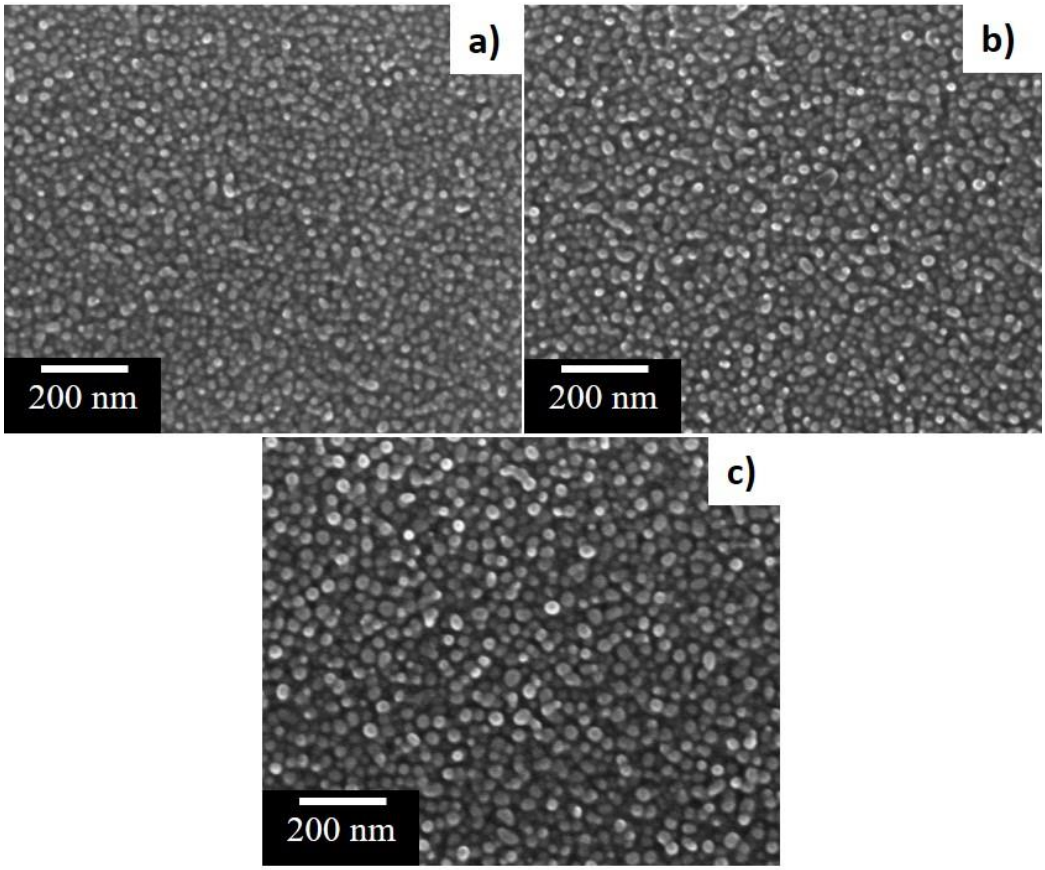

Figure 5-17: SE-SEM micrographs showing γ' precipitates from single-step aged samples; a) sample C (720 ℃-15 hr -WQ), b) sample D (750 ℃-10 hr -WQ), d) sample E (750 ℃-15 hr -WQ).

Table 5-3: Average γ' precipitate size and δ phase fraction from single-step aged samples.

Sample ID	**Heat treatment**	**Average γ' size (nm)**	**δ phase (%)**
A	720 ℃ - 10h - AC	15 ± 3	0.8
B	720 ℃ - 10h - WQ	14 ± 3	0.8
C	720 ℃ - 15h - WQ	18 ± 4	0.8
D	750 ℃ - 10h - WQ	21 ± 3	0.8
E	750 ℃ - 15h - WQ	28 ± 3	0.8
F	900 ℃ - 2h - AC	55 ± 13	1.4

Table 5-3 (cont'd)

G	900 ℃ - 2h - WQ	48 ± 7	1.3
H	910 ℃ - 2h - WQ	59 ± 7	1.8
I	920 ℃ - 2h - WQ	64 ± 9	2.4

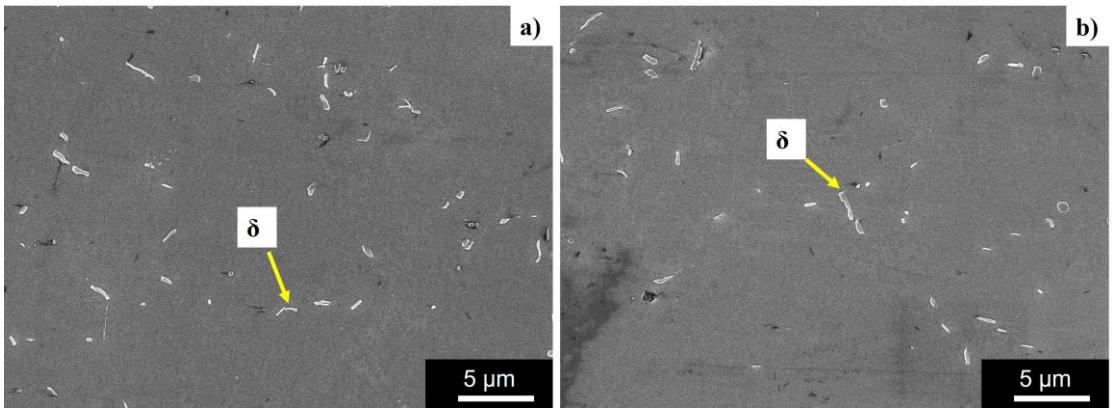

Figure 5-18: SE-SEM micrographs highlighting the δ phase from single-step aged samples: a) sample B (720 ℃-10 hr -WQ), b) sample D (750 ℃-10 hr -WQ).

To obtain larger γ' precipitates, aging treatments at higher temperatures were conducted, samples F-I in Table 4-1. Initially, a temperature of 900 ℃ was chosen with 2 hr of holding time followed by AC and WQ for sample F and G, respectively. Figure 5-19 exhibits the microstructures of sample F having an average γ' precipitate size of 55 ± 13 nm. A PFZ was observed surrounding the δ phase, indicated in Figure 5-19b. This sample also exhibited growth in the volume percent of the δ phase (1.4%) near grain boundaries and twin boundaries compared to the ST sample (0.8%). Sample G exhibited an average γ' precipitate size of 48 ± 7 nm and PFZ around the δ phase; see Figure 5-20. The aging temperature was slightly increased to 910 ℃ and 920 ℃ for samples H and I, resulting in average γ' precipitate sizes of 59 and 64 nm for samples H and I, respectively; seeTable 4-1, Figure 5-21 and Figure 5-22. The average γ' precipitate sizes of all the single-step aged samples are summarized in Table 5-3.

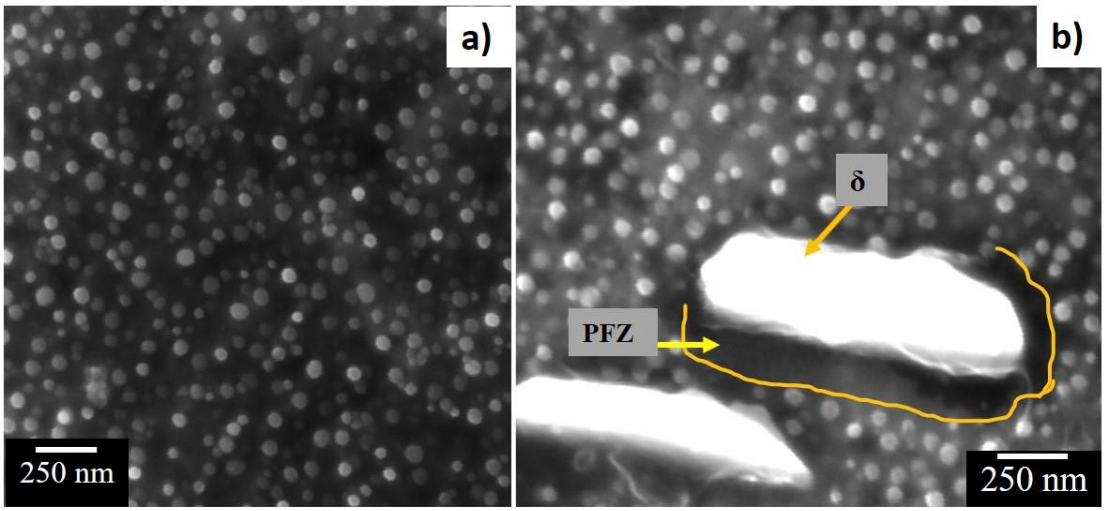

Figure 5-19: SE-SEM micrographs from single-step aged sample F (900 °C-2 hr-AC) highlighting: a) γ' precipitate, b) δ precipitate and PFZ.

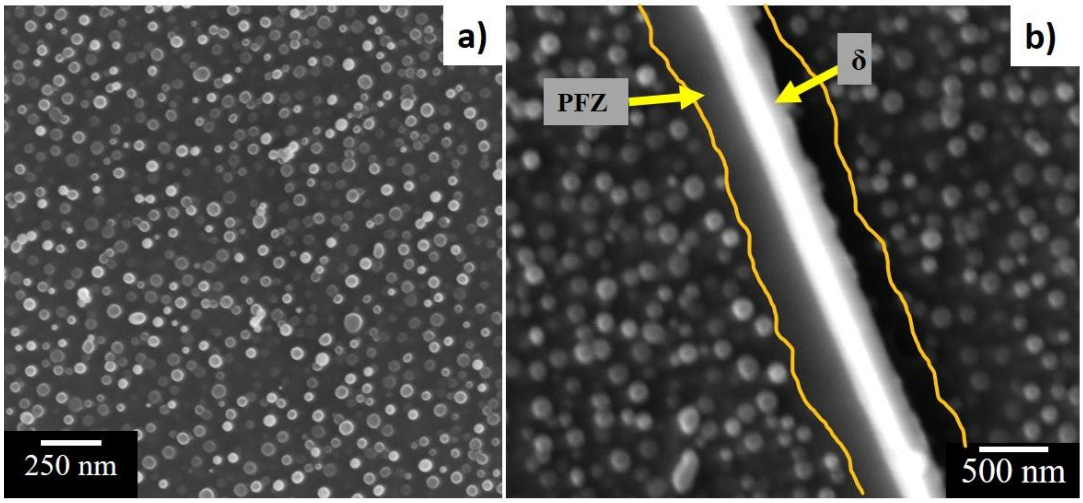

Figure 5-20: SE-SEM micrographs from single-step aged sample G (900 °C-2 hr-WQ) highlighting: a) γ' precipitate, b) δ precipitate and PFZ.

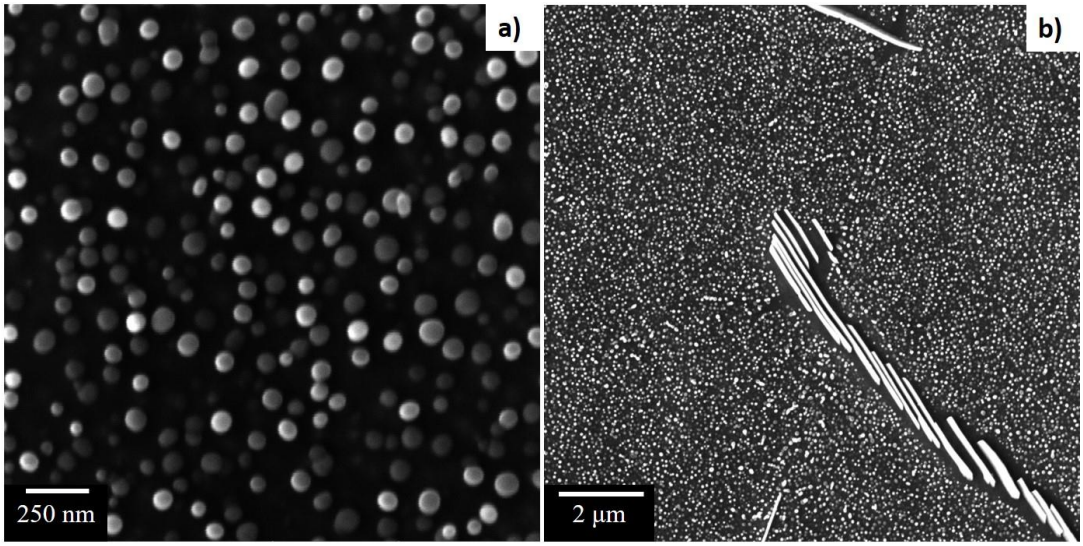

Figure 5-21: SE-SEM micrographs from single-step aged sample H (910 °C-2 hr-WQ) highlighting: a) γ' precipitate, b) δ precipitate and PFZ.

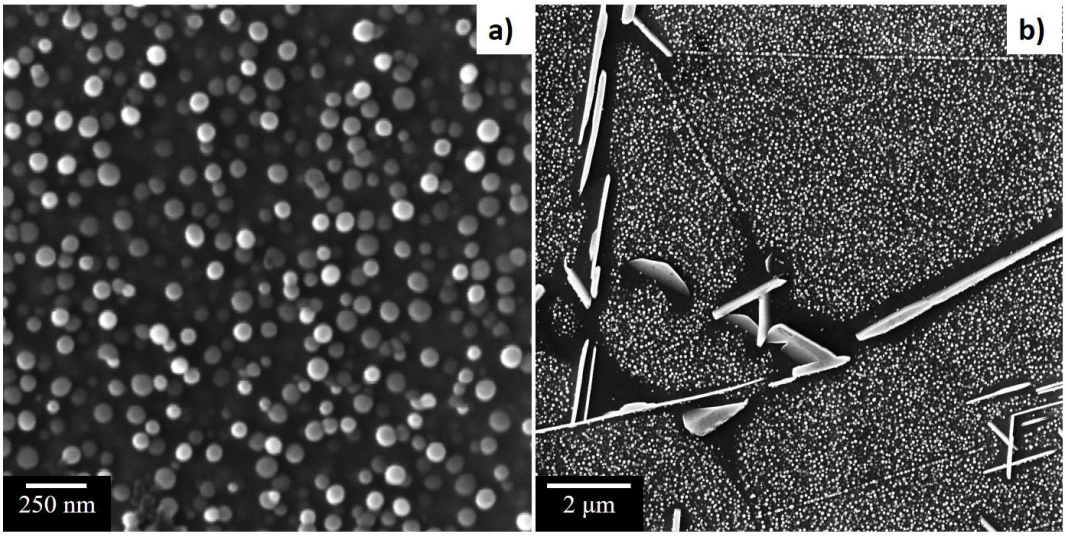

Figure 5-22: SE-SEM micrographs from single-step aged sample I (920 °C-2 hr-WQ) highlighting: a) γ' precipitate, b) δ precipitate and PFZ.

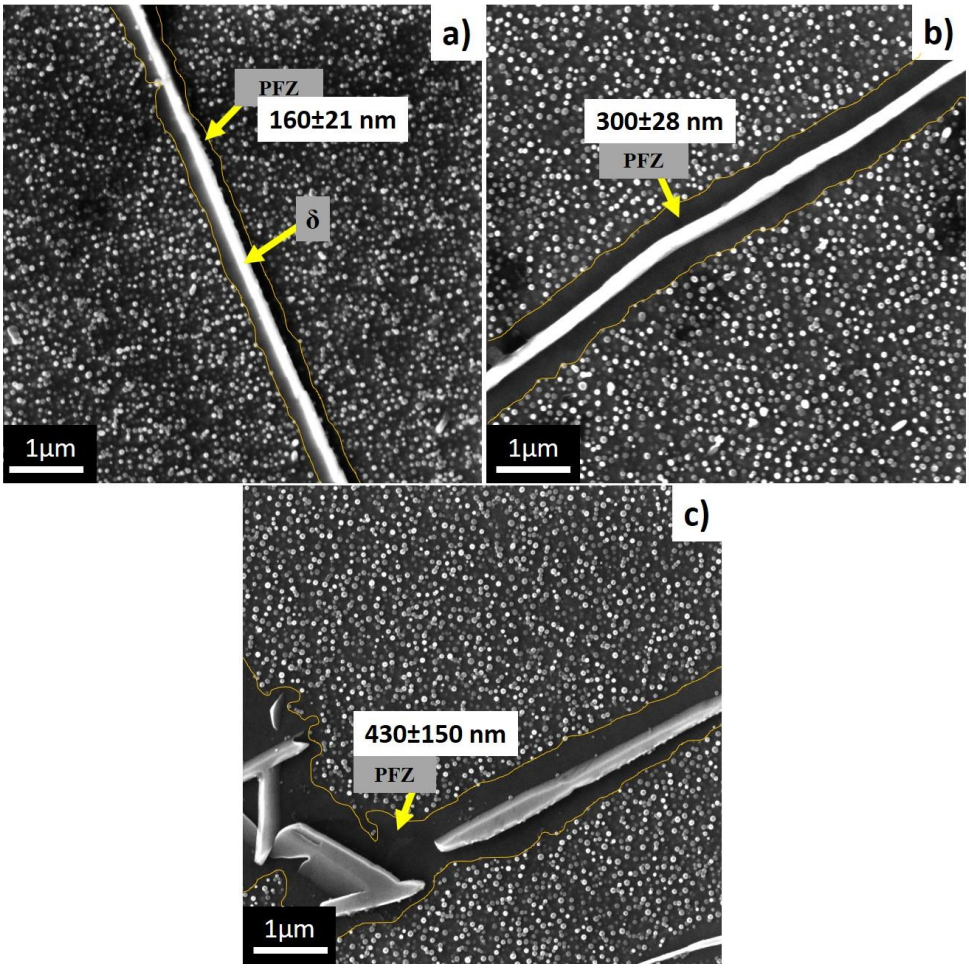

Figure 5-23: SE-SEM micrographs from single-step aged samples highlighting PFZ around the δ phase in a) sample G (900 ℃-2 hr-WQ), b) sample H (910 ℃-2 hr-WQ), c) sample I (920 ℃-2 hr-WQ).

At higher aging temperatures, with the increase in temperature from 900 ℃ to 920 ℃, the area percent of the δ phase increased from 1.3% to 2.4%; see Table 5-3. The width of the PFZ also increased with the growth of the δ phase from 160 nm to 430 nm; see Figure 5-23.

5.2.2 Two-step aging

5.2.2.1 Continuously cooled

Based on the results obtained from single-step aging, two-step aging treatment parameters were chosen; see Table 5-4, to achieve a bimodal γ' precipitate size distribution using continuous cooling

and interrupted cooling; see Figure 4-7. A continuously cooled two-step aging was performed for samples J-L as depicted in Figure 4-7a. Sample J was initially aged at 900 °C for 2 hr followed by FC to 720 °C and held for 10 hr followed by WQ. The microstructure of sample J exhibited 1.5 area percent of the δ phase, which was located primarily near the grain boundaries; see Figure 5-24a. Larger γ' precipitates (59 nm on average) were observed throughout the microstructure; see Figure 5-24b. Unlike the single-step aged samples, this sample did not exhibit PFZs. High-magnification SEM micrographs revealed finer γ' precipitates (10 nm on average), but only in the locations adjacent to the δ precipitates (Figure 5-24c). This was unlike that observed in the single-step aged samples.

Since no fine γ' precipitate nucleation was observed in the matrix away from the δ phase, the aging temperatures were increased from 900 to 930 °C and from 720 to 750 °C; see heat treatments K and L in Table 4-2. The temperature increment was chosen to increase the diffusion of the solutes and change the amount of undercooling. Sample K was aged at 900 °C for 2 hr and FC to 750 °C, then held for 10 hr followed by WQ. The resulting microstructure exhibited a γ' precipitate distribution similar to that for Sample J, which contained larger γ' precipitates in the matrix and finer γ' precipitates only in the region near the δ phase (see Figure 5-25). Raising the second aging temperature led to an increase in the average sizes for both the larger γ' precipitates (64 nm) and the smaller γ' precipitates (19 nm).

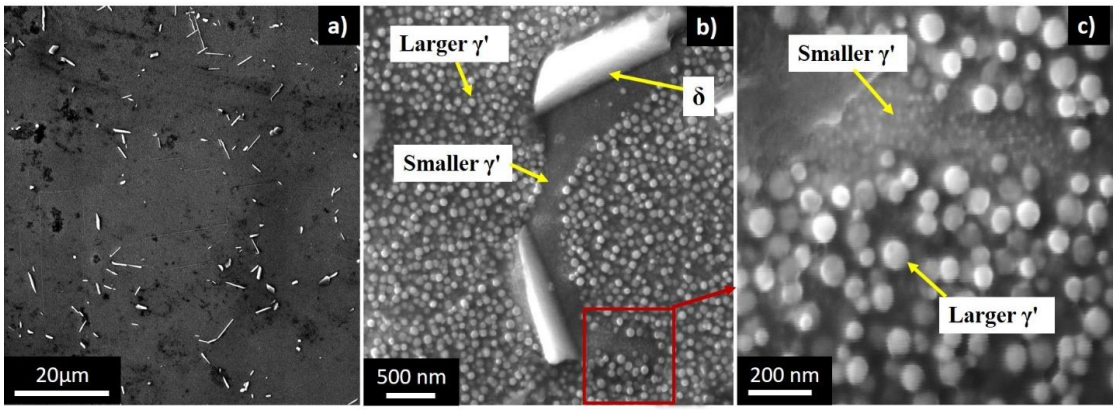

Figure 5-24: SE-SEM micrographs of the two-step aged sample J (900°C-2h-FC to 720°C-10h-WQ) showing a) the δ phase and matrix, b) δ phase and larger and smaller γ' precipitates, and c) smaller and larger γ' precipitates.

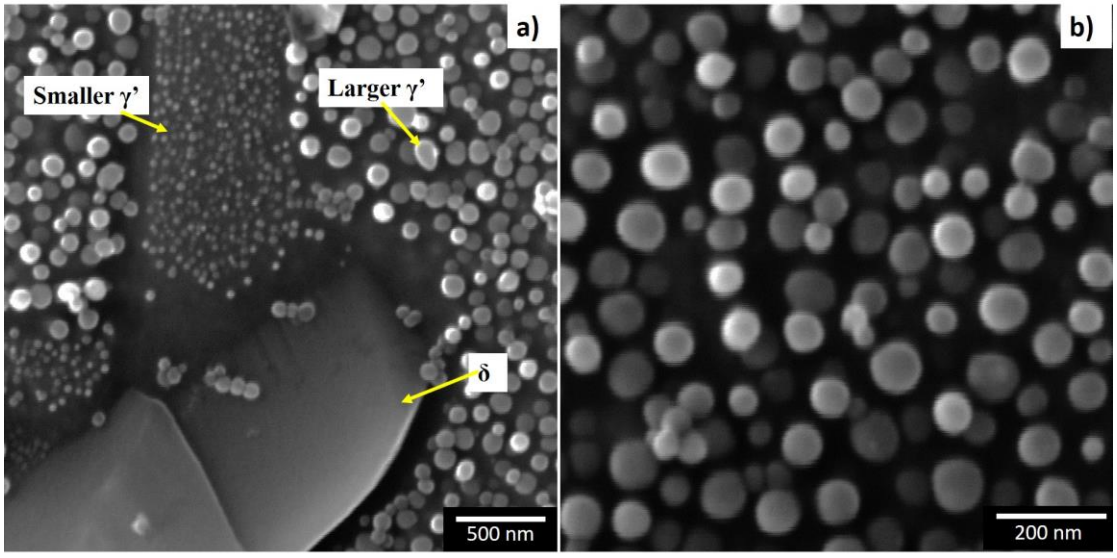

Figure 5-25: SE-SEM micrographs of the two-step aged sample K (900 °C-2 hr-FC to 750 °C-10 hr-WQ) showing a) both larger and smaller γ' precipitates near the δ phase and b) larger γ' precipitates throughout the matrix.

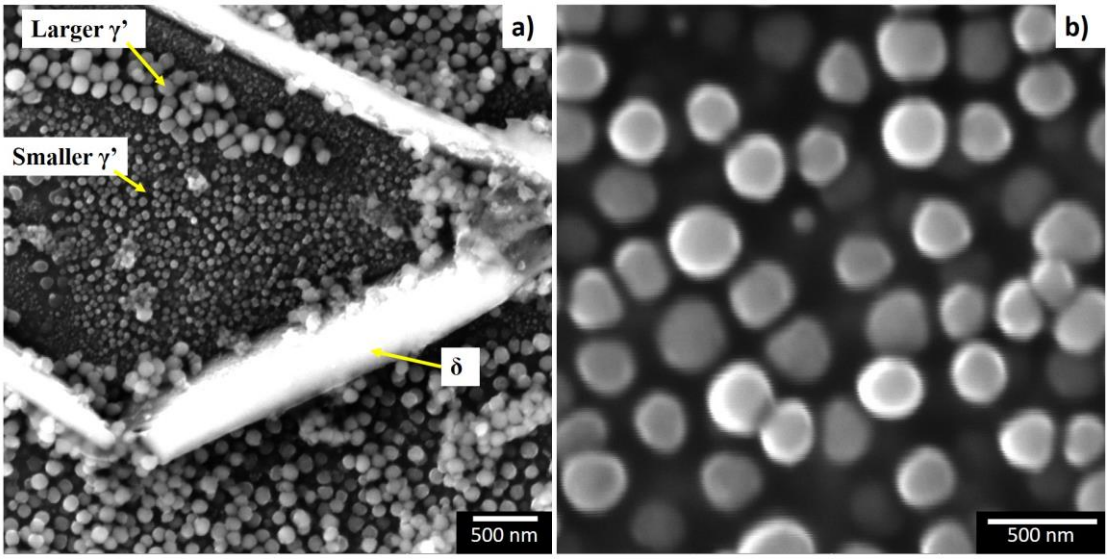

Figure 5-26: SE-SEM micrographs of the two-step aged sample L (930 ℃-2 hr-FC to 720 ℃-10 hr-WQ) showing a) both larger and smaller γ' precipitates near the δ phase and b) larger γ' precipitates throughout the matrix.

The first step aging temperature was increased for sample L. It was aged at 930 ℃ for 2 hr, and then FC to 720 ℃, then held for 10 hr, followed by WQ. The resulting microstructure exhibited average γ' precipitate sizes of 105 and 48 nm for the smaller and larger precipitates, respectively (Figure 5-26). Thus, the continuous cooling between the two aging steps did not result in bimodal γ' precipitate size distributions. A summary of the γ' precipitate sizes for samples J-L are presented in Table 5-4.

Table 5-4: Average γ' precipitate size with standard deviation for continuously cooled two-step aged samples.

Sample ID	**Heat-treatment**	**Average γ' size (nm)**	
		Larger γ'	**Smaller γ'**
J	900 ℃ - 2h - FC (~20 ℃/min) to 720 ℃ - 10h - WQ	59 ± 10	12 ± 3
K	900 ℃ - 2h - FC (~20 ℃/min) to 750 ℃ - 10h - WQ	64 ± 8	19 ± 4
L	930 ℃ - 2h - FC (~20 ℃/min) to 720 ℃ - 10h - WQ	105 ± 7	48 ± 4

5.2.2.2 Interrupted cooled

Two-step aging with interrupted cooling was also conducted; see Figure 4-7b. The temperatures for the aging steps, 900 ℃ and 720 ℃, were selected based on the γ' precipitate size, δ area percent, and the amount of PFZ exhibited in the single-step aged and continuously cooled two-step aged samples. Sample M was first heated to 900 ℃ for 2 hr, followed by WQ, and then the sample was heated to 720 ℃ for 15 hr, followed by WQ. The microstructure shown in Figure 5-27 exhibited a uniform distribution of larger γ' precipitates of size 60 nm. The fine γ' precipitates of size 13 nm were present in the matrix region in between large □□ precipitates and in the PFZ areas, unlike the continuously cooled two-step aged samples (sample J-L). Therefore, interrupted cooled two-step aged samples exhibited a uniform bimodal γ' precipitate size distribution.

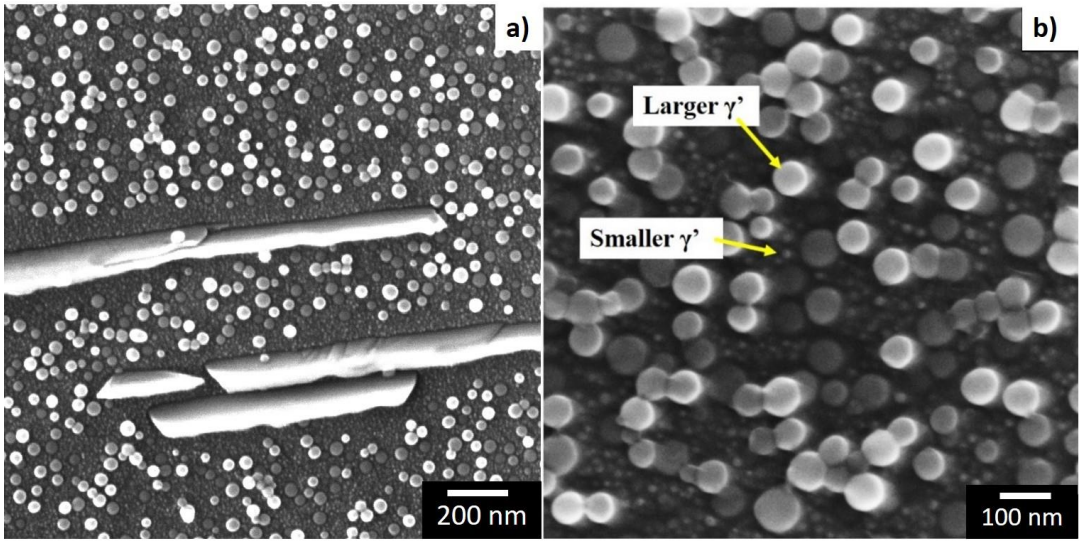

Figure 5-27: SE-SEM micrographs of sample aged at 900 ℃-2 hr-WQ plus 720 ℃-15 hr-WQ (sample M) exhibiting a) larger and smaller γ' precipitate with δ phase, b) uniform bimodal distribution of γ' precipitate.

Table 5-5: Average γ' precipitate size for interrupted cooled two-step aged samples; FT: furnace transfer.

Sample ID	Heat-treatment	Average γ' size (nm)	
		Larger γ'	Smaller γ'
M	900 ℃ - 2h - WQ + 720 ℃ - 15h - WQ	60 ± 7	13 ± 3
N	900 ℃ - 3h - WQ + 720 ℃ - 10h - WQ	46 ± 10	NA
O	900 ℃ - 2h - WQ + 720 ℃ - 10h - WQ	55 ± 5	11 ± 2
P	900 ℃ - 2h - FT to 720 ℃ - 10h - WQ	68 ± 5	none
Q	720 ℃ - 10h - WQ + 900 ℃ - 2h - WQ	49 ± 6	none

After achieving a bimodal microstructure using interrupted cooling between the two steps of aging, other exploratory heat treatments were conducted to develop uniform bimodal γ' precipitate size distributions. The heat-treatment parameters (sample N-Q) were chosen based on sample M heat-treatment. Sample N parameters were kept similar to sample M with regards to the cooling method and aging temperature except for the holding time. This sample was heated at 900 ℃ for 3 hr followed by WQ and then heated at 720 ℃ for 10 hr followed by WQ (Table 4-2). The microstructure exhibited an unimodal γ' size distribution (46 nm) even after following the interrupted cooled two-step aging; see Figure 5-28b. This heat treatment also resulted in a large amount of grain boundary δ phase, Figure 5-28a. For the heat treatment of Sample O, where the aging temperatures were set at 900 ℃ and 720 ℃, respectively, the holding times were selected to be 2 hours for the first step of aging and 10 hours for the second step of aging (refer to Table 4-2). The microstructure resulted in a uniform bimodal distribution of γ' precipitates with an average value of 55 and 11 nm, Figure 5-29.

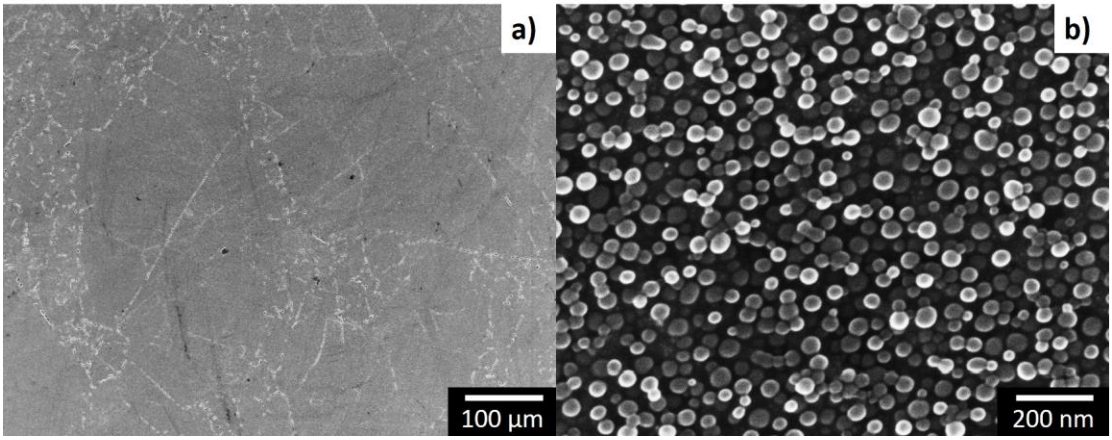

Figure 5-28: SE-SEM micrographs of sample aged at 900 ℃-3 hr-WQ plus 720 ℃-10 hr-WQ (sample N) exhibiting; a) δ phase on the γ matrix grain boundaries, c) unimodal distribution of γ' precipitates.

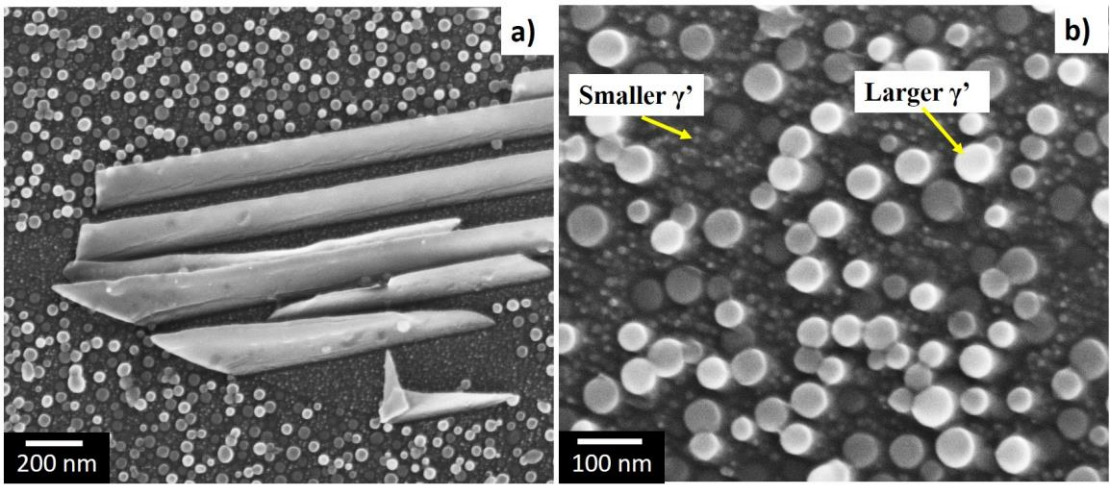

Figure 5-29: SE-SEM micrographs of sample aged at 900 ℃-2 hr-WQ plus 720 ℃-10 hr-WQ (sample O) exhibiting a) larger and smaller γ' precipitate with δ phase, c) uniform bimodal distribution of γ' precipitates.

For all the above two-step interrupted cooled heat treatments, samples were WQ to RT between the two steps of aging. For sample P, the sample was transferred to a pre-heated furnace (720 ℃) at the end of the first aging step (900 ℃ for 2 hr) and held for 10 hr followed by WQ, Table 4-2. It was observed that the slower cooling during the transfer between the two steps could not provide a distinct bimodal γ' precipitate size distribution even after following the exact same aging

temperature and time as sample O, Figure 5-30. The average size of the γ' precipitates was 68 nm for sample P.

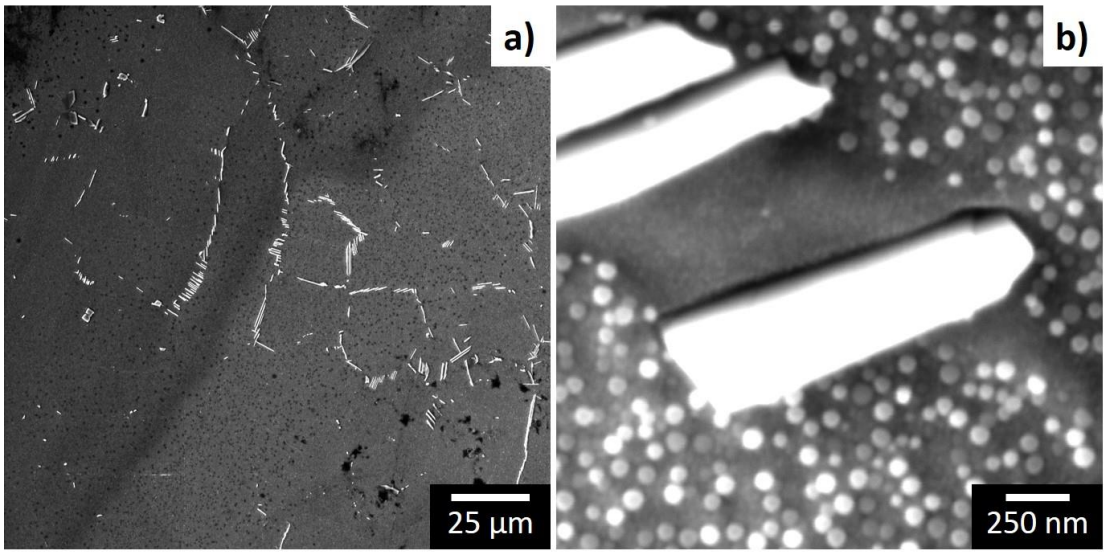

Figure 5-30: SE-SEM micrographs of two-step aged sample P (900 ℃-2 hr- transferred to pre-heated furnace at 720 ℃-10 hr-WQ) exhibiting; a) δ phase on the γ matrix grain boundaries, c) γ' precipitate distribution.

Reversing the two steps of aging was the design for sample Q. This sample was initially heated to 720 ℃ for 10 hr followed by WQ, and then heated to 900 ℃ for 2 hr followed by WQ. It was noticed that the area percent of the grain boundary δ phase significantly increased (Figure 5-31a) compared to that for sample O (aged for similar aging temperatures and times but in reverse order as that for sample Q). An unimodal distribution of the γ' precipitates (49 nm) was observed along with precipitate agglomeration, Figure 5-31b. A summary of the sizes of γ' precipitates for samples L-Q is presented in Table 5-5.

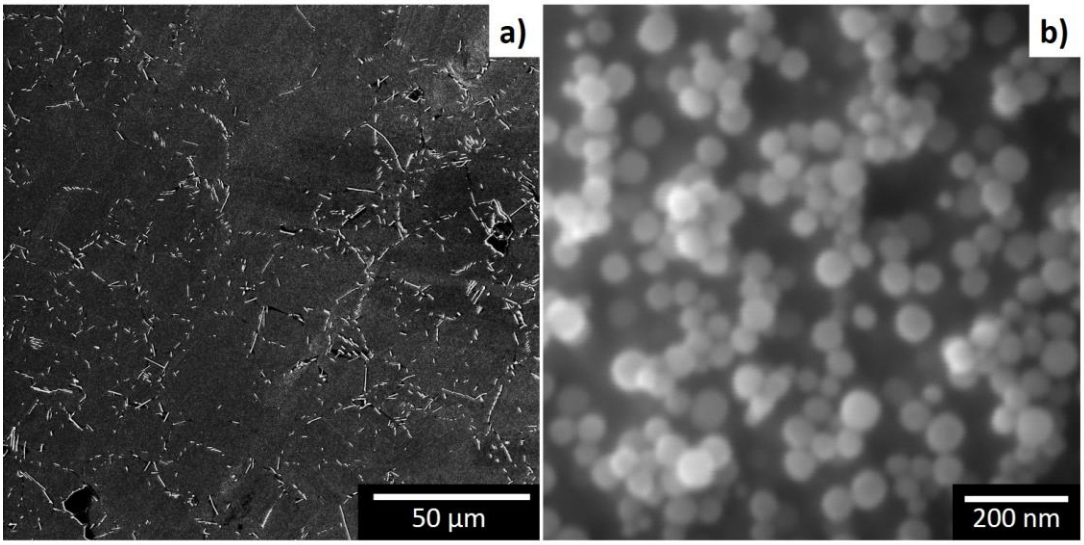

Figure 5-31: SE-SEM micrographs of sample aged at 720 ℃-10 hr-WQ plus 900 ℃-2 hr-WQ (sample Q) exhibiting a) δ phase on grain boundaries, c) unimodal γ' precipitate distribution with precipitate agglomeration.

Sample O (900 ℃-2 hr- WQ plus 720 ℃-10 hr-WQ) was chosen as the baseline bimodal sample for more detailed examination. The larger and the smaller γ' precipitates were evident in the DF TEM images for sample O (Figure 5-32a). The associated selected area diffraction pattern (SADP) exhibited the superlattice reflections (for example, the green-colored open circle) for the γ' precipitates and the fundamental reflections (for example, the yellow-colored open circle) for the γ matrix (Figure 5-32b).

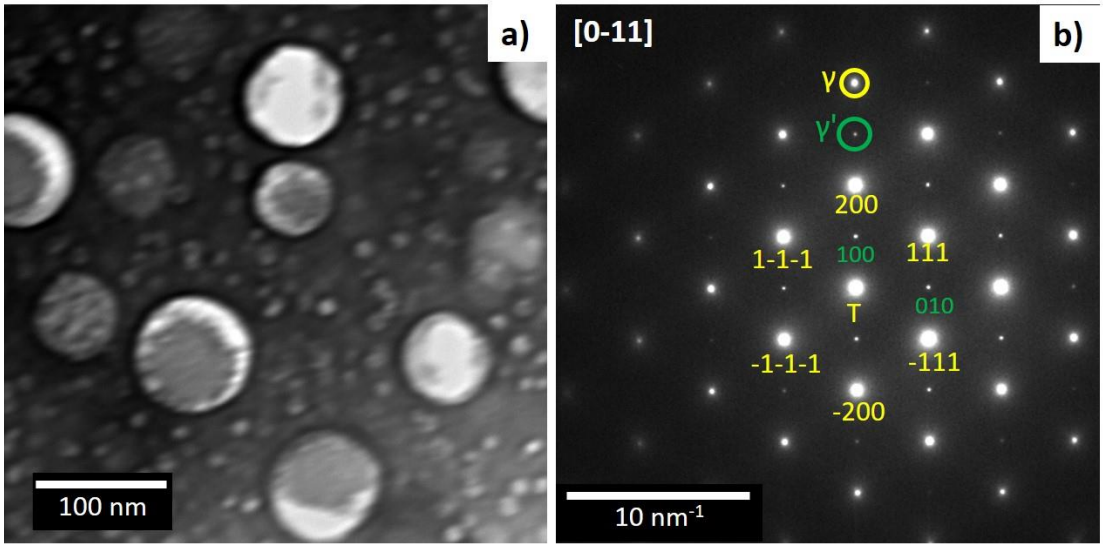

Figure 5-32: TEM micrographs of a two-step aged sample O (900 °C-2h WQ + 750 °C-10h WQ), a) Brightfield image and the associated b) selected area diffraction pattern along the [0-11] zone axis.

5.2.3 Microhardness of the aged samples

The Vicker's hardness of the aged samples, along with the ST sample, are presented in Figure 5-33. The hardness from the single-step aged samples (sample A, B, F, G) and two-step aged samples (sample J-M, O) arecompared. The ST sample, which did not contain any γ' precipitates, exhibited a Vicker's hardness of 171 HV. The hardness of all aged samples is higher than that for the ST sample due to the presence of the γ' precipitates after the aging treatments; see Figure 5-33.

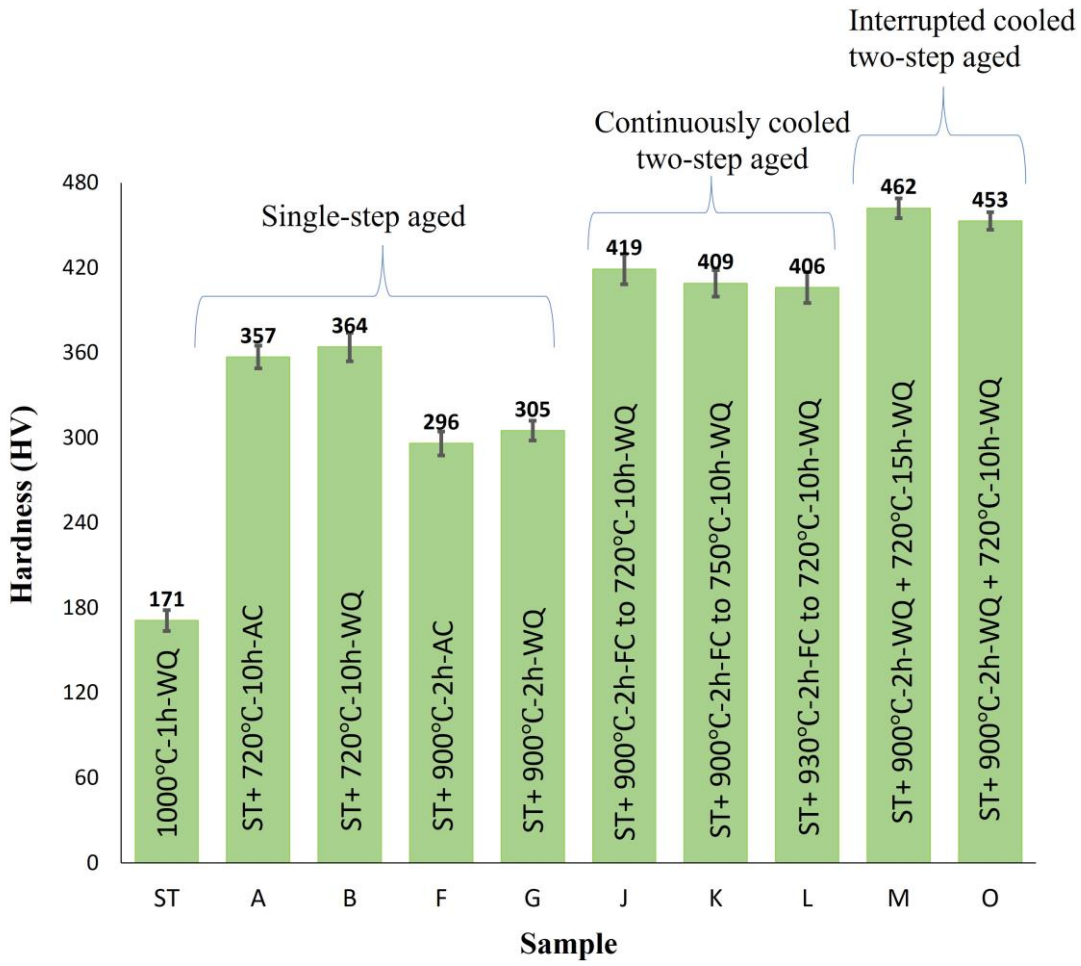

Figure 5-33: Average Vicker's hardness values of all the ST and ST-plus-aged samples.

5.2.4 Chemical composition analysis of aged alloy

5.2.4.1 Single-step aged sample

The concentration of the γ′-forming solute elements in the γ′ precipitate, the δ phase, the PFZ, and the matrix region in between the γ′ precipitates from sample G (900 □C-2h-WQ) were measured using HAADF imaging, Figure 5-34. Figure 5-34a and Figure 5-34c show HAADF-STEM images highlighting the γ' and δ phase morphologies, while Figure 5-34b and Figure 5-34d are the corresponding EDS elemental distribution graphs generated from the locations marked in Figure 5-34a and Figure 5-34c, respectively. The average values of the elements are summarized in Table

5-6. For example, from the Figure 5-34d line scan, the positions on the x-axis for different phases (γ' and γ) were marked, and the associated chemical composition values over that distance were averaged. These measurements were useful for explaining the microstructural evolution.

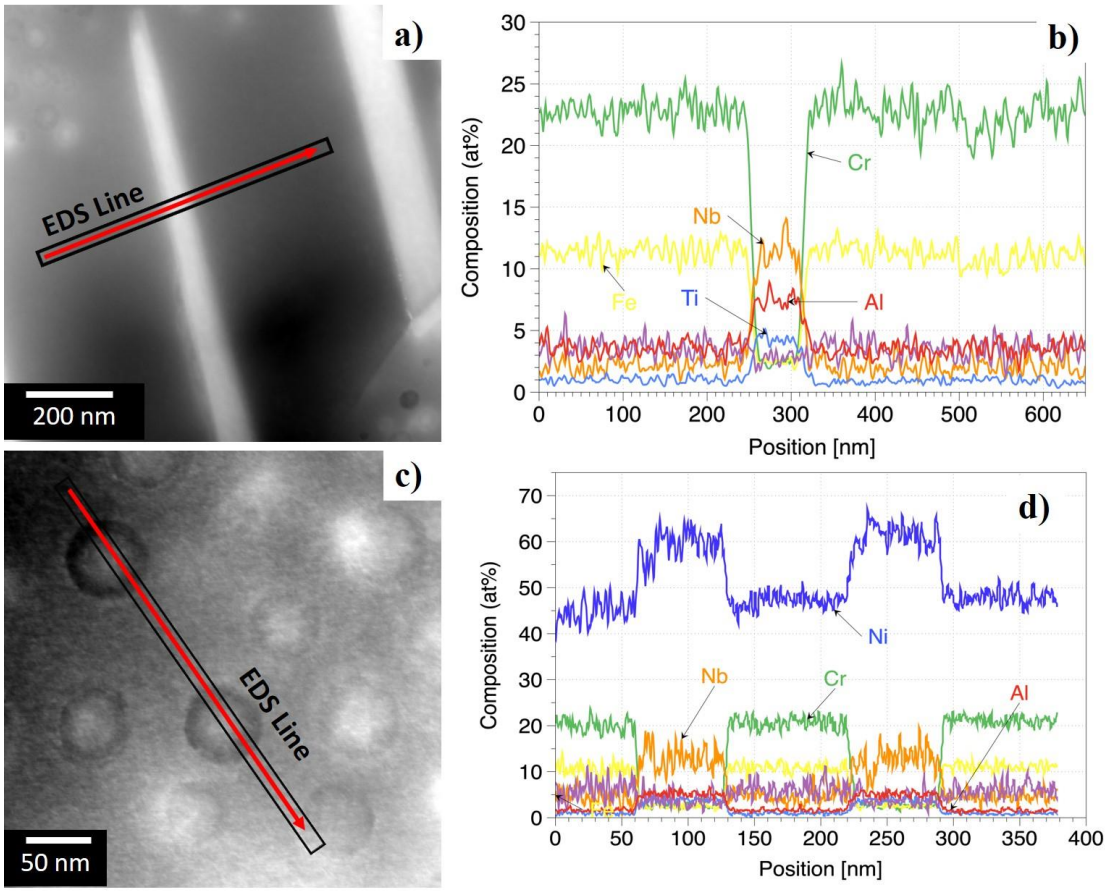

Figure 5-34: Sample G (900-2h-WQ) a) HAADF-STEM image highlighting δ phase and PFZ area with corresponding b) EDS elemental line profile outlined in a). c) HAADF-STEM image with highlighted EDS line across γ' precipitates and matrix and corresponding d) EDS elemental line profile highlighted in c).

Table 5-6: Average chemical compositions of the matrix regions, γ' and δ precipitates for sample G (900-2h-WQ) measured using STEM-EDS.

Sample region	**Concentration in at% of γ′ forming solutes**			
	Ti	**Al**	**Nb**	**Ni**
Matrix near γ'	0.9	2.7	2.2	34.1

Table 5-6 (cont'd)

Matrix near δ (PFZ)	1.1	3.8	2.3	45.0
γ'	3.52	8.25	6.44	44.2
δ	3.7	7.3	8.9	59.4

5.2.4.2 Two-step aged sample

APT was used to study the chemical composition of the smaller and larger γ' precipitates, the matrix regions between the γ' precipitates, and the regions near the δ phase for sample O (900°C-2h WQ + 720°C-10h WQ). Figure 5-35 displays the APT Fe atom maps overlaid with isoconcentration surfaces of 60 at. % Ni in a light pink hue. These surfaces were employed to delineate the interfaces between the γ' precipitates and the matrix. Figure 5-35a represents a proxigram illustrating the composition of the larger γ' precipitates (~55 nm) in conjunction with the matrix. This is achieved by utilizing the larger precipitates as the reference isosurface, which aligns with the zero point of the corresponding histogram on the x-axis. Similarly, Figure 5-35b presents a proxigram depicting the composition of the smaller γ' precipitates (~13 nm) in conjunction with the matrix, where the smaller precipitates serve as the reference isosurface. The average compositions of both the larger and smaller γ' precipitates and matrix regions are provided in Table 5-7. Comparing Table 5-6 and Table 5-7, it is clear that the concentration of γ′-forming solutes in the matrix was reduced considerably at the end of the two-step aging treatment (sample O) compared to the single-step aged sample G. It is noted that the γ' precipitates were richer in Nb than Ti, irrespective of the precipitate size. It is important to note that the two different techniques (APT and HRTEM EDS) have been used. Since the difference in the composition was above their resolution limit (1000 to 10 ppm), the comparison were safely reported here.

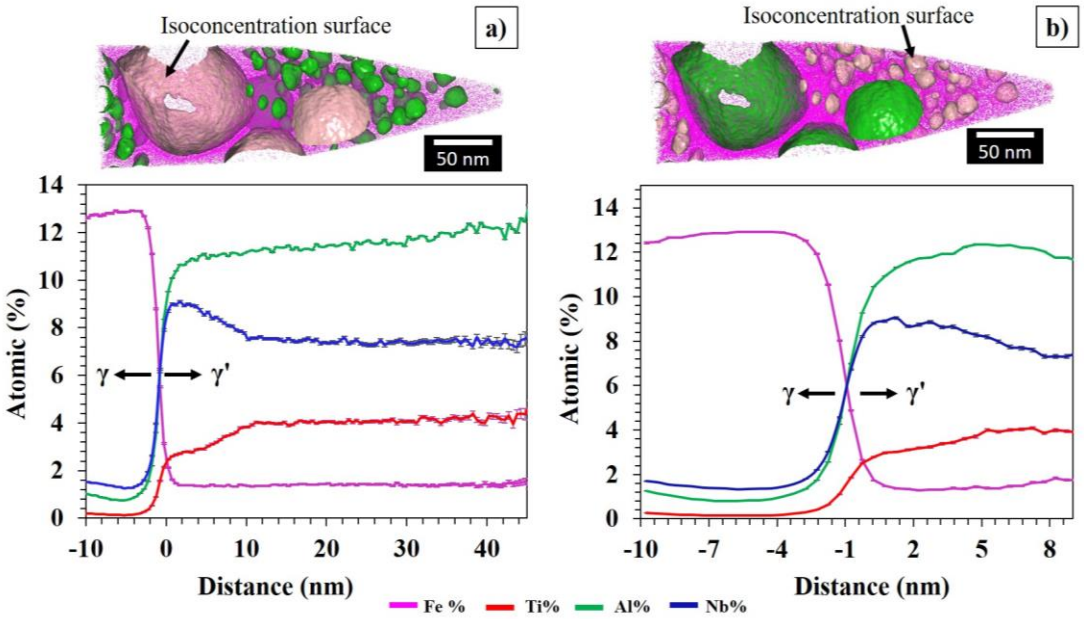

Figure 5-35: APT Fe atom maps with the γ' precipitates highlighted by 60 at. % Ni isoconcentration surfaces and the corresponding a) larger and b) smaller γ' precipitate proximity histograms from sample O (900°C-2h WQ + 720°C-10h WQ). The proximity histograms reveal the composition profile across the γ/γ' interface.

Table 5-7: Average chemical compositions of the matrix regions and γ' precipitates for sample O (900°C-2h WQ + 720°C-10h WQ) measured using APT.

Sample region	**Concentration in at% of γ′ forming solutes**			
	Ti	**Al**	**Nb**	**Ni**
Matrix near Larger and smaller γ'	0.17	0.93	1.44	46.18
Matrix near δ and smaller γ'	0.13	1.07	1.08	45.20
Larger γ'	4.02	11.43	7.45	70.19
Smaller γ'	3.29	11.81	8.67	68.96

5.3 TENSILE DEFORMED ALLOY: INVESTIGATION OF PRECIPITATE - DISLOCATION INTERACTIONS

In this section, the results of the aged-plus-tensile deformed alloys are presented. The section is divided into three sub-sections. The first section contains the microstructural details of the aged alloys used for the precipitate-dislocation study. The second section contains the mechanical property details of these aged alloys. The third and last section contains the details of the aged-plus-deformed samples, including the mechanical data and SEM and TEM characterization.

To study the precipitate-dislocation interaction during tensile deformation, three different aged conditions were chosen with varying γ' precipitate distributions (two conditions having unimodal γ' PSD, smaller and larger γ' precipitate sizes, and the third condition having a bimodal γ' PSD). The dominant deformation mechanisms were studied and rationalized with the present understanding based on the pertinent literature.

The selected heat treatment details and sample nomenclature based on the microstructural results presented in section 5.2 are shown in Table 4-4. Each set of heat treatments was performed on two tensile specimens (dimensions mentioned in Figure 4-19) and a cubic sample to study the undeformed microstructre. Before conducting any mechanical testing, high-magnification micrographs were collected from the cubic samples to ensure the desired γ' precipitate size distributions. The tensile YS from all the samples were calculated using sample geometry illustrated in Figure 4-19a. Another set of tensile tests, based on the geometry illustrated in Figure 4-19b, was conducted so that the samples achieved up to 3-4% plastic strain to generate enough dislocations to study the precipitate-dislocation interactions.

5.3.1 Initial microstructures

The ST sample did not exhibit any γ' precipitates after WQ. However, the sample did exhibit a grain boundary δ phase with an area percent of 0.8%, as shown in Figure 5-11a. Sample 900 had a uniform distribution of γ' precipitates with an average size of 24 ± 8 nm and volume percent of 13 %, as illustrated in Figure 5-36. This aging treatment resulted in a slight increase in the area percent of the δ phase to 1.5%. Sample 720 exhibted finer γ' precipitates with an average size of 7 ± 3 nm, and they have a 5.2 % volume percent. The area percent of the δ phase remained unchanged compared to the ST sample (Figure 5-37). The bimodal sample exhibited two different average γ' precipitate sizes, constituting an overall average volume percent of 18 %. The larger γ' precipitates exhibited an average size of 28 ± 5 nm, whereas the smaller γ' precipitates exhibited an average size of 6 ± 3 nm; see Figure 5-38. The volume percentages of the δ and γ' phases, the average matrix grain size, and the average size of γ' precipitates for all the samples are summarized in Table 5-8. The γ’ precipitate volume percent was consistent with that reported by Srinivasan et al. (Srinivasan et al., 2012). The calculated number fractions and the volume perecent of the smaller and the larger γ' precipitates in the bimodal sample were 0.9 & 13 % and 0.1 & 5 %, respectively.

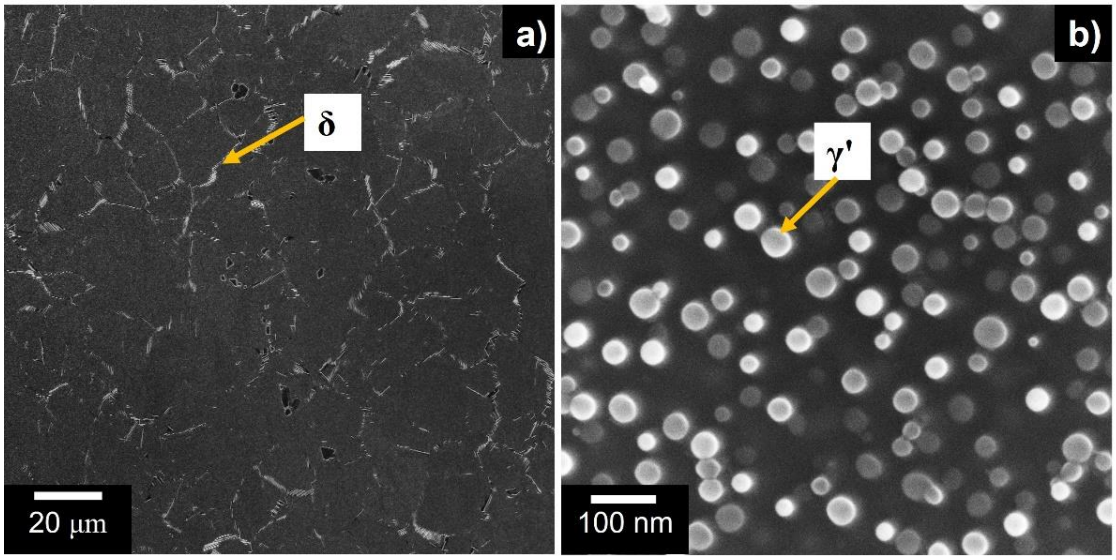

Figure 5-36: SE-SEM micrographs of the sample 900 microstructure exhibiting a) γ-matrix and grain boundary δ phase, b) spherical γ' precipitates.

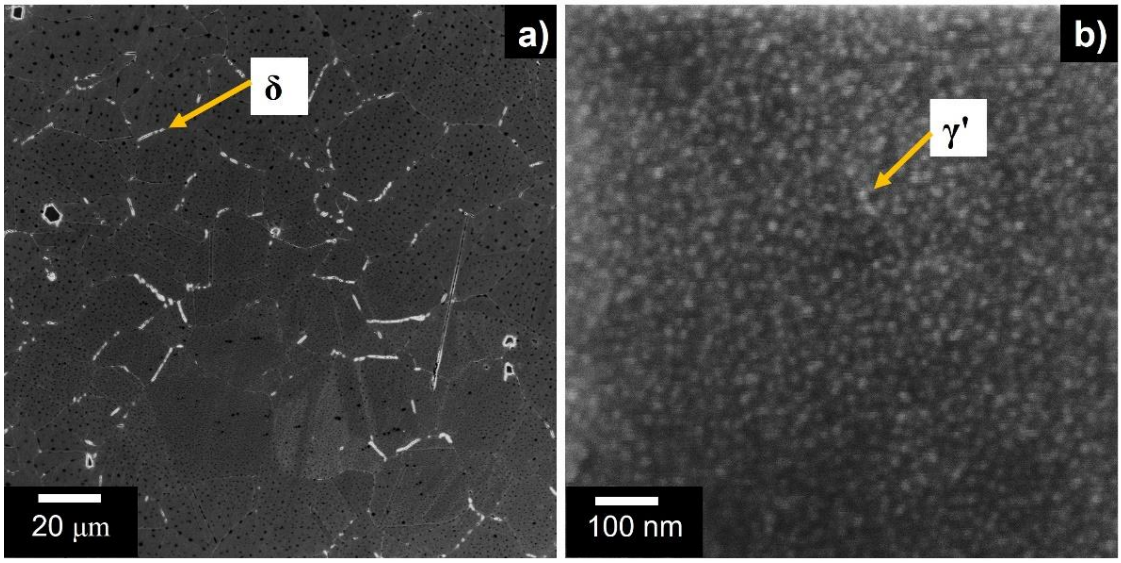

Figure 5-37: SE-SEM micrographs of the sample 720 microstructure exhibiting a) γ-matrix and grain boundary δ phase, b) spherical γ' precipitates.

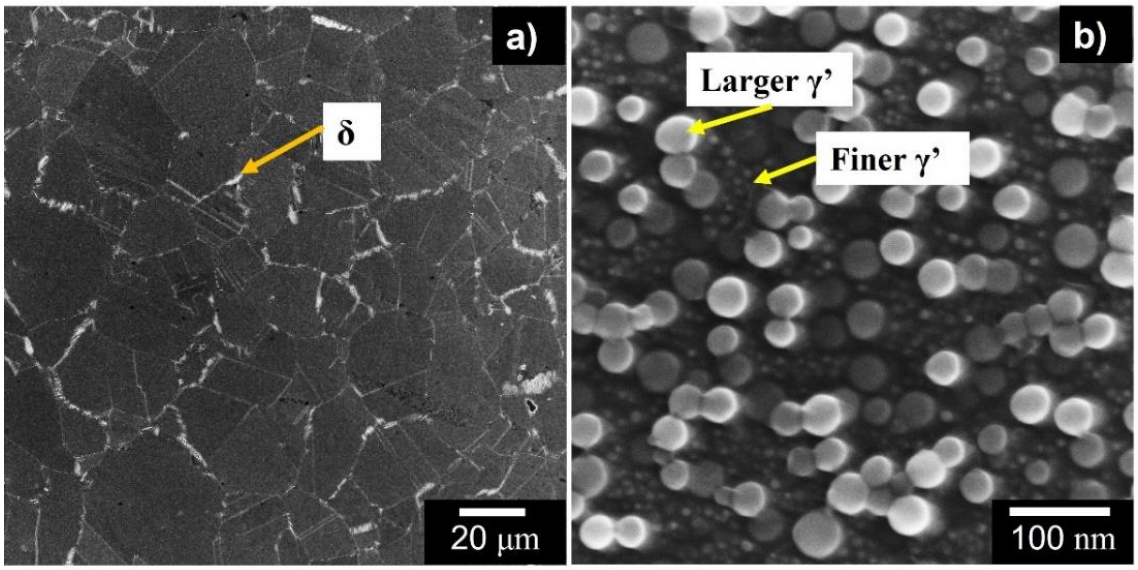

Figure 5-38: SE-SEM micrographs of the bimodal sample exhibiting a) γ-matrix and grain boundary δ phase, b) spherical γ' precipitates.

Table 5-8: Average grain size, γ' precipitate size and volume percent, and δ phase volume percentages as a function of the heat treatments.

Sample	**ST**	**900**	**720**	**Bimodal**
Average grain size (μm)	23 ± 8	24 ± 7	22 ± 9	23 ± 7
Average γ' precipitate radius (nm)	NA	24 ± 8	7 ± 3	28 ± 5 and 6 ± 3
γ' precipitate volume percent (%)	NA	13.1	5.2	18
δ phase area percent (%)	0.8	1.5	0.8	1.5
NA: not applicable				

The histograms of the γ' PSDs in all the aged samples in Figure 5-39, revealed distinct characteristics. The ST-plus-single-step aged samples (sample 900 and sample 720) exhibited unimodal distributions. In contrast, the ST-plus-two-step aged sample displayed a clear bimodal size distribution, suggesting the presence of two distinct average sizes for the γ' precipitates, Figure 5-39c.

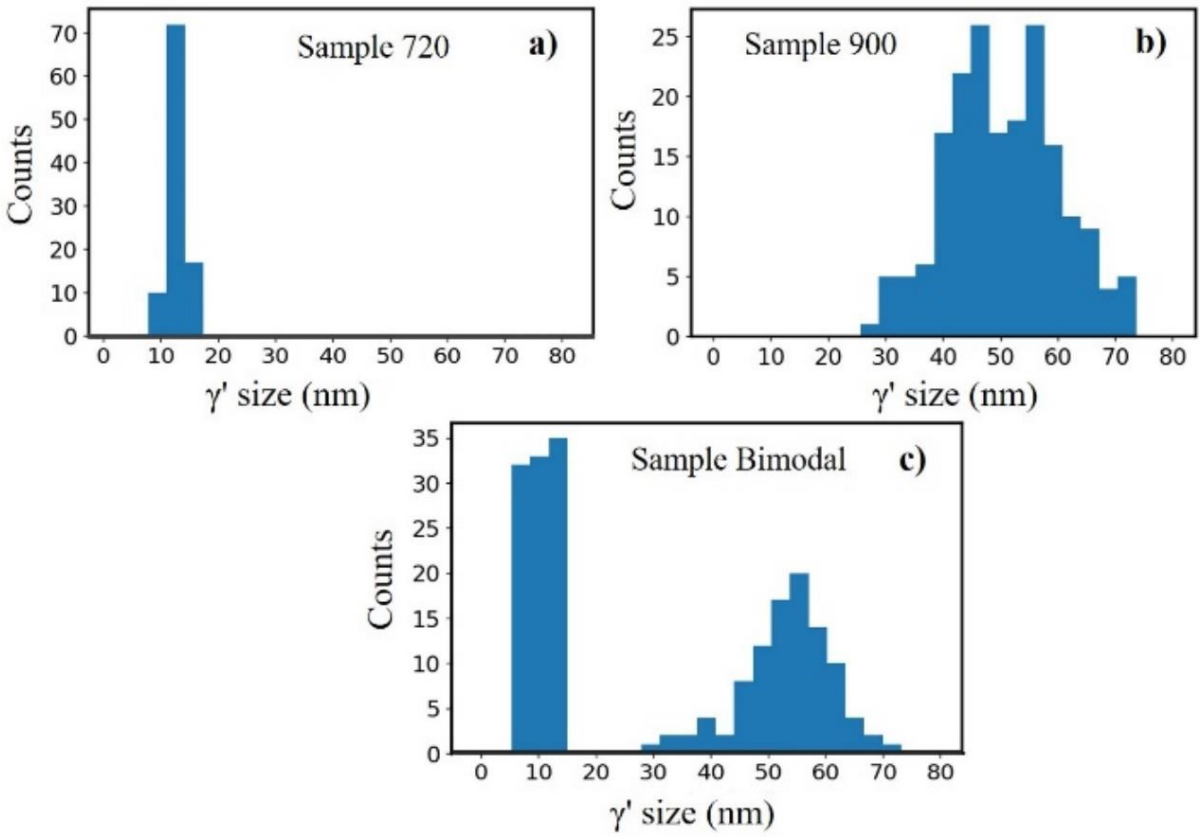

Figure 5-39: γ' PSD showing a) unimodal distribution with an average precipitate diameter of 14 nm in Sample 720, b) unimodal distribution with an average precipitate diameter of 48 nm in Sample 900, c) bimodal distribution with an average precipitate diameter of 12 and 56 nm in Sample Bimodal.

5.3.2 Mechanical Properties

The average Vickers hardness of the ST sample, which did not contain γ' precipitates, was 171±7 HV. The Vickers hardness of all the aged samples was also measured, as summarized in Table 5-9. The hardness of the sample 900 was found to be the lowest (313 HV) among all the aged samples, whereas the samples having the smaller γ' precipitates in the unimodal (sample 720) and bimodal (sample Bimodal) distributions exhibited Vickers hardness values of 425+6 and 454+4 HV, respectively.

Table 5-9: Average values for Vickers hardness of all the ST and ST-plus-aged samples.

Sample	ST	sample 900	sample 720	sample Bimodal
Hardness (HV)	171 ± 7	313 ± 9	425 ± 6	454 ± 4

To determine the YS, ε_f, and UTS, engineering stress-strain plots were constructed using the load-elongation data (Figure 5-40), and the associated mechanical properties are presented in Table 5-10.

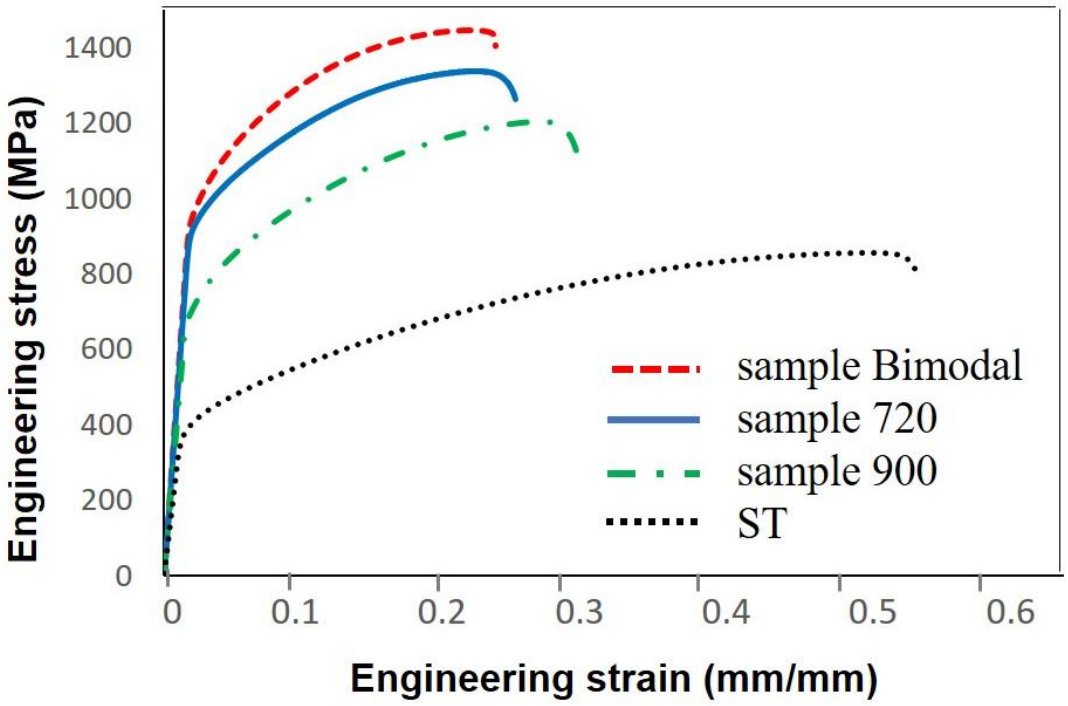

Figure 5-40: Engineering stress versus strain plot for the ST and ST-plus-aged samples.

Table 5-10: Averaged mechanical properties calculated from the tensile tests for the ST and ST-plus-aged samples.

Sample	**Mechanical properties**		
	YS0.2% (MPa)	**ε_f (%)**	**UTS (MPa)**
ST	381	56	856

Table 5-10 (cont'd)

900	690	29	1204
720	908	24	1332
Bimodal	930	22	1445

The hardness values and the tensile properties followed similar trends. The ST sample was the weakest but exhibited the highest ε_f (56 %). With the precipitation of the γ' phase in the microstructures as a result of the aging treatments, the strength and the hardness increased. Sample 900, having an unimodal distribution of the larger γ' precipitates and a γ' volume percentage of 13.1 %, produced the highest ε_f among all the aged samples but the lowest YS (Table 5-10). Sample 720, having a unimodal distribution of the smaller size γ' precipitates and a γ' volume percent of 5.2 %, produced the highest YS and the lowest ε_f. The sample Bimodal, which exhibited a γ' volume percent of approximately 18, resulted in the highest YS (930 MPa) and an ε_f of 22 %. The mechanical properties of the sample Bimodal were most similar to the sample 720.

5.3.3 Particle-dislocation interaction

Figure 5-41 presents TEM BF micrographs obtained from sample 720 showing dislocation pile-ups, paired dislocations, and minimal dislocation bowing. The spacing between the dislocation pairs appeared to be larger than the γ' precipitates, suggesting that weak-pair shearing was more prevalent than strong-pair shearing and bowing. Figure 5-42a presents a TEM DF micrograph obtained from sample 900 showing the γ' precipitates, which were identified using (100) superlattice reflections. Figure 5-42b indicated looping around some precipitates and paired dislocations in some areas. The spacing between the dislocation pairs appears to be smaller than the average size of γ' precipitates, suggesting that strong-pair interactions are occurring between

the dislocations and precipitates. Figure 5-43a and b show DF micrographs displaying γ' precipitates and straight dislocations shearing through these precipitates, respectively, for sample Bimodal. Several sheared γ' precipitates exhibiting stacking faults like fringe contrast in them, noted by the blue arrows in Figure 5-43c. Hardly any pairs of dislocations were observed. It is clear from Figure 5-41 and Figure 5-43 that only shearing of dislocations around γ' particles was observed in sample 720 and sample Bimodal. In contrast, in Sample 900, which contains only large γ' precipitates, both shearing and looping of dislocations around γ' precipitates were observed, as shown in Figure 5-42. These observations are rationalized on the basis of the theoretically calculated CRSS for shearing and looping in the chapter 6.3.

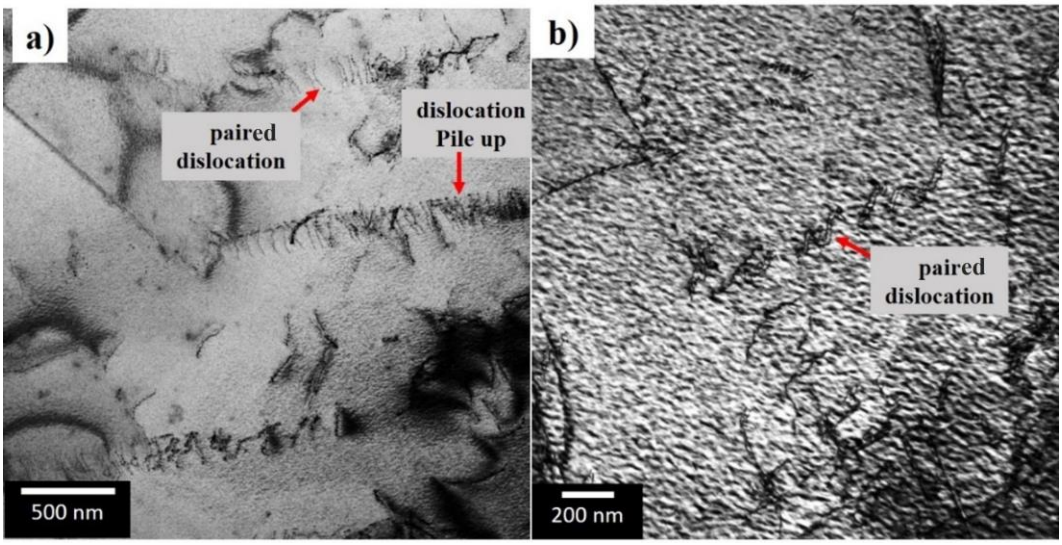

Figure 5-41: TEM BF micrographs for sample 720 with small γ' precipitates: a) paired dislocations and dislocation pile-up, b) paired dislocations at higher magnification.

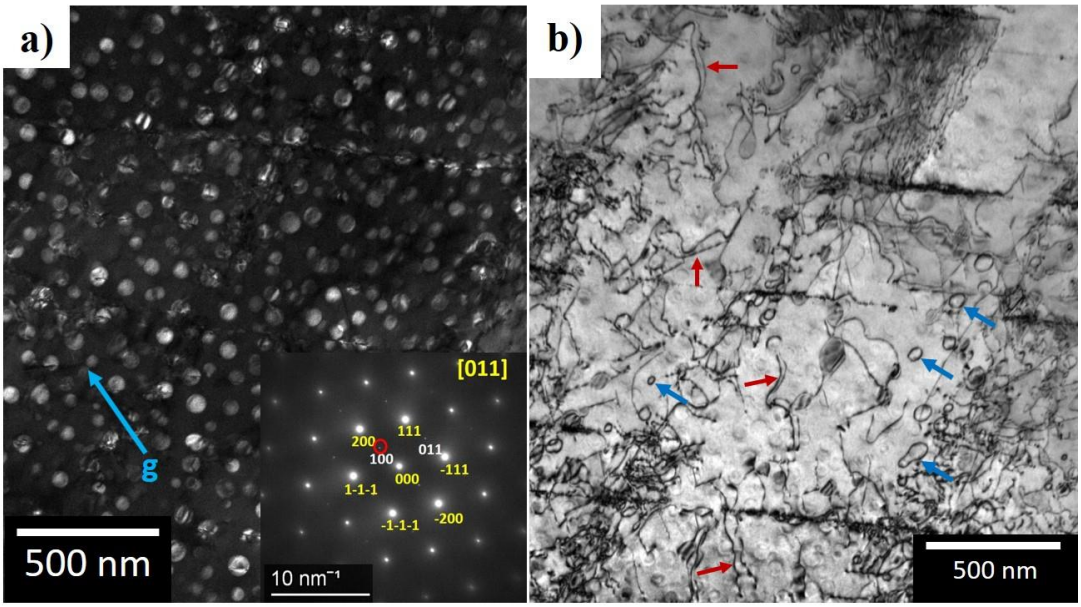

Figure 5-42: TEM micrographs for sample 900 with larger γ' precipitates: a) DF image from 100 superlattice reflection showing γ' precipitates, b) BF image highlighting the dislocation bending/looping (blue arrows) and paired dislocations (red arrows); identified based on having a dislocation line as bright and straight accompanied by a little bent or dashed contast dislocation line.

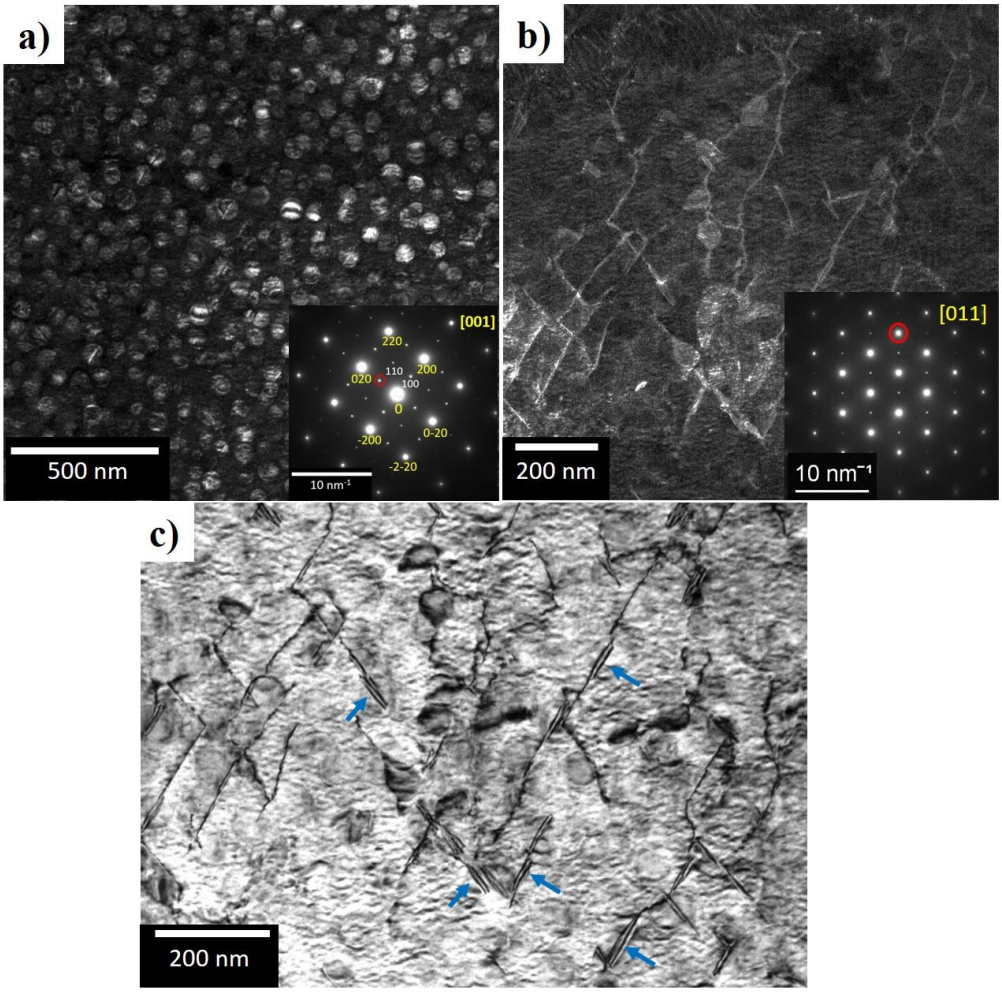

Figure 5-43: TEM micrographs for sample Bimodal: a) DF image using the 110 superlattice reflections with an SAD pattern along the [001] zone axis showing larger γ' precipitates, b) A DF image with the 200 reflections highlighting the dislocation shearing with the an SAD pattern along the [011] zone axis in the inset, c) A BF image highlighting the shearing and stacking faults inside the sheared γ' precipitates (blue arrows).

5.4 CREEP DEFORMED ALLOY: STABILITY OF γ' PRECIPITATE UNDER THERMAL AND TENSILE STRESS APPLICATION

In this section, the results of the aged-plus-creep deformed alloys and aged-plus-thermally-exposed alloys are presented. The section is divided into three sub-sections. The first section presents the mechanical data from the creep studies. The second section presents the microstructural details of the aged-plus-deformed alloys. The third section presents the calculated CRSS for individual grains for a creep-tested sample.

Creep tests were conducted on samples having the bimodal γ' precipitate microstructure to study the effect of applied tensile stress and temperature simultaneously. All the dogbone samples used for the creep testing (hereafter referred to as the creep-deformed samples) had counterpart cubic 1 cm^3 samples that were not loaded but thermally exposed to the same conditions as the creep sample (hereafter referred to as thermally-exposed sample) in order to compare the thermal-exposure effects only. The creep test was interrupted after ~1 % creep strain and characterized using SEM to study the change in γ' precipitate size, morphology, and distribution. The CRSS values for individual grains were calculated for the creep-tested samples using acquired EBSD orientation maps, and the results were related to the γ' precipitate evolution.

5.4.1 Creep properties

Samples containing the bimodal γ' precipitate microstructure (sample O from Table 4-2) were creep tested as described in Table 5-11, which listed the test parameters, including temperature, stress, creep strain, time, and location of fracture. The creep strain versus time curves for sample 20-53 (tested at a temperature of 704 °C and a stress of 650 MPa) and sample 20-56 (tested at a temperature of 680 °C and a stress of 550 MPa) are presented in Figure 5-44. The sample that was creep tested at a higher temperature and stress reached ~ 0.9% creep strain in 58 hours prior to failure and was in the tertiary creep stage for a greater percentage of the test time. The other sample did not transition to the tertiary stage until around 240 hrs, and this was followed by straining to ~ 0.65 % creep strain in 475 hours.

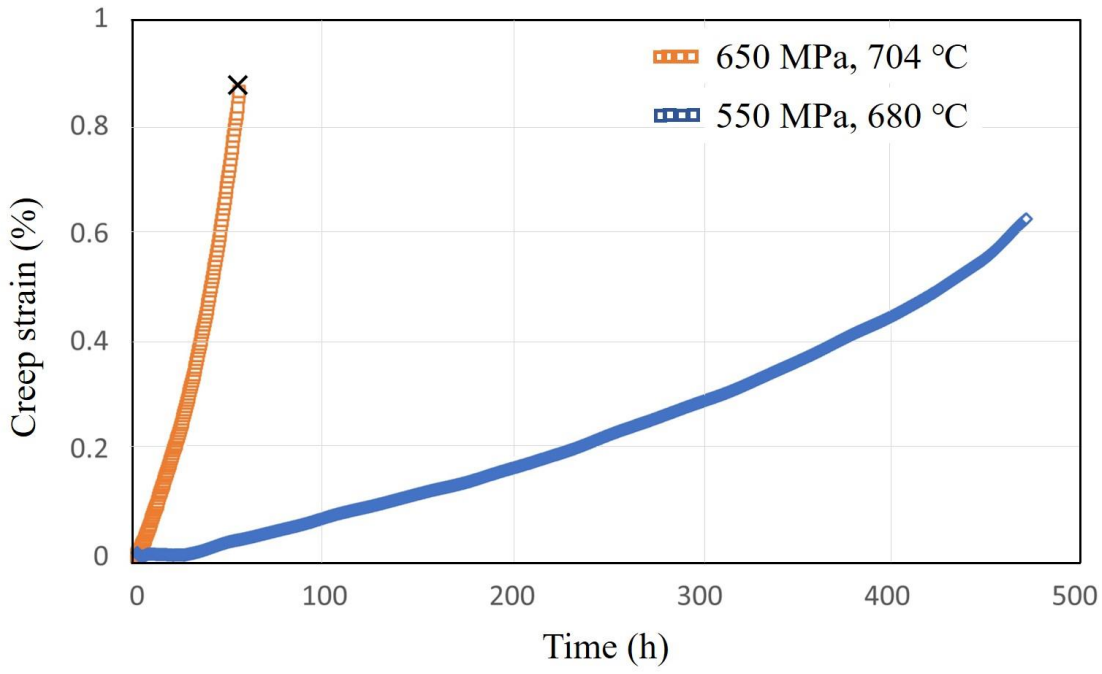

Figure 5-44: Creep strain vs. time curves for sample 20-53 (704 °C, 650 MPa) and 20-56 (680 °C, 550 MPa).

Table 5-11: Summary of the creep testing conditions for the bimodal samples and their failure location.

Test ID	Temp (°C)	Stress (MPa)	Creep strain (%)	Time (h)	Failure point
20-49	680	550	0	1.2	Gage
20-52	704	650	0.15	3.3	Notch
20-53	704	650	0.9	54.2	Gage
20-55	680	550	0	1.1	Notch
20-56	680	550	0.7	482	No fracture
20-57	704	550	0	0.5	Gage
20-58	704	550	0	1	Gage

5.4.1.1 Fractography of the creep-tested samples

Some of the tests mentioned in Table 5-11 failed with little-to-no creep strain (0 - 0.15%). Figure 5-45 and Figure 5-46 present the fractured surfaces. Elevated temperature oxidation led to a change in the surface color, as seen in Figure 5-45a. Intergranular cracking was prominent; see Figure 5-45c and d.

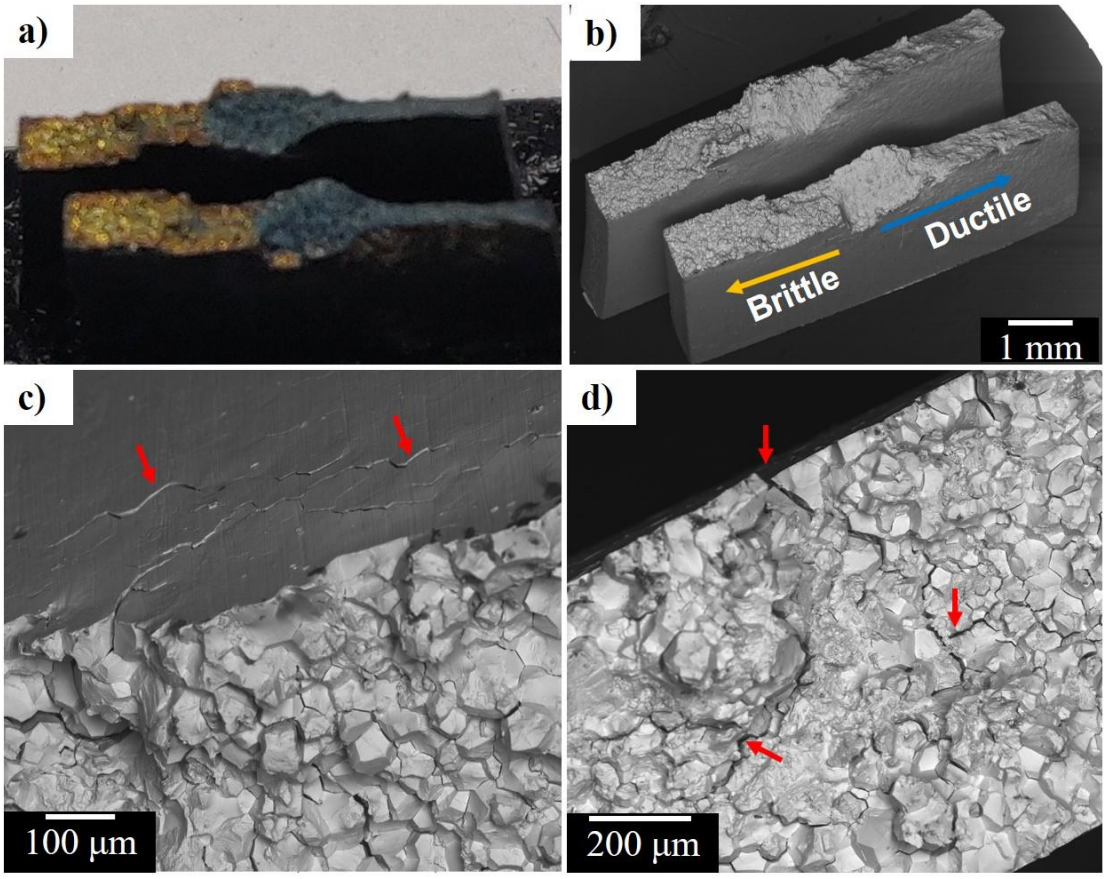

Figure 5-45: Images of the sample creep tested at 680 °C and 550 MPa stress, a) digital image and b) schematic highlighting the more oxidized (blue) region where the primary crack grew and the region of fast fracture (yellow), c and d) BSE-SEM micrographs highlighting the intergranular cracking with red arrows.

It was observed that the thermocouple spot welded area was affected up to around 100 µm, as highlighted in Figure 5-46b. Both ductile (dimples) and brittle (intergranular cracking) features were observed in all the creep-deformed samples (Figure 5-46c and d). The δ phase was observed near the grain boundaries (Figure 5-46f).

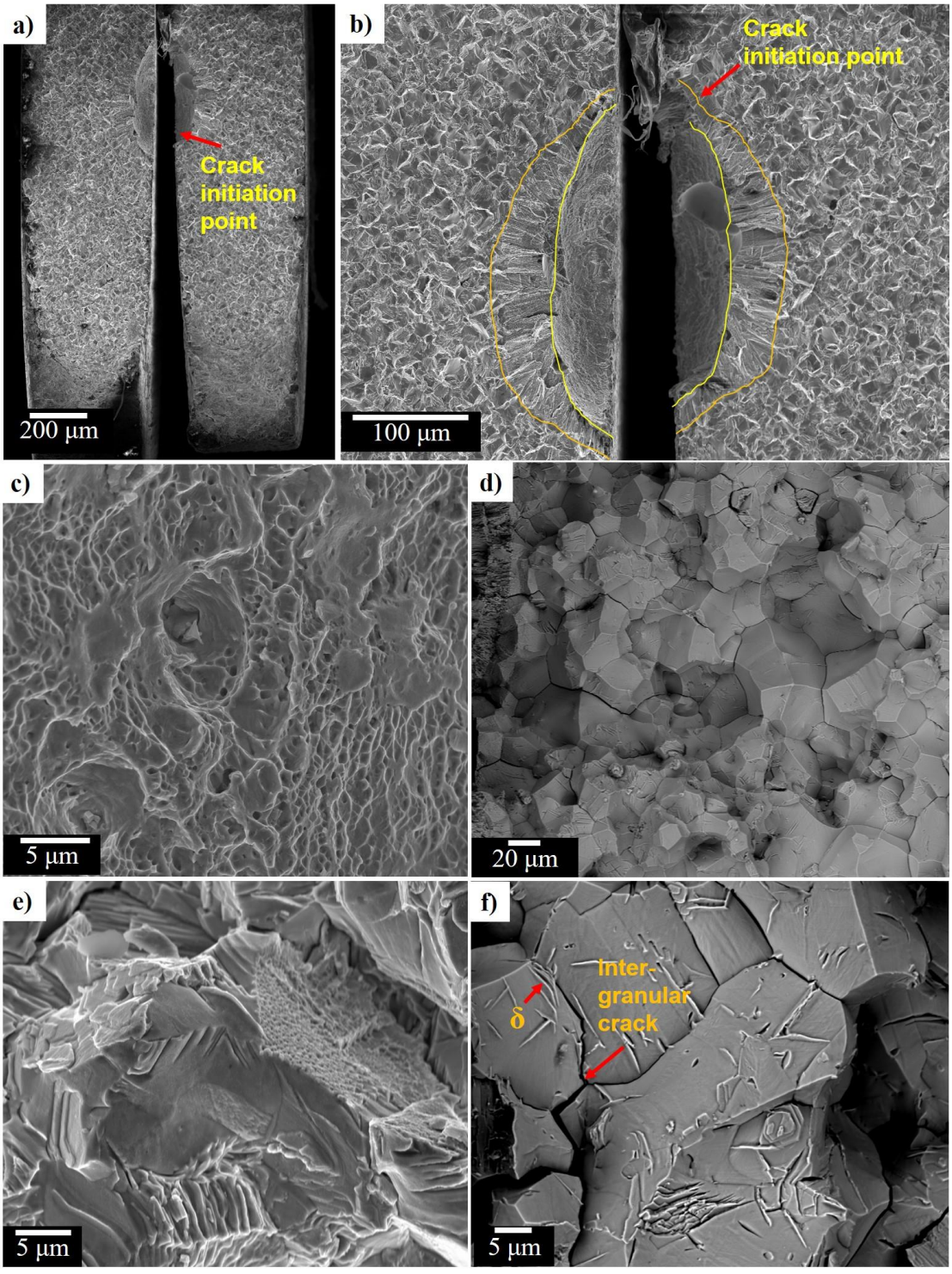

Figure 5-46: SE-SEM micrographs of the sample crept at 704 °C and 550 MPa stress a) and b) highlighting the crack initiation point, c) ductile dimples, d) (BSE micrograph) and e) grain boundary cracking, and f) δ phase near the grain boundaries and intergranular cracking (BSE image).

5.4.2 Microstructural comparison of creep-deformed and thermally-exposed samples

The initial microstructure of sample O before creep testing was presented as the baseline for comparison, Figure 5-47. Sample O exhibited an average grain size of ~24 nm and 2.5 volume percent of the δ phase.

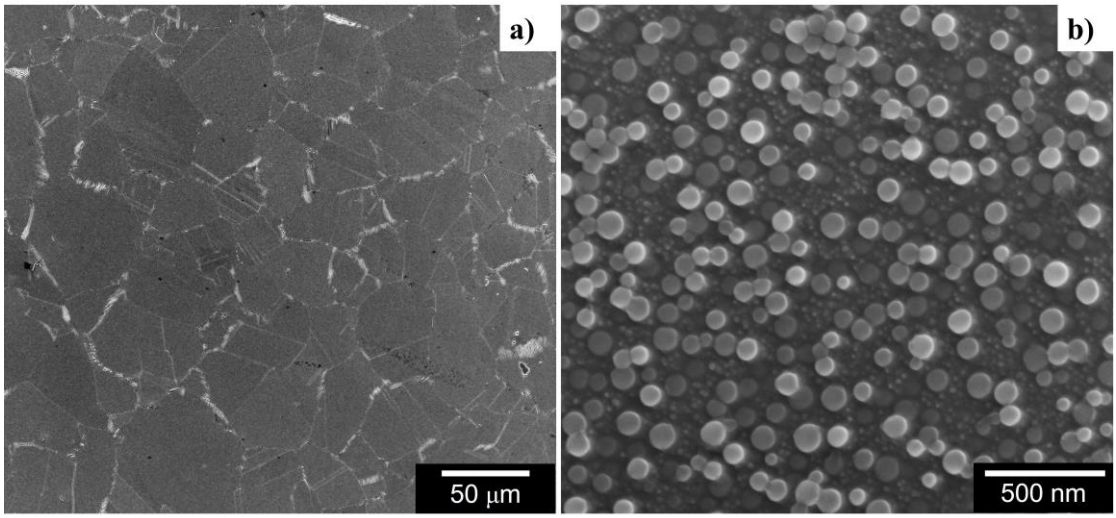

Figure 5-47: SE-SEM micrograph of sample O before creep testing: a) lower magnification highlighting the grains and the grain boundary phase δ, b) higher magnification highlighting the bimodal γ' precipitate size distribution.

Sample 20-53 exhibited an average grain size (~23 μm) for both the creep-deformed sample (Figure 5-48a) and the thermally-exposed sample (Figure 5-48b). The grain boundary δ phase fraction was found to be 2.5 % and 1.8 % for the creep-deformed sample and the thermally-exposed sample, respectively. The loading direction for the creep-deformed sample is indicated as L on the micrograph; see Figure 5-48a. The following changes were observed comparing the γ' precipitate size and distribution: a) the creep-deformed sample exhibited a smaller number density of finer γ' precipitates (Figure 5-49a) compared to the thermally-exposed sample (Figure 5-49b), b) the bimodal average size of γ' precipitates was measured to be 56 ± 13 nm and 13 ± 3 nm for the creep-deformed sample, and 58 ± 8 nm and 17 ± 3 nm for the thermally-exposed sample, c) the creep-

deformed sample exhibited a few elongated γ' precipitates perpendicular to the creep loading direction, whereas for thermally-exposed sample no such elongation was observed. The γ' precipitates size distribution plot for sample 20-53 is presented in Figure 5-50.

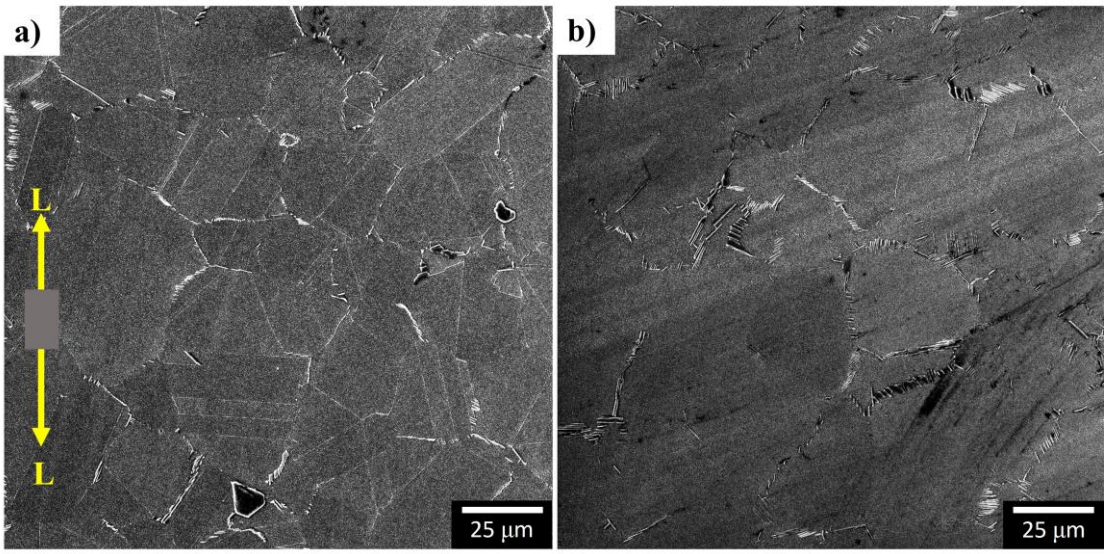

Figure 5-48: SE-SEM micrograph of a) sample 20-53 (creep tested at 704 °C and 650 MPa) highlighting the grains from the gage section where L indicates the loading direction, b) the thermally-exposed (704 °C) sample microstructure.

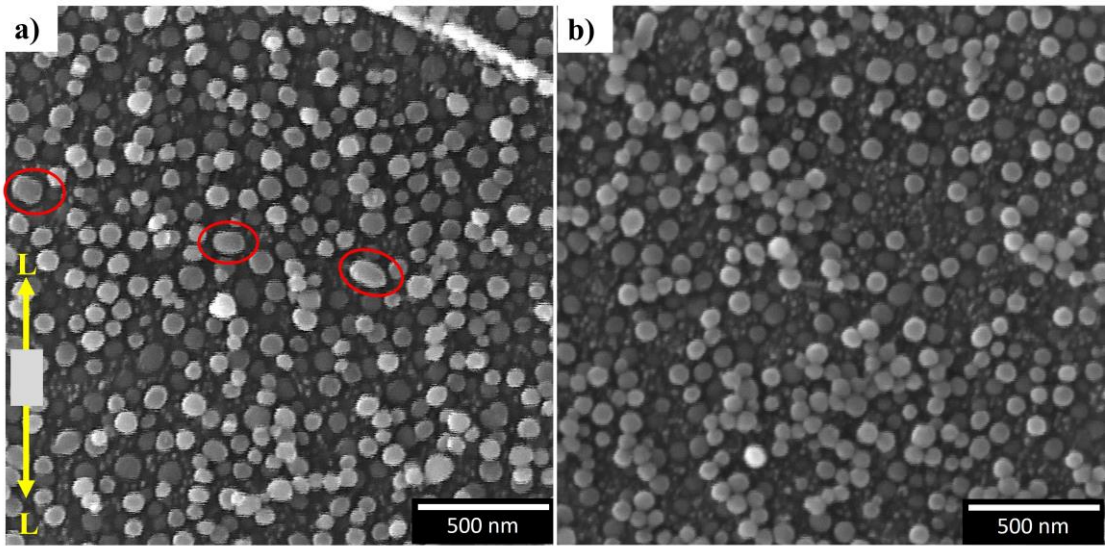

Figure 5-49: SE-SEM micrographs highlighting the γ' precipitates from a) sample 20-53 (creep tested at 704 °C and 650 MPa) in the gage section, b) the thermally-exposed (704 °C) sample.

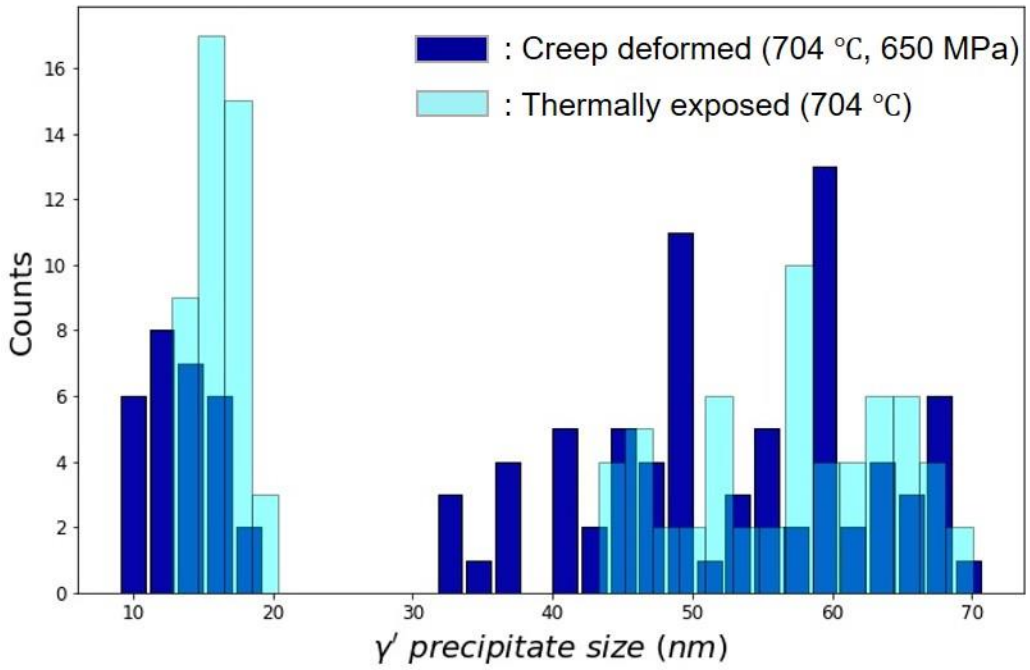

Figure 5-50: γ' precipitates size distribution plot for sample 20-53 (creep-deformed sample at 704 °C and 650 MPa) and the thermally-exposed (704 °C) sample.

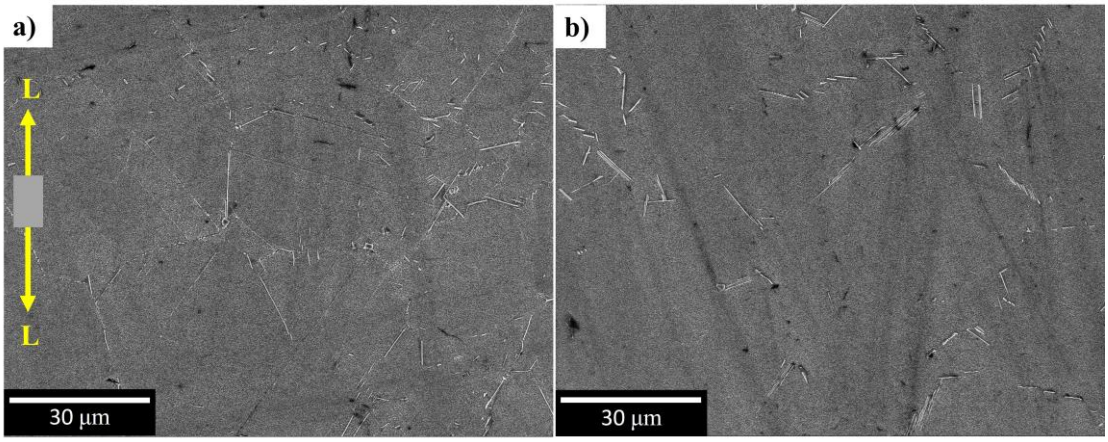

Figure 5-51: SE-SEM micrograph of a) sample 20-56 (creep tested at 680 °C and 550 MPa) highlighting the grains from the gage section where L indicates the loading direction, b) the thermally-exposed (680 °C) sample.

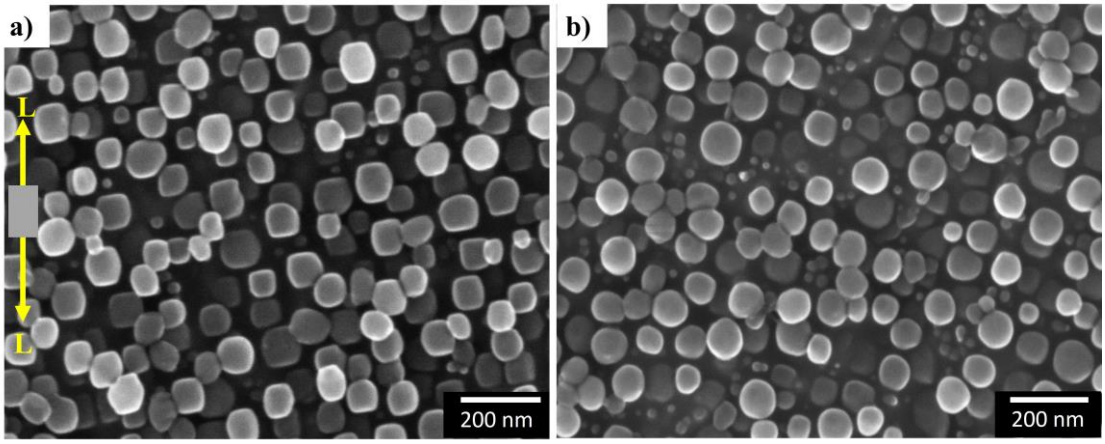

Figure 5-52: SE-SEM micrographs highlighting the γ' precipitates from a) sample 20-56 (creep tested at 680 °C and 550 MPa) from gage section, b) the thermally exposed (680 °C) sample.

Another creep-deformed sample (sample 20-56) exhibited similar trends as that for sample 20-53 with an average grain size of 25 μm and grain boundary δ phase volume percent of 1.8%. These values were obtained for both the creep-deformed sample (Figure 5-51a) and the thermally-exposed sample (Figure 5-51b), even after undergoing creep deformation at 680°C and 550 MPa stress and thermal exposure at 680°C for 480 hours, respectively. The following changes were observed comparing the γ' precipitate size and distribution: a) the creep-deformed sample exhibited almost no small γ' precipitates (Figure 5-52a), whereas the thermally-exposed sample exhibited both the small and larger γ' precipitates (Figure 5-52b), b) the average bimodal size of γ' precipitates were measured to be 76 ± 15 nm and 21 ± 2 nm for the creep-deformed sample and 83 ± 7 nm and 20 ± 5 nm for thermally-exposed sample, c) the creep-deformed sample displayed a near-cuboidal morphology of the γ' precipitates, while in the thermally-exposed sample, near-spherical γ' precipitates were observed. The γ' precipitate size distribution plot comparing the creep-deformed sample with the thermally-exposed sample is presented in Figure 5-53.

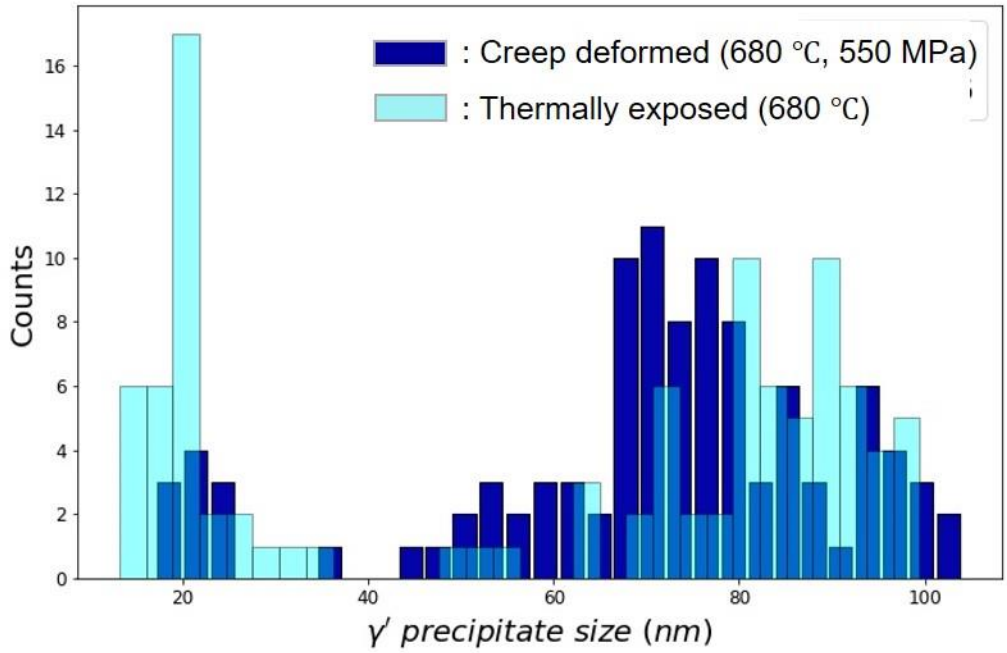

Figure 5-53: γ' precipitates size distribution plot for sample 20-56 (creep tested at 680 ℃ and 550 MPa) and the thermally-exposed (680 ℃) sample.

5.4.2.1 Microstructure (Individual grains)

The presence of cuboidal γ' precipitates in the creep-deformed sample (sample 20-56), which was subjected to simultaneous stress and high-temperature, sparked interest in studying the potential changes, if any, in individual grains. An EBSD orientation map was collected for the creep-deformed sample; see Figure 5-54a, and the corresponding SE-SEM micrograph was collected with five different grains marked; see Figure 5-54b.

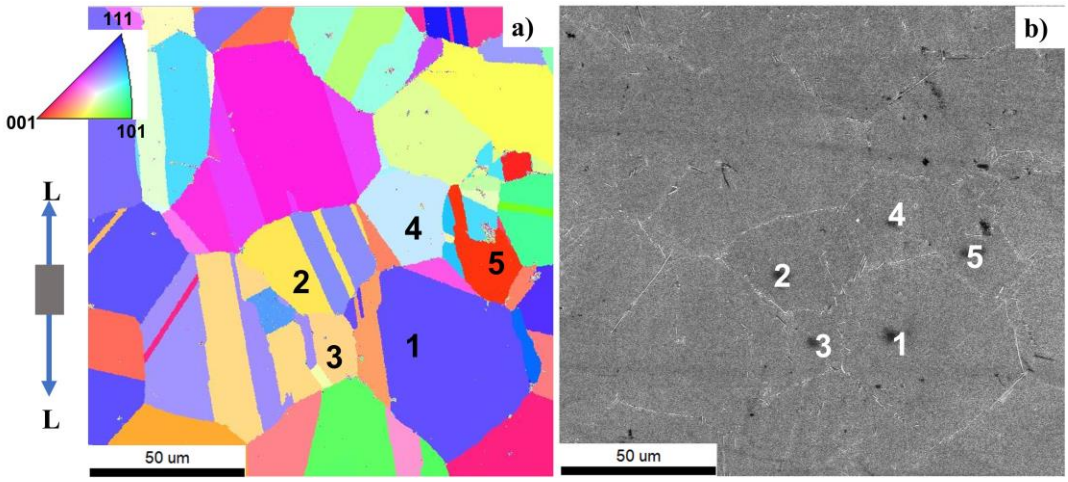

Figure 5-54: SEM data acquired for the creep-tested sample 20-56 (creep tested at 680 ℃ and 550 MPa) a) EBSD inverse pole figure map, b) corresponding SE-SEM micrograph with 5 different γ matrix grains marked.

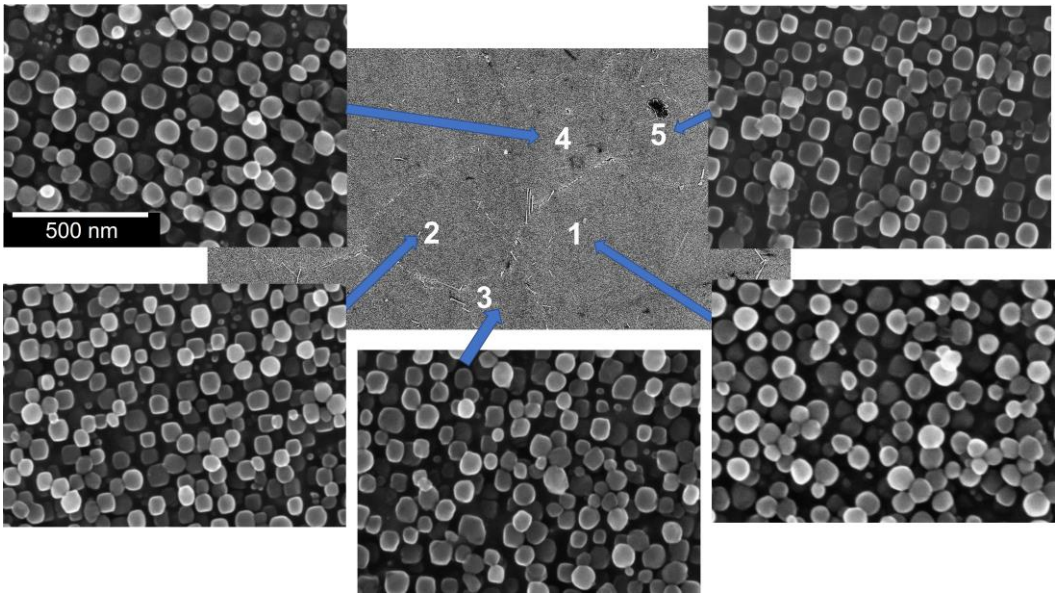

Figure 5-55: SE-SEM micrographs highlighting the γ' precipitates from the five different γ matrix grains shown in Figure 5-54b.

Higher-magnification images from each grain revealed the γ' precipitate size, distribution and morphology; see Figure 5-55. The finer γ' precipitates were not observed in any grains, unlike that of the microstructure before creep testing; see Figure 5-47b. To assess the effect of the applied stress on the creep-deformed sample, the growth of the γ' precipitates in individual grains (Figure

5-54b) was evaluated by measuring the degree of cubicity (λ_c). The crystal orientations, γ' precipitate sizes, and λ_c values are summarized in Table 5-12.

Table 5-12: Individual grain information for the creep-deformed 20-56 sample tested at 680 °C and 550 MPa: crystal orientation, γ' precipitate size and λ_c.

Grain Number	**Crystal orientation (plane normal to [001])**	**γ' precipitate size (nm)**		**Degree of cubicity (λ_c)**
		Larger γ'	Finer γ'	
1	(8 7 10) ~ (1 1 1)	77 ± 13	19	~ 0
2	(8 1 20) ~ (2 0 5)	75 ± 10	21	0.52
3	(4 1 10) ~ (1 0 2)	71 ± 17	15	0.47
4	(9 4 14) ~ (2 1 3)	71 ± 13	18	0.25
5	(1 0 20) ~ (0 0 1)	66 ± 12	16	0.73

5.4.2.2 Critical resolved shear stress calculation

As the sample 20-56 (creep-tested at 680 °C and 550 MP up to 0.65 % creep strain) displayed different microstructures (especially with respect to the γ' precipitates) in individual grains, an investigation into the impact of stress on the CRSS for individual grains was performed. The crystal planes corresponding to each grain with a plane normal to [001] were located on the standard unit triangle IPF map; see Figure 5-56b. To determine the CRSS, the orientation (Euler's angle) of the individual grains was incorporated into the rotation matrix shown in Figure 4-23 and further used in the equation (4.4).

The Schmid factor and CRSS values were computed for each slip system (12 for FCC) to ascertain the likely active slip system using equation (4.5). This was followed by the identification of the

highest CRSS value to identify the active slip system. A summary of the outcomes is presented in Table 5-13.

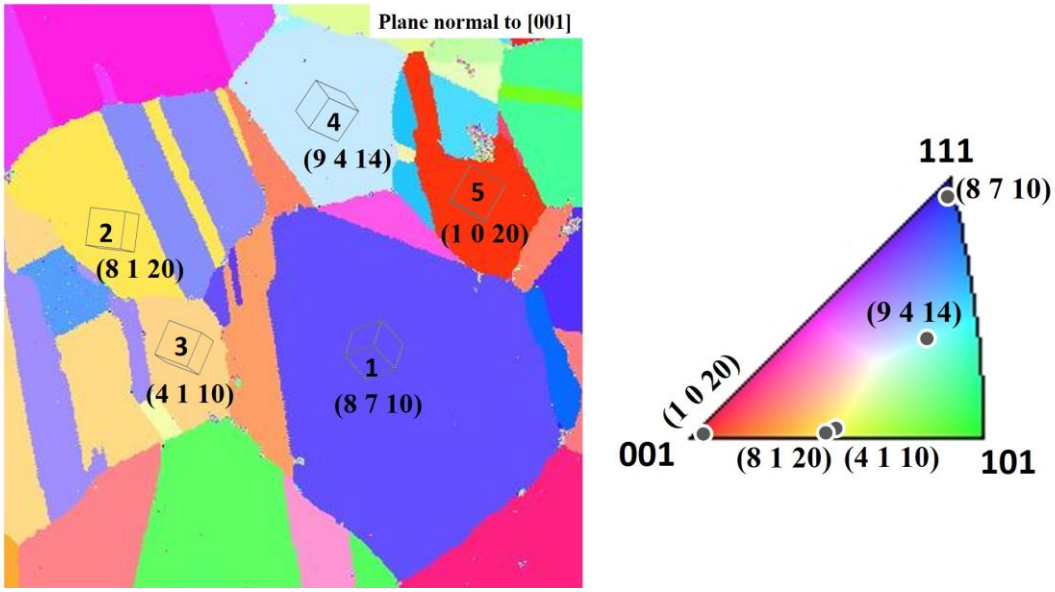

Figure 5-56: a) EBSD inverse pole figure map highlighting the unit cell orientations for the five marked grains in Figure 5-54b, b) FCC unit triangle highlighting the corresponding planes.

Table 5-13: The summary of Euler angles, Schmid factor, active slip system, and CRSS calculated for the five marked grains in Figure 5-54b for the creep-deformed sample 20-56 tested at 680 °C and 550 MPa up to 0.65 % creep strain.

Grain No.	Euler angles (ψ, θ, φ)	Schmid factor (m)	Slip plane	Slip direction	CRSS (MPa)
1	252, 47, 319	0.425	(111)	[01-1]	234
2	263, 88, 202	0.457	(111)	[10-1]	252
3	325, 157, 257	0.466	(111)	[01-1]	262
4	56, 76, 33	0.439	(11-1)	[101]	242
5	150, 90, 20	0.489	(111)	[10-1]	269

CHAPTER 6. DISCUSSION

This chapter delves into the analysis of the results presented in Chapter 5, with a particular emphasis on addressing the objectives outlined in Chapter 3. The discussion is divided into four major sections as follows:

a) The first section discusses the reasoning behind the selection of the specific temperatures for the ST process. It involves a comparative analysis of parameters such as grain size, γ' precipitate distribution, and material hardness between the as-processed microstructure and the ST microstructures.

b) The second section discusses the development of the bimodal γ' precipitate microstructure. It encompasses microstructural findings from samples subjected to different aging processes and establishes a connection with the chemical composition results to gain insight into the bimodal γ' precipitate size distributions.

c) The third section discusses the interaction between the γ' precipitates and the dislocations during the room temperature tensile deformation. It explores the dominant deformation mechanisms within both the unimodal and bimodal γ' precipitate size distribution microstructures. The experimental observations presented in section 5.3 are systematically linked with the theoretically calculated values from section 6.3, employing various strengthening models.

d) The last section discusses the γ' precipitate evolution under the simultaneous influence of stress and temperature. A comparative analysis is conducted between the microstructural observations of samples subjected to creep deformation and those solely exposed to the thermal conditions.

6.1 SOLUTIONIZED ALLOY: SELECTION OF SOLUTION-TREATMENT TEMPERATURE

In this section, the results of the as-processed and ST microstructures are discussed. The first subsection discusses the as-processed alloy microstructures. This was helpful in selecting the parameters for ST, which is the point of discussion for the next two sub-sections.

By scrutinizing various microstructural attributes such as the presence of γ' precipitates, the state of the γ matrix, and changes in hardness resulting from the ST conducted at different temperatures, a pivotal decision was made regarding the specific temperature for ST. The selection process will be discussed below in detail.

6.1.1 As-processed alloy

As shown in Figure 5-2c, It was observed that the as-processed sample was moderately textured and resembled that typically associated with copper texture (Suwas & Ray, 2014). The color gradients observed within individual grains in the EBSD inverse pole figure maps were due to point-to-point misorientations within the grain, as shown in Figure 5-2d. The average misorientation of 10° within a given grain (see Figure 5-2d) and the presence of dislocations (see Figure 5-6c) likely resulted from the processing history (hot-forged) of the as-processed materials. Therefore, to dissolve the existing γ' precipitates and reduce the residual strain in the material, high-temperature (954-1100 °C) solution treatments were conducted based on the solvus temperature range for the γ' and δ phases (Srinivasan et al., 2012; Xie, Xu, et al., 2005).

6.1.2 γ Matrix Grains

The average γ-phase grain sizes are plotted in Figure 6-1. The reason why the average γ-phase grain size after the 954 □C solution temperature was larger with a higher standard deviation than that after the 1000 □C solution temperature may be explained as follows:

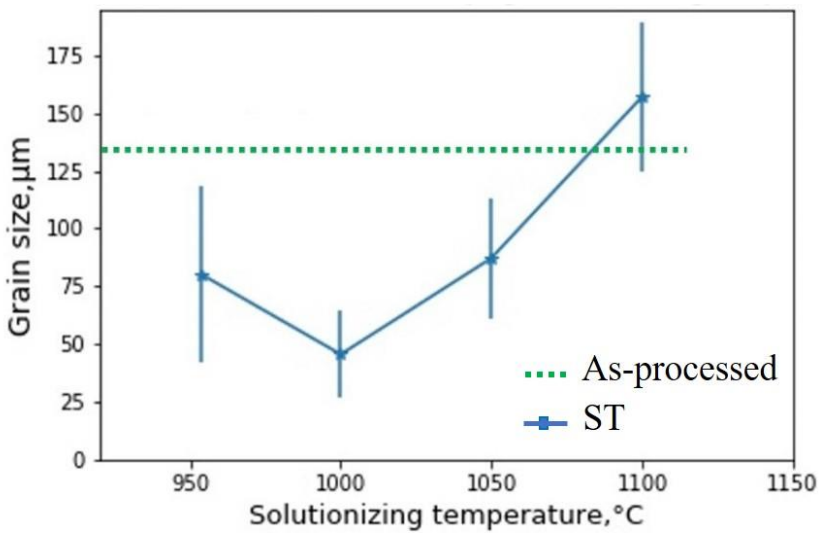

Figure 6-1: Grain size of as-processed and solutionized samples.

At lower temperatures, when recrystallization is incomplete, the recrystallized γ-phase grain size would be expected to be small compared to the already existing/unrecrystallized grains. The smaller γ grains in the sample subjected to the solution treatment at 954 °C; see Figure 5-8a, would be expected to be the recrystallized grains, while the larger grains may correspond to the grains which have yet to undergo the recrystallization. At 1000 °C, it is expected that more recrystallization would have occurred in the same amount of time. Thus, knowing that the average γ-phase grain size is a weighted average of all the grains in a microstructure, it is possible that the unrecrystallized grains in the 954 °C ST sample were responsible for the larger average grain size along with the higher standard deviation (SD) compared to that for the 1000 °C ST sample, refer Figure 5-8. The misorientation inside a grain, see the color gradients in the grains in Figure 5-2b and Figure 5-2d, was due to deformation history during processing. The solutionizing is expected to have induced some recovery and, therefore, changed this misorientation distribution. The average misorientations within the grains after the 954 °C solutionizing were similar to that for the as-processed sample (~10°), whereas in the case of 1000 °C, 1050 °C, and 1100 °C ST samples,

the maximum misorientations were 1.2°, 1.2°, and 1.0° respectively; see Figure 5-9. Hence, it is suggested that solutionizing at 1000 °C or higher resulted in complete recrystallization of the sample, whereas the solutionizing at 954 °C for 1 hr was not sufficient for complete recrystallization of this alloy.

6.1.3 γ' and δ Phase

The solutionizing temperatures chosen were close to the γ' solvus temperature (963 °C), and they were expected to dissolve the γ' precipitates (Srinivasan et al., 2012; Xie, Xu, et al., 2005). The SE-SEM images of the as-processed sample revealed that the γ' phase precipitates could be represented by an unimodal distribution with an average size of approximately 50 nm; see Figure 5-3b. The grain boundary δ phase was ~ 1 μm in diameter; see Figure 5-3a. TEM characterization revealed the finer γ' precipitates of ~ 11 nm as well as the larger (~50 nm) precipitates; see Figure 5-6a. After solutionizing at 954 °C, the growth of the δ phase inside the γ matrix grains and near their grain boundaries was noted (their average size was 2.5 μm); see Figure 5-10a. Incomplete dissolution of the γ' phase was also noted; see Figure 5-10b. The δ phase, which acts like a reinforcing precipitate in the γ-phase matrix, is beneficial for mechanical strength as it pins grain boundaries and dislocations (E. T. McDevitt & Bentley, 2009). However, it can be detrimental if it exists in excess (K. A. Unocic, Hayes, Mills, & Daehn, 2010). Figure 5-10b shows the evolution of the PFZ (or γ' depleted zone) during the growth of the δ phase. This phenomenon is commonly observed in various precipitation-strengthened alloys such as Ni-based superalloys, Al-based alloys, and Ti-based alloys (Russell & Lee, 2005; Sundararaman et al., 1997). Unlike that at 954 °C, the solutionizing at 1000 °C led to complete dissolution of the γ' phase and some dissolution of the δ phase; see Figure 5-11a. The δ phase was located preferentially at boundaries, and its volume percent was lower than that found for the 954 °C ST sample. The δ phase size range was

0.3-1.2 μm (~0.68 μm). Increasing the solutionizing temperature by 50 °C (i.e. 1050 °C) led to more extensive dissolution of the δ phase and complete dissolution of the γ' phase; see Figure 5-11b. The average δ size was 0.33 μm. The highest solutionizing temperature, 1100 °C, resulted in the complete dissolution of both the δ and the γ' phases; see Figure 5-11c. It is well understood that the grain boundary phases, such as δ and the carbides-rich phases, help to pin the movement of the boundaries at high-temperature and hence the absence of the δ phase at the grain boundaries led to significant γ-phase grain growth during the solutionizing at 1050 °C and 1100 °C; see Figure 6-1. The temperatures used for the two-step SA after solutionizing were below the δ phase solvus temperature (1000 °C), therefore, no apparent effect was observed on the δ phase during this 16 h aging time.

As the precipitate phases (γ' and δ) caused changes in the microhardness of the alloy, the HV values were consistent with the microstructural observations. The microhardness of the solutionized samples decreased with increasing solutionizing temperature; see Figure 6-2. The average hardness after 954 °C ST (229 ± 37 HV) was the highest among all the ST samples. Due to incomplete dissolution of the γ' precipitates and the growth of the δ phase in the 954 °C ST sample, the hardness value appeared to be significantly higher than that for the other ST samples; see Figure 6-2.

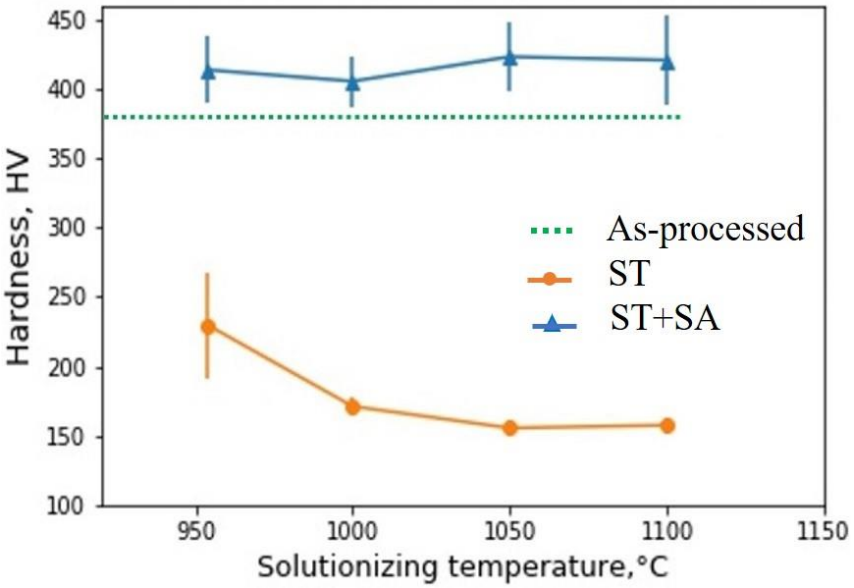

Figure 6-2: The average Vickers hardness after the different heat treatments.

The two-step aging treatment, with controlled cooling, helps in stabilizing metal carbides and in evolving bimodal γ' precipitates in Ni-base superalloys (Lech et al., 2019; Shercliff & Castillo, 1997). Therefore, a bimodal distribution of the γ' phase was expected after the standard two-step aging treatment (788 °C/8 h FC to 704 °C/8 h) on the ST samples. However, a uniform distribution of the γ' phase was observed in all the ST-plus-SA samples. The reasoning behind this could be explained with respect to the cooling rate between the two steps of aging. The cooling rate plays a major role in the final size and distribution of the γ' phase precipitates (Masoumi et al., 2016; Schirra, Reynolds, Huron, Bain, & Mourer, 2004). In the present work, samples were FC, and the furnace provided a slower cooling (22 °C/min) compared with the recommended cooling rate of 56 °C/min (E. McDevitt, 2011). The effect of the γ' precipitates on the hardness of the alloy is illustrated in Figure 6-2. Subsequent aging of the ST samples resulted in an increase in the average hardness value, which was greater than that of the as-processed alloy.

A γ' precipitate size distribution graph for the as-processed and aged samples is provided in Figure 5-15. The γ' precipitate size measurements used in this plot were based on SE-SEM micrographs.

In the case of the 954 °C ST sample, some spherical γ' precipitates remained undissolved, as seen in Figure 5-10b. These residual precipitates had an average size of approximately 62 nm, which was similar to the size of the as-processed γ' precipitates (around 57 nm). Following the aging treatment, new γ' precipitates nucleated, measuring approximately 40 nm in size, and the existing γ' precipitates grew, reaching sizes of up to 110 nm; see Figure 5-14a. Hence, the 954 °C ST-plus-SA sample resulted in a bimodal distribution of the γ' precipitates; see Figure 5-15. The other three heat treatments, 1000 °C ST-plus-SA, 1050 °C ST-plus-SA, and 1100 °C ST-plus-SA, exhibited an unimodal γ' precipitate size distribution. Irrespective of their solutionizing temperature, all the samples exhibited γ' precipitates in the range of 30-40 nm. Hence, it is essential to control parameters such as aging temperature, time, and cooling rate to achieve a desired γ' precipitate size distribution, and this will be further discussed in the following section. Based on the results obtained from the ST sample concerning γ matrix grain size, γ' precipitate phase and the δ dissolution, and extent of recrystallization, the ST at 1000 °C for 1 hr was selected for further investigation in this dissertation work.

6.2 AGED ALLOY: DEVELOPMENT OF THE BIMODAL γ' PRECIPITATE SIZE DISTRIBUTION

In this section, the results of the ST-plus-aged microstructures presented in section 5.2 are discussed. The section is divided into two major sub-sections focusing on the development of unimodal and bimodal γ' precipitate size distributions.

This section highlights the effect of various aging parameters, such as temperature, time, and cooling rate, on the resulting unimodal γ' precipitate size distribution microstructures. It also discusses the chemical compositional change in the unimodal samples. The findings from the study involving the unimodal distributions were used as the basis to explain the development of the

bimodal distribution microstructures. It also discusses the basis used for confirming the presence of the γ' precipitate phase only observed in this dissertation work.

6.2.1 Unimodal size distribution

The samples aged at 720 °C exhibited smaller average γ' sizes (14-15 nm) than those aged at 900 °C (42-55 nm). They also exhibited higher number densities. This is expected as larger undercooling at lower aging temperatures is expected to result in a larger number of nuclei (Porter et al., 2009; Torster et al., 1997). The average γ' precipitate size was smaller due to less diffusional growth at this lower temperature. The measured average γ' precipitate size of all the single-step aged samples is depicted in Figure 6-3. In the case of aging at 900 °C for 2 hr, the AC sample (sample F) exhibited a larger average precipitate size (55 ± 13 nm) compared to the WQ sample (sample G, 48 ± 7 nm). In Figure 6-4, the size distribution for sample F was broader than that for sample G, as indicated by the higher SD in Figure 6-3 for sample F. The value of the ratio of the SD to the average precipitate size for sample F and sample G was 0.24 and 0.18, respectively. This could be explained by further precipitate growth during AC compared with WQ at the end of soaking of 900 °C for 2 hr. At lower undercooling (higher temperature), the γ' precipitates experienced accelerated growth (rapid coarsening). Consequently, during the slow cooling (AC), wherein the sample remained at an elevated temperature for a period of time, precipitate growth continued (Porter et al., 2009; Sarosi et al., 2007). Conversely, rapid cooling (WQ) stopped diffusion of the solute atoms, halting the precipitate growth leading to a smaller mean size and narrower distribution range of γ' precipitates (quantified in Figure 6-4). No distribution plot was generated for the 720 °C for 10 hr aged samples due to image resolution limitations.

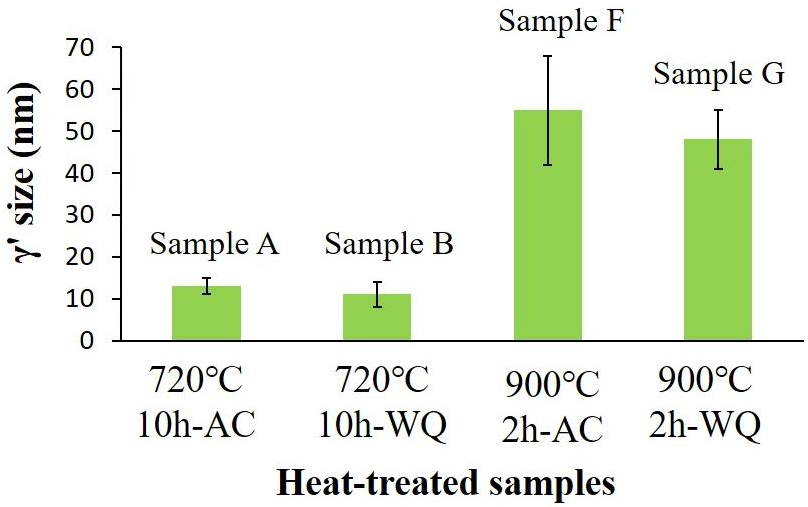

Figure 6-3: A comparative plot for γ' precipitate size as a function of the heat-treatment schedule for the samples that underwent single-step aging. The error bars indicate the SD.

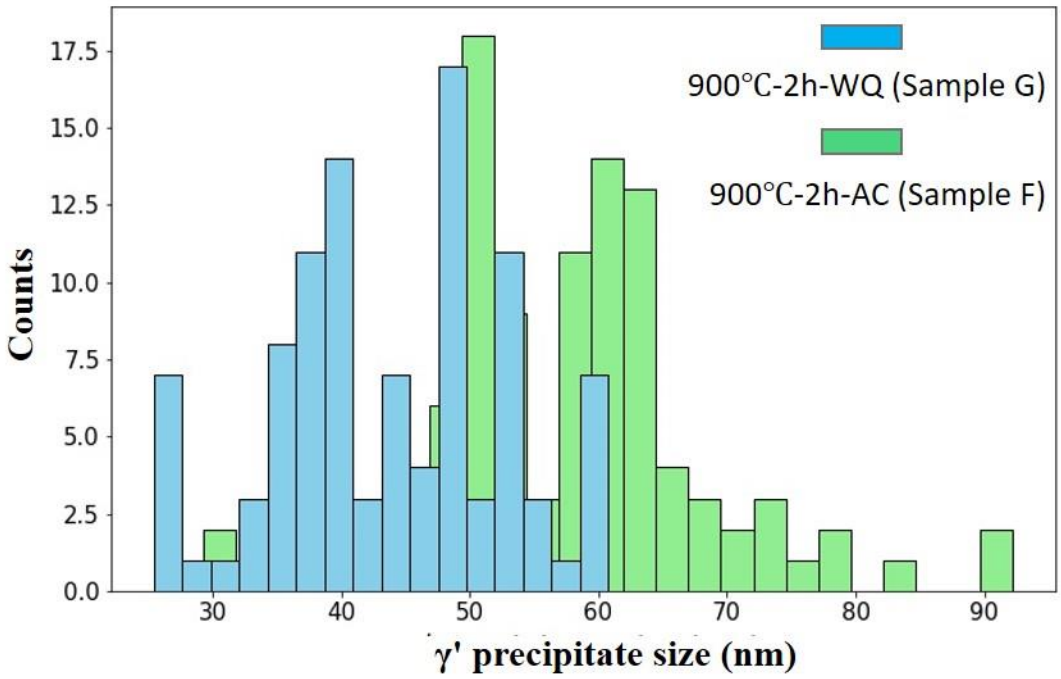

Figure 6-4: Histogram depicting the γ' PSD for sample F (900°C-2h-AC) and sample G (900°C-2h-WQ) showing the prevention of the continuous growth of the γ' precipitates after WQ.

Referring to the hardness plot in Figure 5-33, it is evident that the samples with a unimodal microstructure (single-step aged samples) featuring smaller average γ' precipitate sizes (samples A and B) displayed higher hardness levels (357-364 HV) compared to the samples with a larger

average γ' precipitate size (samples F and G), which showed hardness values of 296-305 HV. Samples (K-M, O) aged with two-step aging resulted in comparatively higher hardness (419-453 HV) than the single-step aged samples, refer to Figure 5-33. This could be attributed to the higher volume percent of the γ' precipitates due to the longer aging exposure during the two-step aging (R C Reed & C.M.F.Rae, 2014; Russell & Lee, 2005).

Evaluation of the solute elements responsible for the γ' precipitate phase formation was performed to better understand the PFZ formation and the γ' precipitation behavior during the second step of aging at 720°C. Hence, the average Al, Ti, Nb, and Ni contents were calculated within the PFZ area and the matrix region between the γ' precipitates for sample G (900°C-2h WQ) (Table 5-6). As evident from Table 5-3, enhanced growth of the δ phase occurred for the samples aged at 900°C (e.g. sample F, sample G) compared to the ST sample. The δ phase (Ni_3Nb, composition) was enriched in Al and Ti, while it was also relatively high in Nb and Ni (Table 5-6). This suggests that the typical γ'-forming elements, especially Al, influenced the growth of the δ phase. The depletion of these elements in the region close to the δ phase would not favor the formation of the γ′ precipitates, hence, this resulted in the formation of the PFZ region around the δ phase. (Löhnert & Pyczak, 2010).

6.2.2 Bimodal distribution

Important parameters that influence the nucleation of the γ' precipitates include the solute concentration in the matrix, diffusion fields of adjacent precipitates, and the extent of undercooling (Porter et al., 2009). Different cooling rates affect these parameters and, therefore, influence the nucleation. AC (i.e., Sample F) provided more time for diffusion compared with WQ (i.e., sample G). Consequently, this facilitated more growth of the γ′ precipitates (compare Figure 5-19 and Figure 5-20) and led to the variation in the solute element (mainly Nb, Al) concentration within

the PFZ and the matrix regions. The morphology of the γ′ precipitates in the continuously cooled sample J, which was furnace cooled from 900 ℃ to 720 ℃, was similar to sample F in that both were slow cooled. In the case of sample J, it is expected that the solute elements in the matrix region would experience accelerated diffusion during cooling. This accelerated diffusion would contribute to the growth of γ' precipitates, leading to the reduction in the concentration of the γ′-forming solutes in the matrix. This decreased solute concentration may not have inhibited fresh nucleation to occur at the beginning of the second step of aging at 720 °C (sample J). However, the Al solute concentration (Table 5-6) in the PFZ (region near the δ phase, 3.8 at. %) was more comparable to that in the matrix locations between the γ′ precipitates (2.7 at. %), and such concentrations appear to be sufficient for the second burst of nucleation (finer γ′ precipitates) in the region near the δ phase (Figure 5-24, Figure 5-25, and Figure 5-26). Therefore, during the second aging step at 720 ℃ – representing the maximum undercooling at a lower temperature and consequently conducive to more nucleation than growth– a second burst of nucleation (yielding finer γ' precipitates) was preferred over the growth of the existing γ' precipitates. This was evident predominantly within the region close to the δ phase, as demonstrated in Figure 5-24. Hence, the continuous cooling two-step aging resulted in the growth of primary γ′ precipitates throughout the matrix and a non-uniform distribution of secondary γ′ precipitates around the δ phase.

In the case of sample O (900 ℃-2 h WQ + 720 ℃-10 h WQ), the concentration of the γ′-forming solute elements in the matrix would be similar at the end of the first aging step at 900 ℃ as at the start of the second aging step at 720 ℃ as limited diffusion occurred during WQ. A comparison of the γ'-forming solute elements in the matrix is provided in Figure 6-5 using the data from Table 5-6 and Table 5-7. Interrupted cooling after the first aging step (similar to sample G) led to a higher

solute concentration in the matrix (higher concentration of Al, Ti, and Nb in Figure 6-5) compared to that at the end of the second step of aging (sample O in Figure 6-5). This higher solute concentration may have been sufficient for the fresh nucleation of γ′ to take place in the matrix, including the region near the δ phase, during the second step of aging at 720 °C.

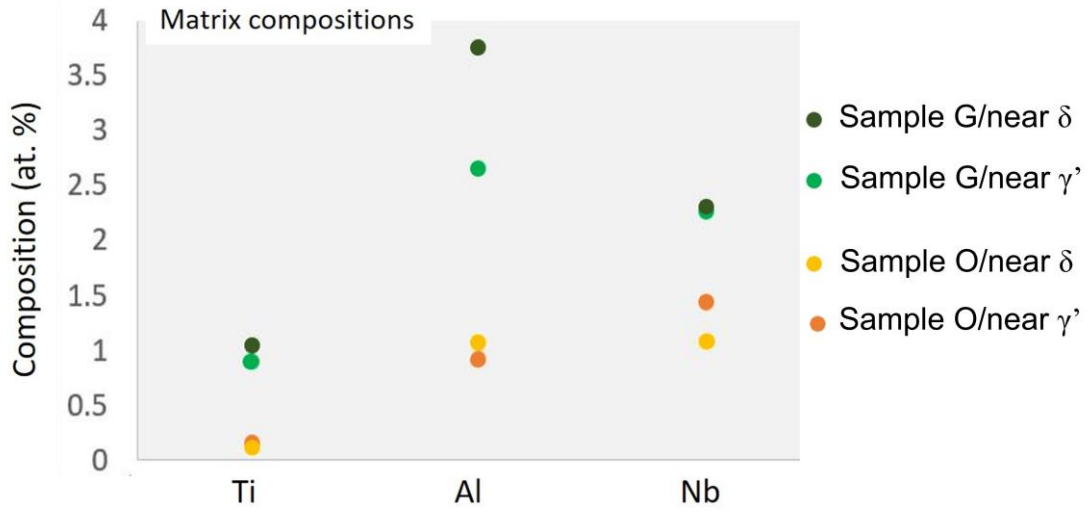

Figure 6-5: Chemical compositions (at. %) of the matrix regions for sample G (900 ℃-2 h-WQ) and O (900 ℃-2 h-WQ plus 720 ℃-10 h-WQ).

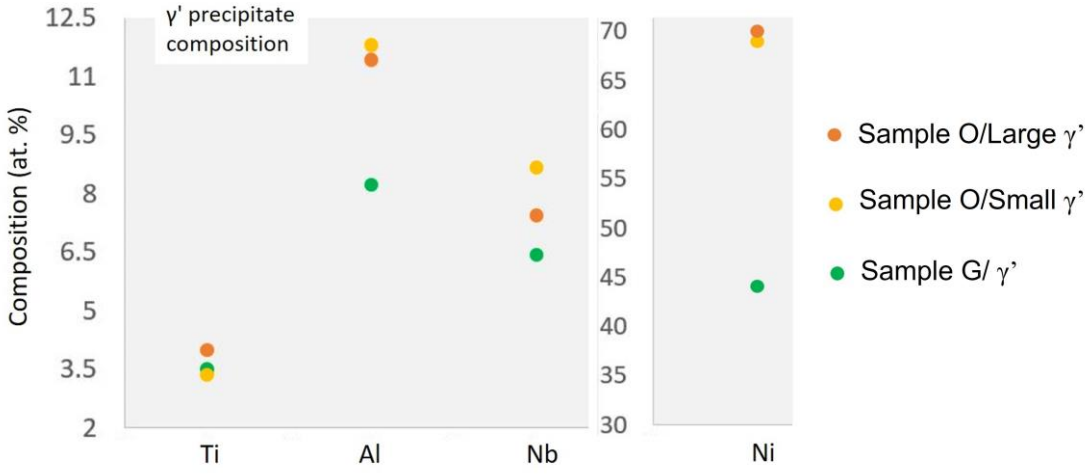

Figure 6-6: Chemical compositions (at. %) of the γ' precipitates for sample G (900 ℃-2 h-WQ) and O (900 ℃-2 h-WQ plus 720 ℃-10 h-WQ).

Comparing the compositions of the γ' precipitates (Figure 6-6), it is evident that the interrupted cooled sample (sample G) resulted in a non-equilibrium composition of γ' (i.e. low amount of Al) compared to the γ' precipitates at the end of the second step of aging (sample O) (Radis et al., 2009; Singh et al., 2011). This supersaturation in the matrix and the non-equilibrium composition of the γ' precipitate provided the driving force during the second step of aging for both fresh nucleation of γ' precipitates as well as the growth of the existing γ' precipitates. Therefore, the interrupted cooling two-step aged sample resulted in the generation of a microstructure having a bimodal size distribution of γ′ precipitates, where larger γ′ precipitate sizes formed at 900 °C and a finer γ′ precipitate sizes formed at 720 °C in the area between the larger γ′ precipitates and the matrix regions near the δ phase.

6.2.3 γ'' precipitate present or absent?

The absence γ″ precipitate was evidently absent in the SEM images of precipitates in Figure 5-27, as well as from DF-TEM images in Figure 5-32a, and [001] zone axis diffraction patterns (Figure 5-32b). Although, the previous reports have shown the co-precipitation of the γ" alongside the γ′ precipitate, but we did not observe any such evidence (Jeniski Jr. & Kennedy, 2006; K. A. Unocic et al., 2010).

In the context of the diffraction pattern in the [001] zone axis, the presence of superlattice reflections corresponding to all three variants becomes apparent when both the γ' and γ" phases coexist (Mignanelli et al., 2017; K. A. Unocic et al., 2010). Some superlattice reflections, such as 100, 010, and 110 may overlap. However, unique superlattice spots corresponding to two variants of γ" (1 ½ 0 and ½ 1 0) distinctly appear in the [001] zone axis (Sundararaman et al., 1988) and the superlattice spots corresponding to the third variant (1 0 ½) coincides with 110 of the γ' phase In most other zone axes, like [110] and [111], superlattice spots overlap, originating from both the

γ' and γ'' phases. In the [112] zone axis, distinct superlattice spots emerge from the γ'' precipitate, albeit from only one variant. This is why the [001] zone axis was chosen to identify the presence or absence of γ'' phase. Since γ'' phase typically exhibits an ellipsoidal morphology compared to the spherical morphology of γ' precipitates, they can be easily distinguished in SEM images. Additionally, γ'' precipitates exhibit higher contrast compared to γ' phases due to the higher concentration of the high atomic number element, Nb. Therefore, the presence of only spherical particles in all the heat-treated samples in this study clearly indicated the formation of γ' precipitates only.

Furthermore, regarding the solutes contributing to the formation of γ' and γ'', mainly Al, Ti, and Nb, our analysis has shown that Al and Nb concentrations are nearly equal in γ' phases. However the Nb concentration was found to be more than double that of Al in γ'' phase, as demonstrated in the work of Guo et al. using EDS analysis associated with TEM (Guo et al., 2022). Regarding the concentration of Ti, it is commonly found to be the lowest among these three elements (Bagot et al., 2017; Guo et al., 2022). As illustrated in Figure 6-6, the Ti concentration was observed to be the lowest in both the sizes of the γ' precipitates (sample O and G), regardless of the measurement technique used (STEM-EDS or APT). Therefore, based on this discussion, we can safely conclude that only γ' phase has precipitated in the alloy after the heat treatments conducted in this study.

6.3 TENSILE DEFORMED ALLOY: INVESTIGATION OF PRECIPITATE - DISLOCATION INTERACTIONS

In this section, the results of the aged-plus-tensile deformed alloys, presented in section 0, are discussed. The section is divided into two subsections. The first subsection focuses on the analysis of the dominant deformation mechanisms. The CRSS models are employed in this discussion to predict the deformation mechanism, which is compared with the deformation mechanism

suggested by the experimental observations based on microscopy data from the deformed samples. The second subsection discusses various strengthening models used to predict the YS in both the unimodal and bimodal microstructures. This section discusses the approach of modifying the existing models to successfully predict the YS in the bimodal microstructure.

6.3.1 Critical resolved shear stress: deformation mechanism

The shear strengthening contributions for τ_p were calculated using equation (2.5). The APB and Orowan looping effects were assessed in the unimodal microstructures using the respective precipitate volume percent in sample 900 and sample 720. Using equations (2.15), (2.16), (2.17), and (2.13), the CRSS for τ_{weak}, τ_{strong}, $\tau_{weak\text{-}strong\ modified}$, and $\tau_{orowan\text{-}modified}$ were determined as a function of particle radius R. The parameters chosen for the calculation are provided in Table 6-1. The contribution from τ_{coh}, $\tau_{mod,}$ and τ_{chem} computed for 718Plus in the existing literature has been used for the calculation [12, 24]. The most substantial strengthening was attributed to the coherency effect, amounting to approximately 50 MPa. The strengthening due to the modulus mismatch was computed to be around 10 MPa as the moduli of the γ matrix and γ' precipitates are relatively similar. The contribution from τ_{chem} was approximately 5 MPa. The total contribution was accounted for as per the equation (2.6).

In the case of sample 720 (Figure 6-7a), a transition from the weak-pair to the strong-pair coupling occurred at a precipitate radius of 26 nm (R_m), whereas the transition from the shearing to looping was observed at 23 nm (R_c). It is clear from Figure 6-7a that the predicted deformation mechanism is weak-pair interaction for the sample 720 microstructure, and the experimental observations in Figure 5-41 are consistent with this. This suggests that weak-pair shearing is the dominant deformation mechanism for microstructures containing low γ' volume percent (5.2 %) and fine PSDs. In contrast, for sample 900 (Figure 6-7b), the transition point was identified as 29 nm (R_m)

and 40 nm (R_c), signifying that an increase in the γ' precipitate volume percent shifts the R_m and R_c to a larger size. It is clear from Figure 6-7b that the strong-pair interaction is the dominant deformation mechanism for sample 900, and the experimental observations in Figure 5-42 are consistent with this. In addition to precipitate shearing by strong-pair coupling, looping around some dislocations was observed. This could be attributed to the wide range of precipitate sizes for sample 900 and/or deending on where the slip plane intersects the precipitates. This variation in the number density and size in different regions may have created suitable conditions for looping to occur.

The observation that the peak of the strengthening contribution at R_m is higher for the sample with 13% γ' precipitates compared to the sample with 5.2% γ' precipitates (166 MPa vs. 131 MPa) reinforces the concept that strengthening increases with an increase in the fraction of γ' precipitates (R C Reed & C.M.F.Rae, 2014). Figure 6-7 also illustrates the outcomes derived from the modified model, equation (2.17), proposed by Galindo-Nava et al., marked as "weak strong modified" (Galindo-Nava et al., 2015). This model demonstrates a smooth transition from the weak-pair to strong-pair coupling mechanisms. The curves align closely for strong-pair strengthening, which suggests that the modified model provides a good fit. However, it appears to overestimate the weak-pair strengthening compared to the classical weak-pair model.

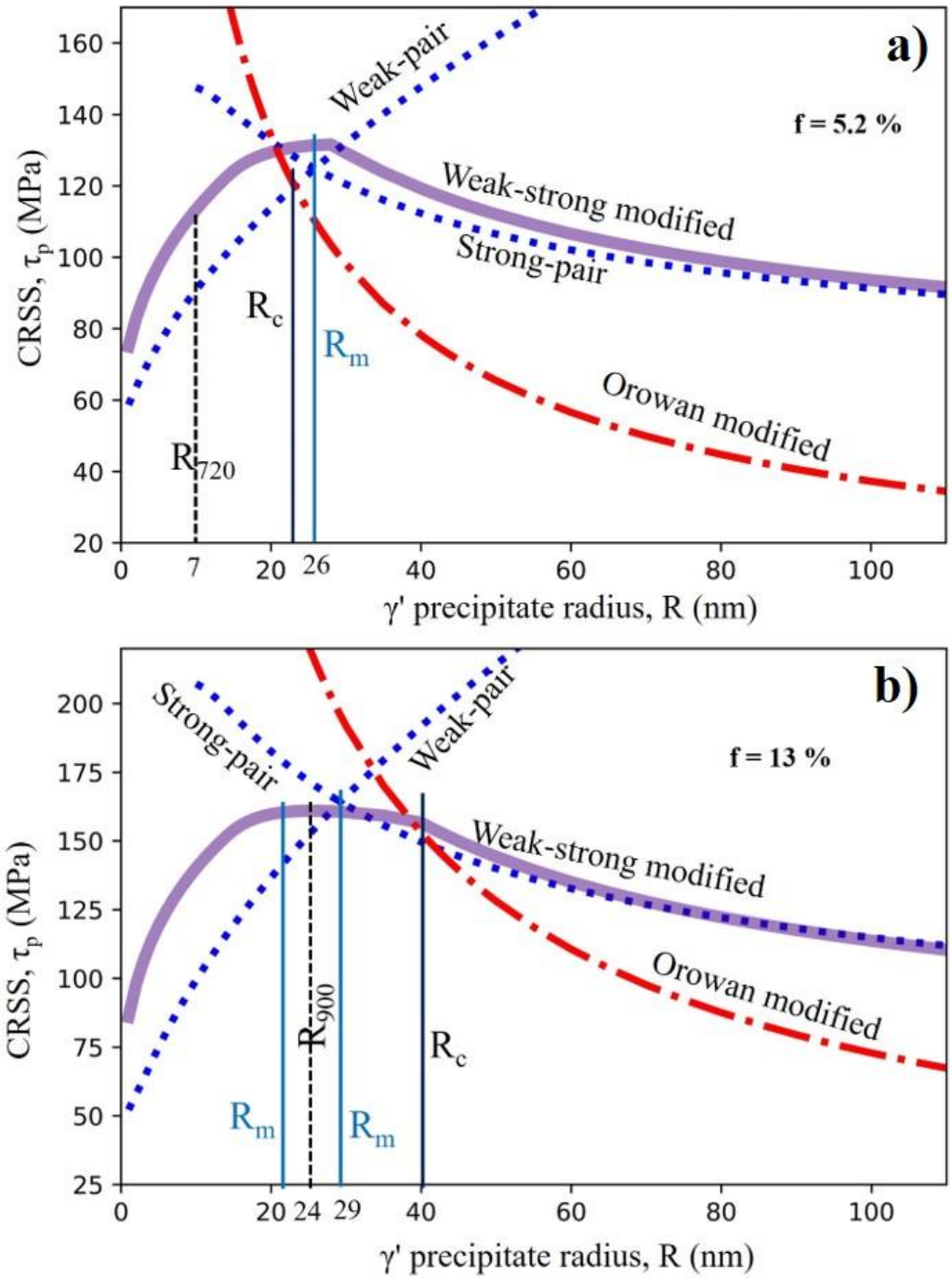

Figure 6-7: The CRSS as a function of the γ' precipitate radius for a) sample 720 and b) sample 900.

Table 6-1: The parameter values used for the YS calculations.

Parameters (unit)	**value**	**Reference**
γ_{APB} (J m^{-2})	0.17	(Fang et al., 2022)
b (nm)	0.25	(Galindo-Nava et al., 2015)
μ (GPa)	80	(Galindo-Nava et al., 2015)
k (MPa $\mu^{-1/2}$)	750	(Fang et al., 2022)
σ_i (MPa)	21.8	(Ahmadi et al., 2014)
M	3.06	(Eckhard Nembach & Neite, 1985)
ν	0.33	(Fang et al., 2022)

With respect to the precipitation strengthening contributions in the sample Bimodal, a similar CRSS versus R plot was generated with the total γ' precipitate volume percent set to 18 %; see Figure 6-8. R_m was found to be 31 nm and 20 nm from the classical shear models and modified shear model, respectively, while Rc was found to be 59 nm. Referring to the individual radii of the smaller (6 nm) and the larger (28 nm) γ' precipitates marked in Figure 6-8, the analysis suggests that shearing is the dominant mechanism for both precipitate sizes. The weighted average radius (R_{wa}) was calculated considering the number fractions w_s and w_l, where $R_{wa} = w_s \times R_s + w_l \times R_l$. The quantified number fraction measured for the larger (w_l) and smaller (w_s) γ' precipitates using equation 16 were 0.1 and 0.9, respectively, which resulted in a value of 9 nm for R_{wa}. The calculated R_{wa} predicts shearing as the dominant deformation mechanism. These predictions aligned with the experimental observations in Figure 5-43. However, the exact nature of the shearing mechanism (whether weak pair or strong pair) in the microstructure is not conclusive since there were hardly any pairs of dislocations observed in Figure 5-43. In summary, the

dominant deformation mechanisms predicted using the CRSS models for Ni-based superalloys were similar to the experimental observations in Figure 5-41, Figure 5-42, and Figure 5-43 for sample 720, sample 900, and sample Bimodal, respectively.

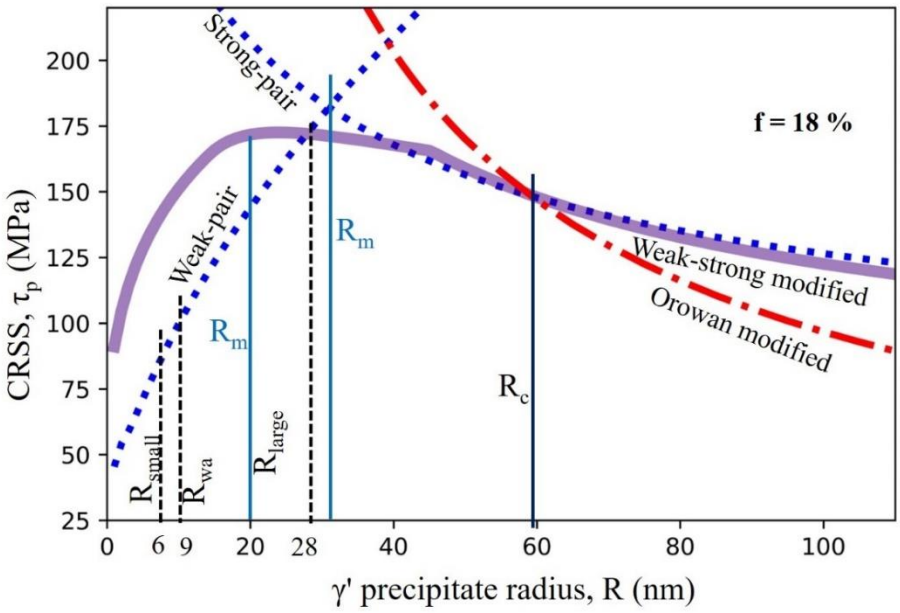

Figure 6-8: The effect of γ' precipitate radius on CRSS for sample Bimodal.

6.3.2 Yield Strength

The YS values were calculated according to the cumulative contributions from each strengthening mechanism per equation (2.2) using the values summarized in Table 6-1, and these values were compared with the experimental values presented in Table 5-10. The individual contributions in equation (2.2) for the YS calculation were as follows:

a) Grain boundary strengthening: The γ-phase matrix grain sizes for the ST and ST-plus-aged samples were found to be in the range of 22-24 μm (Table 5-8), indicating that the presence of the δ phase on the grain boundary suppressed the grain growth during the aging treatments (720-900 °C). The contribution from σ_{gb} was calculated to be 178 MPa with an average grain size of 23 μm using equation (2.3).

b) Solid solution strengthening: The σ_{ss} value was adopted from the research conducted by Ahmadi *et al*. on 718Plus following the equation (2.4) (Ahmadi et al., 2014). The contribution from various elements demonstrated their variability. The most significant contribution was attributed to Nb (around 200 MPa), while Co yielded the lowest contribution (around 12 MPa). This resulted in a combined contribution from elements such as Cr, Co, Nb, Al, Ti, Mo, Fe, and W summed up to 320 MPa prior to undergoing any aging treatment (Ahmadi et al., 2014). With aging, the solid solution strengthening contribution went down to 230 MPa for samples having γ' precipitate volume percentages of 10 % or higher. In this work, a solid solution strengthening contribution of 300, 260, and 250 MPa was assigned to sample 720, sample 900 and sample Bimodal based on their γ' precipitate volume percentage.

c) Precipitation strengthening: The σ_p was calculated by incorporating Taylor's orientation factor (M) into the calculated τ_p in section 6.3.1.

As shown in Figure 6-7, the precipitate shear strengthening was calculated from both the classical model and the modified model; hence, the corresponding total YS was calculated and compared in Table 6-2. The results were also compared with the experimental YS values in Table 6-2. For sample 720, the calculated and experimental YS (908 MPa) value demonstrated a deviation of 12 % (800 MPa) and 20 % (730 MPa) for the modified and classical models, respectively. In the case of sample 900, the modified model's calculated YS value exhibited a deviation of 35 % (930 MPa) from the experimental YS (690 MPa). On the contrary, the classical model yielded a deviation of 30 % (894 MPa) from the experimental value.

Table 6-2: Comparison of the YS strengthening predicted by the various models with the experimental (Exp) YS for sample 720 and sample 900.

Strengthening (MPa)	σ_p classical	σ_p modified	σ_{oro}	σ_p classical	σ_y modified	σ_y (Exp)
Sample 720	82	105	285	730	800	908
Sample 900	149	161	228	894	930	690

To calculate the YS for the sample Bimodal, the following four different methods were incorporated, and values were compared.

Method 1: Using similar equations to those for the unimodal PSD for the classical and modified models (equation (2.15), (2.16), (2.17), and (2.13)), the calculations were performed considering f as 18 %. However, the precipitate radius used was the weighted radius (marked as R_{wa} in Figure 6-9). The determination of R_{wa} was previously outlined in section 6.3.1. The calculated YS from the conventional model was highly underestimated (453 MPa), whereas, from the modified model, it was found to be 879 MPa, which represented an underestimation of the experimental value (930 MPa) by 5 % only, shown as method 1 in Table 6-3.

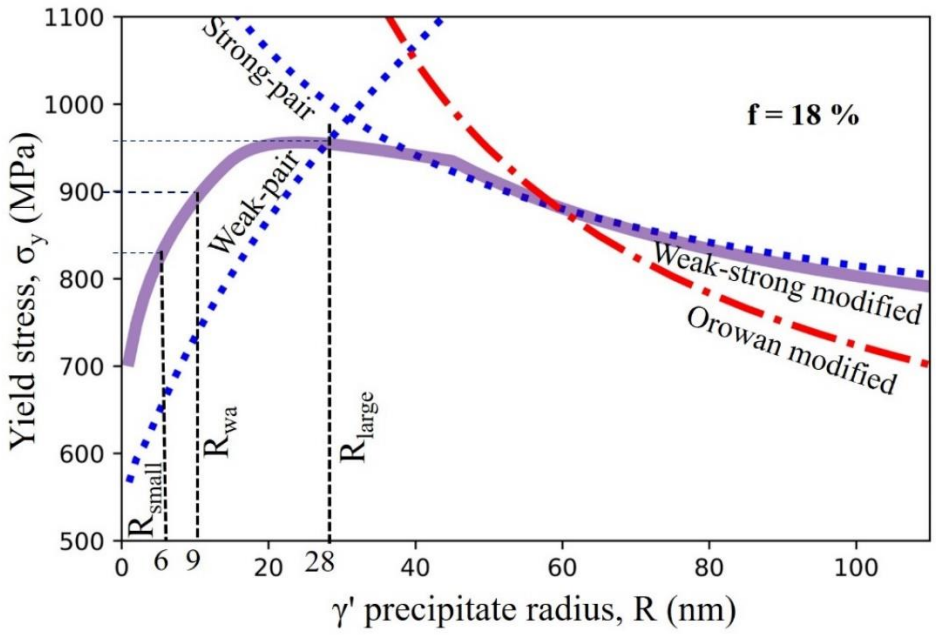

Figure 6-9: The effect of γ' precipitate radius on YS for sample Bimodal.

Method 2: Similar to method 1, the equations of the unimodal strengthening models (equation (2.15), (2.16), (2.17), and (2.13)) were applied. The contributions from the smaller precipitate (6 nm) were calculated, considering the individual volume percentage (5 % for f_s). Similarly, the values were calculated for the larger (28 nm) γ' precipitates considering the volume percent as 13 % for f_l. Subsequently, the final yield strength (YS) was calculated employing equation (2.17).

The calculated YS values for the smaller γ' precipitates, utilizing both the conventional model and the modified model, were found to be 670 MPa and 739 MPa, respectively. In parallel, for the larger γ' precipitates, the calculated YS was determined as 937 MPa using the conventional model and 920 MPa using the modified model, as delineated in Table 6-3. Consequently, the calculated YS value for the larger γ' precipitates surpassed that of the smaller γ' precipitates. As reported in the literature, the smaller (or the tertiary) γ' precipitates exert a more pronounced influence on YS, which aligns with our observation ((Galindo-Nava et al., 2015; Goodfellow, 2018). However, the

magnitude was underestimated by 20 % compared to the experimental value of 930 MPa (refer to Table 6-3).

Table 6-3: Comparison of the YS strengthening predicted by the various models with the experimental (Exp) YS for sample Bimodal.

Methods	**Approach**	**σ_p (modified)**	**σ_y (modified)**	**σ_y (Exp)**
Method 1:	Weighted R with total vol. percent (18 %)	453	879	
Method 2:	Smaller γ' size with individual vol. percent (5 %)	670	738	930
	Larger γ' size with individual vol. percent (13 %)	937	920	
Method 3:	Fractional contribution with individual vol. percent	548	979	

Method 3: Equation (2.21) for the modified models proposed by Galindo-Nava *et al.* for the multimodal distribution was used (Galindo-Nava et al., 2015). Equation (2.8) was employed to calculate the value of L. However, it's important to note that we incorporated individual volume percent for both the smaller (f_s) and larger (f_l) γ' precipitates, with values of 5 % and 13 %, respectively. This approach allowed us to calculate the values of L for the smaller (L_s) and larger (L_l) γ' precipitates, as defined in Equation (6.1a).

$$L_s = \left(\frac{2\pi}{3f_s}\right)^{1/2} R_s \qquad (6.1a)$$

$$L_l = \left(\frac{2\pi}{3f_l}\right)^{1/2} R_l \qquad (6.1b)$$

Similarly, for the calculation of l_1, equation (2.19a) was employed. The value of l_1^s was taken as $2R_s$, as R_s was smaller than the calculated R_m (14 nm), and l_1^l was determined as $2(R_l^2 - (R_l - R_m)^2)^{1/2}$, given that R_l was larger than R_m. When these values were incorporated into equation (2.21), it yielded an APB strengthening of 548 MPa and a yield strength (YS) of 979 MPa, as shown in Table 6-3. This result overestimated the experimental YS of 930 by only 5 %.

The variation in the predicted YS values could be due to the fact that the precipitate composition was assumed to be that of the equilibrium composition. For shorter aging times, the precipitate composition is different from that of the equilibrium value, and hence the concentration of solutes in the matrix could be quite different, and this could ultimately affect the solid solution strengthening (Goodfellow et al., 2018). This could be responsible for the large deviation (up to 35 %) in the YS value for sample 720 and sample 900, as they were underaged. It is likely that in the case of sample Bimodal, which experienced two-step ageing, sufficient time was available for the precipitate composition to achieve the equilibrium composition. Hence, the YS was predicted with the minimum deviation (5 %) using methods 1 and 3 considering weighted radius and the individual volume percentages of the smaller and the larger γ' precipitates, respectively. In conclusion, the inter-particle spacing emerged as a paramount factor in the calculation of CRSS. Instead of particle size, inter-particle spacing can effectively be employed as the X-axis in CRSS plots for varying volume fractions. Each volume fraction exhibits a critical inter-particle spacing where the deformation mechanism transitions from weak-pair shearing to strong-pair shearing and further to looping. This suggests a means to optimize the YS by controlling the volume percent of smaller and larger γ' precipitates and their sizes, and therefore, identify the inter-particle spacings.

6.3.3 Further exploration: change in volume percent

As mentioned in 4.4.6, the volume percent of the bimodal sample was assumed as the sum of the two of the results of the high-temperature (900C) and low-temperature (721C) single-step aging treatments. This assumption has not been experimentally verified in this work due to the limitation of resolving finer γ' precipitates. As evident in the compositional analysis results presented in 5.2.4, the solute concentration or supersaturation changes after the first step of aging at higher temperature (900 ℃). Hence, the second step of aging at lower temperature (720 ℃) might not produce the same volume percent of γ' precipitates as that precipitated at the end of single-step aging at 720 ℃. The variation in the precipitate volume percent impacts the deformation mechanism. An exploratory calculation was conducted to find the range of volume percents that could alter the expected dominant deformation mechanism. The modifed model (weak-strong pair) for shearing and modifed-Orowan looping plots have been presented and compared for a range of γ' precipitate volume percents. As per the literature, 20% is the maximum γ' precipitate volume percent in this alloy (E. McDevitt, 2011). Hence, a range of 12-20% has been used for the calculation presented in Figure 6-10. The critical radius required for the changing the mechanism from shearing to looping (R_c) increased from 36 nm to 68 nm for 12 % to 20 % volume percent precipitate, see Figure 6-10. This suggests that shearing is the preferred mechanism over looping for a fixed size (36-68nm) of the precipitate as the γ' precipitate volume percent increases. . This exercise suggests that changing the weighted avaerge radius can significantly change the deformation mechanism and hence, the mechanical properties. As presented in section 6.3.2,the consideration of the experimentally-obtained weighted average γ' precipitate radius allowed us to predict the deformation mechanism and the yield strength accurately. As indicated in Figure 6-10,

the consideration of the R_{wa} value (9 nm) resulted in shearing as the predicted dominant deformation mechanism irrespective of the change in volume percent.

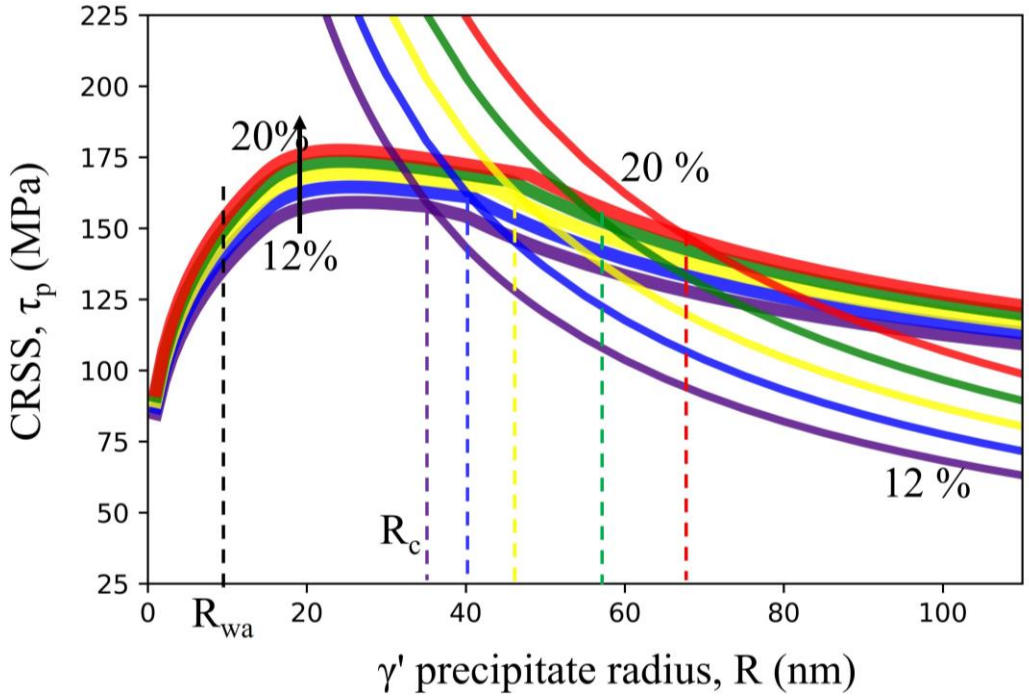

Figure 6-10: The effect of γ' precipitate volume percent (12-20 %) on the critical radius for change from shearing to looping.

6.4 CREEP DEFORMED ALLOY: STABILITY OF γ' UNDER THERMAL AND STRESS APPLICATION

In this section, the results from the aged-plus-creep deformed microstructures and aged-plus-thermally exposed microstructures (see section 5.3.1) are discussed. The section is divided into three sub-sections.

The first section discusses the mechanical property data and the associated creep behavior. The second section discusses the microstructural details of the aged-plus-deformed alloys. The third section discusses the relationships between the applied creep stress and the microstructural changes.

6.4.1 Creep behavior and microstructure relation

The primary creep regime does not constitute a large portion of the creep life for γ' precipitate strengthened superalloys (Chen, Dong, Yao, Ni, & Wang, 2018; Hayes et al., 2015). This is consistent with the results presented in Figure 5-44. The creep behavior varies as a function of the deformation mechanisms and temperatures (R. R. Unocic et al., 2010). During the creep at the highest temperature investigated in this study (704 °C), tertiary creep dominated the creep lifetime. Conversely, at the lower temperature (680 °C), a clearer transition from the secondary creep regime to the tertiary creep regime is evident. Although this study does not dive deeply into the study of creep mechanisms, the research conducted by Unocic et al. on ATI 718Plus indicates that creep at lower temperatures (689 °C) involves the shearing of γ' precipitates by partial dislocations through a stacking fault mode. In contrast, for higher temperature creep (730 °C), micro-twins were observed, and their formation was facilitated by Shockley partial dislocations (R. R. Unocic et al., 2010).

The fractography of the failed sample suggested susceptibility to grain boundary cracking, resulting in brittle fractures. From Figure 5-45a and b, it is evident that the crack initiation occurred at the surface, and as this crack grew, it became exposed to hot air, causing it to turn blue. After the crack grew to a length where the materials' fracture toughness was reached, a rapid brittle fracture ensued, allowing minimal time for the fractured surface to be exposed, resulting in a yellow hue. This phenomenon of sample failure has also been observed by the group of Unocic ((K. A. Unocic et al., 2010). Their study demonstrated that samples with recrystallized or stress-free grains were more prone to intergranular cracking, whereas the presence of dislocation sub-structures resisted grain boundary cracking, although the exact mechanism remained uncertain. As shown in Figure 5-8b, the solution treatment of the sample prior to the aging resulted in a

recrystallized microstructure, thus favoring grain boundary cracking, as illustrated in Figure 5-45 and Figure 5-46. Additionally, the presence of the grain boundary δ phase likely assisted crack growth, leading to the development of multiple crack points along grain boundaries and triple junctions.

Other factors may have also contributed to the failure of the creep samples such as: a) the Heat-Affected Zone (HAZ) from Thermocouple Spot Welding: that generated a non-uniform microstructure in the gage area and could have favored the early failure of the test; b) Thermal Stress-Induced Bending: due to the thinness of the sample (0.7 mm) relative to its length (122 mm) may have caused to bending after WQ following ST. Although attempts were made to flatten the sample mechanically, non-uniform stress could have persisted and caused failure, particularly from the shoulder area. In conclusion, the crack initiation occurred at the sample surface, and the crack growth occurred along the grain boundaries.

6.4.2 Effect of stress and temperature on γ' precipitate growth

The exposure of the samples to elevated temperatures induced changes in the γ' precipitate microstructure, and this effect was further accentuated by the addition of stress in the creep-deformed sample. In the case of sample 20-53, which underwent both higher temperature (704 °C) and higher stress (650 MPa), the kinetics of microstructural changes were considerably accelerated compared to sample 20-56 (exposed to 680 °C and 550 MPa), leading to a more rapid deformation process and failure. Consequently, the exposure time for sample 20-53 was limited, resulting in comparatively less significant microstructural alterations compared to sample 20-56. Still, the changes are observable between the creep-deformed sample and the thermally-exposed sample. Referring to Figure 5-49, the creep-deformed sample exhibited a few elongated γ' precipitates perpendicular to the loading direction. This elongation was absent in the thermally-exposed

sample. Also, the creep-deformed sample had less amount of finer γ' precipitate compared to the thermally-exposed sample. Thus, the application of stress along with the high-temperature exposure caused an accelerated and directional growth of the γ' precipitate. Sample 20-56 clearly exhibited the effect of stress and temperature on the growth of the γ' precipitate. The finer γ' precipitate dissolved and the larger γ' precipitate grew, which ultimately changed the size distribution; see Figure 5-53. The dissolution of the finer γ' precipitate was more prominent in the creep-deformed sample (Figure 5-52a) compared to the thermally-exposed sample (Figure 5-52b). As the spherical γ' precipitates grow, the morphology tends to transform to a cuboidal shape to accommodate the increasing surface energy and strain (Hazotte, Racine, & Denis, 1996). The accelerated growth of γ' precipitates in the creep-deformed sample compared to the thermally-exposed sample is evident from the distinct morphological differences observed (Figure 5-52). The presence of near-cuboidal γ' precipitates in the creep-deformed sample suggests that the application of stress during creep significantly impacts the growth kinetics and morphology of the precipitates; see Figure 5-55. In contrast, the presence of spherical γ' precipitates in the thermally-exposed sample suggest that under those conditions, the growth kinetics may have been slower. The stress applied during creep deformation introduces additional driving forces and influences diffusion rates within the material, enabling faster growth of the precipitate (reference). The stress can also affect the strain distribution and the elastic field around the precipitates, influencing their growth direction and shape (reference).

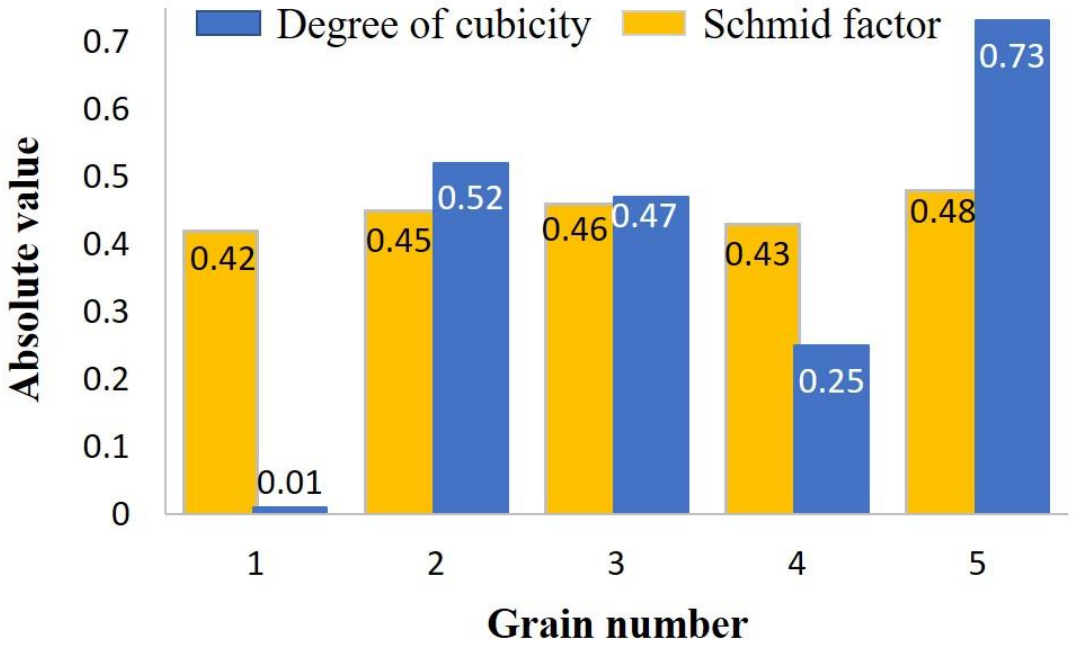

Figure 6-11: Histogram plot for comparing the Schmid factor values and degree of cubicity of the γ' precipitate for individual grains marked in Figures 5-54 – 5-56.

To assess the influence of applied stress in the creep-deformed sample, the growth of γ' precipitates was evaluated by measuring λ_c and CRSS on individual grains, as illustrated in Figure 5-54b. The determined value of λ_c was the highest (0.73) for the grain orientation near the [001] direction (grain 5), and the lowest value (~0) was observed for the orientations closer to the [111] direction (grain 1); see Table 5-12. To quantify the impact of stress, the CRSS was calculated for each grain. Notably, the highest CRSS value was associated with grain 5, while the lowest was attributed to grain 1. A comparison of λ_c and CRSS is depicted in Figure 6-11. These findings collectively affirm that the applied stress indeed played a role in expediating the γ' precipitate growth.

CHAPTER 7. SUMMARY AND CONCLUSIONS

A study on 718Plus was conducted to design and develop heat treatments for obtaining different γ' precipitate containing microstructures to co-relate these microstructures with the room-temperature tensile deformation behavior and also the elevated-temperature creep behavior.

- The importance of the solutionizing temperature to obtain the desired microstructures in 718Plus was studied. Solutionizing at 954 °C for 1 hr was not enough for both complete γ phase recrystallization and dissolution of the γ' precipitate. This also led to preferred growth of δ-phase precipitate volume percent throughout the γ phase matrix and at the boundaries. The γ' precipitate completely dissolved after each of the other three solution treatments (1000 °C, 1050 °C, and 1100 °C), while the dissolution of the δ-phase increased with increasing solutionizing temperature. However, the increase in solutionizing temperature also led to grain growth with the highest grain size value of 157 μm after solutionizing at 1100 °C. It is therefore suggested to heat at 1000 °C to avoid excessive δ-phase formation and minimzing grain growth during solutionizing. The solutionizing temperature did not significantly affect the hardness values of the aged samples.
- The influence of cooling rates such as WQ, AC, and FC on the evolution of the γ' precipitate microstructures was studied. Aging treatments in the temperature range of 720-930 °C were performed via single-step aging and two-step aging. ST samples followed by single-step aging resulted in unimodal γ' size distributions in both the AC and WQ cooled samples. Samples aged at 900°C resulted in larger average γ' precipitate sizes (42-55 nm), growth of the δ phase, and a PFZ surrounding the δ phase, whereas aging at 720°C resulted in smaller average γ' precipitate sizes (11-14 nm) with little-to-no growth of the δ phase, and no PFZ surrounding the δ phase.

- For the same aging temperature (900°C) and time (2 hr), the slower cooling (AC) resulted in a larger average γ' precipitate size (55 ± 13 nm) than that for the WQ sample (42 ± 7 nm). The cooling rates impacted the supersaturation of the solute elements in the matrix, which further influenced the size and distribution of the γ' precipitates during aging.
- The continuously cooled two-step aged sample exhibited a non-uniform distribution of the finer γ' precipitates, which were primarily observed near the δ phase due to the extended growth of the larger γ' precipitates during the slow cooling between the two steps of aging. The two-step aged samples with interrupted cooling generated a uniform distribution of the finer γ' precipitates in the matrix region between larger γ' precipitates and near the δ phase due to sufficient supersaturation of the γ'-forming solute elements. Overall, the two-step aged samples with interrupted cooling resulted in a bimodal size distribution of the γ' precipitates.
- The influence of unimodal and bimodal PSDs on the strengthening and deformation mechanisms during RT tensile deformation was studied. For the unimodal microstructures having γ' precipitate radii of 24 nm and 7 nm, shearing was found to be the dominant mechanism. The weak-pair shearing was preferred for the microstructure containing the smaller precipitates (sample 720), whereas the microstructure containing the larger precipitates (sample 900) exhibited both strong-pair shearing and some looping.
- For the bimodal PSD microstructure, featuring average radii of 28 nm and 6 nm, the adoption of a weighted radius of 9 nm within the models predicted shearing as the dominant mechanism, which was consistent with the experimental observations. The elevated number density of γ' precipitates in the bimodal microstructure led to reduced inter-particle spacing, driving shearing to prevail as the dominant deformation mechanism. The

incorporation of the weighted radius and individual volume percent of the smaller and the larger γ' precipitates allowed for better YS prediction with only a deviation of 5 % from the experimentally measured YS value.

- The effect of tensile stress and thermal exposure on the evolution of the γ' precipitates was studied. The creep-deformed sample, which experienced both tensile stress and thermal exposure, exhibited accelerated growth of the γ' precipitates compared to the sample which underwent only thermal exposure, and the creep sample exhibited near cuboidal precipitates while the thermally-exposed samples exhibited spherical γ' precipitates.
- The degree of cubicity of the γ' precipitates in the creep-deformed sample was highest (0.73) near the (001) plane and lowest (~0) near the (111) plane. The accelerated growth was co-related with the applied stress as the CRSS values were the highest (0.48) for the (001) plane and the lowest (0.42) for the (111) plane. These findings collectively affirm that the applied stress indeed played a role in accelerating the growth of the γ' precipitates.

CHAPTER 8. FUTURE WORK SCOPE

The results and analyses presented in Chapters 5 and 6 have provided substantial answers to the unanswered questions surrounding the microstructure-properties-correlation of bimodal γ' precipitate microstructures. However, they have also unveiled intriguing areas of interest and potential avenues for further exploration, which are listed below:

- ***3-D geometrical characterizations**:* Since the particle volume fraction and inter-particle spacings greatly influence the dominantdeformation mechanism, it is important to accurately measure and incorporated this data into the modelling and microstructure-property-relationship. Careful TEM characterization with the known foil thickness would provide a better precipitate volume fraction measurement. These are some of the teqchniuqes that could be ultized for the foil thickness measurement of a TEM sample:
  a) Electron energy loss spectroscopy (EELS) method by getting the low loss spectrum: the intensity ratio between the plasma peak and the zero loss spectrum can provide the foil thickness information.
  b) TheKossel-Möllenstedt (K-M) fringe under two-beam condition can be used for the calculation of the foil thickness.
  c) Focussing the electron beam to the maximum at the point of interest and then changing the tilt angle for imaging could help to identify the geometry or the foil thickness.
  d) Monte-Carlo simulationto measure the penetration depth of the scanning electron beam could be used to estimate the detection volume used in the calculation of the precipitate fraction.
- ***Optimization of Bimodal γ' Precipitate Size Microstructure***: Building upon the insights grained from this work, a promising research focus lies in the optimization of bimodal γ'

precipitate microstructures. Leveraging the temperature, time, and cooling rate information expounded upon in Section 5.2, researchers can endeavor to precisely control the ratio between smaller and larger γ' precipitates. It was also observed that the smaller γ' precipitates were unstable and dissolved in the initial phase of the creep testing. It would be crucial to investigate and develop a more stable bimodal γ' precipitate microstructure. This optimization holds the potential to impart distinct mechanical properties.

- ***Development of Computational Strengthening Models***: The findings and analyses concerning bimodal γ' PSD presented in this dissertation pave the way for the development of computational models. These models can be developed to predict the deformation mechanisms and the YS featuring multimodal PSD. By harnessing the empirical data presented here, researchers can endeavor to create robust computational tools that enhance our understanding of material behavior.
- ***Optimization of Creep Properties:*** The consistent occurrence of intergranular mode fractures in creep samples, both in the existing literature and within the scope of this dissertation, presents an opportunity. Future research can concentrate on the optimization of creep properties in the context of 718Plus. By comprehensively investigating the mechanisms underlying these fractures, it is possible to enhance the material's performance under high-temperature, long-duration loading conditions.
- ***Exploration of Grain Boundary δ Phase***: The exact mechanisms of failure if induced by the presence of the grain boundary δ phase remain unanswered, particularly during high-temperature deformation.
- ***Machine Learning for Precipitate Volume Percent Measurement***: Researchers working in the area of γ' strengthened superalloys often grapple with the challenge of accurately

measuring the volume percent of fine γ' precipitates (< 10 nm). Potential value addition to this research community lies in the development of efficient machine learning models. These models can streamline the process of volume measurement, offering researchers a robust tool for precise characterization.

BIBLIOGRAPHY

Ahmadi, M. R., **Povoden-Karadeniz, E.**, **Whitmore, L.**, **Stockinger, M.**, **Falahati, A.**, & **Kozeschnik, E.** (2014). Yield strength prediction in Ni-base alloy 718Plus based on thermo-kinetic precipitation simulation. *Materials Science and Engineering A*, **608**, 114–122. https://doi.org/10.1016/j.msea.2014.04.054

Alabbad, B., **Li, L.**, & **Tin, S.** (2019). Controlling the grain boundary morphology and secondary γ′ precipitate size distribution in Ni-base superalloys. *Journal of Alloys and Compounds*, **775**, 931–941. https://doi.org/10.1016/j.jallcom.2018.10.031

Ali, M. A., **López-Galilea, I.**, **Gao, S.**, **Ruttert, B.**, **Amin, W.**, **Shchyglo, O.**, … **Steinbach, I.** (2020). Effect of γ′ precipitate size on hardness and creep properties of Ni-base single crystal superalloys: Experiment and simulation. *Materialia*, **12**(April). https://doi.org/10.1016/j.mtla.2020.100692

An, X. L., **Zhou, L.**, **Zhang, B.**, **Jj**, **Chu, C. L.**, **Han, L. Y.**, … **Chu, P. K.** (2019). Inconel 718 treated with two-stage solution and aging processes: Microstructure evolution and enhanced properties. *Materials Research Express*, **6**(7). https://doi.org/10.1088/2053-1591/ab1290

Anbarasan, N., **Gupta, B. K.**, **Prakash, S.**, **Muthukumar, P.**, **Oyyaravelu, R.**, **Kumar, R. J. F.**, & **Jerome, S.** (2018). Effect of Heat Treatment on the Microstructure and Mechanical Properties of Inconel 718. *Materials Today: Proceedings*, **5**(2), 7716–7724. https://doi.org/10.1016/j.matpr.2017.11.448

Anderson, M. J., **Schulz, F.**, **Lu, Y.**, **Kitaguchi, H. S.**, **Bowen, P.**, **Argyrakis, C.**, & **Basoalto, H. C.** (2020). On the modelling of precipitation kinetics in a turbine disc nickel based superalloy. *Acta Materialia*, **191**, 81–100. https://doi.org/10.1016/j.actamat.2020.03.058

Anderson, M., **Thielin, A. L.**, **Bridier, F.**, **Bocher, P.**, & **Savoie, J.** (2017). δ Phase precipitation in Inconel 718 and associated mechanical properties. *Materials Science and Engineering A*, **679**(January 2016), 48–55. https://doi.org/10.1016/j.msea.2016.09.114

Ardell, A. J. (1985). Precipitation Hardening. *Metallurgical Transactions A*, **16A**(December).

Argon, A. (2007). Strengthening Mechanisms in Crystal Plasticity. In *Oxford university press* (Vol. 9780198516). https://doi.org/10.1093/acprof:oso/9780198516002.001.0001

ASTM E384-17. (2017). Designation: E384-17 Standard Test Method for Microindentation Hardness of Materials. *ASTM International*, (05a), 281–293.

ASTM E8. (2010). ASTM E8/E8M standard test methods for tension testing of metallic materials 1. *Annual Book of ASTM Standards 4*, (C), 1–27. https://doi.org/10.1520/E0008

Atabay, S. E., **Sanchez-Mata, O.**, **Muñiz-Lerma, J. A.**, **Gauvin, R.**, & **Brochu, M.** (2020). Microstructure and mechanical properties of rene 41 alloy manufactured by laser powder bed fusion. *Materials Science and Engineering A*, **773**(December 2019).

https://doi.org/10.1016/j.msea.2019.138849

Babu, S. S., **Miller, M. K.**, **Vitek, J. M.**, & **David, S. A.** (2001). Characterization of the microstructure evolution in a nickel base superalloy during continuous cooling conditions. *Acta Materialia*, **49**(20), 4149–4160. https://doi.org/10.1016/S1359-6454(01)00314-7

Bagot, P. A. J., **Silk, O. B. W.**, **Douglas, J. O.**, **Pedrazzini, S.**, **Crudden, D. J.**, **Martin, T. L.**, … **Reed, R. C.** (2017). An Atom Probe Tomography study of site preference and partitioning in a nickel-based superalloy. *Acta Materialia*, **125**, 156–165. https://doi.org/10.1016/j.actamat.2016.11.053

Baldan, A. (2002). Progress in Ostwald ripening theories and their applications to nickel-base superalloys Part I : Ostwald ripening theories. *Journal of Materials Science*, **37**, 2171–2202.

Balikci, E., & **Erdeniz, D.** (2010). Multimodal precipitation in the superalloy IN738LC. *Metallurgical and Materials Transactions A: Physical Metallurgy and Materials Science*, **41**(6), 1391–1398. https://doi.org/10.1007/s11661-010-0241-3

Bergstrom, D. S., & **Bayha, T. D.** (2005). Properties and Microstructure Allvac® 718Plus™ Alloy Rolled Sheet. *Superalloys 718, 625, 706 and Derivatives*, 243–252. https://doi.org/10.7449/2005/Superalloys_2005_243_252

Boesch, W., & **Canada, H.** (1969). Precipitation reactions and stability of Ni3Cb in Inconel alloy-718. *Journal of Metals*, **21**, 34-.

Bowman, R. (Nasa L. R. C. (2000). Superalloys: A Primer and History. *9th International Symposium on Superalloys*, **3**, 3–6. Retrieved from http://www.tms.org/meetings/specialty/superalloys2000/superalloyshistory.html

C. S. Smith. (1948). Five Decades of the Zener Equation. *Trans, AIME*, **175**(15), 913–924. https://doi.org/10.2355/isijinternational.38.913

Cao, Wei Di, & **Kennedy, R. L.** (2005). New Developments in Wrought 718-Type Superalloys (Acta Met Feb 05).pdf. *Acta Metallurgica Sinica*, **18**(1), 39–46.

Cao, W. D., & **Kennedy, R. L.** (2001). Thermal Stability of Alloys 718 and Allvac 718-ER. *Superalloys 718, 625, 706 and Various Derivatives (2001)*, 455–464. https://doi.org/10.7449/2001/Superalloys_2001_455_464

Cao, Wei-di, & **Kennedy, R. L.** (2004). Role of chemistry in 718-type alloys - Allvac 718Plus alloy development. *TMS Annual Meeting, Superalloy 2004*, *3*, 1–10. https://doi.org/10.7449/2004/Superalloys_2004_91_99

Chen, K., **Dong, J.**, **Yao, Z.**, **Ni, T.**, & **Wang, M.** (2018). A Creep performance and damage mechanism for Allvac 718Plus superalloy. *Materials Science & Engineering A*, **738**(July), 308–322.

Chiou, M.-S., **Jian, S.-R.**, **Yeh, A.-C.**, **Kuo, C.-M.**, & **Juang, J.-Y.** (2016). High temperature creep properties of directionally solidified CM-247LC Ni-based superalloy. *Materials Science and Engineering: A*, **655**, 237–243. https://doi.org/10.1016/j.msea.2015.12.094

Collins, D. M., & **Stone, H. J.** (2014). A modelling approach to yield strength optimisation in a nickel-base superalloy. *International Journal of Plasticity*, **54**, 96–112. https://doi.org/10.1016/j.ijplas.2013.08.009

Connor, L. D., **Stone, H. J.**, **Collins, D. M.**, **Preuss, M.**, **Hardy, M. C.**, & **C.M.F.Rae**. (2014). The Effect of Cooling Rate from Solution on the Lattice Misfit During Isothermal Aging of a Ni-Base Superalloy. *Metallurgical and Materials Transactions A*, **45A**(2442). https://doi.org/10.1007/s11661-014-2197-1

Covarrubias, O. (2010). Development of a New Nickel-base Superalloy for High Temperature Applications. *Materials Research Society Symposium Proceedings*, **1276**.

Dahotre, N. B., **Mccay, M. H.**, **Mccay, T. D.**, **Hubbard, C. R.**, **Porter, W. D.**, & **Cavin, O. B.** (1993). Effect of Grain Structure on Phase Transformation Events in the Inconel 718. *Scripta Metallurgica et Materialia*, **28**, 1359–1364. https://doi.org/10.1016/0956-716X(93)90482-8

Donachie, M. J., & **Donachie, S. J.** (2002). Superalloys A Technical Guide. In *SUPERALLOYS A Technical Guide*. https://doi.org/10.1361/stgs2002p001

E112, A. (2012). Standard Test Methods for Determining Average Grain Size. *Astm E112-13*, 1–27. https://doi.org/10.1520/E0112-13.1.4

Eckhard Nembach, & **Neite, G.** (1985). Precipitation hardening of superalloys by ordered y' particles. *Progress in Materials Science*, **29**, 177–319. https://doi.org/10.1016/0079-6425(85)90001-5

Eksergian, R. (1957). Aircraft gas turbines. *Journal of the Franklin Institute*, **264**(3), 254–255. https://doi.org/10.1016/0016-0032(57)90996-1

Epishin, A., & **Link, T.** (2004). Mechanisms of high-temperature creep of nickel-based superalloys under low applied stresses. *Philosophical Magazine*, **84**(19), 1979–2000. https://doi.org/10.1080/14786430410001663240

Fang, Q., **Huang, Z.**, **Li, L.**, **Huang, Z.**, **Liu, B.**, **Liu, Y.**, … **Liaw, P. K.** (2022). Modeling the competition between solid solution and precipitate strengthening of alloys in a 3D space. *International Journal of Plasticity*, **149**(November 2021). https://doi.org/10.1016/j.ijplas.2021.103152

Fedelich, B., **Epishin, A.**, **Link, T.**, **Klingelhöffer, H.**, **Künecke, G.**, & **Dolabella Portella, P.** (2012). Rafting During High Temperature Deformation in a Single Crystal Superalloy: Experiments and Modeling. *Superalloys 2012: 12th International Symposium on Superalloys*, (6), 491–500.

Fleischer, R. L. (1963). Substitutional solutional hardening. *Acta Metallurgica*, **II**.

Foreman, A. J. E., & **Makin, M. J.** (1966). Dislocation movement through random arrays of obstacles. *Philosophical Magazine*, **14**(131), 911–924. https://doi.org/10.1080/14786436608244762

Furrer, D., & **Fecht, H.** (1999). Ni-based superalloys for turbine discs. *Jom*, **51**(1), 14–17. https://doi.org/10.1007/s11837-999-0005-y

Gabb, T., **Backman, D.**, **Wei, D.**, **Mourer, D.**, **Furrer, D.**, **Garg, A.**, & **Ellis, D.** (2000). Gamma' formation in a nickel-base disk superalloy. *TMS Superalloys 2000*, 405–414. https://doi.org/\url{10.7449/2000/Superalloys{\textunderscore }2000{\textunderscore }405{\textunderscore }414}

Gabb, T. P., **Gayda, J.**, **Telesman, J.**, **Garg, A.**, **Glenn, N.**, & **Rd, B.** (2008). *THE EFFECTS OF HEAT TREATMENT AND MICROSTRUCTURE VARIATIONS ON DISK*. 121–130.

Galindo-Nava, E. I., **Connor, L. D.**, & **Rae, C. M. F.** (2015). On the prediction of the yield stress of unimodal and multimodal γ' Nickel-base superalloys. *Acta Materialia*, **98**, 377–390. https://doi.org/10.1016/j.actamat.2015.07.048

Gerold, V., & **Haberkorn, H.** (1966). On the Critical Resolved Shear Stress of Solid Solutions Containing Coherent Precipitates. *Physica Status Solidi (B)*, **16**(2), 675–684. https://doi.org/10.1002/pssb.19660160234

Ghosh, R. N. ; (2002). Superalloy: Processing and Performance. *Advanced Materials Proceedings of the Indo-Malaysian Joint Workshop(WAM-2002)*, 97–106. Retrieved from http://eprints.nmlindia.org/4191

Goodfellow, A. J. (2018). Strengthening mechanisms in polycrystalline nickel-based superalloys. *Materials Science and Technology*, **34**(15), 1793–1808. https://doi.org/10.1080/02670836.2018.1461594

Goodfellow, A. J., **Galindo-Nava, E. I.**, **Christofidou, K. A.**, **Jones, N. G.**, **Martin, T.**, **Bagot, P. A. J.**, … **Stone, H. J.** (2018). Gamma Prime Precipitate Evolution During Aging of a Model Nickel-Based Superalloy. *Metallurgical and Materials Transactions A: Physical Metallurgy and Materials Science*, **49**(3), 718–728. https://doi.org/10.1007/s11661-017-4336-y

Graef, M. De. (2003). *Introduction to Conventional Transmission Electron Microscopy*. Cambrideg University Press.

Guo, Q., **Ma, Z.**, **Qiao, Z.**, **Li, C.**, **Zhang, T.**, **Li, J.**, … **Liu, Y.** (2022). A new type-γ′/γ″ coprecipitation behavior and its evolution mechanism in wrought Ni-based ATI 718Plus superalloy. *Journal of Materials Science and Technology*, **119**, 98–110. https://doi.org/10.1016/j.jmst.2021.12.033

Hall, E. O. (1951). The Deformation and Ageing of Mild Steel: III Discussion of results. *Proceedings of the Physical Society. Section B*, **44**(8), 3089–3103.

Ham, H., **Park, N.**, **Kim, S. S.**, & **Kim, H. W.** (2014). Evidence of Ostwald ripening during evolution of micor-scale solid carbon spaheres. *Scientific Reports*, 1–4. https://doi.org/10.1038/srep03579

Han, V., **Deb, P.**, & **Chaturvedi, M. C.** (1982). *Coarsening behaviour of y'' and y' particles in Inconel alloy 718*. **16**(December).

Hansen, N. (2004). Hall-petch relation and boundary strengthening. *Scripta Materialia*, **51**(8 SPEC. ISS.), 801–806. https://doi.org/10.1016/j.scriptamat.2004.06.002

Hassan, B., & **Corney, J.** (2017). Grain boundary precipitation in Inconel 718 and ATI 718Plus. *Materials Science and Technology (United Kingdom)*, **33**(16), 1879–1889. https://doi.org/10.1080/02670836.2017.1333222

Hayes, R. W., **Unocic, R. R.**, & **Nasrollahzadeh, M.** (2015). Creep Deformation of Allvac 718Plus. *Metallurgical and Materials Transactions A: Physical Metallurgy and Materials Science*, **46**(1), 218–228. https://doi.org/10.1007/s11661-014-2564-y

Hazotte, A., **Racine, A.**, & **Denis, S.** (1996). Internal mismatch stresses in nickel-based superalloys: A finite element approach. *Journal De Physique. IV : JP*, **6**(1).

Jackson, M. P., & **Reed, R. C.** (1999a). Heat treatment of UDIMET 720Li: The effect of microstructure on properties. *Materials Science and Engineering A*, **259**(1), 85–97. https://doi.org/10.1016/S0921-5093(98)00867-3

Jackson, M. P., & **Reed, R. C.** (1999b). Model for growth and coarsening of two phase systems under diffusional control. *Materials Science and Technology*, **15**(7), 738–749. https://doi.org/10.1179/026708399101506517

Jeniski Jr., R. A., & **Kennedy, R. L.** (2006). Development of ATI Allvac® 718Plus® Alloy and Applications. *Symposium on Recent Advantages of Nb-Contain Materials in Europe*, 1–11.

Jeniski, R., & **Kennedy, R. L.** (n.d.). *Nickel-base superalloy designed for aerospace*.

Joseph, C., **Persson, C.**, & **Colliander, M. H.** (n.d.). *Influence of heat treatment on the microstructure and tensile properties of Ni-base superalloy Haynes 282*. 1–29.

Kamaraj, M. (2003). Rafting in single crystal nickel-base superalloys --- An overview. *Sadhana*, **28**(1), 115–128. https://doi.org/10.1007/BF02717129

Kennedy, R., & **McDevitt, E.** (2008). Metallurgy of ATI 718Plus Alloy. *Advanced Materials and Processes*, **166**(3), 32–33.

Kennedy, R.L. (2005). Allvac 718Plus, Superalloy for the Next Forty Years. *Superalloys 718, 625, 706 and Various Derivatives (2005)*, 1–14. https://doi.org/10.7449/2005/Superalloys_2005_1_14

Kennedy, Richard L., **Cao, W. Di**, **Bayha, T. D.**, & **Jeniski, R.** (2004). Developments in wrought Nb containing superalloys (718 + 100°F). *Proceedings of the International Symposium on Niobium for High Temperature Applications*, 11–21.

Kozar, R. W., **Suzuki, A.**, **Milligan, W. W.**, **Schirra, J. J.**, & **Savage, M. F.** (2009). Strengthening Mechanisms in Polycrystalline Multimodal Nickel-Base Superalloys. Metallurgical and Materials Transactions A, 40. *Metallurgical and Materials Transactions A*, **40**. https://doi.org/10.1007/s11661-009-9858-5

Kracke, A. (2010). Superalloys , the Most Successful Alloy System of Modern Times - Past , Present and Future. *Superalloy 718 and Derivatives*, 13–50.

Kushan, M. C., **Uzgur, S. C.**, **Uzunonat, Y.**, & **Diltemiz, F.** (2012). ALLVAC 718 Plus™ Superalloy for Aircraft Engine Applications. *Recent Advances in Aircraft Technology*, **718**, 75–96. https://doi.org/10.5772/38433

Latief, F. H., **Kakehi, K.**, **Murakami, H.**, & **Kasai, K.** (2012). Influence of crystallographic orientation on creep behavior of aluminized Ni-based single crystal superalloys. *Superalloys 2012 (12th International Symposium on Superalloys)*, 311–320. https://doi.org/10.1016/j.matdes.2013.01.022

Lech, S., **Kruk, A.**, **Cempura, G.**, **Adam Gruszczyn´ski, A. G.**, **Agu¨ero, A.**, **Wusatowska-Sarnek, A. M.**, & **Czyrska-Filemonowicz, A.** (2019). Influence of High-Temperature Exposure on the Microstructure of ATI 718Plus Superalloy Studied by Electron Microscopy and Tomography Techniques. *Journal of Materials Engineering and Performance*, (Vim). https://doi.org/10.1007/s11665-019-04474-5

Leishman, J. G. (2022). *INTRODUCTION TO AEROSPACE FLIGHT VEHICLES*. Embry-riddle aeronautical university.

Lewandowski, C. M. (2015). Pushing the Envelop: A NASA Guide to Engines. *The Effects of Brief Mindfulness Intervention on Acute Pain Experience: An Examination of Individual Difference*, **1**, 1689–1699. https://doi.org/10.1017/CBO9781107415324.004

Lifshitz, I. M., & **Slyzov, V. V.** (1961). *The kinetics of precipitation from supersaturated solid solutions*. **19**(1), 35–50.

Löhnert, K., & **Pyczak, F.** (2010). Microstructure evolution in the nickel base superalloy Allvac® 718Plus™. *7th International Symposium on Superalloy 718 and Derivatives 2010*, **2**, 877–891. https://doi.org/10.1002/9781118495223.ch67

Long, H., **Bakhtiari, S. R.**, **Liu, Y.**, **Mao, S.**, **Wei, H.**, **Chen, Y.**, … **Han, X.** (2020). A comparative study of rafting mechanisms of Ni-based single crystal superalloys. *Materials*

and Design, **196**, 109097. https://doi.org/10.1016/j.matdes.2020.109097

Long, H., **Mao, S.**, **Liu, Y.**, **Zhang, Z.**, & **Han, X.** (2018). Microstructural and compositional design of Ni-based single crystalline superalloys — A review. *Journal of Alloys and Compounds*, **743**, 203–220. https://doi.org/10.1016/j.jallcom.2018.01.224

Mahadevan, S., **Nalawade, S.**, **Singh, J. B.**, **Verma, A.**, **Paul, B.**, & **Ramaswamy, K.** (2012). Evolution of δ Phase Microstructure in Alloy 718. *Superalloy 718 and Derivatives*, 737–750. https://doi.org/10.1002/9781118495223.ch57

Masoumi, F., **Shahriari, D.**, **Jahazi, M.**, **Cormier, J.**, & **Devaux, A.** (2016). Kinetics and Mechanisms of γ′ Reprecipitation in a Ni-based Superalloy. *Scientific Reports*, **6**, 28650. https://doi.org/10.1038/srep28650

Maurer, G. E., **Jackman, L. A.**, & **Domingue, J. A.** (1980). Role of Cobalt in Waspaloy. *TMS Superalloys*, (1), 43–52. https://doi.org/10.7449/1980/superalloys_1980_43_52

McDevitt, E. (2011). ATI 718 Plus ® Alloy Data Sourcebook. *ATI Allvac, Monroe, NC*, **3**(1.2), 1–98.

McDevitt, E. T., & **Bentley, J.** (2009). Microstructure and mechanical properties of direct aged 718plus® alloy. *TMS Annual Meeting*, **1**, 289–296.

McDevitt, E. T., **Oppenheimer, S. M.**, **Kearsey, R. M.**, & **Tsang, J.** (2012). Crack Growth Behavior in ATI 718Plus® Alloy. *Materials Science Forum*, **706**–**709**, 2428–2433. https://doi.org/10.4028/www.scientific.net/MSF.706-709.2428

Mignanelli, P. M., **Jones, N. G.**, **Pickering, E. J.**, **Messé, O. M. D. M.**, **Rae, C. M. F.**, **Hardy, M. C.**, & **Stone, H. J.** (2017). Gamma-gamma prime-gamma double prime dual-superlattice superalloys. *Scripta Materialia*, **136**, 136–140. https://doi.org/10.1016/j.scriptamat.2017.04.029

Morris, D. G., & **Morris, M. A.** (1990). Antiphase domain boundaries and their importance for dislocation behaviour in Ni3Al based alloys. *Philosophical Magazine A: Physics of Condensed Matter, Structure, Defects and Mechanical Properties*, **61**(3), 469–491. https://doi.org/10.1080/01418619008231928

Nathal, M. V. (2008). NASA and Superalloys: A Customer, a Participant, and a Referee. *Superalloys 2008 (Eleventh International Symposium)*, 13–19. https://doi.org/10.7449/2008/Superalloys_2008_13_19

Polkowska, A., **Polkowski, W.**, **Warmuzek, M.**, **Cieśla, N.**, **Włoch, G.**, **Zasada, D.**, & **Purgert, R. M.** (2019). Microstructure and Hardness Evolution in Haynes 282 Nickel-Based Superalloy During Multi-variant Aging Heat Treatment. *Journal of Materials Engineering and Performance*, **28**(7), 3844–3851. https://doi.org/10.1007/s11665-019-3886-0

Porter, D. A., **Easterling, K. E.**, & **Sherif, M. Y.** (2009). Phase Transformations in Metals and Alloys, Third Edition. In *CRC Press*.

Preuss, M., **da Fonseca, J. Q.**, **Grant, B.**, **Knoche, E.**, **Moat, R.**, & **Daymond, M.** (2008). The effect of y' particle size on the deformation mechanism in an advanced polycrystalline nickel-base superalloy. *Superalloys 2008: 11th International Symposium on Superalloys*, (010), 405–414.

Radavich, J. F., & **Carneiro, T.** (2005). A Microstructural Study of Alloy 718 Plus™. *Superalloys 718, 625, 706 and Derivatives*, 329–340.

Radis, R., **Schaffer, M.**, **Albu, M.**, **Kothleitner, G.**, **Pölt, P.**, & **Kozeschnik, E.** (2009). Multimodal size distributions of γ′ precipitates during continuous cooling of UDIMET 720 Li. *Acta Materialia*, **57**(19), 5739–5747. https://doi.org/10.1016/j.actamat.2009.08.002

Raynor, D., & **Silcock, J. M.** (1970). Strengthening Mechanisms in γ′ Precipitating Alloys. *Metal Science Journal*, **4**(1), 121–130. https://doi.org/10.1179/msc.1970.4.1.121

Reed, R C, & **C.M.F.Rae**. (2014). Physical Metallurgy of the Nickel-Based Superalloys. In *Physical Metallurgy* (Fifth Edit, Vol. 3). https://doi.org/10.1016/B978-0-444-53770-6.00022-8

Reed, Roger C. (2006). The superalloys fundamentals and applications. *Cambridge University Press*, 43–2626.

Russell, A. M., & **Lee, K. L.** (2005). Structure-Property Relations in Nonferrous Metals. In *Structure-Property Relations in Nonferrous Metals*. https://doi.org/10.1002/0471708542

Sarosi, P. M., **Wang, B.**, **Simmons, J. P.**, **Wang, Y.**, & **Mills, M. J.** (2007). Formation of multimodal size distributions of γ′ in a nickel-base superalloy during interrupted continuous cooling. *Scripta Materialia*, **57**(8), 767–770. https://doi.org/10.1016/j.scriptamat.2007.06.014

Schirra, J. J., **Reynolds, P. L.**, **Huron, E. S.**, **Bain, K. R.**, & **Mourer, D. P.** (2004). Effect of microstructure (and heat treatment) on the 649°C properties of advanced P/M superalloy disk materials. *Proceedings of the International Symposium on Superalloys*, 341–350. https://doi.org/10.7449/2004/superalloys_2004_341_350

Segersäll, M. (2013). *Nickel-Based Single-Crystal Superalloys temperature properties*.

Shercliff, H. R., & **Ashby, M. F.** (1990a). A process model for age hardening of aluminium alloys-I. The model. *Acta Metallurgica Et Materialia*, **38**(10), 1789–1802. https://doi.org/10.1016/0956-7151(90)90291-N

Shercliff, H. R., & **Ashby, M. F.** (1990b). A process model for age hardening of aluminium alloys-II. Applications of the model. *Acta Metallurgica Et Materialia*, **38**(10), 1803–1812. https://doi.org/10.1016/0956-7151(90)90292-O

Shercliff, H. R., & **Castillo, T.** (1997). *Process model for two step age hardening of 7475 aluminium alloy*. **13**(November), 897–904.

Singh, A. R. P., **Nag, S.**, **Hwang, J. Y.**, **Viswanathan, G. B.**, **Tiley, J.**, **Srinivasan, R.**, … **Banerjee, R.** (2011). Influence of cooling rate on the development of multiple generations of γ′ precipitates in a commercial nickel base superalloy. *Materials Characterization*, **62**(9), 878–886. https://doi.org/10.1016/j.matchar.2011.06.002

Smith, T. M., **Esser, B. D.**, **Antolin, N.**, **Viswanathan, G. B.**, **Hanlon, T.**, **Wessman, A.**, … **Mills, M. J.** (2015). Segregation and η phase formation along stacking faults during creep at intermediate temperatures in a Ni-based superalloy. *Acta Materialia*, **100**, 19–31. https://doi.org/10.1016/j.actamat.2015.08.053

Sofuoglu, M. A., **Cakir, F. H.**, **Gurgen, S.**, & **Kushan, M. C.** (2017). A NEW SUPERALLOY : ALLVAC 718 PLUSTM. *Proceedings of ISER International Conference, Jakarta, Indonesia*, (January), 8–11.

Srinivasan, D., **Lawless, L. U.**, & **Ott, E. A.** (2012). Experimental determination of TTT diagram for ally 718PLUS®. *Superalloys 2012*, **3**, 759–768. https://doi.org/10.1002/9781118516430.ch84

Strudel, J. (1996). Mechanical properties of multiphase alloys. In *Multiphase alloy* (pp. 2190–2194). Elsevier Ltd.

Sundararaman, M., **Mukhopadhyay, P.**, & **Banerjee, S.** (1988a). Deformation behaviour of γ″ strengthened inconel 718. *Acta Metallurgica*, **36**(4), 847–864. https://doi.org/10.1016/0001-6160(88)90139-3

Sundararaman, M., **Mukhopadhyay, P.**, & **Banerjee, S.** (1988b). Precipitation of the y''-Ni3Nb phase in two nickel base superalloys. *Metallurgical Transactions A*, **19**(3), 453–465. https://doi.org/10.1007/BF02649259

Sundararaman, M., **Mukhopadhyay, P.**, & **Banerjee, S.** (1992). Some aspects of the precipitation of metastable intermetallic phases in INCONEL 718. *Metallurgical Transactions A*, **23**(7), 2015–2028. https://doi.org/10.1007/BF02647549

Sundararaman, M., **Mukhopadhyay, P.**, & **Banerjee, S.** (1997). Carbide precipitation in nickel base superalloys 718 and 625 and their effect on mechanical properties. *TMS: Superalloys 718*, 625–706. https://doi.org/10.7449/1997/Superalloys_1997_367_378

Suwas, S., & **Ray, R. K.** (2014). Crystallographic Texture of Materials. In *Springer*. Retrieved from https://books.google.be/books?id=peRKBAAAQBAJ&dq=Crystallographic+Texture+of+Materials&hl=en&sa=X&ei=FqzGVLySH8zdPevEgBA&ved=0CCAQ6AEwAA

Svoboda, J., **Fischer, F. D.**, **Fratzl, P.**, & **Kozeschnik, E.** (2004). *Modelling of kinetics in multi-component multi-phase systems with spherical precipitates I : Theory*. **385**, 166–174.

https://doi.org/10.1016/j.msea.2004.06.018

Technologies, A. A. (2008). *718 Plus ® Data Sourcebook ATI Allvac*.

Tejedor, T. A., **Singh, R.**, & **Pilidis, P.** (2013). Maintenance and repair of gas turbine components. In *Modern Gas Turbine Systems: High Efficiency, Low Emission, Fuel Flexible Power Generation*. https://doi.org/10.1533/9780857096067.3.565

Testa, G., **Brunoro, N.**, & **Giaretta, D.** (1979). Fundamentals of Gas Turbine Engines. *Rivista Di Neurologia*, **49**(3), 259–267.

Thomas, A., **El-Wahabi, M.**, **Cabrera, J. M.**, & **Prado, J. M.** (2006a). High temperature deformation of Inconel 718. *Journal of Materials Processing Technology*, **177**(1–3), 469–472. https://doi.org/10.1016/j.jmatprotec.2006.04.072

Thomas, A., **El-Wahabi, M.**, **Cabrera, J. M.**, & **Prado, J. M.** (2006b). High temperature deformation of Inconel 718. *Journal of Materials Processing Technology*, **177**(1–3), 469–472. https://doi.org/10.1016/j.jmatprotec.2006.04.072

Torster, F., **Baumeister, G.**, **Albrecht, J.**, **Lütjering, G.**, **Helm, D.**, & **Daeubler, M. A.** (1997). Influence of grain size and heat treatment on the microstructure and mechanical properties of the nickel-base superalloy U 720 LI. *Materials Science and Engineering A*, **234**–**236**, 189–192. https://doi.org/10.1016/s0921-5093(97)00161-5

U.F. Kocksa, & **Mecking, H.** (2003). Physics and phenomenology of strain hardening: the FCC case. *Progress in Materials Science*, **48**, 171–273. https://doi.org/10.4324/9781315279015

Unocic, K. A., **Hayes, R. W.**, **Mills, M. J.**, & **Daehn, G. S.** (2010). Microstructural features leading to enhanced resistance to grain boundary creep cracking in ALLVAC 718Plus. *Metallurgical and Materials Transactions A: Physical Metallurgy and Materials Science*, **41**(2), 409–420. https://doi.org/10.1007/s11661-009-0099-4

Unocic, R. R., **Unocic, K. A.**, **Hayes, R. W.**, **Daehn, G. S.**, & **Mills, M. J.** (2010). A TEM study of creep deformation mechanisms in allvac 718plus. *7th International Symposium on Superalloy 718 and Derivatives 2010*, **2**, 607–615. Retrieved from http://www.scopus.com/inward/record.url?eid=2-s2.0-79960981002&partnerID=tZOtx3y1

Viskari, L., **Cao, Y.**, **Norell, M.**, **Sjöberg, G.**, & **Stiller, K.** (2011). Grain boundary microstructure and fatigue crack growth in Allvac 718Plus superalloy. *Materials Science and Engineering A*, **528**(6), 2570–2580. https://doi.org/10.1016/j.msea.2010.11.080

Viswanathan, G. B., **Sarosi, P.**, **Henry, M.**, **Whitis, D.**, & **Mills, M.** (2004). Deformation Mechanisms at Intermediate Creep Temperatures in Rene88 DT. *Superalloys 2004 (Tenth International Symposium)*, 173–178. https://doi.org/10.7449/2004/Superalloys_2004_173_178

Wang, H., **Liu, D.**, **Wang, J.**, **Yang, Y.**, **Rao, H.**, **Wang, H.**, … **Wang, L.** (2021). Study on the

evolution of the γ′ phase and grain boundaries in nickel-based superalloy during interrupted continuous cooling. *Crystals*, **11**(12), 1–12. https://doi.org/10.3390/cryst11121464

Wen, Y. H., **Simmons, J. P.**, **Shen, C.**, **Woodward, C.**, & **Wang, Y.** (2003). Phase-field modeling of bimodal particle size distributions during continuous cooling. *Acta Materialia*, **51**(4), 1123–1132. https://doi.org/10.1016/S1359-6454(02)00516-5

Whitmore, L., **Leitner, H.**, **Povoden-Karadeniz, E.**, **Radis, R.**, & **Stockinger, M.** (2012). Transmission electron microscopy of single and double aged 718Plus superalloy. *Materials Science and Engineering A*, **534**, 413–423. https://doi.org/10.1016/j.msea.2011.11.089

Wilson, G. R. (1976). Size Distributions for Supported Metal Catalysts, coalescence growth versus Ostwald ripening. *Journal of Catalysis*, **477479**, 477–479.

Xie, X., **Wang, G.**, **Dong, J.**, **Xu, C.**, **Cao, W.-D.**, & **Kennedy, R.** (2005). Structure Stability Study on a Newly Developed Nickel-Base Superalloy - Allvac 718Plus. *Superalloys 718, 625, 706 and Various Derivatives (2005)*, 179–191. https://doi.org/10.7449/2005/Superalloys_2005_179_191

Xie, X., **Xu, C.**, **Wang, G.**, **Dong, J.**, **Cao, W. D.**, & **Kennedy, R.** (2005). Ttt Diagram of a Newly Developed Nickel-Base Superalloy - Allvac® 718Plus™. *Superalloys 718, 625, 706 and Derivatives*, 193–202. https://doi.org/10.7449/2005/Superalloys_2005_179_191

Yao, J. H., **K.R.Elder**, **Guo, H.**, & **Grant, M.** (1993). Theory and simulation of Ostwald ripening. *Physical Review B*, **47**(21).

Yu, Z., **Wang, X.**, **Yang, F.**, **Yue, Z.**, & **Li, J. C. M.** (2020). Review of γ' rafting behavior in nickel-based superalloys: Crystal plasticity and phase-field simulation. *Crystals*, **10**(12), 1–24. https://doi.org/10.3390/cryst10121095

Zhao, K., **Lou, L. H.**, **Ma, Y. H.**, & **Hu, Z. Q.** (2008). Effect of minor niobium addition on microstructure of a nickel-base directionally solidified superalloy. *Materials Science and Engineering A*, **476**(1–2), 372–377. https://doi.org/10.1016/j.msea.2007.06.041

APPENDIX A: CODE FOR THE STRENGTHENING MODEL CALCULATIONS

To create the graphs presented in 6.3 using strengthening models, Python was used to generate the code and the calculations. Below is the example of code for one sample case (sample 720) and a calculation for the calculation of YS for sample Bimodal. The code has been exported from Jupyter notebook python 3.0.

```
import math
from math import sqrt
from math import pi
from math import log
from math import exp
import pandas as pd
import numpy as np
from numpy import log as ln
import matplotlib.pyplot as plt
from scipy.stats import norm
from scipy.optimize import curve_fit

mu_p=77.8*10**9 #Pa
mu = 80*10**9 #Pa
b=0.254*10**(-9) ## m
APB=0.175 ## pascal*m from Fang
rm=(mu_p*b*b)/(2*APB) #m
print('rm is ', rm*10**9, 'nm')
T=(mu*b*b)/2 #pa*m^2
rm is  14.340985142857143 nm
For sample 720¶
##Weak pair coupling

Tp7w=[]
x=[1,2,3,4,5,6,7,8,9,10,11,12,13,14,15,16,17,18,19,20,21,22,23,24,25,26,27,28,29,30,35,40,41,4
                2,43,44,45,46,47,48,49,50,55,60,65,70,75,80,85,90,95,100,105,110]
for k in x:
    r=(k)*10**(-9) #m
    f=0.052 #fraction
    a=APB/(2*b)
    k= 6*APB*r*f  #pa.m.m
    q=2*pi*T      #Pa.m.m
    c= sqrt(k/q)
    Tp_weak =a*(c-f) #pa
    Tp_weak= Tp_weak/(10**6)
```

```
   Tp_weak=round(Tp_weak,2)
   Tp7w.append(Tp_weak)
print(Tp7w, 'MPa')

[2.08, 10.36, 16.71, 22.07, 26.79, 31.05, 34.98, 38.63, 42.06, 45.3, 48.39, 51.33, 54.16, 56.88,
            59.51, 62.05, 64.51, 66.9, 69.22, 71.49, 73.69, 75.85, 77.96, 80.02, 82.04, 84.02, 85.96,
            87.86, 89.74, 91.58, 100.35, 108.52, 110.09, 111.64, 113.17, 114.69, 116.18, 117.67,
            119.13, 120.58, 122.02, 123.44, 130.34, 136.93, 143.25, 149.34, 155.21, 160.88,
            166.39, 171.73, 176.93, 181.99, 186.93, 191.75] MPa

### strong pair coupling
Tp7s=[]
x_1=[6,7,                                                                                    9,
            10,11,12,13,14,15,16,17,18,19,20,21,22,23,24,25,26,27,28,29,30,35,40,41,42,43,44,4
            5,46,47,48,49,50,55,60,65,70,75,80,85,90,95,100,105,110]
for k in x_1:
   r=(k)*10**(-9) #m
   f=0.052 #fraction
   w= sqrt(3/2)*(mu*b/r)
   j=(sqrt(f))/(pi**(3/2))
   t= (pi*APB*r)/T
   Tp_strong= w*j*(sqrt(t-1))
   Tp_strong= Tp_strong/(10**6)
   Tp_strong=round(Tp_strong,2)
   Tp7s.append(Tp_strong)
print(Tp7s, 'MPa')

[89.6, 102.05, 108.46, 108.36, 107.39, 105.96, 104.29, 102.5, 100.68, 98.86, 97.07, 95.33, 93.64,
            92.02, 90.45, 88.95, 87.51, 86.12, 84.79, 83.51, 82.29, 81.11, 79.97, 78.88, 73.99,
            69.88, 69.13, 68.41, 67.71, 67.03, 66.37, 65.72, 65.1, 64.49, 63.9, 63.33, 60.66, 58.31,
            56.2, 54.31, 52.59, 51.03, 49.59, 48.28, 47.06, 45.92, 44.87, 43.88] MPa
108.46

##weak strong modified pair coupling

Tp7m=[]
x=[1,2,3,4,5,6,7,8,9,10,11,12,13,14,15,16,17,18,19,20,21,22,23,24,25,26,27,28,29,30,35,40,41,4
            2,43,44,45,46,47,48,49,50,55,60,65,70,75,80,85,90,95,100,105,110]
for k in x:
   r=(k)*10**(-9) #m
   if r<rm:
      l1=2*r #m
   else:
      l1=2*sqrt(r*r-(r-rm)**2)
   f=0.052 #fraction
```

```
    L=sqrt(2*pi/(3*f))*r
    Lamda1=sqrt(T/(APB*r))*L #m
    V1=max(Lamda1, L-l1)
    Tp_modify=(APB*l1)/(2*b*(V1+2*r))
    Tp_modify= Tp_modify/(10**6)
    Tp_modify=round(Tp_modify,2)
    Tp7m.append(Tp_modify)
print(Tp7m, 'MPa')

[26.13, 35.82, 42.87, 48.57, 53.41, 57.66, 61.45, 64.9, 68.06, 70.98, 73.7, 76.25, 78.66, 80.93,
        83.0, 84.68, 86.02, 87.11, 87.99, 88.71, 89.29, 89.76, 90.13, 90.43, 90.66, 90.84, 90.96,
        91.05, 89.79, 88.5, 82.61, 77.59, 76.67, 75.79, 74.93, 74.09, 73.28, 72.49, 71.72, 70.98,
        70.25, 69.55, 66.29, 63.41, 60.86, 58.57, 56.51, 54.64, 52.93, 51.37, 49.93, 48.6, 47.37,
        46.22] MPa

#another orowan from brown and ham # Ahmadi
v=0.33

To7m=[]
x=[1,2,3,4,5,6,7,8,9,10,11,12,13,14,15,16,17,18,19,20,21,22,23,24,25,26,27,28,29,30,35,40,41,4
        2,43,44,45,46,47,48,49,50,55,60,65,70,75,80,85,90,95,100,105,110]
for k in x:
    r=(k)*10**(-9) #m
    f=0.052 #fraction
    Ls=(sqrt(8/(3*pi*f))*2*r)-2*r
    r_i = 2*b
    e=(mu*b)/(2*pi*(sqrt(1-v)))
    c=(pi*r)/(2*r_i)
    Toro_modi=e*(1/Ls)*log(c)
    Toro_modi= round(Toro_modi/(10**6),2)
    To7m.append(Toro_modi)

print(To7m, 'MPa')

[733.51, 591.95, 482.46, 408.58, 355.86, 316.29, 285.42, 260.59, 240.14, 222.97, 208.33, 195.68,
        184.63, 174.88, 166.21, 158.44, 151.44, 145.09, 139.3, 134.0, 129.13, 124.64, 120.47,
        116.61, 113.0, 109.64, 106.48, 103.53, 100.74, 98.12, 86.96, 78.26, 76.74, 75.29,
        73.89, 72.55, 71.27, 70.03, 68.84, 67.69, 66.58, 65.51, 60.68, 56.57, 53.01, 49.92,
        47.19, 44.76, 42.59, 40.64, 38.87, 37.26, 35.79, 34.43] MPa
Precipitation strengthening calculation
#720 weak, strong, modified, orowan, orowan modified
## YS from coh, mod anf inter total 65
q= 1.23
c= 50**q + 10**q +5**q
```

```
#x=[1,2,3,4,5,6,7,8,9,10,11,12,13,14,15,16,17,18,19,20,21,22,23,24,25,26,27,28,29,30,35,40,41,
        42,43,44,45,46,47,48,49,50,55,60,65,70,75,80,85,90,95,100,105,110]
#x_1=[6,7,9,
        10,11,12,13,14,15,16,17,18,19,20,21,22,23,24,25,26,27,28,29,30,35,40,41,42,43,44,4
        5,46,47,48,49,50,55,60,65,70,75,80,85,90,95,100,105,110]

Tp7w1 = [((y**q)+c)**(1/q) for y in Tp7w]
Tp7s1 = [((y**q)+c)**(1/q) for y in Tp7s]
Tp7m1 = [((y**q)+c)**(1/q) for y in Tp7m]

Yield strength calculation¶
## Gb calculation
GB1 = 21.8
gb = 23
k = 750
GB = GB1 + k/sqrt(gb)
print(GB)
178.1858105428061

#720 YS
## YS from GB (178) and SS (300) and Tau from precipitation or orowan
M=3.06
x=[1,2,3,4,5,6,7,8,9,10,11,12,13,14,15,16,17,18,19,20,21,22,23,24,25,26,27,28,29,30,35,40,41,4
        2,43,44,45,46,47,48,49,50,55,60,65,70,75,80,85,90,95,100,105,110]

Tp7w2 = [(y*M)+178+300 for y in Tp7w1]
Tp7s2 = [(y*M)+178+300 for y in Tp7s1]
Tp7m2 = [(y*M)+178+300 for y in Tp7m1]
To71 = [(y*M)+178+300 for y in To7]
To7m1 = [(y*M)+178+300 for y in To7m]

Calculation for bimodal (YS)
#f individual
fs=0.05
fl= 0.13
ftotal=fs+fl
Ns= 90
Nl= 10
ws=Ns/(Ns+Nl)
wl=Nl/(Ns+Nl)
rl=28*10**(-9)/2 #m
rs=6*10**(-9)/2 #m
ravg=ws*rs+wl*rl # universal radius
Ls=sqrt(2*pi/(3*fs))*rs
Ll=sqrt(2*pi/(3*fl))*rl
```

```
l1l=2*sqrt(rl*rl-(rl-rm)**2)
l1s=2*rs
Lamda_s=sqrt(T/(APB*rs))*Ls
V1s=max(Lamda_s, Ls-l1s)
Lamda_l=sqrt(T/(APB*rl))*Ll
V1l=max(Lamda_l, Ll-l1l)
c_s = ws*(l1s/(V1s+2*rs))
c_l= wl*(l1l/(V1l+2*rl))
Tp_bi=(APB/(2*b))*( c_s+ c_l )
Tp_bi =(Tp_bi)/(10**6)# MPa
#for precipitation
q= 1.23
Tp_bi1 = (Tp_bi**q + 50**q + 10**q +5**q)**(1/q)
#for ys
Tp_bi2 = (Tp_bi1*M)+178+250
```

APPENDIX B: SCHMID FACTOR CALCULATION

The expression required for the calculations of the CRSS and the Schmid factor are presented in section 6.4. Here, the method used have been outlined step by step for one grain (Grain 1: 8 7 10), which was repeatedly followed for the other grains. The procedure utilized both the Python and Microsoft Excel as followed:

Firstly, the Euler's angle orientation (252, 46.6, 319) was identified using OIM analysis software using the EBSD data for the grain in the sample co-ordinate. Using the Euler's angle value, an orientation matrix (denoted as g) was generated as per the formula presented in Figure 4-23.

```
p1= 252, p= 46.6, p2= 319
phi1 = (p1*pi)/180
phi = (p*pi)/180
phi2 = (p2*pi)/180
u=math.cos(phi1)*math.cos(phi2)-math.sin(phi1)*math.sin(phi2)*math.cos(phi)
v=-1*math.cos(phi1)*math.sin(phi2)-math.sin(phi1)*math.cos(phi2)*math.cos(phi)
w= math.sin(phi1)*math.sin(phi)

a= math.sin(phi1)*math.cos(phi2)+math.cos(phi1)*math.sin(phi2)*math.cos(phi)
b= -1*math.sin(phi1)*math.sin(phi2)+math.cos(phi1)*math.cos(phi2)*math.cos(phi)
c= -1*math.cos(phi1)*math.sin(phi)
h = math.sin(phi2)*math.sin(phi)
k = math.cos(phi2)*math.sin(phi)
l = math.cos(phi)
g = [u, v, w, a, b, c, h, k, l]
g = [-0.6619257988313488, 0.29043841937954595, -0.6910135754019539, -
0.5784758843899589, -0.7841904488531244, 0.22452392101241744, -
0.4766758731263159, 0.5483528649290039, 0.687087510804423]
```

Further, a dot product of the sample coordinate [1 0 0] for the stress direction and g was calculated to get the stress direction in the crystal orientation using equation (4.4), as shown in Table 8-1.

Table 8-1: The orientation matrix and the sample co-ordinate of the stress direction and their corresponding dot product.

-0.66193	-0.57848	-0.47668	1		-0.66193
0.290438	-0.78419	0.548353	0	=	0.290438
-0.69101	0.224524	0.687088	0		-0.69101

The calculated stress direction was used to calculate the φ (angle between the stress direction and slip plane normal) and λ (angle between stress direction and slip direction), and consecutively, the Schmid factor using equation (4.5). This step was repeated for all the 12 slip systems of FCC, as listed below in Table 8-2.

Table 8-2: The list of all the 12 slip systems for FCC crystal and the correspondingly calculated Schmid factor.

Slip plane	Slip direction	Schmid factor (m)
(11-1)	[011]	0.0523
(11-1)	[101]	0.1765
(11-1)	[1-10]	0.1242
(1-1-1)	[01-1]	0.1047
(1-1-1)	[101]	0.1444
(1-1-1)	[110]	0.0396
(1-11)	[011]	0.2687
(1-11)	[10-1]	0.0195
(1-11)	[110]	0.2492
(111)	[01-1]	0.4257

Table 8-2 (cont'd)

(111)	[10-1]	0.0038
(111)	[1-10]	0.1242

The maximum m corresponds to the highest CRSS following the equation (4.5). Hence, we could identify the corresponding slip system as the active slip system. For example, in Table 8-2 the highest value of was 0.4247 for m. Hence, (111) and [01-1] was identified as the active slip system in the grain 1.